Spring 8-1-2019

Optimal Control Strategies for Complex Biological Systems

Afroza Shirin
University of New Mexico

Follow this and additional works at: https://digitalrepository.unm.edu/me_etds

Part of the Mechanical Engineering Commons

_____

Candidate

_____

Department

This dissertation is approved, and it is acceptable in quality and form for publication:

Approved by the Dissertation Committee:

_____, Chairperson

_____

_____

_____

_____

_____

_____

_____

Optimal Control Strategies for Complex Biological Systems

by

Afroza Shirin

B.Sc, Mathematics, University of Dhaka, 2008

M.S., Mathematics, University of Dhaka, 2010

DISSERTATION

Submitted in Partial Fulfillment of the

Requirements for the Degree of

Doctor of Philosophy

School of Engineering

The University of New Mexico

Albuquerque, New Mexico

July, 2019

Dedication

To my parents.

Acknowledgments

Optimal Control Strategies for Complex Biological Systems

by

Afroza Shirin

B.Sc, Mathematics, University of Dhaka, 2008

M.S., Mathematics, University of Dhaka, 2010

Ph.D., Mechanical Engineering, University of New Mexico, 2019

Abstract

To better understand and to improve therapies for complex diseases such as cancer or diabetes, it is not sufficient to identify and characterize the interactions between molecules and pathways in complex biological systems, such as cells, tissues, and the human body. It also is necessary to characterize the response of a biological system to externally supplied agents (e.g., drugs, insulin), including a proper scheduling of these drugs, and drug combinations in multi drugs therapies. This obviously becomes important in applications which involve control of physiological processes, such as controlling the number of autophagosome vesicles in a cell, or regulating the blood glucose level in patients affected by diabetes. A critical consideration when controlling physiological processes in biological systems is to reduce the amount of drugs used, as in some therapies drugs may become toxic when they are overused. All of the above aspects can be addressed by using tools provided by the theory of optimal control, where the externally supplied drugs or hormones are the inputs to the system. Another important aspect of using optimal control theory in biological systems is to

identify the drug or the combination of drugs that are effective in regulating a given therapeutic target, i.e., a biological target of the externally supplied stimuli.

The dynamics of the key features of a biological system can be modeled and described as a set of nonlinear differential equations. For the implementation of optimal control theory in complex biological systems, in what follows we extract *a network* from the dynamics. Namely, to each state variable x_i we will assign a network node v_i ($i = 1, ..., N$) and a network directed edge from node v_i to another node v_j will be assigned every time x_j is present in the time derivative of x_i. The node which directly receives an external stimulus is called a *driver nodes* in a network. The node which directly connected to an output sensor is called a *target node.*

From the control point of view, the idea of controllability of a system describes the ability to steer the system in a certain time interval towards the desired state with a suitable choice of control inputs. However, defining controllability of large complex networks is quite challenging, primarily because of the large size of the network, its complex structure, and poor knowledge of the precise network dynamics. A network can be controllable in theory but not in practice when a very large control effort is required to steer the system in the desired direction. This thesis considers several approaches to address some of these challenges. Our first approach is to reduce the control effort is to reduce the number of target nodes. We see that by controlling the states of a subset of the network nodes, rather than the state of every node, while holding the number of control signals constant, the required energy to control a portion of the network can be reduced substantially. The energy requirements exponentially decay with the number of target nodes, suggesting that large networks can be controlled by a relatively small number of inputs as long as the target set is appropriately sized. We call this strategy *target control.*

As our second approach is based on reducing the control efforts by allowing the prescribed final states are satisfied approximately rather than strictly. We introduce

a new control strategy called *balanced control* for which we set our objective function as a convex combination of two competitive terms: (i) the distance between the output final states at a given final time and given prescribed states and (ii) the total control efforts expenditure over the given time period. Based on the above two approaches, we propose an algorithm which provides a locally optimal control technique for a network with nonlinear dynamics. We also apply pseudo-spectral optimal control, together with the target and balance control strategies previously described, to complex networks with nonlinear dynamics. These optimal control techniques empower us to implement the theoretical control techniques to biological systems evolving with very large, complex and nonlinear dynamics. We use these techniques to derive the optimal amounts of several drugs in a combination and their optimal dosages. First, we provide a prediction of optimal drug schedules and combined drug therapies for controlling the cell signaling network that regulates autophagy in a cell. Second, we compute an optimal dual drug therapy based on administration of both insulin and glucagon to control the blood glucose level in type I diabetes. Finally, we also implement the combined control strategies to investigate the emergence of cascading failures in the power grid networks.

Contents

Contents

Contents

Contents

Contents

Contents

List of Figures

List of Tables

List of Tables

Glossary

$\mathcal{V}$ Set of all nodes in a network

$\mathcal{D}$ Set of all driver nodes in a network

$\mathcal{T}$ Set of all target nodes in a network

PSOCS   Pseudo-spectral optimal control strategy

Chapter 1

Introduction

1.1 Introduction

To better understand and to improve therapies for complex diseases such as cancer or diabetes, it is not sufficient to identify and characterize the interactions between molecules and pathways in complex biological systems, such as cells, tissues, and the human body. It also is necessary to characterize the response of a biological system to externally supplied agents (such as drugs, hormones) and to define a proper scheduling of these drugs, especially when they are used in combination therapies. This obviously becomes important in applications which involve control of physiological processes, such as controlling the number of autophagosome vesicles in a cell, or regulating the blood glucose level in patients affected by diabetes.

The aim of this thesis is to control a complex biological system where the external agents are used as external control signals. For example, the externally supplied agents are drugs, hormones, etc. Insulin and/or glucagon can be used to regulate the blood glucose level in patients affected by diabetes, where the key features of the physiological process in a diabetic patient represent the complex biological sys-

tem and external insulin and/or glucagon are the external control inputs. Another example is controlling the number of autophagosome vesicles in a cell by using externally supplied drugs, where molecularly targeted drugs are known. The dynamics of the key features of a biological system can be modeled and described as a set of nonlinear differential equations.

A critical consideration when controlling physiological processes in biological systems is to reduce the amount of drugs used, as in some therapies drugs may become toxic when they are overused. All of the above aspects can be addressed by using tools provided by the theory of optimal control, where the externally supplied agents (either drugs or hormones) are the inputs to the system. Another important aspect of using optimal control theory in biological systems is to identify the drug or the combination of drugs that are effective in regulating a given therapeutic target, i.e., a biological target of the externally supplied stimuli.

In order to proceed with the implementation of optimal control theory in complex biological systems, in what follows we extract a network from the dynamics. Namely, to each state variable x_i we will assign a network node $v_i (i = 1, 2, \cdots, N)$ and a network directed edge from node v_i to another node v_j will be assigned every time x_j is present in the time derivative of x_j. A schematic diagram of a simple network with driver and target nodes is presented in Fig. 2.1.

Controllability of complex networks such as gene regulatory networks, neuronal networks, communication networks, networks of infrastructures, food webs, power grids, etc. is not a new topic for the scientific research community [1–14]. From the control point of view, the idea of controllability of a complex network represents the ability to steer the network from an arbitrary initial condition towards a desired state with a suitable choice of control signals.

Different types of control strategies have been presented in [6, 8–12, 14–18] to

control a broad range of networks such as power grids [19, 20], communication networks [21, 22], gene regulatory networks [23], neuronal systems [24, 25], food webs [26], and social systems [27]. However, defining controllability of large complex networks is quite challenging, primarily because of the large size of the network, its complex structure, and imperfect knowledge of the precise network dynamics. A network can be controllable in theory but not in practice when a very large control effort is required to steer the network in the desired direction. This thesis considers several approaches to address some of these challenges.

In chapter 2, we present our first approach to reduce the control effort. The approach is based on reducing the number of the network target nodes. That is, by controlling the states of a subset of the nodes of a network, rather than the state of every node, while holding the number of control signals constant, the required effort to control a portion of the network can be reduced substantially. In the networks, often controlling every member is unnecessary, which makes the control action more 'expensive', by which we mean it requires more effort than needed. For instance, in a foodweb a predator population may need to be reduced in order to increase a prey population, but other species in the foodweb may not need be affected. In marketing, an advertisement agency may want to change the opinion of a certain demographic, but does not need to reach every member of a social network. A certain task, sent to a robotic network may need to be performed by only a subset of its members. There are many control goals that can be conceived of for complex networks, where the desired final state should only be prescribed for some of the members of the network but not for all of them. One of the characterizations to quantify a control effort is the control energy, the cumulative of the square of control action over the time of the control action. We can reduce the amount of control signals used in an attempt to avoid *off-target effects*. We call this control strategy *target control*. We find that the energy requirements exponentially decay as the number of target nodes decreases, suggesting that large networks can be controlled by a relatively

small number of inputs as long as the target set is appropriately sized. In controlling biological system we expect using lower control signals can be beneficial, as in some therapy certain drugs may become toxic when they are overused.

In chapter 3, we present the second control approach. Due to the lack of a proper definition of control objectives, constraints, and the choice of the control strategy, the control efforts may increase and sometimes becomes unfeasible. By composing proper control objectives and constraints, the effort for optimal control can be reduced further. For example, we are driving a car along a road and want to reach a specific position. We could reduce the control effort by compensating some effort by allowing a small deviation from the desired path or the desired final condition. As our second control strategy, we propose that the control effort can be reduced even more if the prescribed final states are not satisfied strictly. We introduce a new control strategy called *balanced control* for which we set our objective function as a convex combination of two competitive terms: (i) the distance between the final output states at a given final time and given prescribed states and (ii) the total control effort expenditure over the given time period. We show how the control energy of complex network can be reduced substantially by following the balance control approach.

The above two optimal control methods are mathematically developed for linear time invariant systems (LTI) associated with a complex network. However, in reality, most complex biological systems evolve based on nonlinear dynamics and so the extracted complex networks from these systems are governed by nonlinear dynamics. Recent work investigates control strategies for complex networks governed by nonlinear dynamical equations. [8, 14, 16, 20, 28–33].

Though our proposed optimal control techniques are derived for LTI systems, the idea of target control and balance control can be applied to biological networks governed by nonlinear dynamics. Optimal control techniques are being used for years

in designing optimal chemotherapies in HIV [34, 35] and cancer [35–39], in optimal vaccination and treatment for epidemics [40, 41], in controlling epidemics [42–44], in controlling cascading failures in power grids [45, 46], and in regulating blood glucose in diabetic patients [47–54]. While controlling such biological networks optimally, we have several objectives: 1) Reduce the amount of control inputs to avoid off-target effects and associated toxicities (in some therapy some drugs become toxic when they are overused). This corresponds to implementation of the target control strategy. 2) Reduce the amount of control action by composing proper control objectives and constraints so that the condition on the target state becomes a *soft constraint.* By this we mean a constraint which is relaxed and fall in some interval around a nominal value, whereas a hard constrain must be exactly satisfied at the nominal value. This corresponds to implementation of the balance control strategy. 3) Identify combinations of control signals that provide a desired control performance.

For a given nonlinear dynamical system, we extract a complex network, identify the driver and target nodes, and design a nonlinear optimal control problem, by keeping in mind the above 3 ideas. As we will see, optimal control strategies that are obtained by following the above steps limit the overall control effort expenditure. Finally, we use pseudo-spectral optimal control (PSOC) [55] and interior point optimization techniques [56] to solve the nonlinear optimal control problem, as mathematical framework exists to solve this type of nonlinear optimal control problems analytically. In chapter 4, we briefly present the pseudo-spectral optimal control and interior point optimization techniques.

For implementation in biological systems, our goal is to design optimal drug dosing schedules that minimize the amount of drug needed to achieve an important activity/process in the system. As we will see, we will achieve this goal by designing combinatorial drug therapies.

In chapter 5, we consider the Glucose-Insulin-Glucagon (GIG) model which de-

scribes the bodily response to exogenously supplied insulin and glucagon in patients affected by Type I diabetes. The model was first proposed in [57] and later updated in [58] and [59]. Insulin and glucagon are pancreatic hormones that help regulate the levels of glucose in the blood. Insulin is produced by the *beta-cells* in the pancreas and carries glucose from the bloodstream to the cells throughout the body. Glucagon releases glucose from the liver into the bloodstream in order to prevent hypoglycemia. In people affected by diabetes insulin is either absent (type I diabetes) or not produced in the proper amount (type II diabetes). In type I diabetes the body's immune system attacks and destroys the beta cells. As a result, insulin is not produced and glucose accumulates in the blood which may cause serious harm to several organs. Type II diabetes is a metabolic disorder in which the beta cells are unable to properly regulate the blood glucose within proper limits. We present a *network* representation of the GIG model in Fig. 1.1. Each one of the state variable x_i, $i = 1, \cdots, 17$, is associated with a node which is shown as a green circle in the figure. A directed edge (shown as a black arrow in the figure) is drawn from node x_i to node x_j, if the state x_i appears in the time derivative of the state x_j. In this model, u_I and u_G are the insulin and glucagon, respectively, i.e., external inputs acting on the nodes I_{sc1} and H_{sc1}. Thus the set of drivers node $\mathcal{D} = \{I_{sc1}, H_{sc1}\}$. In this model the plasma glucose G_p is the main variable we are trying to affect through the control action, thus the set of target nodes $\mathcal{T} = \{G_p\}$. In the figure, the driver nodes are colored cyan and the target nodes are colored magenta. As can be seen, the effect of the control inputs on the target node is mediated by the network structure, thus this particular structure plays an important role in our ability to control the network output. The optimal control theory has been used before to regulate the glucose level for diabetes patients, but most of the works are done where the models were either overly simplified or linear [47–54, 60–67]. Moreover, most of the works done above considered only insulin as a control input. Here, we use both insulin and glucagon as control inputs. An outstanding research question, which we address

here, is the determination of the temporal dosages of both insulin and glucagon, in the case of a dual therapy. We also evaluate the performance limits of the control strategy in the blood glucose problem, and discuss the advantages of the dual drug therapy compared to the single drug therapy.

In chapter 6, we apply optimal control methods to design drug schedules for manipulating autophagy, a stress-relieving/homeostatic cellular recycling process that, when nutrients are in limited supply, generates building blocks for protein synthesis through degradation of cytoplasmic contents [68], such as cytotoxic protein aggregates that are too large for proteosomal degradation and damaged organelles (e.g., depolarized mitochondria). Autophagy also plays an important role in immunity [69, 70]; the autophagic degradative machinery can be directed to target intracellular microbes, such as *Mycobacterium tuberculosis*, for destruction. Cytoplasmic contents that are targeted for autophagic degradation are first trapped in double-membrane vesicles, termed autophagosomes or autophagic vesicles (AVs), and then delivered to lysosomes for digestion [71, 72]. In cancer, and other contexts, autophagy is a double-edged sword [73]. It can protect cancer cells from stresses of the tumor environment (e.g., lack of nutrients because of defective vasculature) or induce cell death if recycling is excessive. Thus, there are potential benefits to be gained by using drugs to either upregulate autophagy (to kill malignant cells through excessive recycling) or downregulate autophagy (to kill cancer cells that rely on autophagy for survival) [74]. Although there is much current interest in using combinations of molecularly targeted drugs to improve outcomes for cancer patients [75, 76], relatively little work has been done in the area of formal therapy design, meaning therapy selection and/or scheduling driven by insights from mathematical models [77, 78]. We use optimal control to design monotherapy and dual therapy to regulate the AVs in cancer cells. The therapy design approach presented in this thesis is flexible and allows for the evaluation of drug combinations.

In chapter 7, we finally consider the implementation of optimal control to power-grid networks. A power-grid system consists of generators, buses, and transmission lines. In the absence of any undesirable external intervention, the power-grid system is synchronized. When a power-grid system experiences this type of intervention, we may identify such intervention as an attack to the system. We aim to identify the sequence of transmission line failures in a power-grid system and also rank the buses in terms of their vulnerability under the assumption that power grid system is under attack such as natural disaster, weapons of mass destruction, deliberate human-made attacks or cyber-attacks. We are interested in both the spatial aspect, i.e., the choice of the targets, and the particular temporal sequence, i.e., the times at which the attacks are scheduled over a given time period. We will attempt to solve a constrained optimization problem, with the goal of calculating the most devastating attack to a known critical infrastructure, given a fixed amount of resources available to the attackers (e.g., only a certain number of attacks can be completed in the given time span). As we will see, the temporal aspect, i.e., the particular sequence of the attacks, will play a crucial role on the overall impact of the coordinated attack, as particular sequences of attacks are more prone to generating cascading failures.

$$\mathcal{V} = \{G_p, G_t, I_l, I_p, I', X^L, Q_{sto1}, Q_{sto2}, Q_{gut}, X, SR_H^s, H, X^H, I_{sc1}, I_{sc2}, H_{sc1}, H_{sc2}\}$$
$$\mathcal{D} = \{I_{sc1}, H_{sc1}\}$$
$$\mathcal{T} = \{G_p\}$$
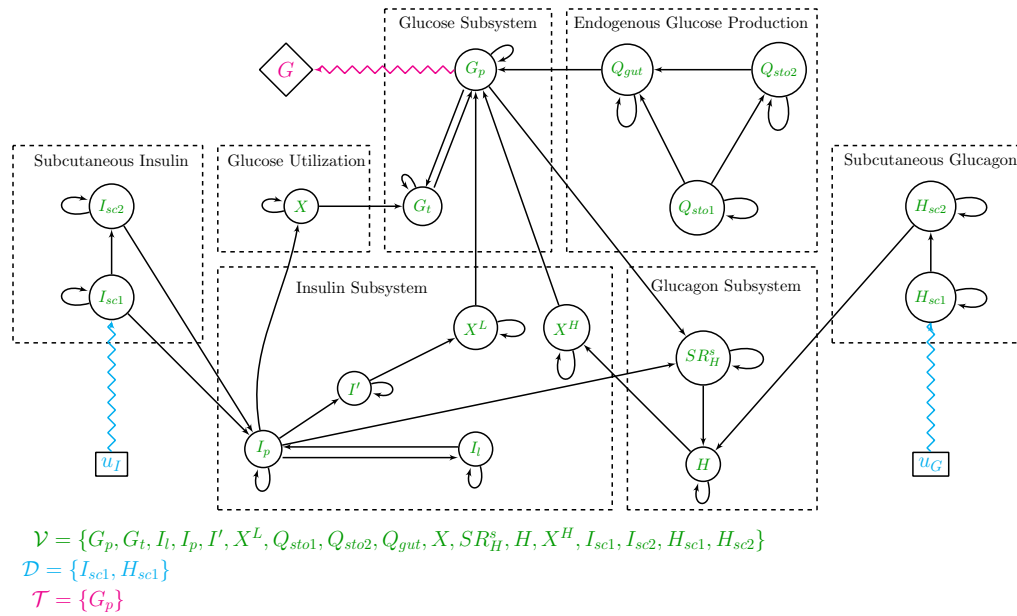
Figure 1.1: Network representation of the GIG model with color-coded input signals (blue) and output sensors (magenta). Nodes directly connected to the pink output is target node, that is, they have a prescribed final state that we wish to achieve in finite time, t_f. The set of node $\mathcal{V}$ in the network, the set of driver nodes $\mathcal{D}$, and the set of target nodes $\mathcal{T}$.

Chapter 2

Target Control of Complex Networks

2.1 Introduction

The most complex networks that arise in science and engineering are governed by nonlinear dynamics, and because of the uncertainty of the precise dynamics, the controllability of complex networks become difficult [6, 79, 80]. Nonetheless, controlling the linear systems have proven to be adequate in many applications by approximating nonlinear systems as linear systems in local regions of state space [81]. Controllability of complex networks governed with linear dynamics such as gene regulatory networks, neuronal networks, communication networks, networks of infrastructures, food webs, power grids, etc. has become intensely focused in the scientific research community [1–14]. From the control point of view, the idea of controllability of complex networks describes the ability to steer the network from an arbitrary initial condition toward the desired state with a suitable choice of a control signal. Different types of control strategies have been proposed in [6, 8–12, 14–18] to control a broad range of networks such as power grid [19, 20], communication networks [21, 22], gene regulatory networks [23], neuronal systems [24, 25], food webs [26], and

social systems [27]. If a network is controllable, the control signal that derives the system from an arbitrary initial condition towards the desired sates is not necessarily unique. One important metric to characterize these control signals is the control energy, the cumulative of the square of control signal over the time of the control action. From optimal control theory, we can define the control signal that, for a given distribution of the control input signals, satisfies both our initial and final conditions as well as minimizes the control energy required to perform the task [82]. However, the controllability concept just provides a yes/no answer that does not take into account the energy needed to control a network [17]. A consequence is that even if a network is controllable with a particular set of driver nodes, the control energy may unrealistically large. Reducing the control energy, with a fixed set of driver nodes, is a more difficult task. Moreover, if the size of a network is prohibitively large, then the network can be controllable in theory but not in practice because unfeasible amounts of control energy are required to steer the system towards the desired direction. While controlling a complex network, thus it becomes essential to reduce the required control energy. The minimum energy framework has been examined in [16, 17] which have shown that based on the underlying network structure, the set of driver nodes, the desired final state, and other parameters, the energy to control a network may lie on a distribution that spans a broad range of orders of magnitude. One of the methods to reduce the required energy was investigated in [18], where additional control signals were added in optimal locations in the network according to each node's distance from the current set of control signals. Refs. [16, 17] have only investigated the control energy for complex networks when the target set coincides with the set of all nodes. Refs. [14, 79] examined methods to choose a minimal set of independent control signals necessary to control just the targets. In addition, in spite of the numerous attempts [16–18, 83–87], no clear strategy has yet emerged for the related problem of reducing and scaling the control energy.

The aim of this chapter is to shed light on reducing the minimum control energy

of complex networks and propose a scaling relation for the minimum control energy. With respect to the current literature, we control the states of a subset of the nodes of a network, rather than the state of every node. We show that by controlling the states of a subset of the nodes of a network, while holding the number of control signals constant, the required energy to control a portion of the network can be reduced substantially. We find that the energy requirements exponentially decay with the number of target nodes, suggesting that large networks can be controlled by a relatively small number of inputs as long as the target set is appropriately sized. We name this control method *target control*. We validate our conclusions in human-maid and real networks with linear dynamics to arrive at an energy scaling law to better design control objectives regardless of system size, energy restrictions, state restrictions, input node choices and target node choices.

2.2   Preliminaries

We begin by introducing some of the basic ideas in the context of dynamical systems, graphs and complex networks.

Graph and Network

A *graph* $\mathcal{G}(\mathcal{V}, \mathcal{E})$, consists of a set $\mathcal{V} = \{x_i\}$, $i = 1, \ldots, n$ to be the set of n nodes and a set $\mathcal{E}$ of edges, where $\mathcal{E}$ is identified with a set of ordered pairs $\{x_i, x_j\}$ of nodes $x_i, x_j \in \mathcal{V}$. If a node x_i affects a node x_j then there exist an edge $\{x_i, x_j\} \in \mathcal{E}$. A *weighted graph* has weights associated with each edge. A *network* is a graph when the point of interests is real phenomena, e.g., physical, biological, social science, etc. In Fig. 2.1, we present the graphical representation of a simple 5 nodes network.

Dynamical System

A dynamical system is a system which is defined by a set of state variables in a space, and each state variable represents a component of the system and evolves according to a first-order differential equation. A dynamical system with n state variables can be mathematically formulated as

$$\dot{\mathbf{x}}(t) = \mathbf{f}((\mathbf{x}(t), t) \tag{2.1}$$

where $\mathbf{x}(t) \in \mathbb{R}^{n \times 1}$ is the time varying state vector, the function $\mathbf{f} \in \mathbb{R}^{n \times 1}$ defines the rule how a state variable evolves with time, and t is the physical time.

Complex Networks or Dynamical Networks

Complex networks typically consist of two parts; a set of nodes with their interconnections that represent the topology of the network, and the dynamics which describe the time evolution of the network nodes. The prescribed dynamics of the nodes can be linear or non-linear. We can construct a dynamic network from a dynamical system, simply by considering a state variable as a node and by drawing a link from a node x_i to another node x_j if x_i is present in the time derivative of x_j. Figure 2.1 demonstrates a simple schematic diagram of a 5 nodes networks in where $\mathcal{V} = \{x_1, x_2, x_3, x_4, x_5\}$ is the set of nodes and $\psi_{i,j}$ represents the interaction between the nodes x_i and x_j.

Controllability of Complex Network

A complex network is controllable if a set of appropriate control signals can drive the network from an arbitrary initial condition to any final condition in finite time.

Driver Nodes and Target Nodes

Driver nodes are the nodes in a network which directly receive the external control signal. *Target nodes* are the nodes in a network which have prescribed states that must be satisfied. We define $\mathcal{D}$ the set of driver nodes and $\mathcal{T}$ the set of target nodes. In Fig. 2.1, we demonstrate the driver nodes which directly receive the external control signals from the cyan nodes and the target nodes which has prescribed state conditions directly connected to the pink output nodes.

2.3 Methods

2.3.1 Problem Formulation

We introduce the minimum energy target control problem for complex networks. We consider linear dynamical systems. The linear time invariant (LTI) network dynamics are,

$$\dot{\mathbf{x}}(t) = A\mathbf{x}(t) + B\mathbf{u}(t)$$
$$\mathbf{y}(t) = C\mathbf{x}(t)$$

(2.2)

where $\mathbf{x}(t) = [x_1(t), \ldots, x_n(t)]^T$ is the $n \times 1$ time-varying state vector, $\mathbf{u}(t) = [u_1(t), \ldots, u_m(t)]^T$ is the $m \times 1$ time-varying external control input vector, and $\mathbf{y}(t) = [y_1(t), \ldots, y_p(t)]^T$ is the $p \times 1$ time-varying vector of outputs, or target states. The matrix $A \in \mathbb{R}^{n \times n}$ is the adjacency matrix that describes the topology, or interaction, of the n nodes, or states. The elements A_{ij} of A is nonzero if node i receives a signal from node j. In addition, the diagonal values of A, a_{ii}, $i = 1, \ldots, n$, which represent self-regulation, such as birth/death rates in food webs, station keeping in vehicle consensus, degradation of cellular products, etc., are chosen to be unique at each node (see proposition 1 in [88]). These diagonal values are chosen to also

guarantee that A is Hurwitz so the system in Eq. (2.2) is internally stable. The matrix $B \in \mathbb{R}^{n \times m}$ is the control input matrix that describes how the m control input signals are injected, and the matrix $C \in \mathbb{R}^{p \times n}$ is the output matrix that expresses the relations between the states that are designated as the outputs. To formulate target control problem we assume that $B(C)$ has columns (rows) that are all versors, i.e., each control input, $u_i(t), i = 1, ..., m$, is directed towards a single node and each output, $y_j(t), j = 1, ..., p$, is the state of a single node. Our selection of the matrix B is due to our assumption that different network nodes may be selectively affected by a particular control signal, e.g., a drug interacting with a specific node in a protein network. A small sample schematic is shown in Fig. 2.1 that demonstrates the graphical layout of our problem emphasizing the graph structure and the role of input and target nodes. In Fig. 2.1 nodes 1 and 3 are driver nodes receiving directly to the external source. We define $\mathcal{D} \subseteq \mathcal{V}$ as the subset of input nodes. Here by an target node, we mean a node that directly connected to the pink outputs, that is they have a prescribed final state that we wish to achieve in finite time, t_f, such as nodes 1, 2 and 4 in Fig. 2.1. We define $\mathcal{T}_p \subseteq \mathcal{V}$ as the subset of target nodes and $p = |\mathcal{T}_p|$ as the number of target nodes. The minimum energy target control problem for complex networks where the word *target* refers to those nodes with a prescribed final condition. The problem is as follows:

$$\min_{\mathbf{u}(t)} \quad J = \frac{1}{2} \int_{t_0}^{t_f} \mathbf{u}^T(t)\mathbf{u}(t)dt \tag{2.3a}$$

$$\text{s.t.} \quad \dot{\mathbf{x}}(t) = A\mathbf{x}(t) + B\mathbf{u}(t) \tag{2.3b}$$

$$\mathbf{y}(t) = C\mathbf{x}(t) \tag{2.3c}$$

$$\mathbf{x}(t_0) = \mathbf{x}_0, \quad \mathbf{y}(t_f) = \mathbf{y}_f \tag{2.3d}$$

After computing the Hamiltonian and solving the resulting system of ODEs, the minimum energy control signal which minimizes the objective function in Eq. (2.3) and derive the system from an arbitrary initial condition to a prescribed final output

states within the finite time interval $[t_0, t_f]$ to be,

$$\mathbf{u}^*(t) = B^T e^{A^T(t_f - t)} C^T \left(CWC^T \right)^{-1} \left(\mathbf{y}_f - e^{A(t_f - t_0)} \mathbf{x}_0 \right) \tag{2.4}$$

For details derivation, please see Appendix A.1. With the optimal control input $\mathbf{u}^*(t)$, the time evolution of the output states is,

$$\mathbf{y}(t) = C e^{A(t - t_0)} \mathbf{x}_0 + C \int_{t_0}^{t} e^{A(t - \tau)} B \mathbf{u}(\tau) d\tau, \tag{2.5}$$

and the states can also be determined,

$$\mathbf{x}(t) = e^{A(t - t_0)} \mathbf{x}_0 - \int_{t_0}^{t_f} e^{A(t - \tau)} B B^T e^{A^T(t_f - \tau)} d\tau C^T \hat{\boldsymbol{\nu}}_f \tag{2.6}$$

Here $\hat{\boldsymbol{\nu}}_f$ is constant vector and is determined by the prescribed final condition for the targeted nodes,

$$\hat{\boldsymbol{\nu}}_f = - \left(CWC^T \right)^{-1} \left(\mathbf{y}_f - e^{A(t_f - t_0)} \mathbf{x}_0 \right) \tag{2.7}$$

The controllability Gramian matrix W is symmetric, positive semi-definite and is given by

$$W = \int_{t_0}^{t_f} e^{A(t_f - \tau)} B B^T e^{A^T(t_f - \tau)} d\tau \tag{2.8}$$

If the system (A, B, C) is output controllable, then the matrix $W_p = CWC^T$ is positive definite. W_p is the output controllability Gramian and is a $p \times p$ principal submatrix of W. The optimal control energy corresponding to the optimal control input $\mathbf{u}^*(t)$ is,

$$E^{(p)} = \left(\mathbf{y}_f - C e^{A(t_f - t_0)} \mathbf{x}_0 \right)^T \left(CWC^T \right)^{-1} \left(\mathbf{y}_f - C e^{A(t_f - t_0) \mathbf{x}_0} \right) = \boldsymbol{\beta}^T W_p^{-1} \boldsymbol{\beta} \tag{2.9}$$

where the vector $\boldsymbol{\beta} = \mathbf{y}_f - C e^{A(t_f - t_0)} \mathbf{x}_0$ is the *control maneuver*. The five node network example of the benefits of target control is shown in Fig. 2.2A-F. In the first scenario, Fig. 2.2A-C, each node has a prescribed final state ($p = n = 5$) and in the second scenario 2.2D-E only 3 nodes are targeted ($p = 3$). The energy is calculated for each

scenario by integrating the curves in Figs. 2.2C and 2.2F from which we find that $E^{(5)} = 1.21 \times 10^4$ and $E^{(3)} = 72.81$. Even though the second scenario has almost one half of the targets, the energy is reduced by 99% (compare also the different scales on the y-axis of Figs. 2.2C and 2.2F).

2.3.2 Worst Case Direction

The optimal energy, $E^{(p)} = \boldsymbol{\beta}^T W_p^{-1} \boldsymbol{\beta}$ in 2.9, associated with the optimal control input $\mathbf{u}^*(t)$ in Eq. 2.4, depends on the number of target nodes p in the target set $\mathcal{T}_p$. According to the choice of the matrix C (rows are linearly independent versors), the reduced Gramian W_p in Eq. (2.8) is a p-dimensional principal submatrix of W. We denote the eigenvalues of W_p as $\mu_i^{(p)}$, $i = 1, \ldots, p$, which are ordered such that $0 < \mu_1^{(p)} \leq \ldots \leq \mu_p^{(p)}$ when the triplet (A, B, C) is output controllable. We define the magnitude of the vector, $|\boldsymbol{\beta}| = \beta$. According to the Min-Max theorem, we can provide an upper and lower bounds for the optical control energy $E^{(p)}$. The upper and lower bounds of $E^{(p)}$ are the functions of the minimum and maximum eigenvalues of W_p, receptively, and given by,

$$0 < \frac{\beta^2}{\mu_p^{(p)}} \leq \boldsymbol{\beta}^T W_p^{-1} \boldsymbol{\beta} \leq \frac{\beta^2}{\mu_1^{(p)}} < \infty. \tag{2.10}$$

The upper bound of the control energy for any control action is $\max\left\{E^{(p)}\right\} \sim \frac{1}{\mu_1^{(p)}}$, which we call the 'worst-case' energy for the minimum control energy problem and denote by $E_{\max}^{(p)}$. For an arbitrary vector $\boldsymbol{\beta}$, which can be represented as a linear combination of the eigenvectors of W_p, the energy can be defined as a weighted sum of the inverse eigenvalues, $1/\mu_i^{(p)}$, which includes the worst-case energy. Moreover, for the large scale-free networks that are of interest in applications, typically $\mu_1^{(p)} <<$ $\mu_j^{(p)}$, $j = 2, \ldots, p$, and $1/\mu_1^{(p)}$ provides the approximate order of the energy required to move the system in any arbitrary direction of state space.

We investigate how the selection of the target nodes affects $E_{\max}^{(p)}$, the inverse of

the smallest eigenvalue of the output Gramian W_p. In order to better understand the role of the number of target nodes on the worst-case energy, we consider an iterative process by which we start from the case when every node is in the target set, $\mathcal{T}_n = \mathcal{V}$, and progressively remove nodes. Say $\mu_j^{(i)}$ ($\mu_j^{(i-1)}$) is an eigenvalue of W_i before (after) removal of a target node. By Cauchy's interlacing theorem we have that,

$$0 < \mu_1^{(i)} \leq \mu_1^{(i-1)} \leq \mu_2^{(i)} \leq \mu_2^{(i-1)} \leq \ldots \leq \mu_{i-1}^{(i)} \leq \mu_{i-1}^{(i-1)} \leq \mu_i^{(i)} \tag{2.11}$$

In particular, from Eq. (2.11), we note that $\mu_1^{(i)} \leq \mu_1^{(i-1)}$, indicating that the smallest eigenvalue cannot decrease after removal of a target node. This implies that the maximum energy $E_{\max}^{(i)} \geq E_{\max}^{(i-1)}$ for all i such that $1 \leq i \leq n-1$.

2.3.3   Choice of Input Nodes

According to our problem formulation, the adjacency matrices A have unique diagonal elements along the main diagonal. These type of matrices of the underlying networks can be controlled with a single control input attached to the power-dominating set (PDS) of the underlying graph. (see Theorem 1 and proof in [88]). The PDS is the smallest set of nodes from which all other nodes can be reached, i.e., there is at least one directed path from the nodes in the PDS to every other node in the network. In our work presented here, we compute an over-estimate of the PDS (that retains the property that all other nodes in the network are reachable) and attach a *unique control input* to each node in the set. We then add additional nodes, chosen randomly, to the set of input nodes until there are m input nodes where m is pre-defined integer less than n. Thus, if there are m input nodes, then there are m control inputs (see the sample network in Fig. 2.1).

2.3.4 Numerical Controllability

A network can be controllable theoretically but it is quite hard to control numerically depending on the dimension and the structure of the network. This issue arises in Gramian based control schemes as the condition number of the Gramian can be quite large for certain 'barely' controllable systems. For this chapter, we use the multi-precision package Advanpix for Matlab so we can examine the trends of the minimum eigenvalue of the output controllability Gramian W_p even when there is a relatively small number of control inputs which would otherwise make some networks be not numerically controllable using double precision. We use the Matlab toolbox Advanpix [89] allows the computation of the eigendecomposition of the Gramian W to be performed in an arbitrarily precise manner. Say μ_i and $\boldsymbol{v}_i$ are the ith eigenvalue and eigenvector, respectively. The average residual error, using Advanpix, is,

$$\langle |W\boldsymbol{v}_i - \mu_i\boldsymbol{v}_i| \rangle = \mathcal{O}(10^{-a}). \tag{2.12}$$

Typical values of a used throughout this paper are 100 to 200.

Also to approximate the integral in Eq. (2.4), we use Legendre-Gauss (LG) quadrature with appropriate weights and points.

$$E_c^{(p)} = \int_{t_0}^{t_f} \boldsymbol{u}_c^{*T}(t)\boldsymbol{u}_c^*(t)dt \approx \frac{t_f - t_0}{2} \sum_{i=1}^{L} w_i \boldsymbol{u}_c^{*T}(\tau_i)\boldsymbol{u}_c^*(\tau_i) \tag{2.13}$$

We choose $L = 50$ and compute the necessary LG weights w_i and LG points τ_i, $i = 1, \ldots, 50$.

2.4 Result

2.4.1 Energy Scaling with Reduction of Target Space

From Eq. (2.11), it is clear, but not obvious that $\mu_1^{(p)}$ increases as p decreases. We would like to determine the rate of increase of $\mu_1^{(p)}$ as p decreases. We assume at each step p, $\mathcal{T}_p$ contains p nodes in the target set (such that $\mathcal{T}_p \subset \mathcal{T}_{p+1}$ and p decreases from $n-1$ to 1) and the output controllability Gramian is partitioned such that W_p is a principal minor of W_{p+1}.

$$W_{p+1} = \begin{bmatrix} w_{pp} & \mathbf{w}_p^T \\ \mathbf{w}_p & W_p \end{bmatrix} \tag{2.14}$$

Here $\bar{W}_p$ is the matrix W_{p+1} except that the first row of W_{p+1} in Eq. (2.14) has been replaced with zeros. The vectors $\mathbf{v}_p$ ($\bar{\mathbf{v}}_p$) is the left (right) eigenvector associated with the smallest eigenvalue of W_p ($\bar{W}_p$). The relation between two consecutive values, $\mu_1^{(p)}$ and $\mu_1^{(p+1)}$, can be expressed linearly as $\mu_1^{(p)} = \mu_1^{(p+1)}\eta_p$ where

$$\log E_{\max}^{(j)} - \log E_{\max}^{(k)} = \sum_{i=k}^{j-1} \log \eta_i = (j-k)\log \bar{\eta}_{(k \to j)}. \tag{2.15}$$

The notation $[\mathbf{a}]_1$ denotes the first value of a vector $\mathbf{a}$. Each value of η_p exactly quantifies the rate of increase at each step of the specific process. η_p also relates the maximum energies between two consecutive steps as,

$$E_{\max}^{(p+1)} = E_{\max}^{(p)}\eta_p. \tag{2.16}$$

This allows us to relate any two target sets of size k and j such that $1 \le k < j \le n$ and $\mathcal{T}_k \subset \mathcal{T}_j$,

$$\log E_{\max}^{(j)} - \log E_{\max}^{(k)} = \sum_{i=k}^{j-1} \log \eta_i = (j-k)\log \bar{\eta}_{(k \to j)} \tag{2.17}$$

where $\bar{\eta}_{(k \to j)}$ is the geometric mean of η_i, $i = k, \ldots, (j-1)$, which is *independent* of the order of the nodes chosen to be removed between $\mathcal{T}_k$ and $\mathcal{T}_j$. To define a network characteristic parameter η, we average Eq. (2.17) over many possible choices of the target sets $\mathcal{T}_k$ and $\mathcal{T}_j$, where we have selected $k = n/10$ and $j = n$,

$$\eta \equiv n \left\langle \log \bar{\eta}_{(\frac{n}{10} \to n)} \right\rangle \tag{2.18}$$

where the symbol $\langle \cdot \rangle$ indicates an average over many possible choices of $n/10$ nodes for the target set. By applying Eq. (2.18) to Eq. (2.17) and by setting $k = n/10$ and $j = p > k$ (for the an extended discussion see Appendix A.2, we achieve the scaling equation used throughout the simulations,

$$\left\langle \log E_{\max}^{(p)} \right\rangle \sim \frac{p}{n} \eta. \tag{2.19}$$

The above relation shows that the energy decays exponentially as p/n decreases. Further details of the scaling law and its relation to the spectral characteristics of the output controllability Gramian can be found in Appendix A.2.

2.4.2 Scaling Law and Network Topology

The rate of this exponential decrease in energy, η, depends on network topology. One common way to characterize the topology of a network is by its degree distribution. Often the in-degree (For each node i we count the number of receiving connections, called the in-degree k_i^{in}) and out-degree (the number of outgoing connections, called the out-degree k_i^{out}) distributions of networks that appear in science and engineering applications are scale-free, i.e., $p(k) \sim k^{-\gamma}$ where k is either the in-degree or out-degree with corresponding γ_{in} and γ_{out}, and most often $2 \leq \gamma \leq 3$ [80].

The average in-degree and average out-degree for a network is k_{av}. We compute the value of η for fifty scale-free model networks, constructed with the static model in Ref. [90] for specific parameters k_{av}, the average degree, and $\gamma_{\text{in}} = \gamma_{\text{out}} = \gamma$, the

power law exponent of the in- and out-degrees, and take the mean over the realizations.

We observe the linear relationship in Eq. (2.19) in Fig. 2.3, where $\frac{p}{n}$ is decreased from 1 (the target set $\mathcal{T}_n = \mathcal{V}$) to 0.1 (the target set consists of 10% of the nodes drawn randomly from the set of all nodes). We see in Fig. 2.3 that η varies with both of the network parameters γ and k_{av}. A large value of η indicates that target control is highly beneficial for that particular network, i.e., the average energy required to control a portion of that network is much lower when the size of the target set is reduced. In Figs. 2.3A and 2.3B, the exponentially increasing value of the worst-case energy $E_{\mathrm{max}}^{(p)}$ is shown with respect to the size of the target set normalized by the size of the network, p/n, for various values of $\gamma_{\mathrm{in}} = \gamma_{\mathrm{out}} = \gamma$ when $k_{\mathrm{av}} = 2.5$ and 8.0, respectively. The bars in Figs. 2.3A and 2.3B are one standard deviation over the fifty realizations each point represents, or in other words, when p nodes are in the target set $\mathcal{T}_p$, it is most likely that $E_{\mathrm{max}}^{(p)}$ will lie between those bars. The decrease of η as γ and k_{av} increase for scale-free networks is displayed in Fig. 2.3B. Overall, we see that η is largest for sparse, nonhomogeneous networks (i.e., low k_{av} and low γ) which are also the 'hardest' to control, i.e., they have the largest worst-case energy when all of the nodes are targeted. This indicates that target control will be particularly beneficial when applied to metabolic interaction networks and protein structures, some of which are symmetric and which are known to have low values of γ [80], as seen in Fig. 2.3C, where both classes of networks are shown to have large values of η.

The effects other network parameters have on η are examined in Fig. 2.4. Figure 2.4A displays some sample curves for $E_{\mathrm{max}}^{(p)}$ for shorter or longer values of $(t_{\mathrm{f}} - t_0)$, the time horizon. We observe the linear relationship in Eq. (2.19) in Fig. 2.4 The inset shows how η increases as the time horizon $(t_{\mathrm{f}} - t_0)$ decreases. We see that when $(t_{\mathrm{f}} - t_0)$ approaches zero from the right, η increases sharply, which shows the increased benefit of target control as the time horizon is reduced. Figure 2.4B examines how

$E_{\mathrm{max}}^{(p)}$ changes for various numbers of input nodes (represented as a fraction of the total number of nodes in the network). The inset collects values of η for different values of n_{d}, which increases as the number of input nodes is decreased. The role of the time horizon [17] and the number of input nodes [16] on the control energy have been discussed in the literature for the case in which all the nodes were targeted.

Comparing the results between both panels in Fig. 2.4 and the results in Fig. 2.3, we see that each parameter has more or less of an effect on the control energy. Shortening the time horizon from the nominal value $t_{\mathrm{f}} = 1$ (which was used in Fig. 2.3) by four orders of magnitude doubled the value of η. Decreasing the value number of input nodes from $n/2$ (the number used in Fig. 2.3) to only $n/5$ also roughly doubled the value of η. In comparison, increasing the heterogeneity of the network, by decreasing the power-law exponent γ, from three to slightly larger than two increased η ten to twenty fold. Clearly the underlying topology, as described by the power-law exponent, plays the largest role in determining (and thus affecting) the control energy.

For the simulations in Figs. 2.3 and 2.4, around 50% of the nodes are chosen to be input nodes (which we have verified yields a controllable pair (A, B)).

2.4.3   Scaling Law and Real Networks

We also analyze datasets collected from various fields in science and engineering to study how the worst-case energy changes with the size of the target set for networks with more realistic structures. We are particularly interested in the possibility that these networks display different properties in terms of their target controllability, when compared to the model networks analyzed. To this end, we consider different classes of networks, e.g., food webs, infrastructure, metabolic networks, social interactions, etc. For each network we choose edge weights and diagonal values from the

uniform distribution as discussed in the section 2.2. Overall we see a similar relationship in terms of the average degree k_{av} and η in Fig. 2.5C as for the model networks in Fig. 2.5C. The real datasets which have a large worst-case energy when all of the nodes are targeted, $E_{\max}^{(n)}$, tend to also have the largest value of η which acts as a measure of the rate of improvement with target control. It should be noted that the value of η varies little within each class of networks (e.g., food webs, infrastructure, metabolic networks, social interactions, etc. as seen in Fig. 2.5C) which suggests that the structure of each class is similar. Fields of study where networks tend to have a large η would benefit the most from examining situations when a control law could be implemented that only targets some of the elements in the network.

For an arbitrary network, η cannot be accurately determined from a single value of $E_{\max}^{(p)}$ as some networks which have a large worst-case energy when every node is targeted can have a much smaller worst-case energy when only a small portion of the network is controlled as compared to other networks. It is interesting to note from Figs. 2.5A and 2.5B that at some target fraction p/n the energy trends of two different real networks may cross. Specifically, in Fig. 2.5A, when every node is targeted, $p/n = 1$, the *s420st* [91] circuit has a larger maximum energy, $E_{\max}^{(n)}$, than the *TM-met* [92] metabolic network. However, when p/n is smaller than 0.6, it requires, on average, more energy to control a portion of the *TM-met* network than an equivalent portion in the *s420st* network. The same type of behavior is seen in Fig. 2.5B between three networks: Food web *Carpinteria* [93], a protein interaction network *prot_struct_1* [91] and social network *FB forum* [94]. In summary, we can see that one can estimate the value of η from the average degree of the network but to determine the worst-case energy, at least one point along the energy curve for a specific cardinality of the target set is also required (as in Figs. 2.5A and 2.5B). We numerically compute values of η for real datasets and compiled in Table 2.1. For the simulations in Figs. 2.5, around 50% of the nodes are chosen to be input nodes the pair (A, B) is controllable.

2.4.4   Practical Computation of η.

Here we provide additional details on how Figs. 2.3, 2.4, and 2.5, which show the exponential scaling of the energy with respect to the cardinality of the target set, were generated. For large networks, computing the mean over all possible sets of target nodes is computationally expensive. Instead, we approximate η by computing the mean value of $\log E_{\max}^{(p)}$ for some sample values of p, $p = n/10, 2n/10, \ldots, n$ by randomly choosing p nodes to be in a target set and computing the inverse of the smallest eigenvalue of W_p. In each of the simulations, we compute the mean and standard deviation of the logarithm of the smallest eigenvalue of W_p for typically 50 iterations. By plotting the values of $\left\langle \log E_{\max}^{(p)} \right\rangle$, we see that a linear model is appropriate and we compute a linear least-squares best fit for the data. The linear curve fit provides a good approximation of $\log E_{\max}^{(p)}$ as shown in Figs. 2.3, 2.4, and 2.5.

2.5   Discussion

In this chapter, we frame an optimal control problem to optimally control a portion of a complex network for assigned initial conditions and final conditions, while holding the input nodes and target nodes fixed. We provide an analytic solution to this problem in terms of a reduced Gramian matrix W_p, where the dimensions of this matrix are equal to the number of target nodes one attempts to control. We show that for a fixed number of input nodes, the energy required to control a portion of the network decreases exponentially when the cardinality of the target set, so even controlling a significant number of nodes requires much less energy than when every node is targeted. We observe the energy reduction, expressed as the rate η, in various networks, both model and real networks. The energy reduction is largest for networks which are heterogeneous (small power-law exponent γ in a scale-free

degree distribution) and sparse (small k_{av}), with a short time horizon and fewer control inputs. The control of these networks typically has especially large control energy demands. Thus target control is most beneficial for those networks which are most difficult to control. The potential applications for developing target controls are numerous, networks from networked robots to economic policies, where the required purpose is to affect only specific sectors. We experiment some of the datasets from the literature in many fields and find that they are also experience the reduced energy benefits from target control. The networks which describe metabolic interactions and protein structures have some of the largest values of η suggesting target control would by the most beneficial in those fields.

The observed decrease of the control energy over many orders of magnitude indicates a substantial potential impact of this research in applications where control over the entire network is not necessarily required. In chapter 5 and 6, we benefit from this target control approach to optimally regulate a specific state of a complex network governed by the nonlinear dynamics. The target control is also applicable to other control actions generated with respect other cost functions that appears often in the control of many real systems The scaling factor η for a network with respect to quadratic cost function remains nearly same with respect to the minimum energy control input in Eq. (2.3) [95].
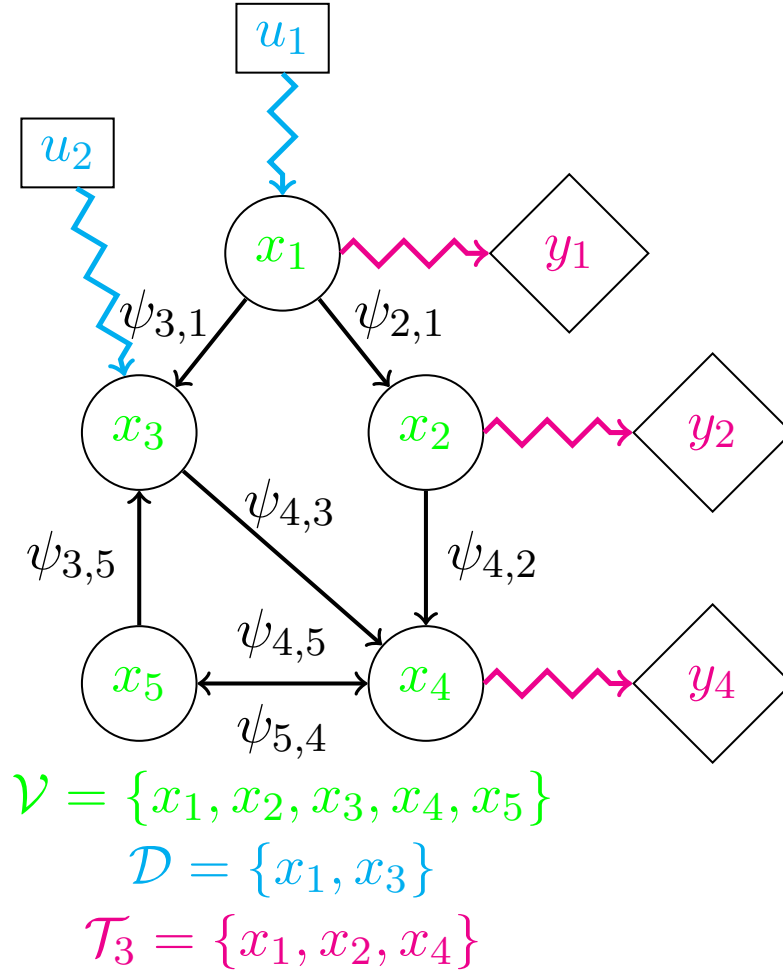
Figure 2.1: A simple network of five nodes and color-coded input signals (blue) and output sensors (pink). Note that each control input is directly connected to a single node, and each output sensor receives the state of a single node. Nodes directly connected to the pink outputs are target nodes, that is, they have a prescribed final state that we wish to achieve in finite time, t_f. The set of nodes in the network $\mathcal{V} = \{x_1, x_2, x_3, x_4, x_5\}$, the set of driver nodes $\mathcal{D} = \{x_1, x_3\}$, and the set of target nodes $\mathcal{T} = \{x_1, x_2, x_4\}$. The interaction function $\psi_{i,j}$ between the nodes x_i and x_j.
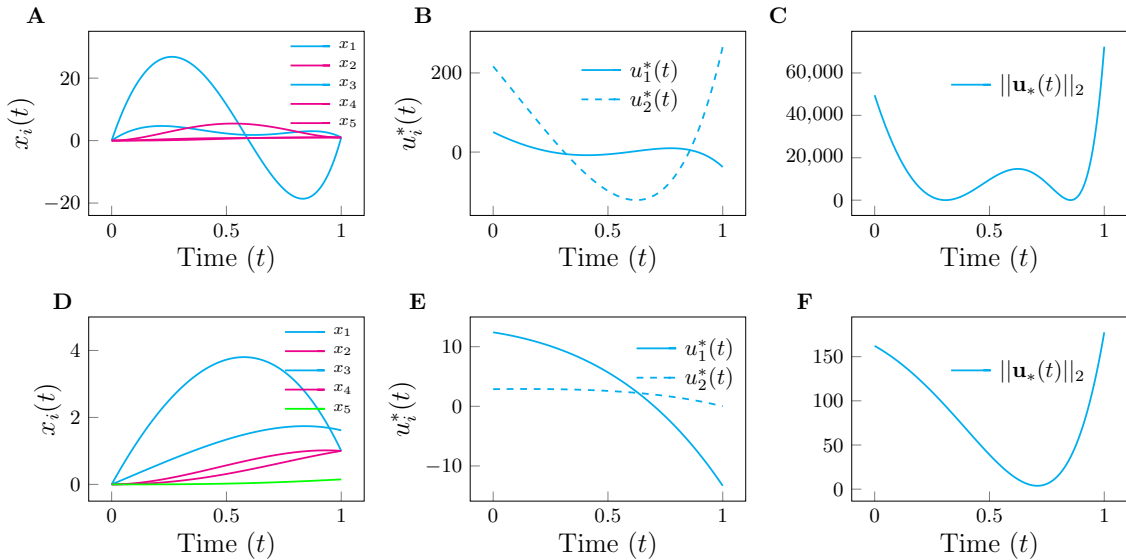
Figure 2.2: (*A*) The state evolution is shown where the initial condition is the origin and the final state for each target node is $y_i(t_\mathrm{f}) = 1$, $i = 1, 2, 3, 4, 5$. (*B*) The optimal control inputs $u_1(t)$ and $u_2(t)$ evolution are shown where the initial condition is the origin and the final state for each target node is $y_i(t_\mathrm{f}) = 1$, $i = 1, 2, 3, 4, 5$. (*C*) The square of the magnitude of the control inputs is also shown. The energy, or the control effort, is found by integrating the square of the magnitude of the the control inputs. For this case, $E = \int |\mathbf{u}(t)|^2 \approx 1.21 \times 10^4$ (a.u.). (*D*) The same network as in (*A*) but now only nodes x_1, x_2 and x_4 are declared as target nodes. The state evolution is shown where the initial condition remains the origin but the final condition is only defined for $y_i(t_\mathrm{f}) = 1, i = 1, 2, 4$. (*F*) The square of the magnitude of the control input is also shown. Note the different vertical axis scale as compared to (*C*). For the second case, $E = \int |\mathbf{u}(t)|^2 \approx 72.81$ (a.u.).

A

B

C
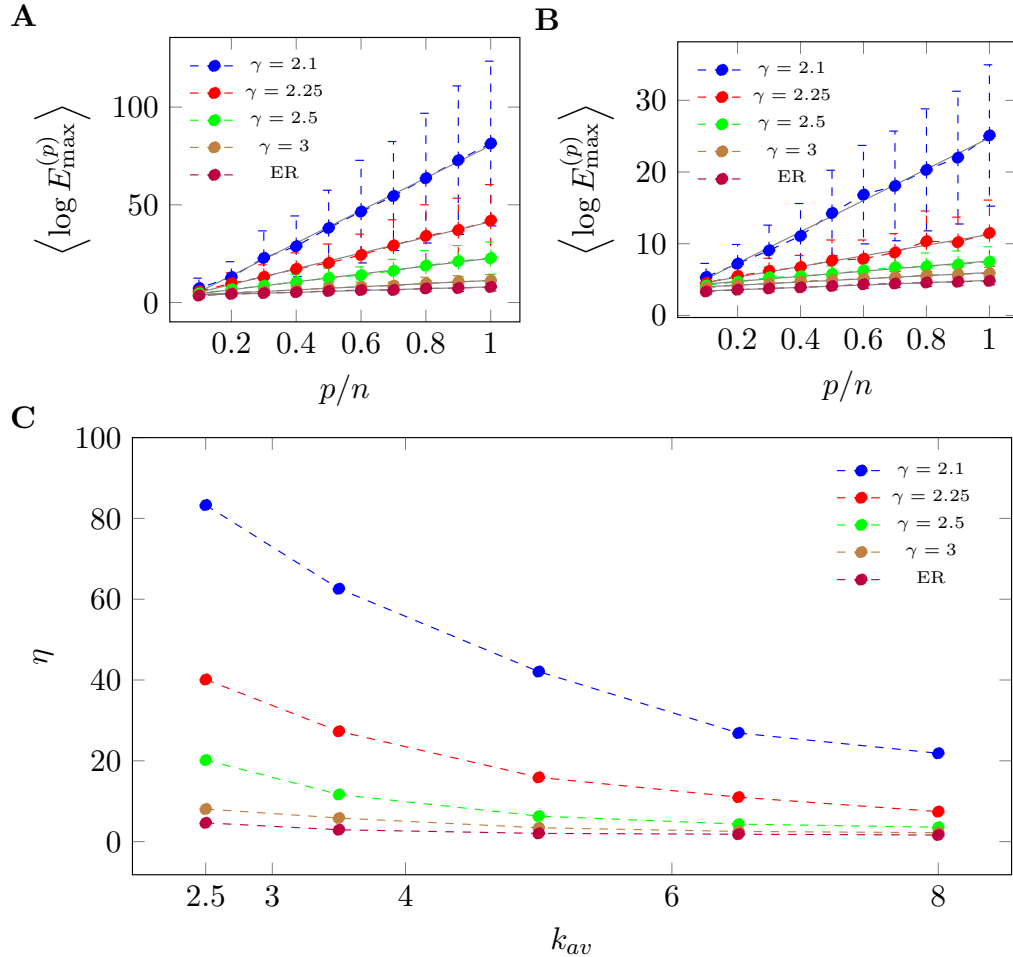
Figure 2.3: **The variation of η with respect to model network parameters.**
(*A*) The maximum control energy is computed for model networks constructed with
the static model and the Erdos-Renyi model while varying the target node fraction.
For the static model, four different power-law exponents are used. The average degree
of each model network is $k_{av} = 2.5$ and its size is $n = 500$. The input node fraction
$n_d = 0.5$, chosen such that the pair (A, B) is controllable. Each set of target nodes
is chosen randomly from the nodes in the network. Each point represents the mean
value of the control energy taken over 50 realizations. The error bars represent one
standard deviation. Note the linear growth of the logarithm of the control energy.
The slopes of these curves are the values of η corresponding to each set of parameters.
A linear fit curve is provided in gray. Also, as γ grows, i.e., the scale free models
become more homogeneous, the slope approaches that of the Erdos-Renyi model.
(*B*) The same study as in (*A*) except that $k_{av} = 8.0$. The same behavior is seen
but note the difference in scales of the vertical axis. Each point is the mean over 50
realizations, and error bars represent one standard deviation. (*C*) The study in (*A*)
and (*B*) is performed for more values of k_{av} and the value of η is computed for each
curve.
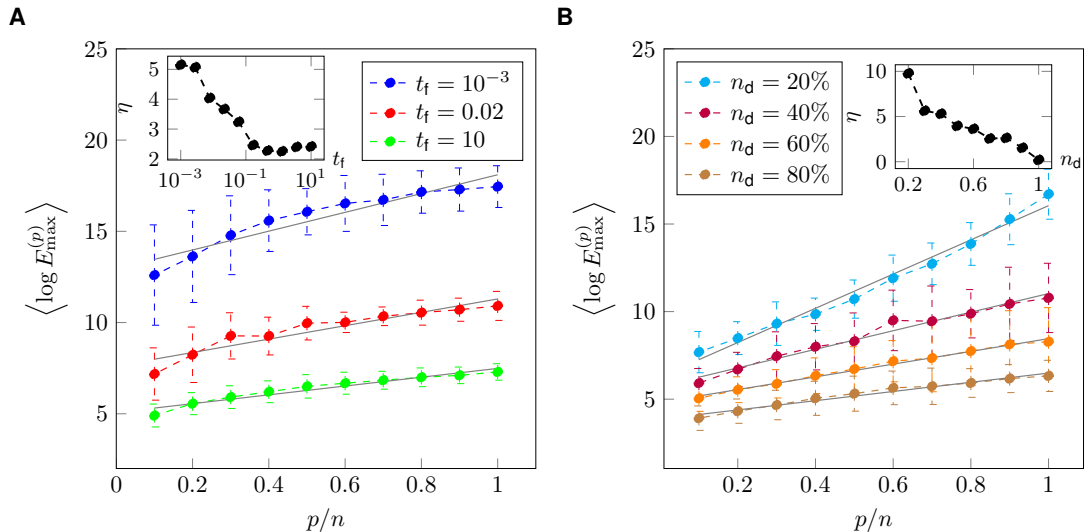
Figure 2.4: **Energy scaling as time horizon and input node fraction are varied.** Besides the average degree and power-law exponent which describe the underlying graph of the network (Fig. 2.3), there are other parameters that can affect the control energy such as the time horizon and the number of designated input nodes. (A) The time horizon, defined as $t_f - t_0$, is varied for networks constructed using the static model with the following properties: $n = 500$, $\gamma_{\text{in}} = \gamma_{\text{out}} = 3.0$, $k_{\text{av}} = 5.0$, and $n_d = 0.5$. As we choose $t_0 = 0$, the time horizon is equivalent to just t_f. The main plot shows how the log of the maximum control energy changes with target node fraction, p/n. Each point represents the mean over 50 realizations, and error bars represent one standard deviation. The inset shows how η changes with the time horizon. We see a sharp increase as the time horizon decreases. (B) We also investigate how η varies with the number of input nodes. The same class of network is examined as in (A): $n = 500$, $\gamma_{\text{in}} = \gamma_{\text{out}} = 3.0$ and $k_{\text{av}} = 5.0$. For both simulations, nodes are randomly and independently chosen to be in each target set. We see that η grows as the number of input nodes decreases as shown in the inset.
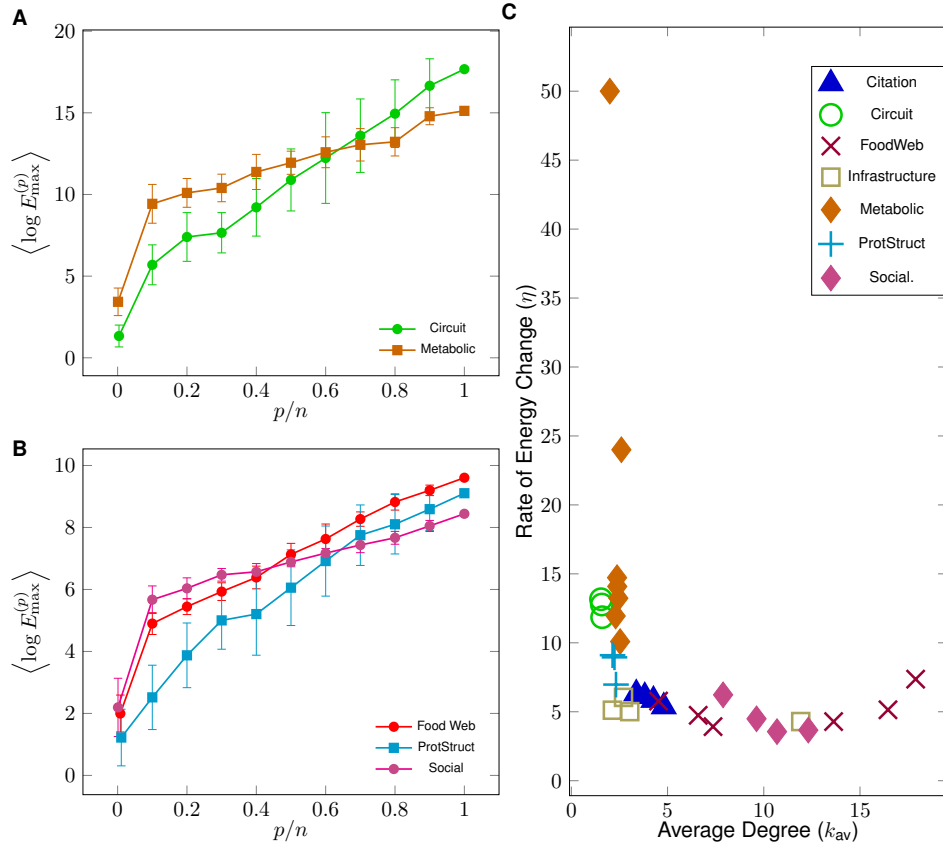
Figure 2.5: *Values of η for real datasets.* (*A*) We compute the maximum control energy required for the s420st circuit network and the TM metabolic network for increasing target node fraction, p/n. Each point represents the mean of fifty realizations where each realization is a specific choice of the nodes in the target node set. Error bars represent one standard deviation. (B) The same analysis performed for the Carpinteria food web, the protein structure 1 network, and a Facebook forum network. Each points represents the mean of fifty realizations where each realization is a specific choice of the nodes in the target node set. Error bars represent one standard deviation. For both (*A*) and (*B*), the linear behavior exists only when the target fraction increases greater than $p/n = 0.1$. (*C*) We numerically compute values of η for real datasets (compiled in Table 2.1) for comparison when $n_d = 0.45$ or larger. The values of η are plotted against each network's average degree as the degree distribution that best describes the degree sequence may or may not be scale-free. Nonetheless, we see a similar trend, that low average degree networks have a larger value of η, as demonstrated in Fig. 2.3(C). Also worth noting is that networks from the same class (as defined in the legend) tend to have similar values of η.

	Name	n	l	k_{av}	d	η
	s208st[91]	122	188	1.54	14	13.16
Circuit	s420st[91]	252	399	1.58	16	12.78
	s838st[91]	512	819	1.6	20	11.86
	Kohonen[96]	3772	12731	3.38	9	6.32
Citation	SG[96]	1024	4919	4.8	11	5.37
	SW[96]	233	994	4.27	7	5.84
	Scien[96]	2729	10413	3.82	13	6.12
	Carpinteria[93]	128	2290	17.89	6	7.36
	Florida[96]	128	2106	16.45	5	5.14
Foodweb	Grassland[96]	113	832	7.36	3	3.92
	LRL[97]	183	2494	13.63	6	4.29
	StMarks[96]	54	356	6.59	7	4.74
	Ythan[98]	92	417	4.53	3	5.77
	AirTrafficControl[99]	1226	2615	2.13	25	5.11
Infrastructure	IEEETG[100]	118	358	3.03	14	5.01
	NorthEuroGrid[101]	236	640	2.71	23	6.04
	USAir500[102]	500	5960	11.92	9	4.29
	CE_met[92]	1173	2864	2.44	30	13.24
	EN_met[92]	916	2176	2.38	28	14.72
	SC_met[92]	1511	3833	2.54	22	10.09
Metabolic	TM_met[92]	830	1980	2.39	18	14.09
	TP_met[92]	485	1117	2.3	15	11.94
	Yu-11 (New)[103, 104]	1144	2293	2.0	16	50.83
	CCSB-YI1 (New)[104, 105]	1278	3450	2.7	14	24.06
	prot_struct_1[91]	95	213	2.24	11	8.95
ProtStruct	prot_struct_2[91]	53	123	2.32	6	7.0
	prot_struct_3[91]	99	212	2.14	10	9.1
	EmailURV[106]	1133	10903	9.62	8	4.49
	FBForum[94]	899	7089	7.89	9	6.23
Social	Jazz[107]	198	5484	27.7	6	3.36
	RHS[108]	217	2672	12.31	6	3.67
	UCIrvine[109]	1899	20296	10.69	8	3.56

Table 2.1: **Real datasets from literature.** Both in the manuscript and here in the supplementary information, we examine how target control may benefit real networks compiled in datasets found throughout the scientific and engineering literature. We include the name, the reference, and some basic properties for each of the networks, as well as our computed value of η. In the table, n is the number of nodes, l is the number of edges, k_{av} is the average degree, d is the diameter of the graph, and η is the scaling of the minimum control energy.

Chapter 3

Balance Control of Complex Networks

3.1 Introduction

In chapter 2, we have seen that by controlling the states of a subset of the nodes of a network, rather than the state of every node, while holding the number of control signals constant, the , the required energy to control a portion of the network can be reduced substantially. In fact, the energy requirements exponentially decay with the reduction of the number of target nodes. In this chapter we reduce the control energy further by relaxing the output final states from their exact prescribed final states to be close as much as possible to the prescribed final states. We introduce a new control strategy called *balanced control* where we set our performance measure as a convex combination of two objective functions: 1) a function which minimizes the distance from the final output states at final time to the desired final states and 2) a function which minimizes the control effort to achieve the first goal over the finite time period.

3.2 Material and Method

3.2.1 Problem Formulation

We introduce the balance control problem for complex networks. In this chapter, similar to 2, we assume the networks have stable dynamics. The scale free model networks we consider throughout the paper are constructed with the static model [90]. Diagonal noise, δ_i, is included, drawn from a uniform distribution between -1 and 1 so that the eigenvalues of the adjacency matrix are all unique. The weighted adjacency matrix A is stabilized with a value ϵ such that each diagonal value of A is $\{a_{ii}\} = \delta_i + \epsilon$ where $i = 1, \ldots, n$. The value ϵ is chosen such that the maximum eigenvalue of A is equal to -1. The matrix B is constructed by choosing which nodes in the network require an independent control signal. The matrices B (C) are composed of m (p) versors as columns (rows). The set of input nodes is chosen in the same way as it was done in chapter 2. A small sample schematic diagram is shown in Fig. $3.1A$ that demonstrates the graphical layout of our problem emphasizing the graph structure and the role of input nodes and targets. Here by an input node, we mean a node that directly receives one and only one control input such as nodes 1 in Fig. $3.1A$ and by a target node we mean a node which corresponds to one and only one output such as nodes 1, 2 and 3 in Fig. $3.1A$. In our optimal balanced control problem, we attempt to minimize the following cost function,

$$
\begin{aligned}
\min_{\mathbf{u}(t)} J = &\frac{1-\alpha}{2}[(\mathbf{y}(t_f) - \mathbf{y}_f)^T (\mathbf{y}(t_f) - \mathbf{y}_f)] \\
&+ \frac{\alpha}{2} \int_{t_0}^{t_f} \mathbf{u}(t)^T \mathbf{u}(t) dt
\end{aligned}
\tag{3.1}
$$

subject to the following constraints,

$$
\dot{\mathbf{x}}(t) = A\mathbf{x}(t) + B\mathbf{u}(t)
\tag{3.2a}
$$

$$
\mathbf{y}(t) = C\mathbf{x}(t), \quad \mathbf{x}(t_0) = \mathbf{x}_0
\tag{3.2b}
$$

Here the final constraints are in the objective function and we call these constraints *soft constraints* as we do not require them to be satisfied exactly. Note that if we set $C = I_n$, where I_n is the $n \times n$ identity matrix, then $\mathbf{y}(t) = \mathbf{x}(t)$. The vector $\mathbf{y}_f$ is the prescribed final output state of the nodes described by the matrix C. Here $\alpha \in (0, 1)$ is a scaling parameter by which we can penalize the two performance measures in the cost function in (3.1) to balance the control energy. Note that in the case in which $\alpha = 1$, the cost function in Eq. (3.1) becomes the cost function associated with the optimal output cost control problem in Eq. (2.3), where different from Eq. (3.1), the final desired state is imposed on as a *hard constraint*. After computing the Hamiltonian and solving the resulting system of ODEs, the minimum energy control signal which minimizes the objective function in Eq. (3.1) over the finite time interval $[t_0, t_f]$ to be,

$$\mathbf{u}^*(t) = -B^T e^{A^T(t_f - t)} C^T U_p^{-1} \left(C e^{A(t_f - t_0)} \mathbf{x}_0 - \mathbf{y}_f \right) \tag{3.3}$$

For details derivation, please see Appendix B.1. With the optimal control input $\mathbf{u}^*(t)$, the time evaluation of the output states is

$$\mathbf{y}(t) = C e^{A(t - t_0)} \mathbf{x}_0 + C \int_{t_0}^{t} e^{A(t - \tau)} B \mathbf{u}^*(\tau) d\tau \tag{3.4}$$

and states can also be determined,

$$\begin{aligned} \mathbf{x}(t) &= e^{A(t - t_0)} \mathbf{x}_0 \\ &- \frac{1 - \alpha}{\alpha} \int_{t_0}^{t} e^{A(t - \tau)} B B^T e^{A^T(t_f - \tau)} d\tau C^T \bar{\boldsymbol{\nu}} \end{aligned} \tag{3.5}$$

where

$$\bar{\boldsymbol{\nu}} = \frac{\alpha}{1 - \alpha} U_p^{-1} \boldsymbol{\beta}, \tag{3.6}$$

the $p \times p$ matrix

$$U_p = \left(\frac{\alpha}{1 - \alpha} I_p + W_p \right) \tag{3.7}$$

and

$$\boldsymbol{\beta} = \left(Ce^{A(t_f - t_0)} \mathbf{x}_0 - \mathbf{y}_f \right). \tag{3.8}$$

Different from the formulation of linear optimal control commonly seen in texts on the subject, we approach the problem in two unique ways. First, we consider the control action that minimizes the cumulative magnitude of the control input, restricted by a left boundary condition applied to the state of the system (the initial condition) and a final condition applied to only the outputs of the system. Second, we make specific the methodology as it applies to networks by restricting our definitions of the matrices B and C matrices as discussed previously.

3.2.2   Optimal Energy

The energy associated with the control input in Eq. (3.3), while only targeting the nodes for balanced control in $\mathcal{T}_p$, is defined as $\epsilon^{(p)} = \int_{t_0}^{t_f} \mathbf{u}^*(t)^T \mathbf{u}^*(t) dt$. Note that $\epsilon^{(p)}$ also depends on which p nodes are in the set, $\mathcal{T}_p$. The energy $\epsilon^{(p)}$ is a measure of the 'effort' which must be provided to achieve the control goal. In the subsequent definitions and relations, when a variable is a function of p, we more specifically mean it is a function of a specific target set under balanced control of size p of which there are $\frac{n!}{p!(n-p)!}$ possible sets. We can define the *minimum balanced control energy* (MBCE) when the control input is of the form in Eq. (3.3) as,

$$\begin{aligned} \epsilon^{(p)} &= \left(\mathbf{y}_f - Ce^{A(t_f - t_0)} \mathbf{x}_0 \right)^T U_p^{-1} W_p U_p^{-1} \\ &\times \left(\mathbf{y}_f - Ce^{A(t_f - t_0)\mathbf{x}_0} \right) = \boldsymbol{\beta}^T M_p \boldsymbol{\beta} \end{aligned} \tag{3.9}$$

where the vector $\boldsymbol{\beta} = Ce^{A(t_f - t_0)} \mathbf{x}_0 - \mathbf{y}_f$ and $M_p = U_p^{-1} W_p U_p^{-1}$ is the $p \times p$ symmetric, real, semi-positive definite matrix. Note that the matrix M_p has the same set of eigenvectors as the matrix W_p. Moreover, the following relation relates the eigenvalues

of M_p and W_p:

$$\mu_i^{(p)} = \left(\frac{\alpha}{1-\alpha} + \lambda_i^{(p)}\right)^{-1} \lambda_i^{(p)} \left(\frac{\alpha}{1-\alpha} + \lambda_i^{(p)}\right)^{-1} \tag{3.10}$$

where, we denote the eigenvalues of M_p as $\mu_i^{(p)}$ and the eigenvalues of W_p as $\lambda_i^{(p)}$, $i = 1, \ldots, p$. It follows that the energy expression (3.9) defines an ellipsoid in the variable $\boldsymbol{\beta}$. The axes of the ellipsoid are unaffected by the particular choice of the parameter α, while the width of each axis changes with the square root of the corresponding eigenvalue of the matrix M_p.

3.2.3 Worst Case Direction

We consider the eigenvalues of M_p as $\mu_i^{(p)}$, $i = 1, \ldots, p$, which are ordered such that $0 \le \mu_1^{(p)} \le \ldots \le \mu_p^{(p)}$. By defining the magnitude of the vector, $|\boldsymbol{\beta}| = \beta$, we can define the 'worst-case' (or maximum) energy according to the Rayleigh quotient,

$$0 \le \beta^2 \mu_1^{(p)} \le \boldsymbol{\beta}^T M_p \boldsymbol{\beta} \le \beta^2 \mu_p^{(p)} < \infty. \tag{3.11}$$

The upper extreme of the control energy denoted by $\epsilon_{max}^{(P)}$, for the control action in Eq. (3.3) is $\max\left\{\epsilon^{(p)}\right\} \sim \mu_p^{(p)}$, which is what we call the 'worst-case' energy for optimal balance control. For an arbitrary vector $\boldsymbol{\beta}$, which can be represented as a linear combination of the eigenvectors of M_p, the energy can be defined as a weighted sum of the eigenvalues, $\mu_i^{(p)}$, which includes the worst-case energy.

3.2.4 Energy Scaling with the Penalizing Factor α

From 2, the minimum energy in Eq. (2.3) for the optimal output cost control is,

$$E^{(p)} = \left(\mathbf{y}_f - Ce^{A(t_f-t_0)}\mathbf{x}_0\right)^T \left(CWC^T\right)^{-1}$$
$$\times \left(\mathbf{y}_f - Ce^{A(t_f-t_0)}\mathbf{x}_0\right) = \boldsymbol{\beta}^T W_p \boldsymbol{\beta}$$

We would like to determine the limiting energy when $\alpha \to 0$ in Eq. (3.9). At each p, $\mathcal{T}_p$, contains p nodes in the target set and U_p is $p \times p$ invertible matrix. When $\alpha \to 0$, $U_p \to W_p$, the output controllability Gramian and MBCE energy on this limit,

$$\lim_{\alpha \to 0} \epsilon^{(p)} = E^{(p)} \tag{3.12}$$

We also provide the limiting behavior on α for the worst case energy direction,

$$\lim_{\alpha \to 0} \epsilon_{max}^{(p)} = E_{max}^{(p)} \tag{3.13}$$

A small, three node example of the benefits of balanced control is shown in Fig. 3.1, where each node is the target set ($p = n = 3$). Fig. 3.1A displays a sample network with the three nodes. Input node (node 1) is in blue and target nodes for balanced control are in magenta (nodes $1, 2, 3$). Node 1 is directly connected to an input u_1 and target nodes 1,2,3 are directly connected to output y_1, y_2 and y_3 respectively. In panel (B), we examine the limiting relationship in Eq. (3.12) for the three node network. From Fig. 3.1B, we also see how the balanced control strategy reduces the control energy as the penalizing factor α increases. For large value of $\alpha = 10^{-1}$, the output states and the optimal control input are provided in panel (C) and (E), respectively. For small value of $\alpha = 10^{-6}$, the output states and the optimal control input are provided in panel (D) and (F), respectively. From panel (E) and (F), the integral of the magenta curves are $\epsilon^{(3)} \approx 4.2$ and $\epsilon^{(3)} \approx 219$ respectively. We see that the energy can be reduced by 55 times in the former case.

3.2.5   Optimal Return in Limiting Case

In the cost function (3.1), the two performance measures are multiplied each by a penalizing factor. It is important to investigate the relationship between the optimal return corresponding to each performance measure as α varies. The optimal return

value corresponding to (3.1) can be written,

$$J^* = \frac{1-\alpha}{2}\zeta^2 + \frac{\alpha}{2}\epsilon^{(p)} = J_1^* + J_2^* \tag{3.14}$$

where $\zeta = ||\mathbf{y}(t_f) - \mathbf{y}_f||$, the final state error at time t_f, $J_1^* = \frac{1-\alpha}{2}\zeta^2$, and $J_2^* = \frac{\alpha}{2}\epsilon^{(p)}$. We call the ratio J_1^*/J^* the optimal error return ratio and J_2^*/J^* the optimal energy return ratio. Note that the sum of the two ratios is equal to 1, i.e., $J_1^*/J^* + J_2^*/J^* = 1$.

Figure 3.2 shows how the ratios J_1^*/J^* and J_2^*/J^* vary with α for the case of a scale free network with $n = 300$, $\gamma_{\text{in}} = \gamma_{\text{out}} = 2.5$, and $\kappa = 8$. We set the fraction of target nodes, $p/n = 0.8$ and the final time $t_f = 1$. The values on the abscissa axis are $-\log\alpha$ so that large values of α are shown on the left hand side and small values of α are shown on the right hand side. When $\alpha \to 0$, $\zeta \to 0$ faster than α (which multiplies $\epsilon^{(p)}$). Therefore, when α is very small J^* is dominated by J_2^*, and we see from Fig. 3.2 that $J_1^*/J^* \to 0$, $J_2^*/J^* \to 1$ as $\alpha \to 0$. On the other hand, from the Fig. 3.2, we see that as α approaches 1, $J_2^*/J^* \to 0$ and $J_1^*/J^* \to 1$. As α increases (decreases), the error component (the energy component) becomes dominant in the optimal return value in Eq. (3.14).

3.2.6   Numerical Controllability

The controllability Gramian, W_p, can be calculated as a function of the eigendecomposition of the state matrix $A = V\Lambda V^{-1}$ as it has been driven in chapter 2. We use the multi-precision package Advanpix for Matlab. The Matlab toolbox Advanpix [89] allows the computation of the eigen-decomposition of W_p to be performed in an arbitrarily precise manner. This precision allows us to calculate the eigen decomposition of W_p, the invertible matrix U_p and the matrix M_p numerically. We also use Advanpix when computing the energy in Eq. (3.9) for the cost function in Eq. (3.1).

3.3   Results

We perform numerical simulations to examine the two important results discussed in subsection 3.2.4. For our simulations in Figures 3.3 - 3.4, we consider scale-free model networks, constructed with the static model in Ref. [90] for specific parameters k_{av}, the average degree, and $\gamma_{in} = \gamma_{out} = \gamma$, the power law exponent of the in- and out-degrees, and we choose the initial state at the origin, $\mathbf{x}_0 = \mathbf{0}$, and final state $||\mathbf{y}_f|| = 1$. We choose 10 different $\mathbf{y}_f$ uniformly distributed on the unit sphere, and we take the mean of all results over 10 realizations. We also consider $t_f = 1$ and the fraction of input nodes $n_d = 0.4$. In Figs. 3.3 - 3.4, the solid line corresponds to the output cost control energy, $E^{(p)}$, where p/n is the associated target set.

On the left half panels of Fig. 3.3, we consider the networks ($n = 300$) are scale-free constructed with the static model such that $k_{av} = 8.0$ in each case. Each point is the average of 10 realizations and the bars represent one standard deviation. The target nodes are chosen from the set of nodes randomly and independently at every iteration. In Fig. 3.3A, the expected limiting relation discussed in the subsection 3.2.4 is seen for each network irrespective of power-law exponent ($\gamma_{in} = \gamma_{out}$). We notice that, when the network is more heterogeneous (γ is low, e.g. $\gamma = 2.5$), the terminal balancing is more beneficial compared to the networks that are more homogeneous (γ is high, e.g. $\gamma = 3$) as the balanced control energy remains close to the output control energy for homogeneous networks. We observe results qualitatively similar for any size of the terminal target set. On the left half panels of Fig 3.3, we consider the networks ($n = 300$) are scale-free constructed with the static model such that $\gamma_{in} = \gamma_{out} = 2.5$ in each case. Each point is the average of 10 realizations and the bars represent one standard deviation. Each set of target nodes is chosen from the set of nodes randomly and independently at every iteration. In Fig. 3.3B, the expected limiting relation discussed in the subsection **II.F** is seen for each network irrespective

of average degree (κ). We notice that, when the network is more sparse (κ is low, e.g. $\kappa = 5$), the terminal balancing is more beneficial compared to the networks that are dense (κ is high, e.g. $\kappa = 15$) as the balanced control energy remains close to the output control energy for dense networks. This result holds for any size of the target sets. In panel (C) - (D), we show the error ζ of the final state at final time t_f for the same target nodes and in panel (E) - (F), we show that the optimal return function J^* decreases as α decreases.

Besides the average degree and power-law exponent which describe the network (Fig. 3.3), there are other parameters that can affect the control energy such as the time horizon and the number of designated input nodes. In Fig. 3.4, each panel of (A) - (F) corresponds to the size of target node set $p/n = 0.8$. The target nodes are chosen from the set of nodes randomly and independently for every iteration. Each point is the average of 10 realizations and the bars represent one standard deviation. The network has properties: $n = 300$, $\gamma_{in} = \gamma_{out} = 2.5$, $k_{av} = 8.0$. On the left half panels, we show the limiting relationship holds as the time horizon defined as $t_f - t_0$ changes. We notice that, when the time horizon is small (e.g. $t_f - t_0 = 0.01$), the terminal balancing is more beneficial compared to large time horizon (e.g. $t_f - t_0 = 10$) as the balanced control energy remains close to the output control energy for large time horizon. On the right half panels, we show the limiting relationship holds as the number of input nodes n_d changes. We notice that, when the number of designated input nodes is small (e.g. $n_d = 0.4$), the terminal balancing is more beneficial compared to large number of input nodes (e.g. $n_d = 1$) as the balanced control energy remains close to the output control energy for large number of inputs. This result holds for any size of the target sets. In panel (C) - (D), we show the error ζ of the final state at final time t_f for the same target nodes and in panel (E) - (F), we show that the optimal return function J^* decreases as α decreases.

We also analyze datasets collected from various fields in science and engineering to study how the worst-case energy for MBCE changes with α and the size of the target set under balanced control for networks with more realistic structures. In Fig. 3.5, we consider six groups of dataset: Circuit [91], Protein Structure [91], Metabolic [92], Food Web [93, 96–98], Social [106–109], and Infrastructure [100–102]. For our simulation, we consider $t_f = 1$ and $n_d = 0.45$ and we take 30 realizations for one particular target fraction and take the mean over several realizations. We only show the results in Fig. 3.5 for $p/n = 0.1$ (for sufficient values of p our results are qualitatively same). For comparison among the real dataset, we choose one network from different groups of networks and plot $\epsilon_{max}^{(p)}$ verses α in Fig. 3.5. We see for small α, say $\alpha = 10^{-10}$, the Metabolic network is benefited more as the control energy for balanced control reduces significantly from output control energy (magenta solid line). On the other hand the Food Web and Social network are not benefited as much as balanced control energy remains approximately the same, in comparison. However, for large values of α, say $\alpha = 10^{-1}$, all of the networks need approximately the same amount of energy for balanced control.

3.4   Conclusion

In this chapter, we provide an energy efficient control strategy we call balanced control strategy. We see that by changing the penalizing factor α in the cost function in Eq. (3.1), the control energy that is needed for balanced control can be reduced dramatically. For example, in Fig. 3.1B, we see that the control energy can be reduced if we relax the final state conditions. We also see the limiting behavior that in the limit $\alpha \to 0$ MBCE approaches the output cost control energy. The above two results are general regardless of the network types, size and other properties. See Figs. 3.1B, 3.3, 3.4, and 3.5. From figure 3.3A,C,A and 3.3B,D,F, we get

the information that sparse and heterogeneous networks can benefit more from our balanced control strategy than dense and homogeneous networks, respectively. We discuss the effect of other parameters, especially time horizon and number of input nodes on the MBCE and its limiting behavior. Several real datasets have also been examined to verify this results. In Fig. 3.5, we compare the results for different groups of real networks and conclude that the biological networks (e.g. metabolic, protein structure) are those that benefit most from the balanced control strategy.
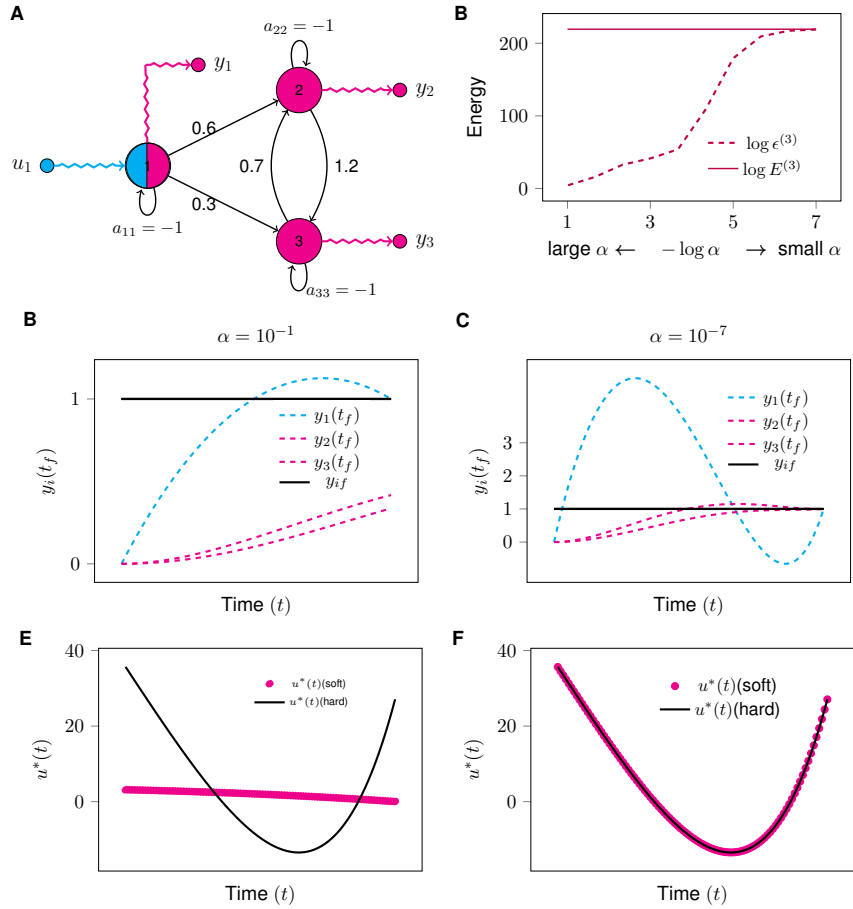
Figure 3.1: **Example Network.** Panel (A) displays a sample network with the three nodes. Each node has self regulation labeled by a_{ii}. Input node (node 1) is in blue and target nodes for balanced control are in magenta (node $1, 2, 3$). Node 1 is directly connected to an input u_1 and target nodes 1,2,3 are directly connected to output y_1, y_2 and y_3 respectively. In panel (B), we examine the limiting relationship in Eq (3.12) for the three node network. For large value of $\alpha = 10^{-1}$, the output states and the optimal control input are provided in panel (C) and (E) respectively. For small value of $\alpha = 10^{-7}$, the output states and the optimal control input are provided in panel (D) and (F) respectively.
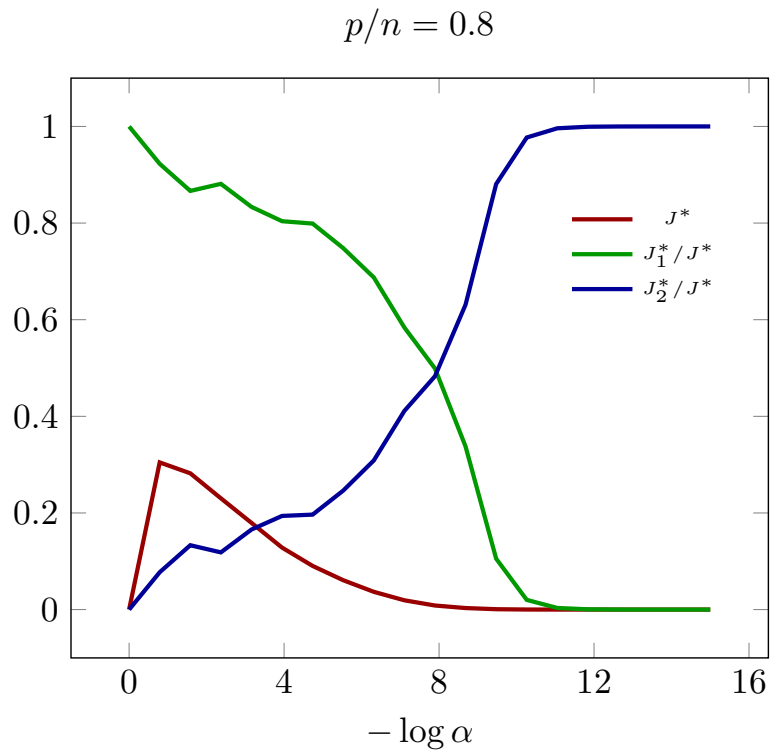
Figure 3.2: **Ratio of optimal return** J^***.** Ratio of optimal error return J_1^*/J^* and ratio of optimal energy return J_2^*/J^* are plotted versus the scaling parameter, α. For the simulation, we choose a scale free network with $n = 300$, $\gamma_{\text{in}} = \gamma_{\text{out}} = 2.5$, and $\kappa = 8$. We set the fraction of target nodes, $p/n = 0.8$ and the final time $t_f = 1$.
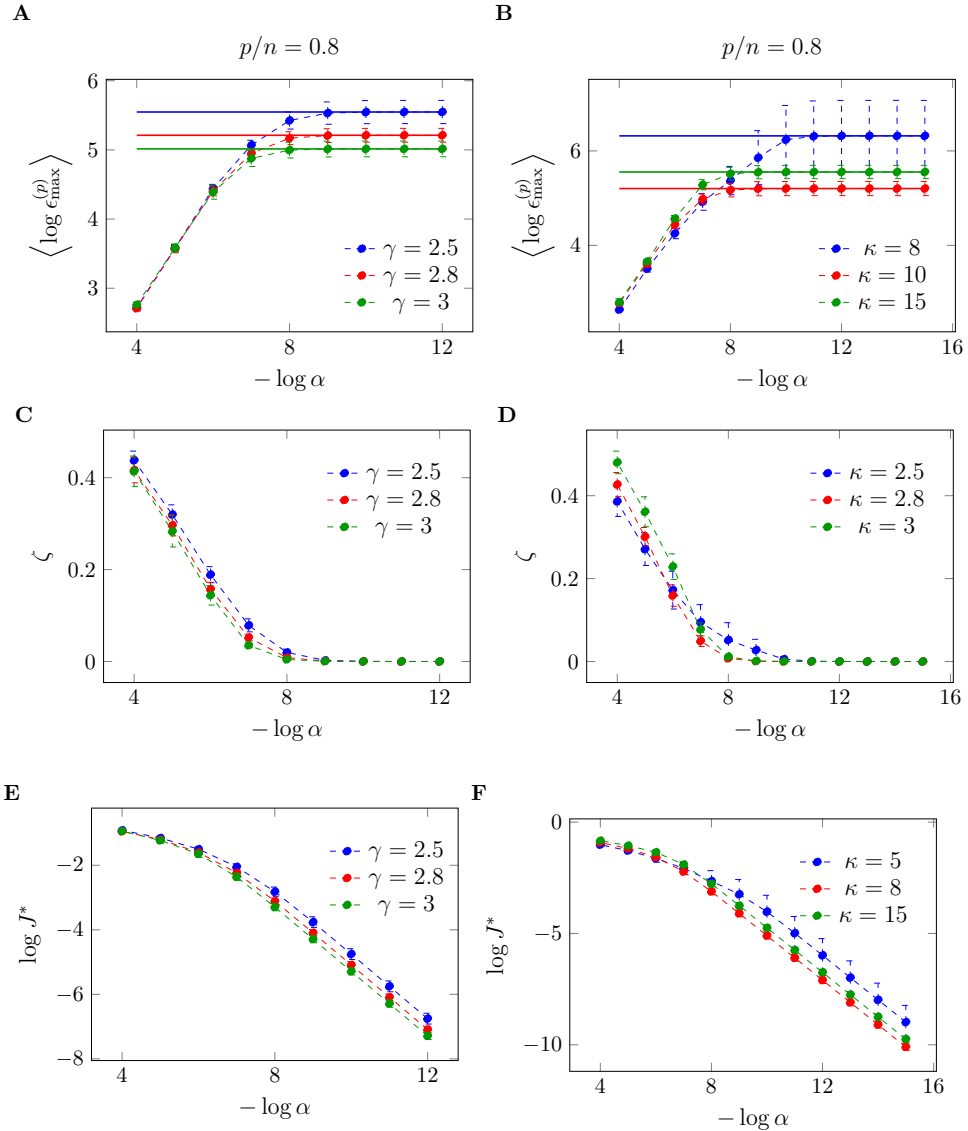
Figure 3.3: **The limiting relationship of $\epsilon^{(p)}$ with respect to model network parameters γ and κ.** Each panel of (A) - (B) corresponds to the size of target fraction, $p/n = 0.8$. On left half panels, the log of the control energy for balance control, $\epsilon^{(p)}$, the final state error ζ and the optimal return J^* corresponding to networks with a fixed *kappa* = 8 and different power-law exponent $(\gamma_{in} = \gamma_{out})$ are plotted versus α, respectively. The solid line corresponds to the output cost control energy, $E^{(p)}$. The expected limiting relation is seen for each network irrespective of power-law exponent $(\gamma_{in} = \gamma_{out})$. On the right half panels, $\log \epsilon^{(p)}$, ζ and $\log J^*$ corresponding to networks with a fixed $\gamma_{in}\gamma_{out} = 2.5$ and different average degree (κ) are plotted versus α, respectively. The expected limiting relation is seen for each network irrespective of average degree (κ).
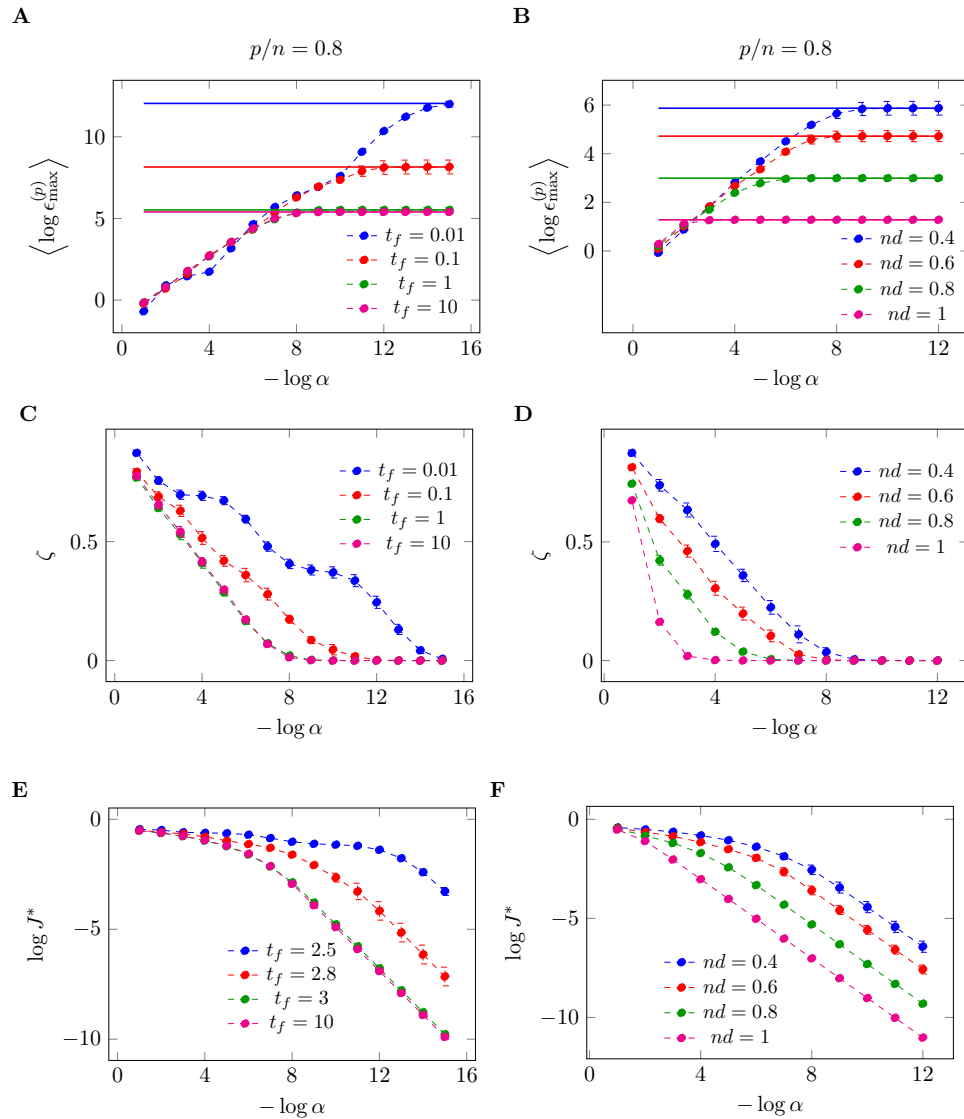
Figure 3.4: **The limiting relationship of $\epsilon^{(p)}$ as Time Horizon and Input Node Fraction are varied.** In of (A) - (B) corresponds to the size of target fraction, $p/n = 0.8$. On left half panels, the log of the control energy for balance control, $\epsilon^{(p)}$, the final state error ζ and the optimal return J^* for different time horizons t_f are plotted versus α, respectively. The solid line corresponds to the output cost control energy, $E^{(p)}$. We show the expected limiting relation for different time horizons. On the right half panels, $\log \epsilon^{(p)}$, ζ and $\log J^*$ for different input node fraction n_d are plotted versus α, respectively. We show the expected limiting relation for different input node fractions.
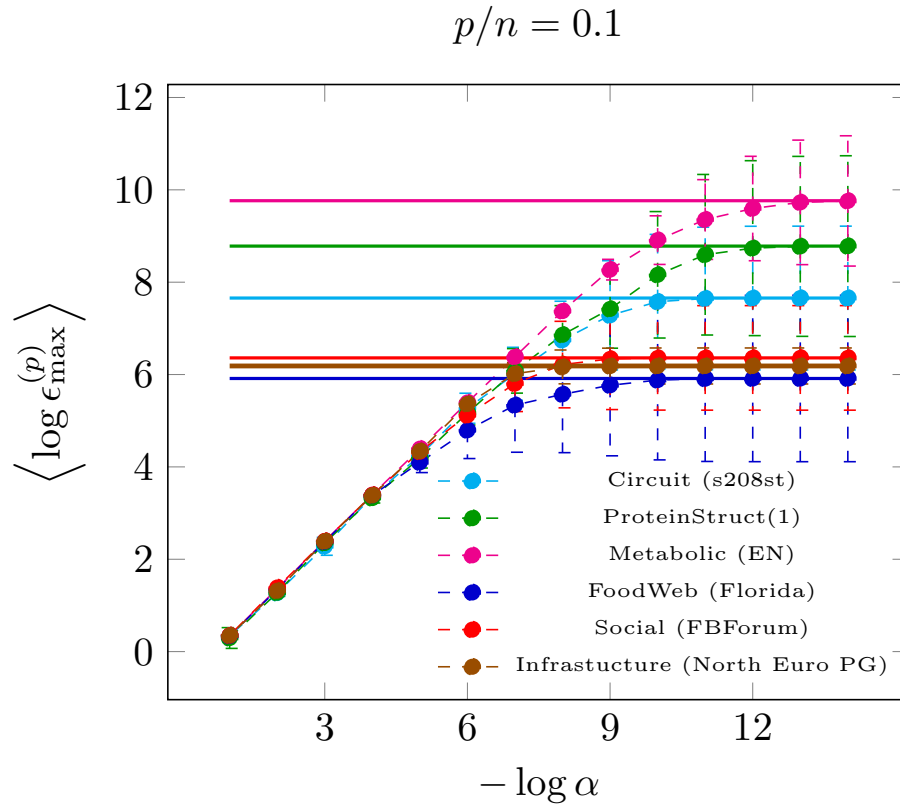
Figure 3.5: *Comparison among the real dataset.* The log of the maximum energy for terminal control, $\epsilon_{\max}^{(p)}$, is plotted versus the scaling parameter, α.

Chapter 4

Overview of Pseudo-Spectral Optimal Control of Networked Systems

4.1 Introduction

Before discussing the Pseudo-Spectral Optimal Control (PSOC), we briefly review the general optimal control problem (OCP) and the set of necessary conditions, derived from Pontryagin's maximum principle, which an optimal solution must satisfy. Afterwards, we describe how PSOC discretizes the OCP, approximating the original OCP as a nonlinear programming (NLP) problem.

4.2 Optimal Control

Optimal control theory combines aspects of dynamical systems, optimization, and the calculus of variations [110] to solve the problem of finding a control law for a given dynamical system such that the prescribed optimality criteria are achieved. A

constrained optimal control problem can generally be written as,

$$
\begin{aligned}
\min_{\mathbf{u}(t)} \quad & J(\mathbf{x}(t), \mathbf{u}(t), t) = E\left(\mathbf{x}(t_0), \mathbf{x}(t_f), t_0, t_f\right) + \int_{t_0}^{t_f} F\left(\mathbf{x}(t), \mathbf{u}(t), t\right) dt \\
\text{s.t.} \quad & \dot{\mathbf{x}}(t) = \mathbf{f}(\mathbf{x}(t), \mathbf{u}(t), t) \\
& \mathbf{e}^L \leq \mathbf{e}(\mathbf{x}(t_0), \mathbf{x}(t_f), t_0, t_f) \leq \mathbf{e}^U \\
& \mathbf{h}^L \leq \mathbf{h}(\mathbf{x}(t), \mathbf{u}(t), t) \leq \mathbf{h}^U \\
& t \in [t_0, t_f]
\end{aligned}
\tag{4.1}
$$

The OCP is solved by finding a time varying control input $\mathbf{u}^*(t)$ that minimizes the quantity $J(\mathbf{x}(t), \mathbf{u}(t), t)$ subject to a system's dynamics and other constraints in Eq. (4.1). The objective function (or cost function) $J(\mathbf{x}, \mathbf{u}, t)$ is composed of two parts, (i) $E : \mathbb{R}^n \times \mathbb{R}^n \times \mathbb{R} \times \mathbb{R} \mapsto \mathbb{R}$ which is a cost associated with the endpoint behavior of the system $\mathbf{x}(t_0)$ and $\mathbf{x}(t_f)$, and (ii) $F : \mathbb{R}^n \times \mathbb{R}^m \times \mathbb{R} \mapsto \mathbb{R}$ which is a running cost over the entire time interval $[t_0, t_f]$. The system dynamics is described by the function $\mathbf{f} : \mathbb{R}^n \times \mathbb{R}^m \times \mathbb{R} \mapsto \mathbb{R}^n$. Constraints on the endpoints ($\mathbf{x}(t_0)$ and/or $\mathbf{x}(t_f)$) are described by $\mathbf{e} : \mathbb{R}^n \times \mathbb{R}^n \times \mathbb{R} \times \mathbb{R} \mapsto \mathbb{R}^e$. While we only specify initial conditions, more complicated relations between the endpoints of the states can be specified as well. Finally, path constraints, such as bounds on the states or control inputs, are described by $\mathbf{h} : \mathbb{R}^n \times \mathbb{R}^n \times \mathbb{R} \mapsto \mathbb{R}^h$.

4.3 Pseudo-Spectral Optimal Control

In general, there exists no analytic framework that is able to provide the optimal time traces of the controls $\mathbf{u}^*(t)$ and the states $\mathbf{x}^*(t)$ in (4.1), and so we must resort to numerical techniques.

Pseudo-Spectral Optimal Control (PSOC) is a computational method for solving optimal control problems. Here we present a brief overview of the theory of pseudo-

spectral optimal control. PSOC has become a popular tool in recent years [55, 111] that has let scientists and engineers solve optimal control problems like (4.1) reliably and efficiently in applications such as guiding autonomous vehicles and maneuvering the international space station [55]. PSOC is an approach by which an OCP can be discretized by approximating the integrals by quadratures and the time-varying states and control inputs with interpolating polynomials. Here we summarize the main concept of the PSOC. We choose a set of $N+1$ discrete times $\{\tau_i\}$ $i = 0, 1, \ldots, N$ where $\tau_0 = -1$ and $\tau_N = 1$ with a mapping between $t \in [t_0, t_f]$ and $\tau \in [-1, 1]$. The discretization scheme that includes the endpoints and is normalized by the mapping,

$$t = \frac{t_f - t_0}{2}\tau + \frac{t_f + t_0}{2} \tag{4.2}$$

The times $\{\tau_i\}$ are chosen as the roots of an $(N+1)$th order orthogonal polynomial such as Legendre polynomials or Chebyshev polynomials. The choice of dicretization scheme is important to the convergence of the full discretized problem. For instance, if we choose the roots of a Legendre polynomial as the discretization scheme, the associated quadrature weights can be found in the typical way for Gauss quadrature. The time-varying states and control inputs are found by approximating them with Lagrange interpolating polynomials,

$$\hat{\mathbf{x}}(\tau) = \sum_{i=0}^{N} \hat{\mathbf{x}}_i L_i(\tau) \tag{4.3a}$$

$$\hat{\mathbf{u}}(\tau) = \sum_{i=0}^{N} \hat{\mathbf{u}}_i L_i(\tau), \tag{4.3b}$$

where $\hat{\mathbf{x}}(\tau)$ and $\hat{\mathbf{u}}(\tau)$ are the approximations of $\mathbf{x}(\tau)$ and $\mathbf{u}(\tau)$, respectively, and $L_i(\tau)$ is the ith Lagrange interpolating polynomial. The Lagrange interpolating polynomials are defined as,

$$L_i\tau = \prod_{j=0, j\neq i}^{N} \frac{\tau - \tau_j}{\tau_i - \tau_j} \tag{4.4}$$

The dynamical system is approximated by differentiating the approximation $\hat{\mathbf{x}}(\tau) = \sum_{i=0}^{N} \hat{\mathbf{x}}_i L_i(\tau)$ with respect to time.

$$\frac{d\hat{\mathbf{x}}}{d\tau} = \sum_{i=0}^{N} \hat{\mathbf{x}}_i \frac{dL_i}{d\tau} \tag{4.5}$$

Let $D_{k,i} = \frac{d}{d\tau} L_i(\tau_k)$ which allows one to rewrite the original dynamical system constraints in (4.1) as the following set of algebraic constraints.

$$\sum_{i=0}^{N} D_{k,i}\hat{\mathbf{x}}_i - \frac{t_f - t_0}{2}\mathbf{f}(\hat{\mathbf{x}}_k, \hat{\mathbf{u}}_k, \tau_k) = \mathbf{0}_n, \quad k = 1, \ldots, N$$

$$\hat{\mathbf{x}}_N - \hat{\mathbf{x}}_0 - \sum_{k=1}^{N}\sum_{i=0}^{N} w_k D_{k,i}\hat{\mathbf{x}}_i = \mathbf{0}_n \tag{4.6}$$

The last set of algebraic constraints arise from the consistency condition $\int_{t_0}^{t_f} \dot{\mathbf{x}}(t)dt = \mathbf{x}(t_f) - \mathbf{x}_0$. Similarly to the consistency condition, the integral in the cost function is,

$$J = \int_{t_0}^{t_f} F(\mathbf{x}, \mathbf{u}, t) \approx \hat{J} = \frac{t_f - t_0}{2}\sum_{k=1}^{N} F(\hat{\mathbf{x}}_k, \hat{\mathbf{u}}_k, \tau_k) \tag{4.7}$$

The original time-varying states, control inputs, the dynamical equations constrained and the cost function are now discretized approximation of the continuous NLP problem. Thus the discretized approximation of the original OCP is compiled into the following nonlinear programming (NLP) problem.

$$\min_{\substack{\mathbf{u}_i \\ i=0,\ldots,N}} \quad \hat{J} = \frac{t_f - t_0}{2}\sum_{i=0}^{N} w_i f(\hat{\mathbf{x}}_i, \hat{\mathbf{u}}_i, \tau_i)$$

$$\text{s.t.} \quad \sum_{i=0}^{N} D_{k,i}\hat{\mathbf{x}}_i - \frac{t_f - t_0}{2}\mathbf{f}(\hat{\mathbf{x}}_k, \hat{\mathbf{u}}_k, \tau_k) = \mathbf{0}, \ k = 0, \ldots, N$$

$$\hat{\mathbf{x}}_N - \hat{\mathbf{x}}_0 - \sum_{k=1}^{N}\sum_{i=0}^{N} w_k D_{k,i}\hat{\mathbf{x}}_i = \mathbf{0}_n \tag{4.8}$$

$$\mathbf{e}^L \leq \mathbf{e}(\hat{\mathbf{x}}_0, \hat{\mathbf{x}}_N, \tau_0, \tau_N) \leq \mathbf{e}^U$$

$$\mathbf{h}^L \leq \mathbf{h}(\hat{\mathbf{x}}_k, \hat{\mathbf{u}}_k, \tau_k) \leq \mathbf{h}^U, \ k = 0, \ldots, N$$

$$t_i = \frac{t_f - t_0}{2}\tau_i + \frac{t_f + t_0}{2}$$

With the above results, we now present the application to the full multi-phase optimal control problem. In general, let us assume there are $p > 1$ phases where we set $p = 2$ for simplicity. Each phase is active within the interval $t \in [t_0^{(p)}, t_f^{(p)}]$. In each phase there is a cost function $J^{(p)}$, a dynamical system $\mathbf{f}^{(p)}$, a set of endpoint constraints $\mathbf{e}^{(p)}$, and a set of path constraints $\mathbf{h}^{(p)}$. If two phases, p and q, are linked, then there also exists a set of linkage constraints $\Phi^{(p,q)}$.

$$
\min_{\mathbf{u}^{(p)}} \sum_{p=1}^{P} J^{(p)} = \sum_{p=1}^{P} \int_{t_0^{(p)}}^{t_f^{(p)}} F^{(p)}(\mathbf{x}^{(p)}, \mathbf{u}^{(p)}, t)dt
$$

$$
\text{s.t.} \quad \dot{\mathbf{x}}^{(p)}(t) = \mathbf{f}^{(p)}(\mathbf{x}^{(p)}, \mathbf{u}^{(p)}, t)
$$

$$
\mathbf{h}^{L,(p)} \leq \mathbf{h}^{(p)}(\mathbf{x}^{(p)}, \mathbf{u}^{(p)}, t) \leq \mathbf{h}^{U,(p)}
$$

$$
\mathbf{e}^{L,(p)} \leq \mathbf{e}^{(p)}(\mathbf{x}^{(p)}(t_0^{(p)}), \mathbf{x}^{(p)}(t_f^{(p)}), t_0^{(p)}, t_f^{(p)}) \leq \mathbf{e}^{U,(p)}
$$

$$
\Phi^{L,(p,q)} \leq \Phi^{(p,q)}(\mathbf{x}^{(p)}, \mathbf{x}^{(q)}, \mathbf{u}^{(p)}, \mathbf{u}^{(q)}) \leq \Phi^{U,(p,q)}
$$

(4.9)

Each phase is discretized with its own set of points, $\{\tau_i^{(p)}\}$ so that,

$$
\mathbf{x}^{(p)}(\tau) \approx \hat{\mathbf{x}}^{(p)}(\tau) = \sum_{i=1}^{N} \hat{\mathbf{x}}_i^{(p)} L_i(\tau)
$$

(4.10)

so that the full multi-phase NLP is,

$$
\min_{\mathbf{u}_i^{(p)}} \sum_{p=1}^{P} \frac{t_f^{(p)} - t_0^{(p)}}{2} \sum_{k=1}^{N} F^{(p)}(\hat{\mathbf{x}}_k^{(p)}, \hat{\mathbf{u}}_k^{(p)}, \tau_k)
$$

$$
\text{s.t.} \quad \sum_{i=0}^{N} D_{k,i} \hat{\mathbf{x}}_i^{(p)} - \frac{t_f^{(p)} - t_0^{(p)}}{2} \mathbf{f}^{(p)}(\hat{\mathbf{x}}_k^{(p)}, \hat{\mathbf{u}}_k^{(p)}, \tau_k) = \mathbf{0}_n, \quad p = 1, \dots, P, \quad k = 1, \dots, N
$$

$$
\hat{\mathbf{x}}_N^{(p)} - \hat{\mathbf{x}}_0^{(p)} - \frac{t_f^{(p)} - t_0^{(p)}}{2} \sum_{k=1}^{N} \sum_{i=0}^{N} w_k D_{k,i} \hat{\mathbf{x}}_i = \mathbf{0}_n, \quad p = 1, \dots, P
$$

$$
\mathbf{e}^{L,(p)} \leq \mathbf{e}^{(p)}(\hat{\mathbf{x}}_0^{(p)}, \hat{\mathbf{x}}_N^{(p)}, t_0^{(p)}, t_f^{(p)}) \leq \mathbf{e}^{U,(p)}, \quad p = 1, \dots, P
$$

$$
\mathbf{h}^{L,(p)} \leq \mathbf{h}^{(p)}(\hat{\mathbf{x}}_k^{(p)}, \hat{\mathbf{u}}_k^{(p)}, \tau_k) \leq \mathbf{h}^{U,(p)}, \quad k = 1, \dots, N, \quad p = 1, \dots P
$$

$$
\Phi^{L,(p,q)} \leq \Phi^{(p,q)}(\hat{\mathbf{x}}_0^{(p)}, \hat{\mathbf{u}}_0^{(p)}, \hat{\mathbf{x}}_N^{(q)}, \hat{\mathbf{u}}_N^{(q)}) \leq \Phi^{U,(p,q)}, \quad p, q = 1, \dots, P
$$

(4.11)

To perform the discretization described in this subsection, we use the open-source C++ PSOC package $\mathcal{PSOPT}$ [112].

Next we show that Eq. (4.11) can be expressed in the typical NLP form [56]. Let $\mathbf{z}^{(p)}$ contain all of the variables for phase p.

$$
\mathbf{z}^{(p)} = \begin{bmatrix} \hat{\mathbf{x}}_0^{(p)} \\ \vdots \\ \hat{\mathbf{x}}_N^{(p)} \\ \hat{\mathbf{u}}_0^{(p)} \\ \vdots \\ \hat{\mathbf{u}}_N^{(p)} \end{bmatrix} \in \mathbb{R}^{(n+m)} \tag{4.12}
$$

Next, let $\mathbf{z}$ contain the variables for every phase,

$$
\mathbf{z} = \begin{bmatrix} \mathbf{z}^{(1)} \\ \vdots \\ \mathbf{z}^{(P)} \end{bmatrix} \in \mathbb{R}^{(N+1)(n+m)} \tag{4.13}
$$

With some algebraic manipulation, the entire discretized multi-phase OCP can be rewritten as an NLP in the typical form.

$$
\begin{aligned}
\min_{\mathbf{z}} \quad & c(\mathbf{z}) \\
\text{s.t.} \quad & \mathbf{g}(\mathbf{z}) = \mathbf{0} \\
& \mathbf{d}(\mathbf{z}) \leq \mathbf{0}
\end{aligned} \tag{4.14}
$$

To solve the large-scale NLP in Eq. (4.14) we employ an interior-point algorithm [56]. Specific details of the algorithm are outside the scope of this paper. We used the open-source C++ package IPOPT [113] to solve each instance of Eq. (4.14). We direct interested readers who would like to learn more about the technical detailed involved when solving Eq. (4.14) to the documentation provided with IPOPT.

The optimal solution returned, $\mathbf{z}^*$, is separated into its component parts; first by splitting it into the phases $\mathbf{z}^{(p)*}$, and second by reconstructing the discrete states and

control inputs, $\hat{\mathbf{x}}_i^*$ and $\hat{\mathbf{u}}_i^*$. The continuous time control inputs and states are then reconstructed using the Lagrange interpolating polynomials in Eq. (4.3). With the continuous time states and control inputs, $\mathbf{x}^*(t)$ and $\mathbf{u}^*(t)$, we then verify that the necessary conditions are met to within an acceptable tolerance.

4.4   Necessary Conditions of PSOC Solutions

We can use the Pontryagin's principle to drive a set of necessary conditions which a candidate solution must satisfies to be an optimal solution of the OCP in (4.1) [114]. In Ref. [114], the so-called HAMVET procedure has been proposed based on a slightly modified version of Pontryagin's principle to provide the necessary conditions for the general OCP in (4.1). We use the conditions to verify that the solution is optimal. The HAMVET procedure is based on the following steps:

- Construction of the Hamiltonian : (H)

- Adjoint equations : (A)

- Minimization of the Hamiltonian : (M)

- Evaluation of the Hamiltonian Value condition : (V)

- Evolution of the Hamiltonian : (E)

- Transversality conditions : (T)

In what follows, we construct the necessary conditions for the general OCP based on the HAMVET procedure. A detailed analysis can be found in Ref. [114].

4.4.1 Construction of the Hamiltonian

The *Hamiltonian H* corresponding to the general OPC problem is

$$H(\boldsymbol{\lambda}, \mathbf{x}, \mathbf{u}, t) = F(\mathbf{x}, \mathbf{u}, t) + \boldsymbol{\lambda}^T \mathbf{f}(\mathbf{x}, \mathbf{u}, t) \tag{4.15}$$

where $\boldsymbol{\lambda}(t) \in \mathbb{R}^n$ is the *adjoint covector* which is a function of time t. The control input that minimizes the OCP satisfies the Hamiltonian Minimization Condition (HMC), that is,

$$(HMC) \quad \begin{cases} \min_{u(t)} \quad H(\boldsymbol{\lambda}, \mathbf{x}, \mathbf{u}, t) \\ \text{s.t.} \quad \mathbf{h}^L \leq \mathbf{h}(\mathbf{x}, \mathbf{u}, t) \leq \mathbf{h}^U \end{cases} \tag{4.16}$$

4.4.2 Adjoint equations

The Karush-Kuhn-Tucker (KKT) conditions can be used to solve the HMC. We define the *Lagrangian of the Hamiltonian* $\bar{H}$ as

$$\bar{H}(\boldsymbol{\mu}, \boldsymbol{\lambda}, \mathbf{x}, \mathbf{u}, t) = H(\boldsymbol{\lambda}, \mathbf{x}, \mathbf{u}, t) + \boldsymbol{\mu}^T \mathbf{h}(\mathbf{x}, \mathbf{u}, t) \tag{4.17}$$

where $\boldsymbol{\mu}(t) \in \mathbb{R}^h$ is the *path covector* which is a function of time t. Then the evolution of the adjoint covector $\boldsymbol{\lambda}(t)$ is given by,

$$-\dot{\boldsymbol{\lambda}} = \frac{\partial \bar{H}}{\partial \mathbf{x}} \tag{4.18}$$

Note that condition in (4.18) enforces the continuity but not differentiability of $\boldsymbol{\lambda}(t)$. So, the piecewise continuity of $\boldsymbol{\lambda}(t)$ is a necessary condition for an optimal control

solution.

4.4.3   Minimization of the Hamiltonian

By the KKT condition, the minimization condition for the Hamiltonian yields

$$\frac{\partial \bar{H}}{\partial \mathbf{u}} = \mathbf{0} \tag{4.19}$$

with the complementary conditions for path constraints,

$$
\begin{cases}
\mu_i \leq 0 & if & h_i(\mathbf{x}, \mathbf{u}, t) = h_i^L \\
\mu_i = 0 & if \quad h_i^L < h_i(\mathbf{x}, \mathbf{u}, t) < h_i^U \\
\mu_i \geq 0 & if & h_i(\mathbf{x}, \mathbf{u}, t) = h_i^U \\
\mu_i \text{ unrestricted} & if & h_i^L = h_i^U
\end{cases}
\tag{4.20}
$$

If there are path constraints, then one of the necessary conditions is

$$\mu_i(t)(h_i - h_i^L)(h_i - h_i^U) = 0 \tag{4.21}$$

Along with the minimization of the Hamiltonian, there is an endpoint minimization condition (EMC) as well. The endpoint minimization problem is defined as

$$(EMC) \quad \begin{cases} \min & E(\mathbf{x}(t_0), \mathbf{x}(t_f), t_0, t_f) \\ \text{s.t.} & \mathbf{e}^L \leq \mathbf{e}(\mathbf{x}(t_0), \mathbf{x}(t_f), t_0, t_f) \leq \mathbf{e}^U \end{cases} \tag{4.22}$$

To solve the EMC by KKT, we define the *endpoint Lagrangian* $\bar{E}$ as

$$\bar{E}(\boldsymbol{\nu}, \mathbf{x}(t_0), \mathbf{x}(t_f), t_0, t_f) = E(\mathbf{x}(t_0), \mathbf{x}(t_f), t_0, t_f)$$
$$+ \boldsymbol{\nu}^T e(\mathbf{x}(t_0), \mathbf{x}(t_f), t_0, t_f) \tag{4.23}$$

where $\boldsymbol{\nu} \in \mathbb{R}^e$ is the *endpoint covector*. Note that, $\boldsymbol{\nu}$ is a constant vector. The complementary conditions for event constraints are given by

$$
\begin{cases}
\nu_i \leq 0 & if & e_i(\mathbf{x}(t_0), \mathbf{x}(t_f), t_0, t_f) = e_i^L \\
\nu_i = 0 & if \quad e_i^L < e_i(\mathbf{x}(t_0), \mathbf{x}(t_f), t_0, t_f) < e_i^U \\
\nu_i \geq 0 & if & e_i(\mathbf{x}(t_0), \mathbf{x}(t_f), t_0, t_f) = e_i^U \\
\nu_i \text{ unrestricted} & if & e_i^L = e_i^U
\end{cases}
\tag{4.24}
$$

4.4.4 Hamiltonian Value condition

The *lower Hamiltonian* $\mathcal{H}$ is defined as the Hamiltonian evaluated at $\mathbf{u}(t) = \mathbf{u}^*(t)$, the solution to the HMC problem, i.e.,

$$\mathcal{H} = \min_{\mathbf{u} \in \mathbb{U}} H(\boldsymbol{\lambda}, \mathbf{x}, \mathbf{u}, t) \tag{4.25}$$

where $\mathbb{U}$ is the set of feasible control inputs, i.e., they satisfy all of the constraints imposed by Eq. (4.1). The lower Hamiltonian must satisfy the endpoint value conditions as a regular Hamiltonian

$$\mathcal{H}(\boldsymbol{\lambda}(t_0), \mathbf{x}(t_0), t_0) = \frac{\partial \bar{E}}{\partial t_0}$$
$$\mathcal{H}(\boldsymbol{\lambda}(t_f), \mathbf{x}(t_f), t_f) = -\frac{\partial \bar{E}}{\partial t_f} \tag{4.26}$$

which provides another necessary conditions to check for the optimal control solution.

4.4.5 Time Evolution of the Hamiltonian

As the lower Hamiltonian $\mathcal{H}$ is obtained from the evaluation of the Hamiltonian at the $\mathbf{u}^*(t)$, $\mathbf{x}^*(t)$ and $\boldsymbol{\lambda}^*(t)$, where $\mathbf{x}^*(t)$ and $\boldsymbol{\lambda}^*(t)$ are the states and costates associated with the optimal control solution $\mathbf{u}^*(t)$, $\mathcal{H}$ is a function of time t only. Thus the evolution of the lower Hamiltonian $\mathcal{H}$ can be defined as

$$\dot{\mathcal{H}} = \frac{d\mathcal{H}}{dt} = \frac{\partial H}{\partial t} \tag{4.27}$$

If H in (4.15) does not depend explicitly on time, then another necessary condition is

$$\dot{\mathcal{H}} = 0 \quad \text{or} \quad \mathcal{H} = \text{constant} \tag{4.28}$$

4.4.6 Transversality conditions

The endpoints of the adjoint covector $\boldsymbol{\lambda}(t)$ are related to the partial derivatives of the endpoint Lagrangian $\bar{E}$. The transversality conditions for the adjoint covector $\boldsymbol{\lambda}(t)$ are

$$\boldsymbol{\lambda}(t_0) = -\frac{\partial \bar{E}}{\partial \mathbf{x}(t_0)} \quad \text{and} \quad \boldsymbol{\lambda}(t_f) = \frac{\partial \bar{E}}{\partial \mathbf{x}_f} \tag{4.29}$$

In chapter 6, we verify the necessary conditions for the optimal control problem that we formulate and solve in that chapter.

Chapter 5

Optimal Regulation of Blood Glucose Level in Type I Diabetes using Insulin and Glucagon

5.1   Introduction

As our first implementation o the optimal control strategies, as discussed in chapter 1 to biological systems, we consider the Glucose-Insulin-Glucagon (GIG) model [57–59, 115] which describes the response of the body to exogenously supplied insulin and glucagon in patients affected by Type I diabetes. Common therapies for diabetes involve the administration of exogenous insulin. Currently glucagon is not typically included in therapies because it does not preserve its chemical properties at room temperature and also because diabetic patients are still able to produce it.

The control of glucose levels in diabetic patients is an active field of research [47–50, 60–64, 116–121]. The approval by the FDA of a simulator which replaces *in-vivo* with *in-silico* therapy testing has greatly benefited this area of research. This

simulator implements a mathematical model, first proposed in [57] and updated in [58, 59, 115], and provides an alternative to often slow, dangerous and expensive human testing.

Typically, insulin is administered manually approximately half an hour before each meal where the amount is determined from the current glucose level (measured through a blood sugar test), the expected glucose intake, and the patient's sensitivity to insulin. In what follows we will refer to this as the *standard therapy*. In 1992 the first insulin pumps were introduced to the market. They delivered both a consistent basal amount of insulin and an insulin bolus determined by the patients based on their glucose level. It was only in 2016 that the first autonomous system for glycemic control was approved by the FDA. The system consists of an insulin pump, a sensor that measures the blood glucose level continuously in time, and control software that is able to regulate the insulin level in the blood without needing any input from the patient.

Many control techniques have been proposed and tested to regulate blood glucose levels using insulin pumps including PID (proportional–integral–derivative) control [60–65], fuzzy logic control [117–119] and bio-inspired techniques [120] which do not rely on a mathematical model. In [66] closed loop control has been used on a so called "minimal model" [122–124]. In [47–51] a linear model predictive control (MPC) has been used in a model with fixed structure but for which parameters are constantly updated to adapt to the patient's response. In [52] linear MPC has been used *in silico*. In [53] MPC has been applied to a system linearized around the operating points of a physically derived nonlinear model and in [67] multiple model probabilistic predictive control has been used. In [54] MPC has been applied together with a moving horizon estimation technique to a linear model. Most of the models used when designing the above controllers are simplified versions of the FDA approved model and all the control techniques considered only use insulin (but not

glucagon) as control input.

Because insulin delivered exogenously is not subject to normal physiological feed-back regulation, hypoglycemia is common in patients with Type 1 diabetes who undergo treatment [125]. For these patients it has been proposed that exogenous insulin can be used to lower their blood glucose level and exogenous glucagon can be used to prevent hypoglycemia [126, 127]. Currently, a commercial pump that delivers both insulin and glucagon is not available, and the development of a two-hormones artificial pancreas is still the subject of clinical research [128–136]. An outstanding research question, which we address in this paper, is the determination of the temporal dosages of both insulin and glucagon, in the case of the dual therapy.

Following the study in [137] which optimized multi-drug therapies for autophagy regulation, here we seek to determine an optimal strategy for delivery of both insulin and glucagon. We consider the combined effects of insulin and glucagon in regulating blood glucose levels in patients with Type 1 diabetes, using the model in [58] and nonlinear optimal control theory. Additionally, the objective function that we seek to minimize is the Blood Glucose Index which is a well known tool to measure the risk for a patient to enter either hyperglycemia or hypoglycemia. To design the optimal control problem, we use the balance control technique of ref. [138], which introduces a trade-off between the error allowed with respect to a state based cost (Blood Glucose Index) and the control effort. Our goal is to evaluate the performance limits of a control algorithm in the blood glucose problem, and to discuss the advantages of the dual therapy compared to the single therapy. Note that even though we do not attempt to design a closed-loop control strategy that works without the patient's intervention, the solution we propose can be adapted for that purpose.

From solving the optimal control problem for a family of objective functions derived from the balance control paradigm, we observe the emergence of a pattern, from which we propose a simple rule for the delivery of insulin and glucagon similar

to the standard therapy, but for the case that both insulin and glucagon are used. While this therapy is suboptimal, we see that it still performs better than the optimal solution with insulin alone.

Finally, we test the robustness of the optimal solution. While optimal control does not guarantee robustness of the optimal solution with respect to model uncertainty or parameter mismatches, we see that our proposed solution still performs well in the presence of model parameter perturbations and variations affecting the time and glucose intake of the meal.

5.2   Model and Parameters

We consider the model in [58, 59] which is a system of nonlinear ordinary differential equations (ODEs). The equations are given in Eqs. (C.1)-(C.9) in the section C.1 in Appendix C. We write the ODEs in Eqs. (C.1)-(C.9) in the form

$$
\begin{aligned}
\dot{\mathbf{x}}(t) &= \mathbf{f}(\mathbf{x}(t), \mathbf{u}(t), D(t), \Theta) \\
G(t) &= x_1/V_G
\end{aligned}
\tag{5.1}
$$

where the state vector is $\mathbf{x} = [x_1(t), x_2(t), ..., x_{17}(t)]^T$ and t is the physical time (in min). In Table 5.1 we tabulate all of the variables x_i and their names. The control input vector is $\mathbf{u}(t) = [u_I(t), u_G(t)]^T$, where $u_I(t) \geq 0$ is the exogenous insulin infusion rate (in insulin Unit/min) and $u_G(t) \geq 0$ is the exogenous glucagon infusion rate (mg/min). Both $u_I(t)$ and $u_G(t)$ are the external inputs to the system in Eq. (5.1). The scalar quantity $D(t)$ represents the exogenous glucose input, that is, the glucose intake with a meal. The output of the system is the quantity $G(t)$, which measures the density of glucose in the blood, obtained as the ratio between the plasma glucose and the distribution volume of glucose V_G.

When $u_I(t) = 0$, $u_G(t) = 0$ and $D(t) = 0$, the model reaches (for physically

meaningful parameters) a steady state, also known as the *basal condition* of a patient. The basal condition depends upon the parameters of the models Θ. We denote by Θ_{G_b} a set of parameters for which the basal glucose level G is equal to G_b. The basal levels for the other states are found according to Eqs. (C.11).

Table 5.1: Variables and their physical meaning

Variables	Names	Representing
x_1	G_p	Mass of glucose in plasma
x_2	G_t	Mass of glucose in tissue
x_3	I_l	Mass of insulin in liver
x_4	I_p	Mass of insulin in plasma
x_5	I'	Mass of delayed in compartment 1
x_6	X^L	Amount of delayed insulin action on EGP (Endogenous glucose production)
x_7	Q_{sto1}	Amount of solid glucose in stomach
x_8	Q_{sto2}	Amount of liquid glucose in stomach
x_9	Q_{gut}	Amount of glucose in intestine
x_{10}	X	Amount of interstitial fluid
x_{11}	SR_H^s	Amount of static glucagon
x_{12}	H	Amount plasma glucagon
x_{13}	X^H	Amount of delayed glucagon action on EGP
x_{14}	I_{sc1}	Amount of nonmonomeric insulin in the subcutaneous space
x_{15}	I_{sc2}	Amount of monomeric insulin
x_{16}	H_{sc1}	Amount of glucagon in the subcutaneous space 1
x_{17}	H_{sc2}	Amount of glucagon in the subcutaneous space 2

5.3   Problem Formulation

We formulate a nonlinear optimal control problem with two control goals. The first goal is to regulate the glucose at levels corresponding to low clinical risk of either hyperglycemia or hypoglycemia during a time period over which a meal is consumed. We assume that a meal is ingested at time $t = \tau_D$, which we assume to be modeled as a Dirac delta function $D(t) = D\delta(t - \tau_D)$. To evaluate the clinical risk of a particular

glycemic value, Kovatchev et al. [139, 140] proposed the *Blood Glucose Index* (BGI), defined as

$$BGI\left(G(t)\right) = 10\left(1.509\left((\ln G(t))^{1.084} - 5.3811\right)\right)^2,$$

where a small BGI value corresponds to low risk of either hyperglycemia or hypoglycemia. This metric also takes into account the fact that (i) the target blood glucose range as defined by the Diabetes Control and Complications Trial [141] (between 70 and 180 mg/dL) is not symmetric about the center of the range and (ii) hypoglycemia occurs at glucose levels closer to the basal level than hyperglycemia. The second goal is to limit the overall usage of insulin and/or glucagon over the period $[t_0, t_f]$.

We formulate the optimization problem according to these two goals,

$$\min_{\mathbf{u}(t)} \quad J = \int_{t_0}^{t_f} \left[\alpha_p BGI\left(G(t)\right) + \alpha_I u_I^p(t) + \alpha_G u_G^p(t)\right] dt, \tag{5.2}$$

subject to the following constraints,

$$\dot{\mathbf{x}}(t) = \mathbf{f}(\mathbf{x}(t), \mathbf{u}(t), D\delta(t - \tau_D), \Theta_{G_b}), \quad \mathbf{u}(t) = [u_I(t) \quad u_G(t)]^T \tag{5.3a}$$

$$G^L < G(t) < G^U \tag{5.3b}$$

$$u_I^L \le u_I(t) \le u_I^U \tag{5.3c}$$

$$0 \le u_G(t) \le u_G^U \tag{5.3d}$$

$$0 \le \int_{t_0}^{t_f} u_I(t)dt \le \phi_I^U \tag{5.3e}$$

$$0 \le \int_{t_0}^{t_f} u_G(t)dt \le \phi_G^U \tag{5.3f}$$

$$\mathbf{x}(t_0) = \bar{\mathbf{x}} \tag{5.3g}$$

In Eqs. (5.2) and (5.3), the insulin infusion rate $u_I(t)$ and the glucagon infusion rate $u_G(t)$ are the two control inputs. The three coefficients α_p, α_I and α_G in Eq. (5.2) are tunable factors through which we may vary the weight associated with each of

the three terms in the cost function J. The first coefficient, α_p is dimensionless while the units of α_I and α_G are $(\text{U/min})^{-p}$ and $(\text{mg/min})^{-p}$, respectively. Note that by setting $u_G = 0$ in Eq. (5.3d), we have an optimal control problem in terms of insulin only.

The first term in the objective function (5.2) defines a regulation problem, i.e., we try to maintain the glucose at low risk levels. The second and third terms in the cost function are chosen to avoid using excess insulin or glucagon. For $p = 1$ in Eq. (5.2), the second and third terms define a *'minimum fuel'* problem, thus we call the optimization problem ReMF (Regulation and Minimum Fuel). In this case, we expect the optimal solution to consist of pulsatile inputs $u_I^*(t)$ and $u_G^*(t)$ [110, 142]. For $p = 2$, the second and third term inside the cost function define a *'minimum energy'* problem, thus we call the optimization problem ReME (Regulation and Minimum Energy). In this case, we expect the optimal control inputs $u_I^*(t)$ and $u_G^*(t)$ to be continuous. The set of equations in (5.3a) coincide with the ODEs in Eqs. (C.1)-(C.9)of the supplemental information. In Eq. (5.3b) G^L and G^U are the lower and upper bounds for $G(t)$, they can be set in order to avoid undesired hypoglycemic or hyperglycemic states. In Eqs. (5.3c) and (5.3d) u_I^U and u_G^U are upper bounds for the insulin and glucagon delivery rates, respectively. These constraints are set by the maximum infusion rates allowed by the insulin pump. In Eq. (5.3c) $u_I^L \geq 0$ is the lower bound for $u_I(t)$, i.e., a minimum insulin delivery rate that can be used to set a basal insulin infusion rate to counteract endogenous glucose production [143]. Finally, in Eqs. ((5.3e), (5.3f)), ϕ_I^U and ϕ_G^U set limits to the total limits of insulin and glucagon that can be delivered over the time period $[t_0, t_f]$. The initial condition $\bar{\mathbf{x}}$ in Eq. (5.3g) defines the patient's condition before administration of the therapy. In the Results section, we discuss how we choose the bounds on $G(t)$, $u_I(t)$, $u_G(t)$, ϕ_I, ϕ_G, the control time period $[t_0, t_f]$ and the initial condition $\bar{\mathbf{x}}$.

Our goal is to find an optimal solution which satisfies the constraints in Eq. (5.3)

and minimizes the objective function (5.2). Note that the BGI only depends upon $G(t)$: we are making no attempt to control the states of the system, only its output. In the literature, such an approach is often referred to as target control [95, 110].

5.4 Method

The equations (5.2) and (5.3) together form a constrained optimal control problem, which can generally be written as Eq. (4.1). We have used $\mathcal{PSOPT}$ [112], an open-source PSOC library, to perform the above PSOC discretization procedure. The NLP in (4.8) can be solved with a number of different techniques, but here we use an interior point algorithm [56] as implemented in the open-source software Ipopt [113].

5.5 Results

We now describe in more detail the optimal control problem in Eqs. (5.2) and (5.3) by setting the constraint and parameter values. In Fig. 5.1(A) we plot the function $BGI(G)$ versus the glucose G. The minimum $BGI(G)$ occurs at $G = G_d = 112.51$ mg/dL, which corresponds to a clinical target set for the glucose level [141]. Based on the data in [144], the average fasting plasma glucose level of patients with type I diabetes is $G_b = 130$ (mg/dL). Thus, we set the the basal glucose level $G_b = 130$ (mg/dL). The parameters Θ_{G_b} are set so that the steady state glucose is 130 (mg/dL) in the absence of a meal and of exogenously supplied insulin, i.e., we compute Θ_{130}.

We set the upper and lower bounds for the glucose level, G^L and G^U in Eq. (5.3b), to satisfy the target blood glucose range, $90 \leq G(t) \leq 180$ [141]. The control time period is $[t_0, t_f] = [0, 300]$ minutes, and we assume that a meal with 70 grams
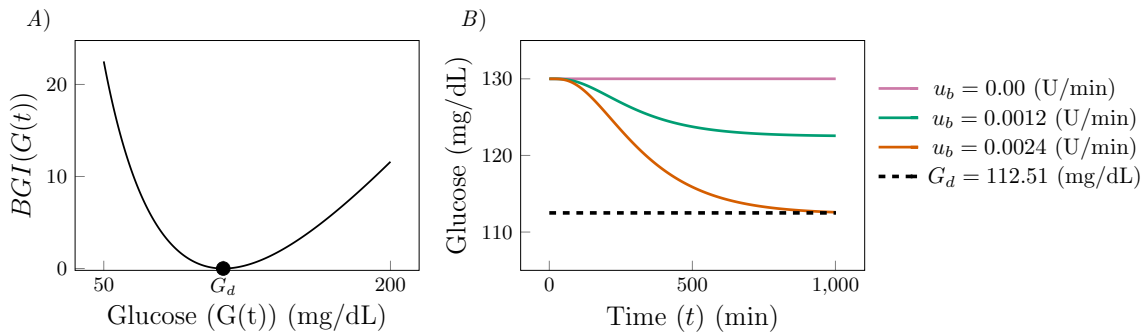
Figure 5.1: (*A*) The Blood Glucose Index ($BGI(G(t))$) as a function of the blood glucose $G(t)$. The function is minimized at $G(t) = G_d = 112.51$ (mg/dL). (*B*) The response of glucose ($G(t)$) to different time-constant basal insulin infusion rates in the absence of a meal. We see that as u_b increases, the glucose is further down regulated.

of glucose is consumed at time $t = 60$ min (i.e. $D(t) = 70\delta(t - 60)$).

We consider a situation in which the patient's glucose level is partially controlled by providing a constant but low insulin infusion rate $u_b > 0$ (which is common for patients who use an insulin pump) [143] and serves to compensate for the endogenous glucose production. In figure $5.1B$ we show glucose response $G(t)$ for different values of constant u_b in the absence of a meal. We observe that for $u_b = 0.0024$ (U/min), $G(t)$ converges to the desired glucose level G_d. We thus set the lower bound of $u_I(t)$ in Eq. (5.3c), $u_I^L = u_b$, while its upper bound is set to $u_I^U = 15$ (in U/min), the maximum insulin flow allowed in commercial pumps [145]. In the absence of commercially available glucagon pumps, we will assume that a pump mechanically similar to an insulin pump is used to deliver glucagon. Since the maximum flow rate for an insulin pump is 0.15 mL/min (1 mL of insulin solution contains 100 U of insulin), and normally 1 mg of glucagon is diluted in 1 mL of solution, the maximum glucagon flow rate in Eq. (5.3d) is set to $u_G^U = 0.15$ mg/min.

The amount of insulin administered in a bolus to a patient with a basal glucose level lower than 150 mg/dL normally ranges between 0.12 and 0.2 U/kg [146]. As

the body mass of the *in-silico* patient we consider is 78 kg, we set $\phi_I^U = 16$ U in Eq. (5.3e). The maximum total amount of glucagon administered in one shot to a patient who is in a hypoglycemic state is 1 mg, and a second identical shot can be administered after thirty minutes. We thus choose the maximum total amount of glucagon used (as defined in Eq. (5.3f)) throughout the five hour therapy to be $\phi_G^U = 1$mg.

The choice of the initial condition $\bar{\mathbf{x}}$ in Eq. (5.3g) is critical. We select the initial condition so that the solution of our optimal control problem only attempts to regulate glucose in response to a meal. In the results presented we have set the initial condition equal to the values of the states when $u_I(t) = u_b$ after a period of fasting (the final point of the blue curve in Fig. 5.1(B). If we were to select any alternative initial condition then the solution to the optimal control problem would try to 'correct' the initial condition as well, making comparisons between solutions difficult.

Once the parameters, bounds, the control time period and the initial condition are set, we solve the nonlinear optimal control problem using $\mathcal{PSOPT}$. We first solve the optimal control problem without glucagon (i.e. $u_G^U = 0$), and then we solve the optimal control problem using both insulin and glucagon.

To evaluate the effectiveness of the obtained results, we introduce the following measures.

- The cumulative insulin $r_I(t)$ and cumulative glucagon $r_G(t)$ used up to time t,

$$r_I(t) = \int_{t_0}^{t} u_I(\tau)d\tau, \qquad r_G(t) = \int_{t_0}^{t} u_G(\tau)d\tau.$$

- The total amount of insulin $\phi_I = r_I(t_f)$ and the total amount of glucagon $\phi_G = r_G(t_f)$ used up to final time t_f.

- The integral of BGI over the entire time period $[t_0, t_f]$,

$$\Delta = \int_{t_0}^{t_f} BGI(G(t))dt.$$

  where a large Δ indicates that the patient is at higher risk of either hypergly-
  cemia or hypoglycemia for a prolonged period of time.

- The maximum and minimum values attained by the blood glucose level over
  the entire time period $[t_0, t_f]$,

$$G^{\max} = \max_{t \in [t_0, t_f]} G(t), \qquad G^{\min} = \min_{t \in [t_0, t_f]} G(t),$$

  which measure the risk for either hyperglicemia or an hypoglicemia [140, 147],
  respectively.

5.5.1 Insulin as Control Input

In this section we use only insulin as control input, i.e., we set $u_G = 0$ in Eq. (5.3a).
As the orders of magnitude of the terms BGI and u_I^p in the objective function are
different, it is important to find the appropriate values of the scaling factors α_p and
α_I. In what follows, we use a *Pareto-front* analysis to determine these values. We
first rewrite the objective function as

$$J = \int_{t_0}^{t_f} \left[\varepsilon BGI(G(t)) + u_I^p \right] dt \tag{5.4}$$

where $\varepsilon = \alpha_p / \alpha_I$. In Figs. 5.2($A$–$D$) we plot Δ, $G^{\min}$, $G^{\max}$ and ϕ_I as functions
of the coefficient ε. By looking at these plots, we see that the four measures can
be divided into two groups. On the one hand, Δ and $G^{\max}$ (panels (A) and (C)),
improve (decrease) as ε increases, with a sharp transition around $\varepsilon = 10$ for the
ReMF problem and around $\varepsilon = 10^3$ for the ReME problem. On the other hand,
$G^{\min}$ and ϕ_I (panels (B) and (D)), behave in the opposite way, i.e., they improve
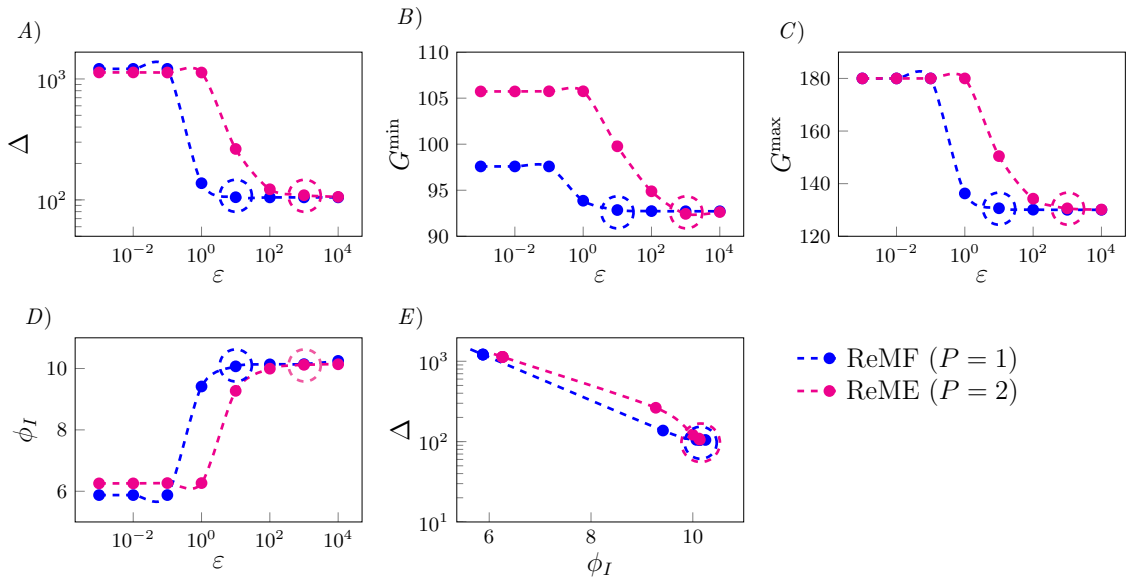
Figure 5.2: Performance of the optimal control solution as a function of ε. Large (small) values of ε correspond to a large (small) weight associated with the BGI index in the objective function, compared to the weight for insulin expenditure. The first four plots show our metrics as functions of the objective function coefficients: (A) Δ vs. ε, (B) G^{min} vs. ε, (C) G^{max} vs. ε, and (D) ϕ_I vs. ε. (E) We also project the Pareto front into the Δ - ϕ_I plane. We see a clear trade-off between Δ and ϕ_I as we vary ε. By increasing ε we can decrease the values of Δ and G^{max}. However, the values of Δ and G^{max} do not further decrease for ε larger than 10 for the ReMF problem ($p = 1$) and the value of Δ does not further decrease for ε larger than 10^3 for the ReME problem ($p = 2$). We choose $\varepsilon = 10$ for $p = 1$ and $\varepsilon = 10^3$ for $p = 2$, which are indicated by dashed circles in the figure, for the remaining simulations.

(insulin decreases and the minimum glucose level increases) as ε decreases, again with a sharp transition around $\varepsilon = 10$ for the ReMF problem and around $\varepsilon = 10^3$ for the ReME problem. Because the four curves in Figs. 5.2(A–D) are monotone, all the points are Pareto-efficient, i.e., it is not possible to improve one objective (e.g. Δ) without worsening the other one (e.g. ϕ_I). We notice that past a certain value of ε (10 in the ReMF case, 10^3 in the ReME case) Δ and G^{max} do not further decrease and G^{min} and ϕ_I remain unchanged. We choose as weights $\alpha_p = 10$ and $\alpha_I = 1$ for $p = 1$, while we choose $\alpha_p = 10^3$ and $\alpha_I = 1$ for $p = 2$ (these are highlighted

by dashed circles in Fig. 5.2). The reason for these choices (for both values of p) is that these values yield $\phi_I \sim 10$ units, which is equal to two thirds of the maximum amount of insulin that can be supplied (ϕ_I^U), and $G^{\min} \sim 93$mg/dL, which is far from the hypoglycemic risk region.

In Fig. 5.2(E), we plot a projection of the Pareto front in the Δ and ϕ_I plane. Looking at this plot, the trade-off between Δ and ϕ_I is evident; if the total amount of insulin expenditure increases, Δ decreases and vice-versa. The ReMF and the ReME therapies can also be compared in Fig. 5.2(E). The ReMF Pareto front dominates the ReME one (both Δ and ϕ_I are lower on the blue curve ($p = 1$) compared to the magenta curve ($p = 2$)). This indicates that a shot of insulin (the optimal solution of a ReMF problem is typically a pulsatile function) performs slightly better in terms of Δ than a therapy in which the insulin is delivered over a longer period of time while using less insulin.

Figure 5.3 shows the results of the optimal control problem for the selected values of α_p and α_I. The blue and magenta curves are the optimal solutions of the ReMF and of the ReME problem, respectively. The orange curve corresponds to the case that 10 U of insulin are injected 30 minutes before the time of the meal, i.e., the standard therapy. We observe that for $P = 1$ the optimal insulin infusion rate is pulsatile with a pulse appearing at $t \sim 20$ minutes, which is 40 minutes before the time of the meal. We obtained qualitatively similar results for different choices of the model parameters, with the pulse typically appearing at a time in the interval $t \in [20, 30]$ minutes. It is noteworthy that the optimal solution is close to the standard insulin based therapy for glucose regulation in diabetics. The optimal insulin infusion rate is continuous when we solve the ReME problem, also shown in the inset of Fig. 5.3(B). Note that the ReMF and ReME therapies perform very similarly with respect to glucose as the peak insulin infusion rate occurs at approximately the same time and the total amount of insulin administered is nearly equal.

5.5.2   Insulin and Glucagon as Control Inputs

In the previous section we tuned the weights α_p and α_I inside the objective function (5.2). We now consider the case that $u_G > 0$ and we tune α_G, the weight associated with the glucagon expenditure in the objective function (5.2), by keeping $\alpha_p = 10$, $\alpha_I = 1$ for $P = 1$ and $\alpha_p = 10^3$, $\alpha_I = 1$ for $p = 2$, as previously determined.

A)

	ReMF ($P=1$)	ReME ($P=2$)	Standard Therapy
Δ	105.17	109.27	153.83
$G_{\min}$ (mg/dL)	92.85	92.43	88.10
$G_{\max}$ (mg/dL)	130.65	130.62	121.72
ϕ_I (U)	10.07	10.10	10
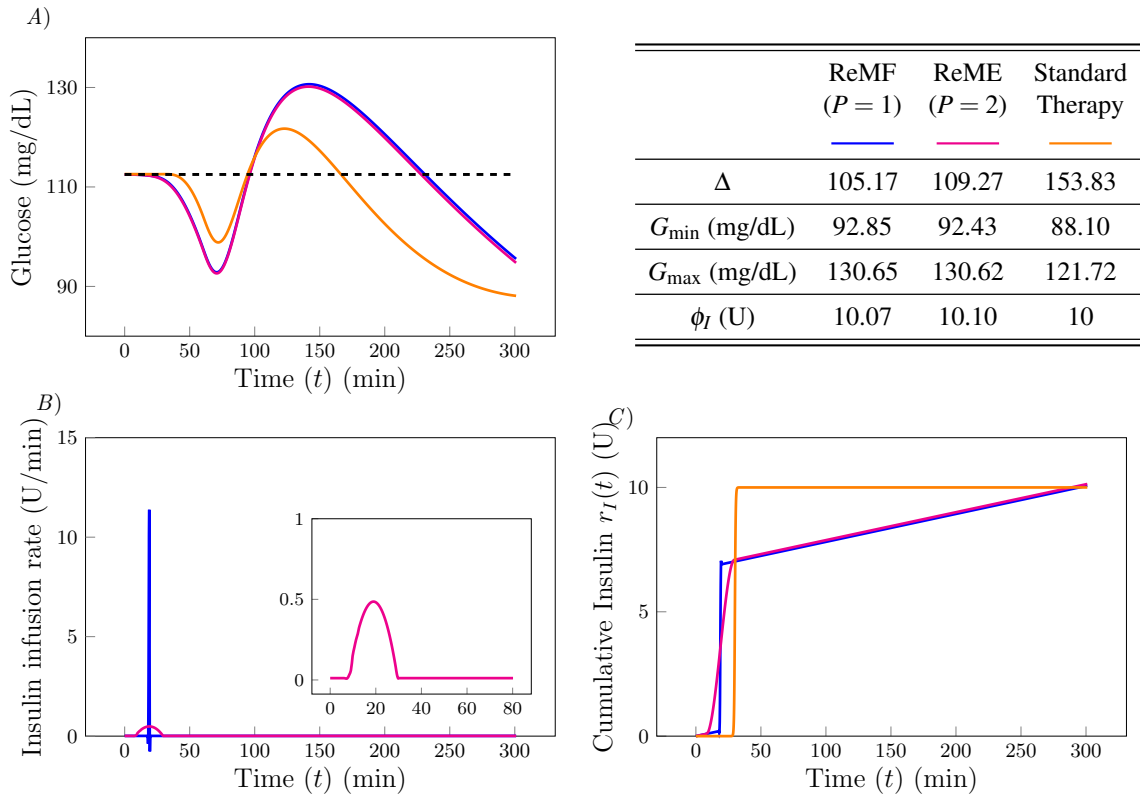
Figure 5.3: (A) The time evolution of glucose $G(t)$ (in mg/dL). The blue curve corresponds to the pulsatile optimal insulin supply rate $u_I(t)$ (shown in (B) obtained by solving the ReMF problem. The magenta curve corresponds to the continuous optimal insulin supply rate $u_I(t)$ (shown in (B) obtained by solving the ReME problem. The orange curve is the time evolution of $G(t)$ corresponding to the standard therapy (10 U of insulin injected 30 minutes before the time of the meal). (B) Time evolution of the optimal insulin infusion rates $u_I(t)$ (in U/min). Color code is consistent with (A). (C) Cumulative insulin supply $r_I(t)$ (in U) as a function of t.
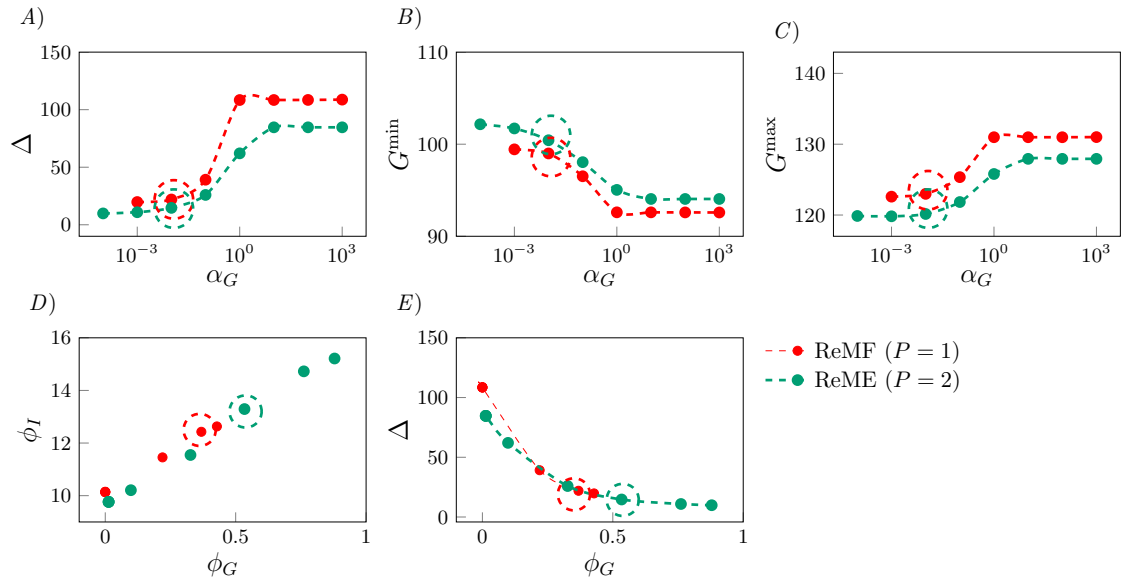
Figure 5.4: Performance of the optimal control solution as a function of α_G. (emphA) Δ vs. α_G. (B) $G_{\min}$ vs. α_G. (C) $G_{\max}$ vs. α_G. (D) ϕ_I vs. ϕ_G. (E) Δ vs. ϕ_G. We select $\alpha_G = 10^{-2}$ for both of the REMF and REME problems, which are indicated by dashed circles in the figure.

In Fig. 5.4(A), 5.4(B) and 5.4(C), we plot the optimal Δ, $G^{\min}$ and $G^{\max}$ as functions of the parameter α_G, respectively. A large value of α_G indicates that we are placing a large weight on the expenditure of glucagon within the objective function (5.2), i.e., the larger the value of α_G, the less glucagon we use. By looking at Fig. 5.4(A), we observe that the values of Δ decrease as α_G decreases, i.e. we can obtain lower (improved) values of Δ if we allow for a larger expenditure of glucagon. We note that past a certain value of α_G (10^{-2} in the both the ReMF and ReME problems) no further reduction in Δ is observed. As in the previous case, the maximum glucose level $G^{\max}$, shown in Fig. 5.4(C), improves (decreases) when Δ improves (decreases). Interestingly, different from the previous case, also the minimum glucose level $G^{\min}$ (Fig. 5.4(C) improves (increases) with Δ and $G^{\max}$: this is a consequence of the fact that we are using both insulin and glucagon as control inputs, which enables us to avoid both hypoglycemia and hyperglycemia.

In Fig. 5.4(D) we plot the projection of the Pareto front in the (ϕ_I, ϕ_G) plane. By looking at the figure, ϕ_I and ϕ_G appear to be positively correlated and related by an approximately linear relation. While the timing of administration of insulin and glucagon is different, we see that overall the more insulin is used in the optimal solution, the more glucagon is used as well. This is because the two hormones have opposite effects in the regulation problem and thus they work so as to balance each other. This is also consistent with the observation that with the dual therapy (insulin and glucagon) it becomes possible to simultaneously improve Δ, G^{min}, and G^{max}. From the data in Fig. 5.4(D) we derive the following approximate linear relationship between ϕ_G and ϕ_I,

$$\phi_G(\phi_I) = 0.1596\phi_I - 1.5796 \tag{5.5}$$

Obviously, glucagon should be used only when $\phi_G(\phi_I) > 0$.

Panel 5.4(E) shows a projection of the Pareto front on the (ϕ_G, Δ) plane. We see again that the ReMF front dominates the ReME one, i.e., a pulsatile therapy gives better results than a continuous therapy in terms of Δ and also uses lower amounts of the two hormones (smaller ϕ_G, and thus smaller ϕ_I due to the positive correlation found in Fig. 5.4(D).

The Pareto front is monotonically decreasing in Fig. 5.4(E) which indicates a trade-off between the total amount of hormones used and the achievable glucose control performance. We choose the value of α_G for which the ratio between the increase in Δ and the decrease in ϕ_G is minimized, i.e. $\alpha_G = 10^{-2}$ for both ReMF and ReME problems, which are indicated by dashed circles in the figure.

Figures 5.5(A) and 5.5(B) show the results of the optimal control problem for $\alpha_p = 10$, $\alpha_I = 1$ and $\alpha_G = 10^{-2}$ when $P = 1$; and $\alpha_p = 10^3$, $\alpha_I = 1$ and $\alpha_G = 10^{-2}$ when $p = 2$. In Fig. 5.5(A) we plot the time evolution of glucose $G(t)$ for the different optimal solutions. The blue curve corresponds to the solution of the ReMF problem

when only insulin is used (the blue curve in Fig. $5.3(A)$. The red and green curves correspond to the solution of the ReMF and the ReME problems for the dual therapy. We observe that $G(t)$ reaches the desired level G_d faster if we use both insulin and glucagon as control inputs, compared to the case that only insulin is used. We also see that in this case both G^{max} decreases and G^{min} increases. We therefore conclude that the therapy with both insulin and glucagon performs better than the therapy with only insulin, as the risks for both hypoglycemia and hyperglycemia are reduced and glucose fluctuations are suppressed.

In Fig. $5.5(B)$ we plot the optimal insulin infusion rates and in Fig. $5.5(C)$ we plot the cumulative insulin supply $r_I(t)$ as a function of time t. We observe that for the ReMF problem, the pulse in insulin appears at $t = 32$ minutes in the case that both insulin and glucagon are used (28 minutes before the meal), whereas the pulse appears at $t = 20$ minutes when only insulin is used. From Fig. $5.5(D)$, we see that, for the ReMF problem, the glucagon delivery function is pulsatile with a main pulse appearing at $t = 145$ min (one hour and 25 minutes after the meal) and a secondary pulse appearing at $t = 203$. The dual therapy shows a noticeable difference between the ReMF solution and the ReME solution. As expected, the solutions of the ReME problem are continuous. The glucose response to the ReME therapy is better than the glucose response to the ReMF solution. Specifically, the green curve has smaller oscillations (in panel (A) at the cost of small increases in the total amounts of used insulin and glucagon (compare panels (C) and (E)).

Based on the results in Fig. 5.5, we propose a possible *ad-hoc* dual therapy to be used as an alternative to the standard therapy. Rather than administering insulin half an hour before the meal (standard therapy), better glucose regulation can be achieved with a slightly larger insulin injection half an hour before a meal followed by a glucagon injection one hour and thirty minutes after a meal. The insulin injection of the *ad-hoc* dual therapy is 25% larger than the one used in the standard therapy,

which is consistent with the relation between ϕ_I for the monotherapy ReMF optimal solution and the one used in the dual therapy.

In Fig. 5.6 we present a comparison between the glucose response to the standard insulin base therapy (orange curve) and the proposed *ad-hoc* dual therapy (cyan curve) for the case of a meal with 70 grams of glucose (for the particular patient considered this corresponds to 10 units of insulin half an hour before the meal) and the proposed *ad-hoc* dual therapy (which consists of 12.43 units of insulin thirty minutes before the meal and 0.40 mg of glucagon one hour and thirty minutes after the meal). We observe that the *ad-hoc* dual therapy performs better in terms of all of the proposed measures (Δ, G^{min}, G^{max}, ϕ_I and ϕ_G) as opposed to the standard insulin based therapy.

5.6 Robustness Analysis

We now analyze the robustness of the optimal control therapies we have proposed with respect to model parameter mismatches, which is a fundamental step for implementation of model based control. We consider two different types of mismatches. The first type accounts for variability in the patient's behavior, in terms of both the time of the meal τ_D and the amount of glucose intake D. The second type accounts for deviations in the parameter estimation, as well as the temporal variability of the parameters that a patient may experience during the day [59].

5.6.1 Robustness Against Variability of the Meal Time and Glucose Intake

In this section we analyze the robustness of the optimal ReMF therapies (both monotherapy and dual therapy) with respect to the two "control" parameters the patient

has. The first one is the variation in the meal time, $(\bar{\tau}_D - \tau_D)$ (min), where $\bar{\tau}_D$ is the time of a meal and τ_D is the time of a meal we assumed in order to compute the optimal therapies. The second one is the variation of glucose in the meal, $(\bar{D} - D)$, where $\bar{D}$ is the glucose intake in a meal and D is the glucose intake we assumed to compute the optimal therapies. We consider variations in the meal time $\bar{\tau}_D$ in the interval $[30, 90]$ min and variations of the glucose intake $\bar{D}$ in the interval $[40, 100]$ g.

The results of this study are illustrated in Fig. 5.7. Figure 5.7 provides a visual assessment of the quality of the optimal therapies in terms of the three proposed measures Δ, G^{max} and G^{min} (the over-bar stands for evaluation at the perturbed parameter values $(\bar{\tau}_D, \bar{D})$). The color in Fig. 5.7 varies according to the control performance from green (good) to red (dangerous). In the upper panels $(A–C)$ we consider the optimal ReMF monotherapy, while in the lower panels $(D\text{-}F)$ we consider the optimal ReMF dual thearpy. Cross symbols indicate the application of the optimal control therapies under ideal condition, i.e., when $\bar{\tau}_D = \tau_D$ and $\bar{D} = D$. The black curves labeled by 180, 90 and 70 in Figs. 5.7(B), 5.7(C), 5.7(D), 5.7(E) are the curve level plots for $\bar{G}^{\text{max}} = G^U$, $\bar{G}^{\text{min}} = G^L$ and $\bar{G}^{\text{min}} = 70$, respectively. The black curves labeled by 180 in Figs. 5.7(B), and 5.7(E), are the curve level plots for $\bar{G}^{\text{max}} = G^U$.

We see from Figs. 5.7(A) and 5.7(D) that the optimal therapies for the ReMF problem (using only insulin or both insulin and glucagon) are robust with respect to variations in the control parameters: $\bar{\Delta}$ remains well bounded in most of the considered parameter space. In particular we see from Figs. 5.7(B) and 5.7(E) that the proposed optimal therapies are robust against hyperglicemic events: for example, even if $\bar{D}$ exceeds D by 50% and $\bar{\tau}_D$ exceeds τ_D by 30 minutes, the patient will not enter the hyperglicemic regime ($G^{\text{max}} > 300$). Figures 5.7(C) and 5.7(F) reveal that the proposed therapies suffer from a certain lack of robustness with respect to hypoglycemic events ($G^{\text{min}} < 70$), the most dangerous ones. The dangerous cases

are, however, confined to extreme situations in which $\bar{D} < 0.5D$ and $\bar{\tau}_D = \tau_D + 30$ minutes. Figures $5.7(C)$ and $5.7(F)$ show also that the optimal therapy for the ReMF problem with both insulin and glucagon is more robust (larger green region and smaller yellow region) than the optimal therapy for ReMF problem with only insulin (smaller green region and larger yellow region): thus the use of glucagon alleviates the risk of severe, life-threatening hypoglycemia.

We obtain qualitatively similar results when performing the same analysis for the other therapies we proposed (the ReME therapies and the *ad-hoc* dual therapy).

5.6.2   Robustness to Parameter Mismatches

We consider perturbation of the model parameters up to 20% of their nominal values,

$$\bar{\Theta}_i = \Theta_i(1 + \varphi), \tag{5.6}$$

where φ is a random number from a normal distribution $\mathcal{N}(0, 0.067^2)$, Θ_i is a nominal parameter for a given patient with basal glucose level G_b and $\bar{\Theta}_i$ represents the associated perturbed parameter. We then apply the optimal insulin and glucagon dosing, calculated for the unperturbed system, to 100 perturbed systems. This is analogous to testing the computed optimal control therapy on a specific patient, but the patient's parameters may vary due to imperfect knowledge or due to the parameter variability throughout the day. The results of this study are illustrated with a Control Variability Grid Analysis (CVGA), see Fig. 5.8. The CVGA provides a simultaneous visual and numerical assessment of the overall performance of the glycemic control strategies in terms of the achieved minimum/maximum glucose values in the space of parameters mismatches. In Fig. 5.8, points in the light green region indicate accurate blood glucose control while points in the dark green regions indicate the patient is not immediately at risk of either hypoglycemia or hyperglycemia. Points

in the top two yellow/orange regions indicate an elevated risk of hyperglycemia and points in the the right two yellow/orange regions indicate an elevated risk of hypoglycemia. Finally, points in the red corner region indicate an elevated risk of both hyperglycemia and hypoglycemia. Each point reported in the figure is a plot of G^{max} vs. G^{min}. Here, the black dots correspond to the glucose response when a certain therapy is applied to a system with perturbed parameters. Cross symbols indicate application of the optimal control therapies to the unperturbed systems.

For the of monotherapy (ReMF in Fig. 5.8A and ReME in Fig. 5.8B) we find that the control is 67% and 61% accurate, respectively. For the dual therapy case (ReMF in Fig. 5.8(C) and ReME in Fig. 5.8(D) we find the control is more accurate than for the case of monotherapy, 92% and 94% accurate, respectively. The least robust control is obtained with the standard therapy (shown in Fig. 5.8(E), attaining only 37% accuracy. Note that the optimal dual therapies (Figs. 5.8(C) and 5.8(D)) are not only more robust than the optimal insulin therapies (Figs. 5.8(A) and 5.8(B)), but also than the standard therapy (Fig. 5.8(E)). We also see that the *ad hoc* therapy (Fig. 5.8(E)) is more robust than the standard therapy (Fig. 5.8(E)).

5.7 Discussion

In this paper we have used the Glucose-Insulin-Glucagon mathematical model proposed in [58, 59, 115], which describes how the body responds to exogenously supplied insulin and glucagon in patients affected by Type I diabetes and designed an optimal dosing schedule of either insulin or insulin and glucagon together to regulate the blood glucose index (BGI), while limiting the total amount of insulin and glucagon administered. The numerical optimal control software $\mathcal{PSOPT}$ has been used to solve this optimal control problem. While the numerical solution requires knowledge of the set of model parameters, which are patient specific, the solutions we obtain

provide insight into the best possible glucose regulation with insulin or with insulin and glucagon together. Our approach is in agreement with the results of references [148–150], in which simplified models are used to analytically establish general theoretical properties and control limitations for the glucose regulation problem.

Two distinct regulation problems have been considered: the minimum fuel problem (ReMF) which yields pulsatile (shot-like) type solutions and the minimum energy problem (ReME) which yields longer periods of time over which insulin is administered but with smaller delivery rates. This has allowed us to compare standard therapies which typically consist in shots of insulin with therapies in which insulin is delivered continuously. In [151, 152] it has been proven that the optimal control is pulsatile when the aim of the control is to minimize the variation in the maximum and minimum output response, the system is positive (like the one we are considering) and the disturbance (the meal, in our case) is pulsatile. Our work indicates that pulsatile control is still a good choice when more complex objective functions are chosen. Moreover, a pulsatile control appears to be optimal for alternative more realistic models of the meal (for example, a meal that is consumed over a window of 15 minutes). We also see that a continuous hormones delivery can achieve better results in the case of the dual therapy, thus pointing out the importance of developing a commercial pump able to deliver both insulin and glucagon.

For both the ReMF and ReME problems, we compute the optimal hormone dosing schedules when only insulin is available and when both insulin and glucagon are available. The solution of the insulin only ReMF problem, astoundingly, is nearly equal to the standard method of insulin based glucose regulation. Similarly, the solution of the ReMF problem when insulin and glucagon are used is also pulsatile, except that the amount of insulin administered is larger and the administration time is closer to the time of the meal, while the glucagon is mostly delivered in a shot about an hour and thirty minutes after the meal.

The solution for the ReME problem when insulin only is available as well as when both insulin and glucagon are available is different from the ReMF solution in that, rather than being pulsatile, insulin and possibly glucagon are delivered at a slower rate over longer periods of time. Nonetheless, the total amount of insulin and possibly glucagon is about the same, and the peak of the longer delivery time occurs approximately at the same time of the shot according to the solution of the ReMF problem. The obtained glucose profiles for the optimal ReMF and ReME problem solutions do not differ too much from each other: taken together, these results indicate that the amounts of insulin and glucagon, and the peak times of delivery, are the most important factors to determine when computing the optimal solutions.

Based on the above results, we have proposed the following *ad hoc* therapy when insulin and glucagon are used in combination: *Administer a shot of insulin (with 25% more insulin than the amount required by the standard therapy based on the planned meal)* 30 *minutes before eating. Administer a shot of glucagon of an amount specified by Eq.* (5.5) *one hour and thirty minutes after completing the meal.* This therapy should be used with caution as the amount of insulin injected can lead to hypoglycemia if the shot of glucagon is not administered as well.

All optimal dosing schedules we computed were tested for robustness with respect to variations in the meal timing and size and with respect to variability of the parameters. The therapies we proposed typically maintain the patient in the healthy region even under variable conditions and patient behavior. Note, however, that the proposed therapies are open-loop, thus cannot compensate for unexpected behavior that can arise due to modeling simplifications (e.g. we do not consider how physical activity influences the blood glucose levels [153, 154]), measurement noise or bias. A step towards the real application of our methodology is a real-time closed-loop strategy; this is possible, since the typical time needed to compute an

optimal solution on a standard laptop (i7-8550U CPU with 16GB RAM) is around 2 minutes. Another main limitation of our study is that real life constraints and long term physiological effects may make a therapy based on exogenous administration of both insulin and glucagon impractical.

Our optimal control strategies require knowledge of the meal time and meal glucose amount. This is somewhat undesirable, as recent advances in diabetes therapy have moved towards devices that do not require the user to provide information about the meals. Our results emphasize the importance of incorporating information about the meals in the dosing schedules and indicate a potential benefit of providing the pump with the ability to interpret the patient's behavior. The results from this chapter have been published in [155].

A)

	ReMF $(P = 1)$	ReME $(P = 2)$	ReMF $(P = 1)$
	—	—	—
Δ	21.96	14.66	105.17
G_{min} (mg/dL)	99	100.43	92.85
G_{max} (mg/dL)	123	120.15	130.65
ϕ_I (U)	12.43	13.29	10.07
ϕ_G (mg)	0.37	0.53	

B)

C)

D)

E)
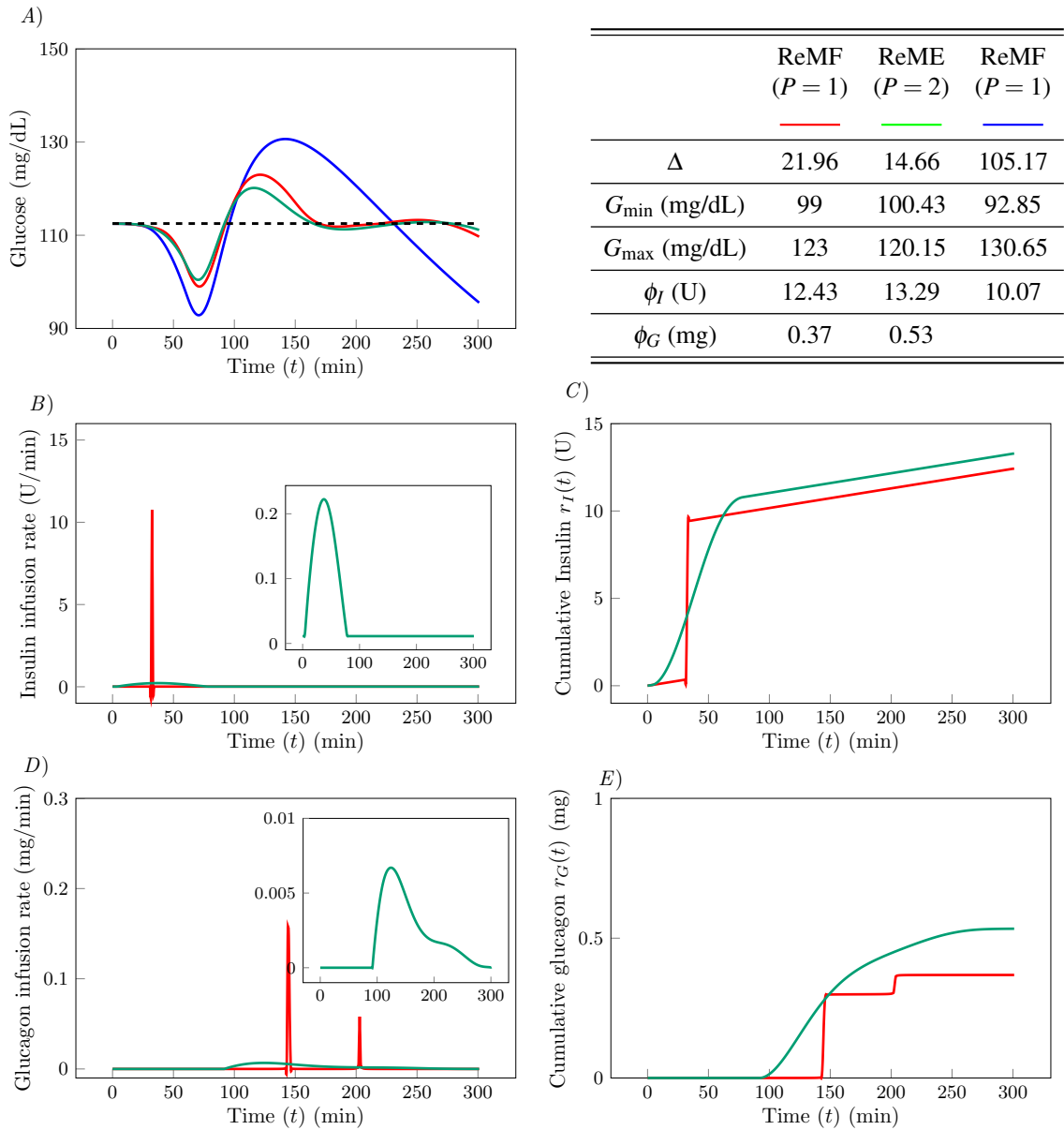
Figure 5.5: (A) Time evolution of glucose $G(t)$ (in mg/dL). The blue curve corresponds to $u_I(t)$ obtained by solving the ReMF problem . The red curve corresponds to $u_I(t)$ and $u_G(t)$ obtained by solving the ReMF problem using the dual therapy. The green curve corresponds to $u_I(t)$ and $u_G(t)$ obtained by solving the ReME problem using the dual therapy. (B) Time evolution of the insulin infusion rate $u_I(t)$ (in mg/dL). Color code is consistent with (A). (C) The cumulative insulin supply $r_I(t)$ as a function of time t. (D) Time evolution of the glucagon infusion rate $u_G(t)$ (in mg/dL). (E) The cumulative glucose supply $r_G(t)$ as a function of time t.

	Standard Therapy	*ad-hoc* Therapy
Δ	153.83	62.26
$G_{\min}$ (mg/dL)	88.10	96.82
$G_{\max}$ (mg/dL)	121.72	112.59
ϕ_I (U)	10	12.43
ϕ_G (U)		0.40
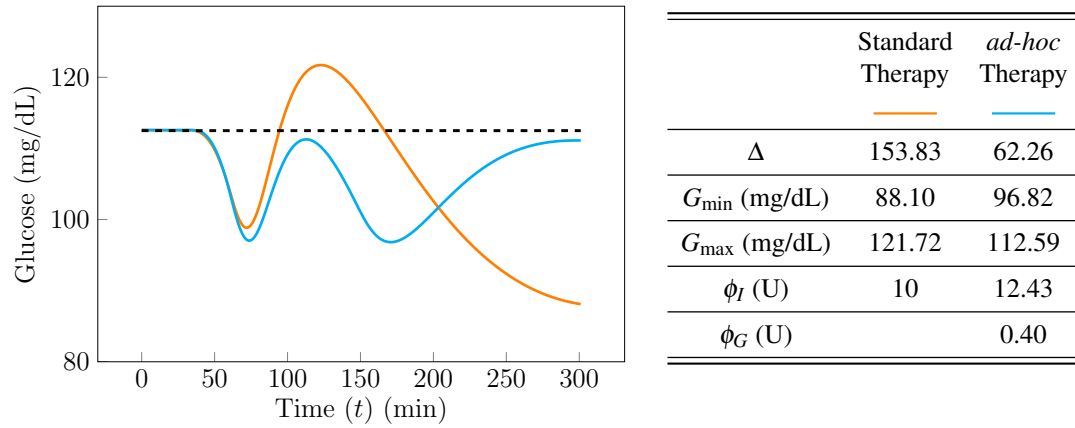
Figure 5.6: Comparison between the glucose response to the standard insulin base therapy (orange curve) and the proposed *ad-hoc* dual therapy (cyan curve).
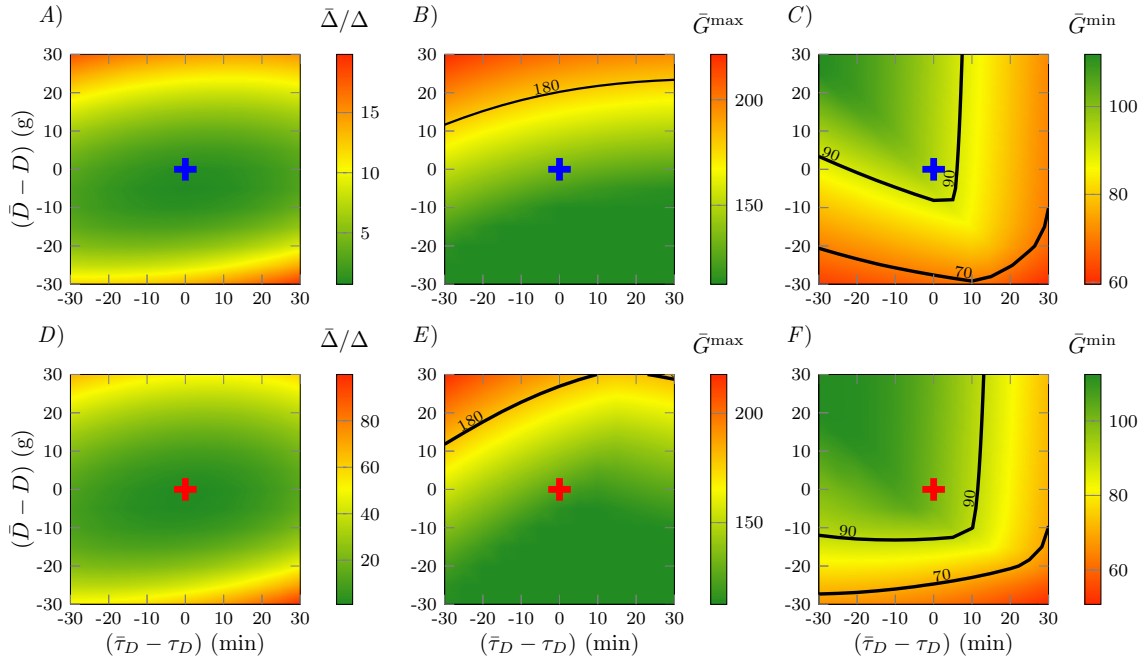
Figure 5.7: Robustness of the optimal control solution against variations in the meal timing and the amount of glucose in the meal. (A)–(C) show the results obtained for the ReNF problem $(P = 1)$ with only insulin provided, (D)-(F) ReMF $(P = 1)$ problem with both insulin and glucagon provided. Cross symbols indicate the application of the optimal control therapies for $\bar{D} = D$ and $\bar{\tau}_D = \tau_D$. The blue cross symbols correspond to the optimal therapies for the ReMF problem with only insulin. The red cross symbols correspond to the optimal therapies for the ReMF problem with both insulin and glucagon. (A) and (D) are plots of $\bar{\Delta}/\Delta$ in the control parameters space $(\bar{\tau}_D, \bar{D})$. (B) and (E) are the plots of $\bar{G}^{\max}$ in the control parameters space $(\bar{\tau}_D, \bar{D})$. (C) and (F) are the plots of $\bar{G}^{\min}$ in the control parameters space $(\bar{\tau}_D, \bar{D})$.
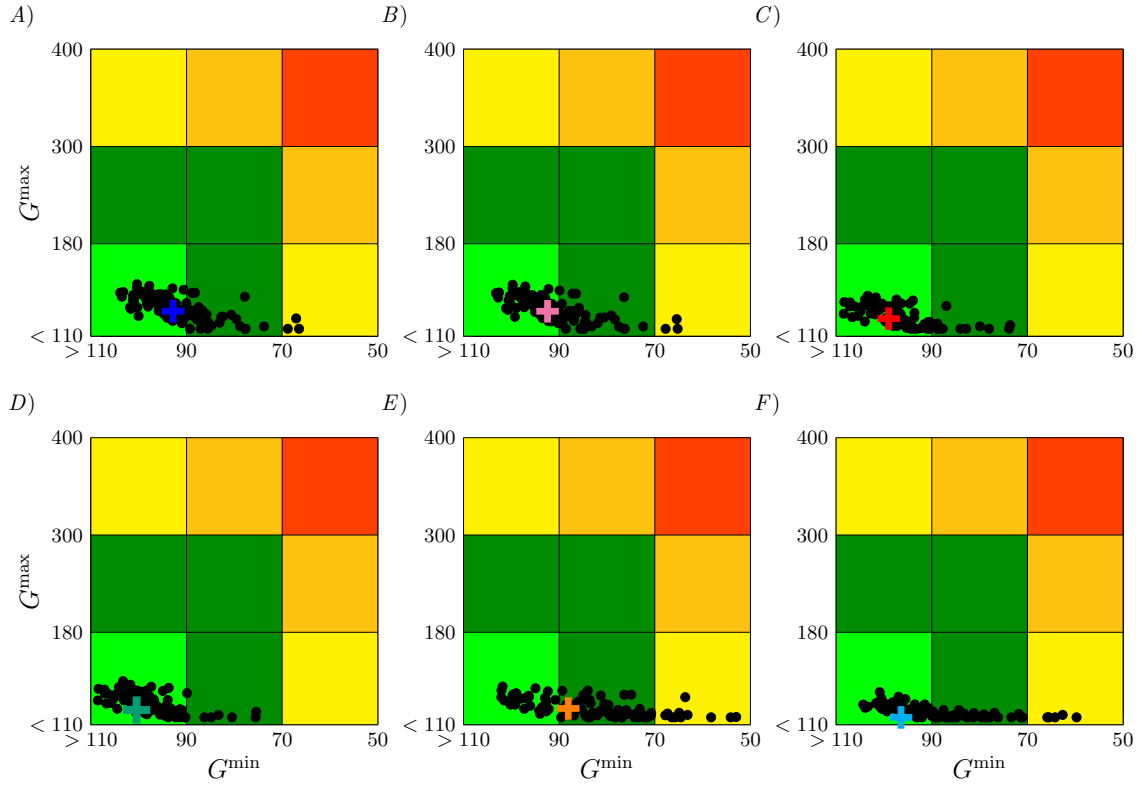
Figure 5.8: Robustness of the optimal control solution against parameter perturbations of the system and CVGA in the G^{min}, G^{max} plane. The analysis is performed for (A) ReMF $(P = 1)$ problem with only insulin provided, (B) ReME $(p = 2)$ problem with only insulin provided, (C) ReMF $(P = 1)$ problem with both insulin and glucagon provided, (D) ReME $(p = 2)$ problem with both insulin and glucagon provided, (E) the standard therapy, and (F) the proposed *ad-hoc* dual therapy. Cross symbols indicate the application of the optimal control therapies to the unperturbed systems.

Chapter 6

Prediction of Optimal Drug Schedules for Controlling Autophagy

6.1 Introduction

For implementation of optimal control approaches in biological systems, our goal is to design optimal drug dosing schedules that minimize the amount of drug needed to achieve an important activity/process in a system. Our second aim is to design combinatorial drug therapies. Formal approaches to combinatorial drug therapy design are potentially useful for at least three reasons. First, all possible combinations of drugs may be difficult, if not impossible, to evaluate experimentally simply because of the large number of possible combinations. Second, an ability to extrapolate accurately beyond well-characterized scenarios with the aid of predictive models would be valuable for individualized treatment, especially in cases where molecular causes of disease are diverse and vary from patient to patient, as in many forms of cancer [156]. Third, it is often non-obvious how the immediate effects of drug perturbations propagate through a cellular regulatory network to affect cellular phenotypes and

fates [157] or how combinations might be deployed to avoid or delay the emergence of resistance, a common response of malignant cells to targeted therapies [158].

Although there is much current interest in using combinations of molecularly targeted drugs to improve outcomes for cancer patients [75, 76], relatively little work has been done in the area of formal therapy design, meaning therapy selection and/or scheduling driven by insights from mathematical models [77, 78]. Formal approaches to therapy design are potentially useful for at least three reasons. First, all possible combinations of drugs may be difficult, if not impossible, to evaluate experimentally simply because of the large number of possible combinations. Second, an ability to extrapolate accurately beyond well-characterized scenarios with the aid of predictive models would be valuable for individualized treatment, especially in cases where molecular causes of disease are diverse and vary from patient to patient, as in many forms of cancer [156]. Third, it is often non-obvious how the immediate effects of drug perturbations propagate through a cellular regulatory network to affect cellular phenotypes and fates [157] or how drug combinations might be deployed to avoid or delay the emergence of resistance, a common response of malignant cells to targeted therapies [158]. Predictive models promise to help identify new robust therapies.

Here, we apply mathematical modeling and optimal control methods to design drug schedules for manipulating autophagy, a stress-relieving/homeostatic cellular recycling process that, when nutrients are in limited supply, generates building blocks for protein synthesis through degradation of cytoplasmic contents [68], such as cytotoxic protein aggregates that are too large for proteosomal degradation and damaged organelles (e.g., depolarized mitochondria). Autophagy also plays an important role in immunity [69, 70]; the autophagic degradative machinery can be directed to target intracellular microbes, such as *Mycobacterium tuberculosis*, for destruction.

Cytoplasmic contents that are targeted for autophagic degradation are first trapped in double-membrane vesicles, termed autophagosomes or autophagic vesicles (AVs),

and then delivered to lysosomes for digestion [71, 72]. The production of AVs is controlled by an intricate regulatory network, in which three protein kinase-containing complexes are prominent: the heterotrimeric AMP-activated kinase (AMPK), which senses energy (glucose) supply through interactions with adenosine derivatives (AMP and ATP) [159, 160]; MTOR complex 1 (MTORC1), which senses amino acid supply and growth factor signaling through interactions with small GTPases localized to lysosomal surfaces (Rag proteins and RHEB) [161, 162]; and the ULK1 complex, which is activated by AMPK and repressed by MTORC1 [163–165]. A fourth complex, which contains a lipid kinase, VPS34, also plays an important role [166, 167]. Interestingly, VPS34 and MTOR are phylogenetically related: they are both members of the phosphoinositide 3-kinase (PI3K) family. Drugs with specificity for each of these kinases are available, and because of the relationship between MTOR and VPS34, drugs are also available with dual specifity for this pair of kinases [168–170].

In cancer, and other contexts, autophagy is a double-edged sword [73]. It can protect cancer cells from stresses of the tumor environment (e.g., lack of nutrients because of defective vasculature) or induce cell death if recycling is excessive. Thus, there are potential benefits to be gained by using drugs to either upregulate autophagy (to kill malignant cells through excessive recycling) or downregulate autophagy (to kill cancer cells that rely on autophagy for survival) [74].

To investigate how single drugs and drug pairs might be best used for these purposes, we constructed a system of nonlinear ordinary differential equations (ODE) that captures regulatory interactions between MTORC1, ULK1, AMPK, and VPS34, as well as the idealized pharmacokinetics of kinase inhibitors specific for MTORC1, ULK1, AMPK, and VPS34, such as rapamycin [171], SBI-0206965 [172], dorsomorphin [173], and SAR405 [174], respectively. We also considered an allosteric activator of AMPK (e.g., PF-06409577[175]) and a kinase inhibitor with dual specificity for MTORC1 and VPS34 (e.g., buparlisib[176]). Although the model is min-

imalist by design, it reproduces key behavioral features of earlier, more mechanistically detailed models [177, 178], such as oscillatory responses to intermediate levels of nutrient or energy stress. We then applied optimization methods implemented in the open-source $\mathcal{PSOPT}$ software package [112] to find locally optimal dosing schedules that minimize the total amount of drug needed to drive the network to a desired, non-attracting operating point (corresponding to low or high AV count/turnover) and maintain it there. The dosing schedules are non-obvious, and synergistic drug pairs were predicted (drug 6 plus drug 1, 2 or 3), such as the combination of a VPS34 inhibitor and a dual specificity PI3K inhibitor, which acts on both VPS34 and MT-ORC1. This drug pair requires less total drug to achieve the same effect than either of the individual drugs alone and is relatively fast acting, which may be important for preventing or slowing the emergence of resistance.

The approach illustrated here differs from earlier applications of control theory concepts in the area of formal therapy design [35–39] in that 1) the system being controlled is a cellular regulatory network, 2) the control interventions are injections (i.e., inputs) of (combinations of) molecularly targeted drugs, and 3) the control objective is manipulation of a cellular phenotype, namely the number of AVs per cell, which is related to the rate of AV turnover, with minimization of total drug used and a constraint on the maximum instantaneous drug concentration. The rationale for minimizing drug use is to avoid offtarget effects and associated toxicities. Our work is distinct from earlier studies of (non-biological) nonlinear network control [33, 179–181], in that our control goal is not to drive the system to an attractor (e.g., a stable steady state or limit cycle), but to an arbitrary point in phase space (i.e., the multidimensional space defined by the state variables of a system) and to then maintain the system there indefinitely. The approach is both flexible and generalizable and provides a means for computationally prioritizing drug dosing schedules for experimental evaluation.

6.2   Model: Model for cellular regulation of auto-phagy and the effects of targeted drug interventions

A prerequisite for formal therapy design is a mathematical model that captures the relevant effects of drugs of interest. Given our interest in using drugs to modify the process of (macro)autophagy, we constructed a model for regulation of the rate of synthesis of autophagic vesicles (AVs) that accounts for the enzymatic activities and interactions of four kinases that play critical roles in regulating autophagy, all of which are potential drug targets. The model further considers the effects of achievable drug interventions and idealized drug pharmacokinetics, meaning instantaneous drug injection according to a time-dependent control function and first-order clearance. The model is illustrated in Fig. 6.1.

The model was constructed in two steps. First, we constructed a minimalist model for physiological regulation of autophagy consistent with key features of earlier, more mechanistically detailed models [177, 178] (see D.1). These features include the time scale of drug-stimulated autophagy induction and the dynamic range of regulation characterized by Martin *et al.*[178] and the qualitative system behaviors characterized by Szymańska *et al.*[177], including a steady, low level of autophagy at low stress levels, oscillatory behavior at intermediate stress levels, and a steady, high level of autophagy at high stress levels. Simulations based on the present model—generated through numerical integration of the equations given below—and simulations based on earlier, related models[177, 178] are compared in Fig. D.1. Simulations of AV dynamics are compared to measured AV dynamics[177] in Fig. D.2.

The model of Fig. 6.1 is intended to provide an idealized representation of regulation of AV synthesis in a single (average) cell in response to changes in the cellular

supplies of energy and nutrients, which are treated in the model as external inputs that modulate the serine/threonine-specific protein kinase activities of AMPK and MTORC1, respectively. Thus, the model reflects regulation of AMPK activity by the cellular AMP:ATP ratio, which is affected by glucose availability, for example, and regulation of MTORC1 activity via, for example, the various amino acid-sensing regulators of Ragulator-associated heterodimeric Rag proteins, which recruit MTORC1 to lysosomes for activation in a manner that depends on their regulated guanine nucleotide binding states. The model further accounts for regulatory interactions among AMPK, MTORC1, a third serine/threonine-specific protein kinase ULK1, and a class III phosphoinositide 3-kinase (PI3K) VPS34. As noted earlier, these kinases are key regulators of autophagy, and each is a potential drug target.

In the second step of model construction, we added idealized consideration of six distinct drug interventions, which correspond to interventions achievable through use of available small-molecule compounds, such as rapamycin[171] (an inhibitor of MTORC1 kinase activity), buparlisib[176] (an inhibitor of PI3K-family kinases that has specificity for both MTORC1 and VPS34), SBI-206965[172] (an inhibitor of ULK1 kinase activity), dorsomorphin[173] (an inhibitor of AMPK kinase activity), PF-06409577[175] (a direct activator of AMPK kinase activity), and SAR405[174] (an inhibitor of VPS34 kinase activity). Each drug $i \in \{1, \ldots, 6\}$ (Fig. 6.1) is taken to be cleared via a pseudo first-order process and introduced in accordance with a specified, time-dependent injection function u_i.

The model was formulated as a coupled system of nonlinear ordinary differential

equations (ODEs):

$$T\dot{x}_1(t) = (1 - x_1)C_{\text{Nu}}H(w_1)H(w_2) - x_1 h_{12}(x_2)h_{13}(x_3), \tag{6.1a}$$

$$T\dot{x}_2(t) = (1 - x_2)h_{23}(x_3)H(w_3) - x_2 h_{21}(x_1), \tag{6.1b}$$

$$T\dot{x}_3(t) = (1 - x_3)k_1 H(w_4) - C_{\text{En}}x_2 x_3 H(w_5), \tag{6.1c}$$

$$T\dot{x}_4(t) = (1 - x_4)h_{42}(x_2)H(w_2)H(w_6) - k_2 x_4, \tag{6.1d}$$

$$T\dot{x}_5(t) = k_3 x_4 - k_4 x_5, \tag{6.1e}$$

$$T\dot{w}_i(t) = b_i u_i(t) - \delta_i w_i(t), \ \ i = 1, \ldots, 6. \tag{6.1f}$$

In these equations, t is time (in min) and T is a timescale, which we specify as 1.0 min. The variable x_1 represents the fraction of MTORC1 that is active, the variable x_2 represents the fraction of ULK1 that is active, the variable x_3 represents the fraction of AMPK that is active, the variable x_4 represents the fraction of VPS34 that is active, and the variable x_5 represents the AV count or number of AVs per cell (on a continuum scale). Thus, x_i always lies somewhere in the interval $[0, 1]$ for $i = 1, \ldots, 4$. The AV count is bounded $0 \leq x_5 \leq k_3/k_4$ because $x_5(t) = 0$ implies $\dot{x}_5(t) \geq 0$ and $x_5(t) = k_3/k_4$ implies $\dot{x}_5 \leq 0$ (by the previously stated bound on $x_4(t)$). The variables $w_1, \ldots, w_6$ represent the dimensionless concentrations of drugs 1–6. Thus, $w_i \geq 0$ for each i. The non-dimensional parameters C_{En} and C_{Nu} are condition-dependent constants that define the supplies of energy and nutrients. An increase in energy supply is taken to positively influence the rate of deactivation of AMPK, and an increase in nutrient supply is taken to positively influence the rate of activation of MTORC1. The non-dimensional parameters k_1 and k_2 influence the rate of activation of AMPK and the rate of deactivation of VPS34, respectively. The non-dimensional parameter k_3 is the maximal rate of VPS34-dependent synthesis of AVs, and the non-dimensional parameter k_4 is the rate constant for clearance of AVs. Taking the rate of AV synthesis to be proportional to VPS34 activity is consistent with the model of Martin *et al.*[178], as is (pseudo) first-order clearance of AVs. The non-dimensional parameters $\delta_1, \ldots, \delta_6$ are rate constants for clearance of drugs 1–6.

Each $h_{ji}(x_i)$ is a non-dimensional Hill function that has the following form:

$$h_{ji}(x_i) = r_{b,ji} + (r_{m,ji} - r_{b,ji}) \frac{x_i^{n_{ji}}}{x_i^{n_{ji}} + \theta_{ji}^{n_{ji}}} \tag{6.2}$$

where n_{ji} (the Hill coefficient), $r_{b,ji}$, $r_{m,ji}$ and θ_{ji} are non-negative constants. The h functions account for regulatory influences among the four kinases considered in the model; the influences considered are the same as those considered in the model of Szymańska *et al.*[177] (cf. Fig. 6.1 and Figs. 1 and 2 in Ref. 33). Each $H(w_i)$ is a non-dimensional Hill function that has the following form:

$$H(w_i) = r_m - (r_m - r_b) \frac{w_i^n}{w_i^n + \theta^n} \tag{6.3}$$

where n (the Hill coefficient), r_b, r_m and θ are non-negative constants. The H functions account for drug effects on kinase activities. The parameters b_i $(i = 1, \ldots, 6)$ in Eq. (6.1f) are Boolean variables introduced for convenience, for the purpose of defining allowable drug combinations. Recall that the u_i terms represent drug injection/input functions, which will be determined by solving an optimal control problem (described in the following section).

Parameter settings are summarized in Tables D.1 and D.2. Each δ parameter was assigned a value consistent with a known drug half-life[175, 182–186] (Table D.2). Other parameters were assigned values that allow the model to reproduce the qualitative signaling behaviors of the AMPK-MTORC1-ULK1 triad characterized in the theoretical study of Szymańska *et al.*[177] and to reproduce the timescale of autophagy induction and the range of regulation quantified experimentally in the study of Martin *et al.*[178]. According to Szymańska *et al.*[177], at low levels of energy/nutrient stress, ULK1 activity, which can be expected to correlate with autophagic flux and AV count, is steady and low; at intermediate levels of stress, ULK1 activity is oscillatory; and at high levels of stress, ULK1 activity is steady and high. As noted earlier, in Figure D.1, we compare simulations based on Eq. (6.1) with simulations based on models of Szymańska *et al.*[177] and Martin *et al.*[178], and in Fig.

D.2, we compare simulations of AV dynamics based on Eq. (6.1) with experimental measurements of AV dynamics reported by Martin *et al.*[178]. Parameter settings are further explained in D.1. InD.1, we also elaborate on how earlier models[177, 178] guided our formulation of Eq. (6.1) and how these models differ from Eq. (6.1).

Model-predicted physiological regulation of autophagy, by energy and nutrients, is summarized in Fig. 6.2. Figure 6.2*A* shows how qualitative long-time behavior depends on the supplies of energy and nutrients, when these supplies are maintained at constant levels and in the absence of external control inputs ($u_i = 0, i = 1, \ldots, 6$). Figures 6.2*B–E* show time courses of autophagy induction or repression triggered by different energy/nutrient changes. All together, these plots show that model predictions of responses to physiological perturbations (i.e., changes in C_{En} and C_{Nu}) are consistent with expectations based on the studies of Martin *et al.*[178] and Szymańska *et al.*[177].

Dose-response curves predicted by the model for single-drug, constant-concentration perturbations are shown in Fig. 6.3. As can be seen, with increasing dosage, drugs 1 and 5 tend to increase the number of AVs per cell, whereas the other drugs tend to decrease the number of AVs per cell. These results are consistent with negative regulation of autophagy by MTORC1 and positive regulation of autophagy by ULK1, AMPK, and VPS34. As is the case for some physiological conditions (Fig. 6.2), AV count oscillates at some of the drug doses, depending on the supplies of energy and nutrients. All together, the plots shown in Fig. 6.3 indicate that responses to single-drug, constant-concentration perturbations are consistent with accepted regulatory influences of MTORC1, ULK1, AMPK and VPS34 on autophagy.

As can be seen in Fig. 6.3, the ability of each drug i to influence x_5 depends on the supplies of energy and nutrients, meaning the values of C_{En} and C_{Nu} (cf. the left and right panels in each row). In this figure, two energy/nutrient conditions are considered ($C_{\mathrm{En}} = C_{\mathrm{Nu}} = 0.1$ and 0.6); additional conditions are considered in Figs.

D.3 and D.4 . Taken together, these results define the condition-dependent ranges over which x_5 can be feasibly controlled by each drug i.

6.3 Problem Formulation: Therapy design as an optimal control problem

To design optimal therapies, we must first introduce design goals. Below, we introduce a series of goals/constraints that we will require optimal therapies to satisfy. However, let us first introduce notation useful for referring to therapies. We will refer to the set of six available drugs, or more precisely, drug types, as $\mathcal{D} = \{1, \ldots, 6\}$, and we will refer to a therapy involving k drugs chosen from $\mathcal{D}$ as $\mathcal{T}_k$, where

$$\mathcal{T}_k \subseteq \mathcal{D} \quad \text{s.t.} \quad |\mathcal{T}_k| = k. \tag{6.4}$$

Thus, for example, we will use $\mathcal{T}_1$ to refer to a monotherapy, and $\mathcal{T}_2$ to refer to a dual therapy. There are six possible monotherapies and, in general, C_k^6 distinct therapies that combine k of the six drugs. Here, we will focus on monotherapies and dual therapies, leaving the evaluation of higher-order combination therapies for future work. As a simplification, we will assume that drugs used together in a combination do not interact. Thus, for example, for dual therapy with drugs 2 and 6 (Fig. 6.1), we consider these drugs to bind/inhibit VPS34 independently (i.e., non-competitively).

Our first, and most important, therapy design goal can be described (somewhat informally) as follows. Starting from a stationary (or recurrent) state at time $t = 0$, we wish to use drug injections (i.e., drug inputs) according to a schedule defined by $\mathbf{u}(t) = (u_1(t), \ldots, u_6(t))$ to eventually maintain, after a transient of duration t_0, the number of AVs in an average cell, x_5, near (to within a tolerance ϵ) a specified target level, x_5^f, for a period of at least $t_f - t_0$ ($t_f > t_0 > 0$), thereby achieving sustained control of the level of autophagic degradative flux in a cell, which is given by $k_4 x_5$

according to Eq. (6.1). In our analyses, we will consider $t_0 = 120$ min and $t_f = 240$ min because these times are longer than typical transients (Figs. 6.2B–E).

A second therapy design goal of interest is minimization of the total amount of drug used, which is motivated by a desire to avoid drug toxicity arising from dose-dependent offtarget effects. In the optimal control literature, a problem entailing this type of constraint is called a *minimum fuel* problem [110, 187]. The constraint can be expressed mathematically as follows:

$$\min_{\substack{u_i(t), \\ i \in \mathcal{T}_k}} J\{u_i\} := \sum_{i \in \mathcal{T}_k} \int_0^{t_f} u_i(t) \ \mathrm{d}t \tag{6.5}$$

where $u_i(t) \geq 0$ for $i = 1, \ldots, 6$. As a simplification, we are considering an objective functional $J\{u_i\}$ that treats the different drugs equally, i.e., the sum in Eq. (6.5) is unweighted. With this approach, we are assuming that the different drugs of interest have equivalent toxicities. If drugs are known to have different toxicities, this assumption can be lifted simply by introducing weights to capture the toxicity differences, with greater weight assigned for greater toxicity. Indeed, arbitrary modifications of the form of the objective functional $J\{u_i\}$ would be feasible if such modifications are needed to capture problem-specific constraints on drug dosing.

A third design goal is to disallow the instantaneous concentration of any drug i, $w_i(t)$, from ever rising above a threshold $w_i^{\max}$. The rationale for this constraint is again related to a desire to eliminate or minimize dose-dependent drug toxicity. In other words, we are assuming that a drug i is tolerable so long as its concentration w_i is below a toxicity threshold $w_i^{\max}$. In our analyses, we set the toxicity threshold of a drug as a factor (> 1) times its EC_{50} dosage, which we define as the concentration of the drug at which its effect on x_5, negative or positive, is half maximal (see Eqs. (6.2) and (6.3)).

We are now prepared to formulate the problem of (combination) therapy design as a constrained, optimal control problem. The problem, for a given $\mathcal{T}_k$ (Eq. (6.4)),

is to find a drug schedule $\mathbf{u}(t)$ that minimizes the objective functional defined in Eq. (6.5) and that also satisfies the following constraints:

$$\dot{\mathbf{X}}(t) = \mathbf{f}(\mathbf{X}(t), \mathbf{u}(t)), \quad 0 \le t \le t_f, \tag{6.6a}$$

$$b_i = \begin{cases} 1, & \text{if } i \in \mathcal{T}_k, \\ 0, & \text{otherwise}, \end{cases} \tag{6.6b}$$

$$x_5^f - \epsilon \le x_5(t) \le x_5^f + \epsilon, \quad t_0 \le t \le t_f, \tag{6.6c}$$

$$0 \le w_i(t) \le w_i^{\max}, \quad i = 1, \dots, 6, \tag{6.6d}$$

$$0 \le u_i(t), \quad i = 1, \dots, 6, \tag{6.6e}$$

$$\mathbf{X}(0) = [\mathbf{x}(0), \mathbf{w}(0)] \equiv [\mathbf{x}_0, \mathbf{0}]. \tag{6.6f}$$

Here, $\mathbf{X}(t)$ is defined as $[\mathbf{x}(t), \mathbf{w}(t)]$, where $\mathbf{x}(t) = (x_1(t), \dots, x_5(t))$ and $\mathbf{w}(t) = (w_1(t), \dots, w_6(t))$, and $\mathbf{f}(\mathbf{X}(t), \mathbf{u}(t))$ is the vector field of Eq. (6.1). The initial condition $\mathbf{X}_0 = \mathbf{X}(0)$ is taken to be a stationary (or recurrent) state of Eq. (6.1) where supplies of energy and nutrients are constant (i.e., C_{En} and C_{Nu} are fixed) and drugs are absent (i.e., $\mathbf{u}(t) = 0$). With this formulation, it should be noted that we are attempting to drive the system variable x_5 to a specified final value x_5^f (to within a tolerance ϵ), but we are making no attempt to control the other system variables x_1, x_2, x_3, and x_4. This approach is called target control [95, 138]. In all of our analyses, we set $\epsilon = 1$.

A useful measure of the amount of 'fuel' used to achieve drug control of autophagy is the total dosage of drug i used up to time t during a therapy $\mathcal{T}_k$, which we denote as $r_{i,k}^*(t)$. This quantity is calculated using

$$r_{i,k}^*(t) = \int_0^t u_i^*(\tau)d\tau, \tag{6.7}$$

where $u_i^*(t)$ for $i \in \mathcal{T}_k$ is the solution of the nonlinear optimal control problem defined by Eqs. (6.5) and (6.6).

6.4 Method

The equations (6.5) and (6.6) together form a constrained optimal control problem, which can generally be written as Eq. (4.1). We have used $\mathcal{PSOPT}$ [112], an open-source PSOC library, to perform the above PSOC discretization procedure. The NLP in (4.8) can be solved with a number of different techniques, but here we use an interior point algorithm [56] as implemented in the open-source software Ipopt [113].

6.5 Result

6.5.1 Simulations

Simulations were performed by numerical integration of the model ODEs. The parameter settings used in calculations are provided in the Tables D.1 and D.2 in Appendix D

6.5.2 Optimal monotherapies

We will illustrate generic features of solutions to the nonlinear optimal control problem defined by Eqs. (6.5) and (6.6) by focusing on a particular (severe) energy/nutrient stress condition (i.e., the condition where $C_{\mathrm{Nu}} = C_{\mathrm{En}} = 0.1$). For this condition, the system represented by Eq. (6.1) has a near maximal, steady-state AV count of approximately 37 per cell (i.e., $x_5 \approx 37$). Let us focus for the moment on monotherapy with drug 4 (an AMPK inhibitor) to downregulate the number of AVs to a target level of 10 per cell (i.e., $x_5^f = 10$) over the time period between $t_0 = 120$ min and $t_f = 240$ min from an unperturbed steady state (i.e., dynamics with $u_i = 0$)

at $t = 0$.

We solved the optimal control problem using the approach outlined in the Methods section and described in more detail in "Pseudo-Spectral Optimal Control" in D.2. The solution, represented by the optimal cumulative dosage of drug 4 (i.e., $r_{4,1}^*(t)$) (Eq. (6.7)), is presented in Fig. 6.4A. The optimal solution exhibits several generic features of the system's dynamics, regardless of its parameterization. First, the computation suggests an optimal earliest time to apply the drug. In this particular example, this time is $t \lesssim 60$ min. The difference between the target time t_0 and the earliest time to apply the drug quantitatively measures the speed of action of the drug. Secondly, the function $r_{4,1}^*(t)$ exhibits a staircase behavior, indicating that the optimal strategy of drug administration for this particular problem is to intermittently inject a specific dosage of drug into the system at specific times. Mathematically, this is due to the fact that the objective functional (Eq. (6.5)) is a linear combination of the L^1 norm of the injection/input rate u_i's—see Sections 5.5 and 5.6 in Kirk[110].

Figure 6.4B depicts how the drug concentration $w_4(t)$ evolves subject to the optimal protocol $u_4^*(t)$. We observe surges of $w_4(t)$ in response to the drug being applied to the system in large quantities over small intervals, and slow decays in between applications of the drug (caused by the natural decay of the drug concentration in the absence of external drug inputs dictated by δ_i.) As a consequence, the optimal solution is to inject a relatively large dose of a drug periodically, and to continuously supply small amounts of that drug to replenish drug cleared from the system to stably maintain autophagic flux (i.e., constant AV count and constant degradative flux, which we take to be proportional to the AV count).

Figure 6.4C illustrates the time evolution of x_5 (AV count) subject to the optimal drug administration protocol. As can be seen, for $t \geq 120$ min, x_5 is maintained within the desired interval $x_{5_f} \pm \epsilon = 10 \pm 1$. The time evolution of the non-target

variables x_1, x_2, x_3 and x_4 (i.e., the activities of the regulatory kinases) are presented in Fig. 6.4D. Together, Figs. 4C and D provide a full representation of the time evolution of the system represented by Eq. (6.1) (the target and non-target variables) under the influence of the optimal drug administration schedule. Because our procedure to find the optimal solution to the nonlinear optimal control problem is numerical, we have verified that the optimal control solution satisfies the necessary conditions that it must satisfy for optimality. See "Pseudo-Spectral Optimal Control" in D.1 for details.

Given that cancer cells may be killed by using drugs to either elevate or suppress autophagy [74], we will now consider optimal control solutions that either upregulate or downregulate autophagic flux by using a single drug. We will identify the drugs which can perturb and maintain the system near the target AV count. Perhaps more importantly, our analysis will deliver optimal protocols which include the precise times to inject the drugs, whose dosages are also tightly controlled to minimize the total quantities of drugs that are supplied.

Let us consider the case of intermediate energy/nutrient stress before treatment (i.e., the condition corresponding to $C_{\mathrm{Nu}} = C_{\mathrm{En}} = 0.6$; see Fig. 6.2), for which the system exhibits oscillations in the range $[20, 27]$ without treatments. For this scenario, our goal is to either downregulate the number of AVs to $x_5^f \approx 9$ (shown in Figs. 6.4E–H) or to upregulate the AVs to $x_5^f \approx 37$ (shown in Figs. 6.4I–L). We have performed extensive numerical solutions of the monotherapy optimal control problem with various settings of the parameters w_i^{max}, t_0, t_f and x_5^f. We set the control window in the interval between $t_0 = 120$ min and $t_f = 240$ min and imposed a constraint on each drug concentration w_i, requiring it not to exceed $w^{\mathrm{max}} = 4 \times \mathrm{EC}_{50}$.

We found drug 2 to be best suited for downregulation for two reasons. First, drug 2 is able to drive x_5 nearly to zero (in contrast with the case for drug 3 or 4). See Figs. 6.2B and 6.2H and compare with Figs. 6.2C, 6.2D, 6.2I, and 6.2J. Second,

drug 2 (in contrast with drug 6) is able to overcome the autonomous oscillatory be-
havior in x_5. In the analysis summarized in Fig. D.7, we found that drug 6 cannot
eliminate oscillatory behavior; thus, it is incapable of maintaining a low, steady AV
level. Drug 6 becomes viable if we remove the lower bound from the constraint of Eq.
(6.6c). Without the lower bound, oscillations in x_5 are permitted. We choose to keep
the constraint of Eq. (6.6c) as written to avoid oscillatory solutions because, depend-
ing on period and amplitude, oscillations in x_5 may allow for autophagy-addicted
cells to survive periods of relatively low autophagy by thriving during periods of
relatively high autophagy. In the other direction (i.e., drug-induced upregulation of
autophagy), it is only possible to use drug 5 to upregulate autophagy to the target
value $x_5^f = 37$ (Fig. 6.3). Figs. 6.4*E–H* and 6.4*I–L* illustrate the optimal solutions
using drugs 2 and 5 to downregulate and upregulate autophagy, respectively.

Although the selection of a single drug to achieve a given qualitative change in
x_5 is intuitive, especially given the results of Fig. 6.3, optimization of drug schedul-
ing (Fig. 6.4) delivers better solutions in the sense that the total dosage applied to
achieve the same effect (compared to constant input) is lower (minimized). Further-
more, the generic staircase-like solutions for $r_{i,k}^*$ illustrated in Fig. 6.4 persist for
all the parameter sets we have tested (see below), indicating that variable, tightly
controlled dosages should be injected into the system at controlled times. Given a
particular type of drug, the central result of our optimal control analysis is to provide
injection/input times and the amounts of drugs to be injected/added.

6.5.3 Optimal combination therapies

Let us now consider dual therapies ($k = 2$). The motivation is to identify therapies—
protocols involving lower quantities of drugs and faster responses—that are even more
efficient than optimal monotherapies. We have evaluated all possible dual therapies

($C_2^6 = 15$) for each of two energy/nutrient stress conditions: $C_{\text{En}} = C_{\text{Nu}} = 0.1$ (corresponding to severe stress) and $C_{\text{En}} = C_{\text{Nu}} = 0.6$ (corresponding to moderate stress). With an identical control objective and identical constraints $w_i^{\max} = 2.0$ $t_0 = 120$, $t_f = 240$, $x_5^f = 10$, and $\epsilon = 1$, we found four pairs of drugs that are each more efficient than the optimal monotherapy with either of the two drugs included in the combination. These dual therapies are illustrated in Fig. 6.5. Additional results from our analyses of dual therapies are presented in appendix D.4 and Figs. D.3–D.10.

We found that when baseline autophagy is high ($C_{\text{En}} = C_{\text{Nu}} = 0.1$), the only combination of drugs that can drive AV count down to the target x_5^f is the combination of drugs 2 and 6. The dynamical response of the system is shown in Figs. 6.5*A*–*D*. For this particular combination, either drug alone cannot lower x_5 to 10 without violating one or both of the constraints $w_i < w_i^{\max}$ ($i = 2, 6$). However, with use of drugs 2 and 6 in combination, it is possible to achieve the target AV count because the effects of the drugs are multiplicative (Eq. (6.1d)) and drug 2 directly affects both MTORC1 (Eq. (6.1a)) and VPS34 (Eq. (6.1d)).

Our analysis predicts non-trivial synergistic activities between drugs when the baseline level of autophagy is intermediate (on average) and exhibits oscillatory behavior ($C_{\text{En}} = C_{\text{Nu}} = 0.6$). The results are summarized in Figs. 6.5*E*–*P*. In this scenario, multiple drug combinations (drugs 1 and 6, 2 and 6, and 3 and 6) are able to downregulate and stabilize x_5, whereas drug 6 alone cannot do so. Using drug 6 alone results in oscillations in x_5, causing a violation of the constraint of Eq. (6.6c). More interestingly, the optimal application of the drugs reveals a clear sequential protocol: first apply a drug other than drug 6 (1, 2, or 3) to suppress oscillations (see Figs. 6.5*H*, *L* and *P*), then apply drug 6 to drive AV count down to the desired level. The combination of drugs 1 and 6 is peculiar in that in this case application of drug 1 drives the system out of the oscillatory regime (Fig. 6.5*O*) but also up-

regulates autophagy; subsequent application of drug 6 is effective in downregulating autophagy.

It is important to emphasize that the two drugs acting together in any given combination therapy are, for simplicity, modeled as non-interacting, which may or may not be reasonable, depending on the mechanisms of actions of specific drugs of interest. The drug synergies detected in our analyses arise from the nonlinear dynamics of the regulatory network controlling autophagy. Without the formal framework presented here for therapy design, it would arguably be difficult to identify these synergies.

6.6   Discussion and Conclusions

Here, we have taken up the problem of designing targeted therapies to control a cellular phenotype of cancer cells, namely, their commitment to recycling of cytoplasmic contents through the process of autophagy, as measured by cellular autophagic vesicle (AV) count. Autophagy generates building blocks needed for *de novo* protein synthesis in support of growth (and proliferation). Modulation of autophagy, up or down, in autophagy-addicted cancer cells has the potential to selectively kill these cells [74].

Our approach was to first construct a mathematical model for autophagy regulation that captures the effects of key physiological stimuli—changes in the supplies of energy and nutrients—and the idealized effects of six available drug types (Eq. (6.1), Figs. 6.1–6.3) and to then pose the question of therapy design as a constrained, optimal control problem (Eqs. (6.4)–(6.6)). Numerical solution of this problem, through optimization of a control input accounted for in the model (i.e., an adjustable time-dependent drug injection/input rate), yielded monotherapy drug schedules that require a minimum amount of drug, maintain drug concentration be-

low a specified threshold at all times, and that bring about desired effects in the most efficient manner possible (Fig. 6.4), in a well-defined sense. Furthermore, through the essentially same approach, but with consideration of adjustable time-dependent drug injection/input rates for two different drugs, we were able to predict synergistic drug pairs (Fig. 6.5).

Optimal monotherapies were found to entail intermittent pulses of drug injection/input at irregular, non-obvious intervals and doses (Fig. 6.4). These features of optimal drug schedules—the pulsatile nature of drug administration and the irregularity of drug administration in terms of both timing and dosage—appear to be generic and each is discussed in further detail below.

The pulsatile nature of optimal monotherapy arises from the optimal control problem that we posed (Eqs. (6.4)–(6.6)), which can be viewed as a minimum-fuel problem, in that our control problem calls for usage of a minimal total amount of drug. The rationale for this control objective is that drugs typically have dose-dependent offtarget effects, which may contribute to drug toxicity. Thus, by seeking drug schedules that achieve desired endpoints while using only a minimal total amount of drug, we seek to mitigate the possible negative consequences of offtarget drug effects. Mathematically, our minimum-fuel objective function, Eq. (6.5), leads to pulsatile drug administration because the Hamiltonian of the optimal control problem is linear in the control inputs $u_i(t)$, $i \in \mathcal{T}_k$ (see "Pseudo-Spectral Optimal Control" in D.2 for a detailed derivation). Optimal control problems which have Hamiltonians that are linear in the control input are well-known to have singular arcs, that is, discontinuities jumping between upper and lower bounds of the control input (see Chapter 5 in Kirk[110] for the derivation of singular arc behavior and the brief overview of this issue in "Pseudo-Spectral Optimal Control" in D.2). Because we do not impose an upper bound on $u_i(t)$, the discontinuities we expect to see are Dirac delta type functions, a pulse of infinite magnitude but infinitesimal width.

With the use of numerical methods to find solutions of the optimal control problem, we cannot capture the Dirac delta behavior exactly. Instead, we see finite pulses of finite width, which, while likely suboptimal, are more physically realistic.

Although pulses of drug input are consistent with convenient drug delivery modalities, such as oral administration of a drug in pill form or intravenous injection, optimal schedules do not entail uniform drug doses, nor uniform periods of drug administration. This irregular nature of optimal drug administration depends on the structure of the nonlinear cellular network that controls the synthesis of AVs. In particular, in our model, each drug specifically targets individual nodes of the cellular network, and therefore, different drugs play dynamically distinct roles and cannot be treated as equivalent control inputs. Thus, it may be critically important to better understand the interplay between targeted therapies and archetypical cellular regulatory network dynamics if we are to design the best possible therapies for populations of patients. Because network dynamics can be expected to vary between patients, patient-specific variability in network dynamics, which we have not considered in our analyses here, is a factor that likely affects the efficacy of individualized targeted therapy and that therefore should receive attention in future studies. The study of Fey *et al.*[188] points to the feasibility of considering patient-specific parameters in mathematical models. In this study, gene expression data available for individual patients were used to set the abundances of gene products in patient-specific models for a cell signaling system. Because mutations can be detected in the tumors of individual patients, effects of oncogenic mutations could also potentially be accounted for in patient-specific models. The study of Rukhlenko *et al.*[157] provides an example of a study where the effects of an oncogenic mutation were considered in a mathematical model. In the study of Fröhlich *et al.*[189], gene expression and mutational profiles were both considered in cell line-specific models.

The therapy design approach presented here is flexible and allows for the evalu-

ation of drug combinations. In our analyses, we focused on dual therapies. Somewhat surprisingly, we found several drug pairs that together are more effective than either drug alone (according to our model). These pairs are drug 2 and drug 6 when $C_{\mathrm{Nu}} = C_{\mathrm{En}} = 0.1$ (severe energy/nutrient stress) and the combination of drug 6 with drug 1, 2, or 3 when $C_{\mathrm{Nu}} = C_{\mathrm{En}} = 0.6$ (moderate energy/nutrient stress). In the latter cases, drug 6 alone is incapable of downregulating autophagy to the desired level, but it sensitizes the network to drugs 1–3 when one of these drugs is used in conjunction with drug 6. According to the model (and its parameterization), the most potent synergistic drug pair is the combination of drugs 2 and 6. With this combination, the total amount of drug 2 used was reduced by more than 5-fold (see the D.4 and Fig. D.5) in comparison to the case where drug 2 is used optimally in isolation. More striking perhaps is that drug 6 when used alone is incapable of achieving the performance objective. Interestingly, our results provide mechanistic insight into the optimal sequence of drug delivery: therapy is optimal when drug 2 is injected about 80 minutes earlier than drug 6. That is, the best outcome was achieved when first inhibiting MTORC1, thus halting the intrinsic oscillations of the network dynamics, and then only inhibiting VPS34 to reduce synthesis of AVs. It should be noted that in our evaluation of this drug pair, we have assumed that there is no interaction between drugs 2 and 6, an idealization that may not be appropriate for specific examples of drugs of these types.

The same optimal control approach that we have demonstrated for 2-drug combinations can be applied for combinations involving more than two drugs. Indeed, our approach was presented for the general case of k drugs used in combination. Our expectation is that effective combinations involving more than two drugs may be more likely to exist than effective combinations involving only two drugs, because controllability would presumably increase with the availability of more drugs. However, finding an effective combination may be more computationally expensive because of the larger number of possible combinations, and 2-drug combinations may

be preferable to higher-order combinations because of drug side effects.

As reported by Palmer and Sorger [190], many clinically used drug combinations are effective for reasons other than drug synergy, which is rare. In essence, the majority of clinically available drug combinations are, for all intents and purposes, equivalent to monotherapy at the level of individual patients. The basis for their effectiveness at the population level is simply that tumors in different subpopulations of patients have distinct drug sensitivities. Thus, new methods for predicting promising, non-obvious synergistic drug combinations, such as the approach reported here, could be helpful in developing combination therapies that derive their effectiveness from drug synergy. Synergistic drug combinations would seemingly offer significant benefits over monotherapy, or what is effectively monotherapy, in terms of delaying or perhaps eliminating the emergence of drug resistance. We note that our analysis identified synergies between pairs of drugs that are predicted to manifest without fine tuning of the doses used or the timing of drug administration. We admit that these predictions could perhaps have been found through an *ad hoc* model analysis. Nevertheless, we see value in leveraging an optimal control framework for model analysis, even if an optimal control strategy is not sought, because with this type of approach it is less likely that interesting behavior will be missed.

There is presently cautious optimism that effective drug combinations will be identified through high-throughput screening experiments [191], or through learning from data. However, the sheer number of possible drug combinations poses a barrier to experimental discovery of efficacious drug combinations and it is not clear that the data requirements of machine learning approaches can be met in the near term. Thus, it is important to consider alternatives, such as the approach presented here, which leverages available mechanistic understanding of how regulatory protein/lipid kinases influence the synthesis of AVs, which we have consolidated in the form of a mathematical model (Eq. (6.1)), designed to be useful for computational character-

ization of drug combinations. We note that our model was formulated specifically for this purpose, and it was not designed to make predictions outside this limited domain of application. Indeed, to facilitate our computational analyses, the model was handcrafted to be as simple as possible while still reproducing key behaviors of more mechanistically detailed models [177, 178]. This approach was helpful in making calculations feasible. Unfortunately, to our best knowledge, there are no proven approaches for systematically and automatically deriving a suitable surrogate model for therapy design from a more detailed, mechanistic model of a cellular regulatory network. Pursuit of such a capability seems like an important subject of future research.

Our intent at the start of this study was to investigate how control engineering concepts might be introduced into formal therapy design. Thus, we have only attempted to demonstrate that our methodology is capable of generating interesting (and testable) predictions of effective drug schedules and drug combinations. Development of novel therapies will, of course, require experimental validation of candidate combinations, which is beyond the intended scope of the present study. Thus, we caution that our predictions of optimal drug schedules and synergistic drug combinations are only intended to demonstrate methodology. The merit of this methodology is not in reaching final conclusions but in prioritizing experimental efforts and thereby accelerating experimental validation of targeted therapies. Because kinase inhibitors of each type considered in our analysis are available for experimental characterization and autophagy is a cellular phenotype that can be readily assayed, as in the study of Martin *et al.*[178] or du Toit *et al.*[192], a logical next step would be to probe for the predicted drug synergies in cell line experiments. It might be especially interesting to evaluate a combination of an ULK1-specific inhibitor, such as ULK-101 [193], and a VPS34-specific inhibitor, such as VPS34-IN1 [194]. We predict that this combination will be synergistic, and the combination targets the two kinases considered in our analysis that are most proximal to the cellular machinery for producing autophago-

somes. On the computational side, to increase confidence in predictions, sensitivity analysis techniques tailored for optimal control problems could be applied to characterize the robustness of predictions [195, 196], and experimental design techniques could be applied to aid in generating data useful for reducing parameter uncertainty [197, 198]. Several studies strongly support the potential value of formal therapy design [199–201], and the main contribution here is a new approach to this subject. Two important distinguishing features of this approach are 1) the consideration of a mathematical model for a cellular regulatory network that controls a cellular phenotype and 2) application of sophisticated methods from automatic control theory.
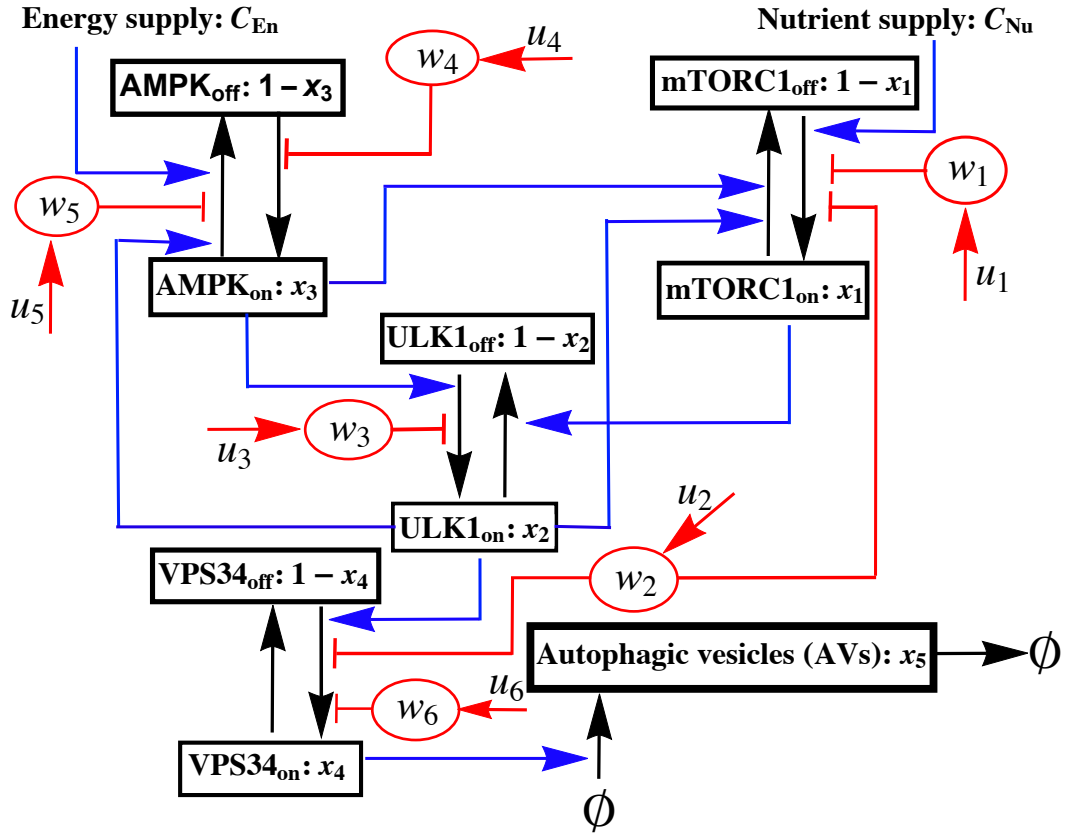
Figure 6.1: Schematic diagram of a minimalist mathematical model for regulation of autophagy and the effects of targeted drug interventions. The model accounts for two physiological inputs (energy and nutrient supply) and regulatory influences, stimulatory or inhibitory, within a network of interacting kinases. Each kinase is taken to have a constant total abundance and to be dynamically distributed between active and inactive forms. The active fractions of MTORC1, ULK1, AMPK, and VPS34 are represented by x_1, x_2, x_3 and x_4, respectively. Targeted drugs, denoted by red ovals, promote kinase inactivation or activation as indicated. Six drug types are considered: 1) a kinase inhibitor specific for MTORC1, 2) a kinase inhibitor specific for both MTORC1 and VPS34, 3) an ULK1 kinase inhibitor, 4) an allosteric activator of AMPK, 5) an AMPK kinase inhibitor, and 6) a VPS34 kinase inhibitor. The supplies of cellular energy and nutrients (C_{En} and C_{Nu}), together with drug concentrations ($w_1, \ldots, w_6$), determine the kinase activities of MTORC1, ULK1, AMPK, and VPS34 and thereby the rate of synthesis of autophagic vesicles (AVs). The control parameters are drug injection/input rates ($u_1, \ldots, u_6$). Note that drug clearance is not indicated in this diagram but is considered in the model equations.
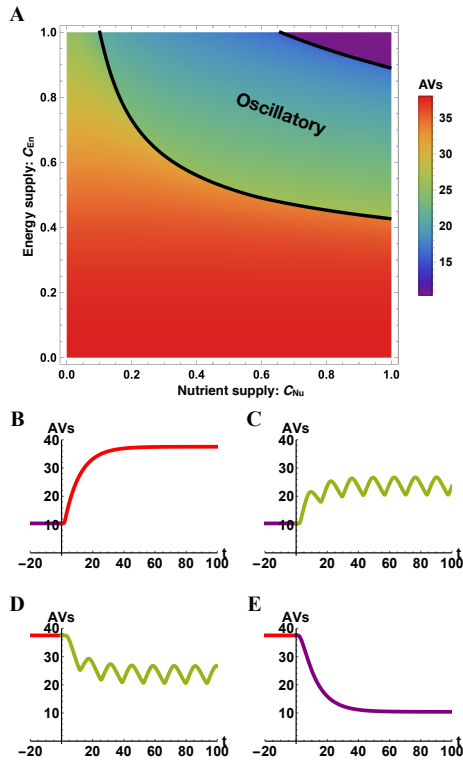
Figure 6.2: Predicted dependence of AV count on energy and nutrient supplies according to the model for autophagy regulation (Eq. (6.1)). (A) Long-time behavior. In this panel, the stationary or time-averaged value of $x_5(t)$ for constant supplies of energy and nutrients as $t \to \infty$ is indicated by color over the full ranges of the two physiological inputs of the model: energy supply (C_{En}) and nutrient supply (C_{Nu}). The solid black curves delimit the regions where long-time behavior of x_5 is oscillatory or not. If behavior is oscillatory, the time-averaged value of x_5 is reported; otherwise, the stationary value is reported. A bifurcation analysis indicates that long-time behavior is characterized by a stable fixed point, the coexistence of a stable fixed point *and* a stable limit cycle, or a stable limit cycle. The region labeled 'oscillatory' indicates the conditions for which a stable limit cycle exists; however, this diagram is not intended to provide a full characterization of the possible qualitative behaviors and bifurcations of Eq. (6.1). As indicated by the color bar, the (average) AV count varies over a range of roughly 2 to 37 vesicles per cell. (B–E) Transient behavior. Each of these plots shows x_5 as a function of time t after a coordinated change in energy and nutrient supplies. The plot in panel B shows the predicted response to a steep, step increase in stress level, i.e., a change in conditions from $C_{En} = C_{Nu} = 1$ to 0.2. The plot in panel C shows the predicted response to a moderate, step increase in stress level, i.e., a change in conditions from $C_{En} = C_{Nu} = 1$ to 0.6. The plot in panel D shows the predicted response to a moderate, step decrease in stress level, i.e., a change in conditions from $C_{En} = C_{Nu} = 0.2$ to 0.6 The plot in panel E shows the predicted response to a steep, step decrease in stress level, i.e., a change in conditions from $C_{En} = C_{Nu} = 0.2$ to 1.
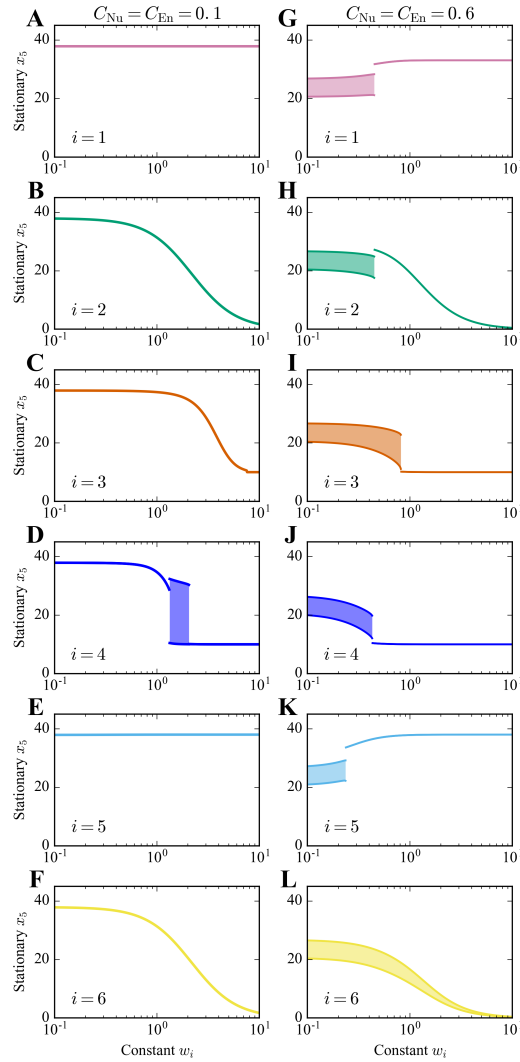
Figure 6.3: Predicted dependence of AV count (x_5) on drug dose according to Eq. (6.1). In each panel, we show the long-time effects of monotherapy with drug $i \in \{1, \ldots, 6\}$; the drug considered in each panel is maintained at the constant (dimensionless) concentration indicated on the horizontal axis. Drugs 1–6 are considered from top to bottom. Responses to drugs depend on the supplies of energy and nutrients. The left panels (A–F) correspond to conditions for which $C_{\mathrm{Nu}} = C_{\mathrm{En}} = 0.1$ (severe energy/nutrient stress), and the right panels (G–L) correspond to conditions for which $C_{\mathrm{Nu}} = C_{\mathrm{En}} = 0.6$ (moderate energy/nutrient stress). The long-time behavior of x_5 under the influence of monotherapy can be stationary (with a stable fixed point) or oscillatory (with a stable limit cycle). The shaded regions indicate where there is oscillatory behavior. At a given drug dose, the top and bottom bounds of a shaded region delimit the envelope of oscillations (i.e., the maximum and minimum values of x_5).
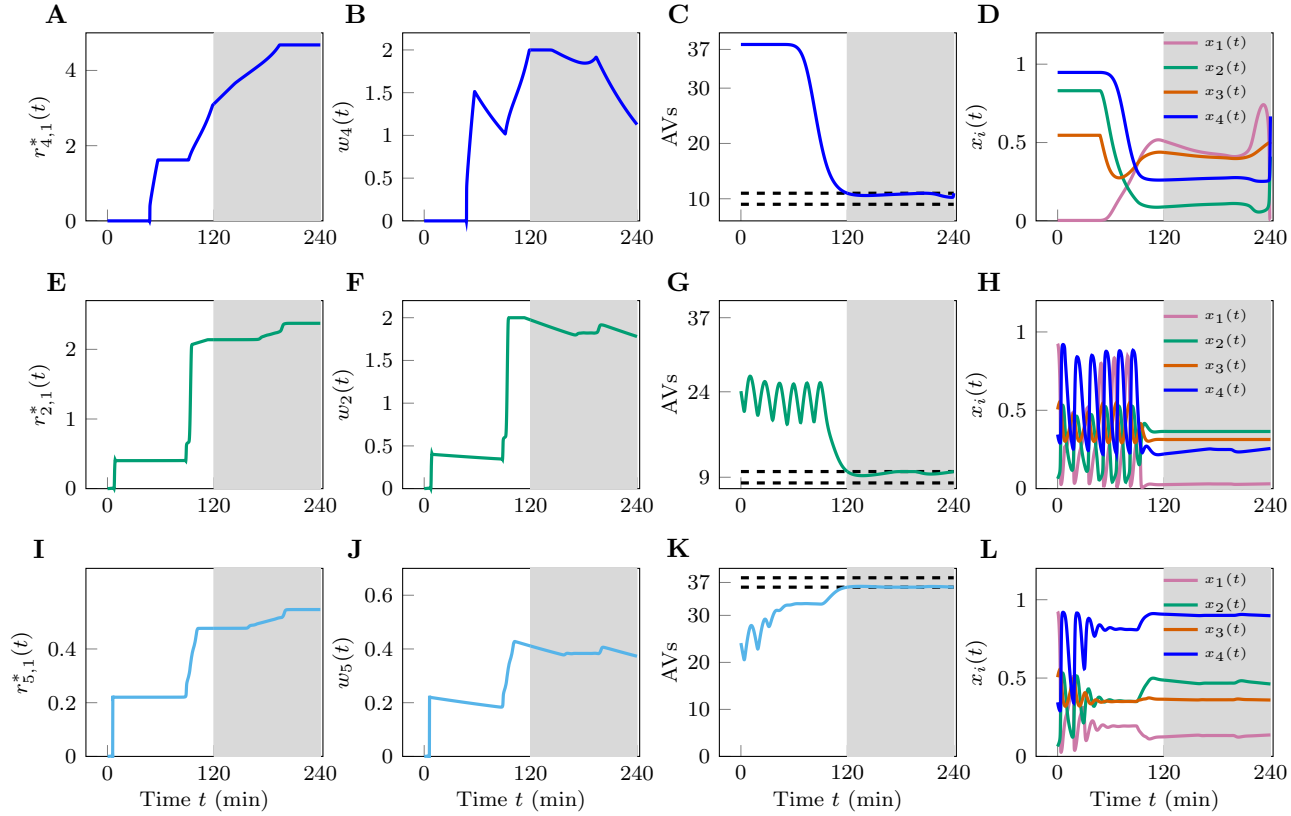
Figure 6.4: Best performing monotherapies. (*A–D*) Panels *A–D* are from a numerical experiment for which we set $C_{\mathrm{Nu}} = C_{\mathrm{En}} = 0.1$ and attempt to use drug 4 to downregulate the AV count. (*E–H*) Panels *E–H* from a numerical experiment for which we set $C_{\mathrm{Nu}} = C_{\mathrm{En}} = 0.6$ and attempt to use drug 2 to downregulate the AV count. (*I–L*) Panels *I–L* are from a numerical experiment for which we set $C_{\mathrm{Nu}} = C_{\mathrm{En}} = 0.6$ and attempt to use drug 5 to upregulate the AV count. The plots in the first column are cumulative drug dosages for the monotherapies considered. The plots in the second column are the drug concentrations. The plots in the third column show $x_5(t)$ and the plots in the fourth, or rightmost, column show $x_1(t)$, $x_2(t)$, $x_3(t)$, and $x_4(t)$ that we are making no attempt to control. In all simulations, the upper bound on the allowable concentration of drug i, w_i^{max}, was set at 2. For panels *A–H*, the target AV count was 10 (i.e., $x_5^f = 10$). For panels *I–L*, the target AV count was 37 (i.e., $x_5^f = 37$). The white region corresponds to the time interval $[t_0, t_f]$ when we either upregulate or downregulate the AV count The shaded region corresponds to the time interval $[t_0, t_f]$ when the AV count is maintained within the interval $x_5^f \pm \epsilon$.
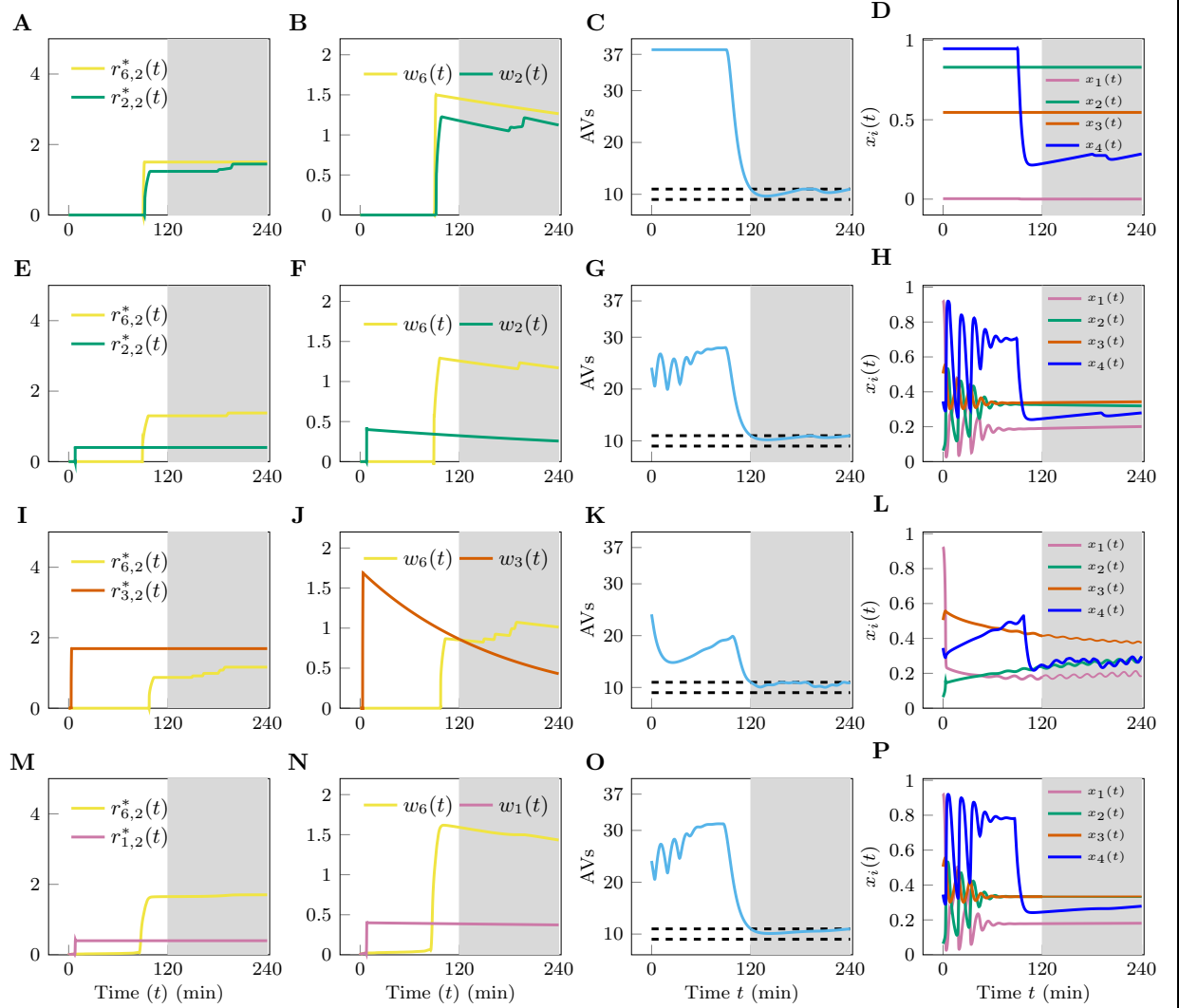
Figure 6.5: Optimal dual therapies. (A–D) Panels A–D are from a numerical experiment for which we set $C_{\mathrm{Nu}} = C_{\mathrm{En}} = 0.1$ and attempt to use a combination of drugs 2 and 6. (E–H) Panels E–H are from a numerical experiment in which we set $C_{\mathrm{Nu}} = C_{\mathrm{En}} = 0.6$ and attempt to use a combination of drugs 2 and 6. (I–L) Panels I–L are from a numerical experiment in which we set $C_{\mathrm{Nu}} = C_{\mathrm{En}} = 0.6$ and attempt to use a combination of drugs 3 and 6. (M–P) Panels M–P are from a numerical experiment in which we set $C_{\mathrm{Nu}} = C_{\mathrm{En}} = 0.6$ and attempt to use a combination of drugs 2 and 6. The plots on the first column are cumulative drug dosages for the dual therapies considered. The plots on the second column are drug concentrations. The plots in the third column show $x_5(t)$ and the plots in the fourth, rightmost, column show $x_1(t)$, $x_2(t)$, $x_3(t)$, and $x_4(t)$, which we did not attempt to control. In all the simulations, the target value for AV count was 10 (i.e., $x_5^f = 10$) and the upper bound on each drug concentration w_i was 2 (i.e., $w_i^{\max} = 2$). The white region corresponds to the time interval $[t_0, t_f]$ when we either upregulate or downregulate the AV count The shaded region corresponds to the time interval $[t_0, t_f]$ when the AV count is maintained within the interval $x_5^f \pm \epsilon$.

Chapter 7

Design of Attacks in Power Grid Networks

7.1 Introduction

In chapter 5, we have implemented the optimal control strategies for complex networks to control blood glucose level in Type I diabetes by using insulin and glucagon. In chapter 6, we have implemented the optimal control strategies to predict the optimal drug scheduling and the best therapy for controlling autophagy in a cell. In this chapter, we will show an example how to design an attack perpetrated against a power grid network. We are interested in both the spatial aspect, i.e., the choice of the targets, and the particular temporal sequence, i.e., the times at which the attacks are scheduled over a given time period. We will approach this problem using the optimal control strategies, by considering **the point of view of the attackers**. Namely, we will attempt to solve a constrained optimization problem, with the goal of calculating the most devastating attack to a known critical infrastructure, given a fixed amount of resources available to the attackers (e.g., only a certain number

of attacks can be completed in the given time span). As we will see, the temporal aspect, i.e., the particular sequence of the attacks, will play a crucial role on the overall impact of the coordinated attack, as particular sequences of attacks are more prone to generating cascading failures.

There is a large literature on characterizing the propagation of dynamic failures and dynamic attacks over critical infrastructures. We focus on the literature on power grids, but analogous studies have been performed in the context of hydraulic networks [202–206], computer networks [207–211], and interdependent networks [212–216], to name a few works.

Recent examples of cascading failures in power grids include the 2003 blackout in the Northeastern United States [217], the Italian blackout of 2003 [218], the major European blackout of 2006 [219] and the Indian blackout of 2012 [220]. In all these cases the escalation of an initially localized event caused major disruptions at the grid level and considerable economical losses. In 2013-2014 two malware programs BlackEnergy2 and Havex [221] were deployed against companies of the energy sector and in 2015-2016 a cyberattack brought down portions of the Ukrainian power grid [222]. These very recent attacks raised the level of alertness towards the threats posed by cyberattacks on physical infrastructure. More generally, cyberterrorism is perceived as a concern both by the technical community [223] and by the policy makers [224].

Based on previous observations, the timescales on which a cascade event may occur range from seconds to hours. For example, in [225] the authors claimed that the cascade of events that caused the 2003 blackout in the Northeastern United States lasted 4 hrs. In [226] the authors noted that the cascade of events that caused the Italian grid failure of 2003 developed over several minutes and the 2006 European grid failure developed over several seconds. Data from [227] showed that in average 1.4 line failures per minute occur in the early phase of a cascade and 4 line failures

per minute occur in the escalation phase of the cascade. This data provides evidence that: (i) power-grid operators may or may not have time to take corrective measures to avoid a cascading failure, based on the rate at which the cascade is progressing and whether it is in its early phase or escalating phase; and (ii) it is actually possible to schedule a sequence of temporally spaced actions (a coordinated attack) so as to generate a synergistic effect on the electric grid.

Simplified models for the propagation of cascading failures on networks have been proposed in [228–230]. More realistic models, based on the swing equation [231] for the propagation of cascading failures in a power grid have been proposed in [232, 233]. For a comprehensive review of using complex networks to represent power grids is presented in [20].

A very recent paper has started investigating the effects of multiple coordinated attacks on the power grid, showing the high potential impact of such an attack [234]. References [46, 235] studied the effects of *dynamic load altering attacks* (DLAAs) on power system stability, where here 'dynamic' means that the attack itself is a function of time.

Several papers have considered strategies for the mitigation of attacks on networks. For example, in Ref. [208] it was shown that a careful rewiring of a limited number of lines of the European power supply system and of the global Internet at the level of service providers could lead to a substantial increase of the overall network robustness. This is an example of a *static mitigation strategy*. More recently, a dynamical approach has been proposed to counteract the effects of malicious attacks, see e.g., our recent work [236]. We call this a *dynamic mitigation strategy*.

While there is a large literature on the effects of failures and intentional attacks on power grids and more in general on critical infrastructure, a characterization of the most devastating attacks in terms of both their spatial and temporal character-

ization is lacking. By filling this gap in the literature, we plan to achieve a better understanding of critical infrastructures and of protection schemes against possible (optimized) threats.

Reference [237] studied mitigation of cascading failures in the interdependent power-grid and communication networks. Reference [45] is also related to mitigation of cascading failures in power grids through optimal load shedding. An algorithm is proposed to compute optimal amounts of load to shed in order to stop further propagation of line failures in both deterministic and stochastic settings of line outages. Reference [238] formulated the cascading failure attack problem from a game-theory perspective, where both attackers and power-system operators try to maximize their corresponding rewards which are: maximize load shedding and minimize load shedding, respectively. They also prove the convergence of the game to a Nash equilibrium.

7.2   A model for the power grid dynamics

The swing equation is a fundamental tool that has been broadly used to describe the power grid dynamics, by focusing in particular on its dynamical synchronization properties. The model of the power grid network is coarse-grained where every node (also called a bus) in the system represents a rotating machine, every transmission line represents an electrical connection (including transformers) between two nodes, and the nodes are strongly coupled via the lines. There are two types of nodes, generator nodes that supply power to the power grid network and non-generator nodes that consume power from the grid.

We model N rotating machines, each corresponding to a node of a power grid network and L transmission lines, each corresponding to an edge of the network. The

swing equations of the power grid system are,

$$\dot{\theta}_i = \omega_i, \quad i = 1, 2, \cdots, N \tag{7.1a}$$

$$I_i \dot{\omega}_i = P_i - \gamma_i \omega_i + \sum_{j=1}^{N} K_{ij} \sin(\theta_j - \theta_i) \tag{7.1b}$$

Here θ_i is the mechanical rotor angle and ω_i is the angular velocity (relative to the reference frame of $\Omega = 2\pi$ (50 or 60 Hz) of machine i, for each $i \in \{1, 2, \cdots, N\}$. Also a machine i either provides power (a generator) or absorbs power (a consumer or a non generator bus). If a machine i is generator then $P_i > 0$, and if a machine i is consumers then $P_i < 0$. We write,

$$P_i = \begin{cases} P_i^M > 0, & \text{if } i \text{ is a generator node} \\ P_i^L < 0, & \text{if } i \text{ is a non-generator node} \end{cases} \tag{7.2}$$

P_i^M is the mechanical power generated at generator i and incorporates two terms,

$$P_i^M(t) = K_i^P \omega_i + K_i^I \int_0^t \omega_i d\tau \tag{7.3}$$

where, $K_i^P > 0$ and $K_i^I > 0$ are the proportional and integral controller coefficients, respectively. The proportional term is the turbine-governor controller and the integral term is the load-frequency controller [239].

In Eq. (7.1b) γ_i is the damping coefficient, I_i is the inertia constant and $K = \{K_{ij}\}$ is the coupling matrix, where $K_{ij} = K_{ji}$ represents the admittance between nodes i and j. While the swing equation has been used to dynamically update the angles $\theta_i(t)$ as functions of time, real-time estimates of the flows F_{ij} on each line (i, j) with coupling K_{ij} at time t can be modeled as,

$$F_{ij} = K_{ij} \sin(\theta_j - \theta_i) \tag{7.4}$$

A power grid network at its operational point is characterized by all machines running in synchrony at the reference angular velocity ω, i.e., $\omega_i = 0 \forall i \in \{1, \cdots, N\}$. The fixed points of Eqs. (7.1b) are obtained by solving for the angles θ_i^* in the following equation:

$$P_i + \sum_{j=1}^{N} K_{ij} \sin(\theta_j^* - \theta_i^*) = 0 \tag{7.5}$$

7.3 Modeling line failures

Here we briefly describe the model proposed in [233] for the propagation of line failures as a consequence of an initial set of line failure(s). The initial line failures are considered as an exogenous perturbation, such as, for example, a transmission line failing due to a lightning strike or to extreme heat during the summer. In order to model cascading failures in power grid networks, we use the swing equations in Eq. (7.1) together with Eq. (7.4). The actual power flow F_{ij} along the transmission line (i, j) of the network is compared to the actual available capacity C_{ij} of line (i, j), i.e., to the maximum flow that the line can tolerate. The capacity C_{ij} is set to be a tunable percentage of K_{ij}. In order to prevent damage from overload, the line (i, j) is then shutdown if the flow on it exceeds the value αK_{ij}, where $\alpha \in [0, 1]$ is a control parameter of the model. Thus the overload condition on the line (i, j) at time t is given by:

$$|F_{ij}| > C_{ij} = \alpha K_{ij} \tag{7.6}$$

We say that the grid is stable or in synchrony, if the network has a stable fixed point and the flows on all lines are within the bounds of the capacity, i.e., do not

violate the overload condition Eq.(7.6), where the flows are calculated by inserting the fixed-point solution into Eq. (7.4). When the flow on a line exceeds its capacity, that line fails.

7.3.1   Numerical simulation of cascading failures

In order to illustrate how the dynamical model of cascading failures occurs in a power grid network as consequence of an initial line failure, we consider the power grid network with $N = 5$ nodes and $L = 7$ transmission lines shown in Fig. 7.1. We assume that the network has two generators and 3 non generator buses [233]. Nodes 2 and 5 are generators, and Nodes 1, 4 and 3 are non-generator nodes. A schematic diagram of the network is shown in Fig. 7.1. The power generated at the generators is equal to $P_i^G = 1.5s^{-2}$. The power consumed at the non generator nodes is equal to $P_i^L = -1s^{-2}$. For simplicity we adopt here a modified 'per unit system' obtained by replacing real machine parameters with dimensionless multiples with respect to reference values [233]. For instance, here a 'per unit' mechanical power $P_{\text{per unit}}$ corresponds to the real value $P_{\text{real}} = 100MW$. The controller coefficients are set to $K_1^I = 0.9133$, $K_2^I = 0.8121$, $K_1^P = K_2^P = 1$.

Moreover, for simplicity we consider homogeneous coupling, $K_{ij} = Ka_{ij}$ for each transmission line (i, j) with $K_{ij} = 1.63$ and unweighted adjacency matrix $A = \{a_{ij}\}$, i.e., $a_{ij} = a_{ji}$ is equal to 1 if nodes i and j are connected and is equal to zero, otherwise. We further set $\gamma_i = 0.1$ and $I_i = 1$ for all $i = 1, \cdots, N$. We initialize the system from its stable state, corresponding to its working condition. To do so, we solve Eq. (7.5) and calculate the corresponding flows at equilibrium. We then set the threshold value $\alpha = 0.6$. A failure of line (i, j) occurs every time the absolute normalized flow $|F_{ij}(t)|/K_{ij}$ on transmission line (i, j) exceeds the threshold value 0.6. From Fig. 7.2A and 7.2B, we observe that when there is no line failure,

the system remains in its stable steady state and the power flow on each line also remains constant. We now consider the effect of an exogenous perturbation. At time $t = 1$ we perturb the stable steady state, by failing the line $(2, 4)$. Because of the capacity criterion in Eq. (7.6) as shown in Fig. 7.2B, at time $t = 1.9$ second, i.e., approximately 1 second after the initial failure, the line $(2, 3)$ becomes overloaded (the flow exceeds the capacity), which causes a secondary failure, leading in turn to additional overloads on other lines and their failure in a cascading process that eventually leads to the disconnection of the entire grid. The whole cascade of failures induced by the initial removal of transmission line $(2, 4)$ is shown in Figs. 7.2A and 7.2B. Not always the new line failures occur in lines adjacent to those previously failed, i.e., the failure propagation model is *nonlocal*, which is in agreement with previous models and observations [240, 241].

7.3.2 Line Health Dynamics

We modify the model of dynamically induced cascading failures, described above, to incorporate a time-varying variable to characterize the *health* of a transmission line. We propose the following dynamical equation for the time evolution of the health of a transmission line,

$$
\dot{l}_{ij}(t) = \begin{cases} -\mu l_{ij}(t)\{(1 - l_{ij}(t))(b - l_{ij}(t))\}, & \text{if } b \leq 1 \\ -\mu l_{ij}(t)\{(b - l_{ij}(t))^2 + b - 1\}, & \text{if } b > 1 \end{cases} \tag{7.7}
$$

Here, $0 \leq l_{ij}(t) \leq 1$ represents the health of the transmission line $\{i, j\}$ at any time t, $l_{ij} = 0$ indicates the line is failed and $l_{ij} = 1$ indicates the line is in perfect health and $\mu > 0$ in Eq. (7.7) is a tunable parameters, which depends on the structure of the power grid network and its dynamics. In Eq. (7.7), $b = \frac{|F_{ij}(t)|}{C_{ij}}$ and $C_{ij} \neq 0$. When $b < 1$, Eq. (7.7) has 3 fixed points $l_{ij}^* = 0, b, 1$ of which 0 and 1 are stable fixed points

and b is an unstable fixed point. When $b = 1$, the fixed point b coincide with 1 and Eq. (7.7) has 2 fixed points $l_{ij}^* = 0, 1$ of which 0 is a stable fixed point and 1 is a saddle point. When $b > 1$, the fixed point 1 and b disappear and Eq. (7.7) has only one fixed point $l_{ij}^* = 0$ which is a stable fixed point.

By putting together Eq. (7.1) and the line health dynamics Eq. (7.7), we obtain the following set of equations,

$$\dot{\theta}_i(t) = \omega_i(t) \tag{7.8a}$$

$$I_i \dot{\omega}_i(t) = P_i - \gamma_i \omega_i + \sum_{j=1}^{N} K_{ij} l_{ij}(t) \sin(\theta_j - \theta_i) \tag{7.8b}$$

$$\dot{l}_{ij}(t) = \begin{cases} -\mu l_{ij}(t)\{(1 - l_{ij}(t))(b - l_{ij}(t))\}, & \text{if } b \leq 1 \\ -\mu l_{ij}(t)\{(b - l_{ij}(t))^2 + b - 1\}, & \text{if } b > 1 \end{cases} \tag{7.8c}$$

We also introduce a smooth version of Eq. (8c), which we will use in what follows,

$$\dot{l}_{ij}(t) = -\mu l_{ij}(t) \left[\{(1 - l_{ij}(t))(b - l_{ij}(t))\} \frac{1}{1 + e^{-k(1-b)}} + \{(b - l_{ij}(t))^2 + b - 1\} \frac{1}{1 + e^{-k(b-1)}} \right] \tag{7.9}$$

First we initialize the system so that all the transmission lines are in their healthy state $l_{ij} = 1$ and set $\theta_i(0) = \theta_i^*$, $i = 1, ..., N$, i.e., all the flows are at equilibrium. We set a threshold value of $\alpha = 0.6$, i.e., if the absolute normalized flow $|F_{ij}(t)|/K_{ij}$ on transmission line (i, j) exceeds 0.6, then line (i, j) fails. In Fig. 7.3A), we repeat the calculations in Fig. 2 but incorporating the line health dynamics, Eqs. (9), for $\mu = 100$ and $k = 400$. By comparing the flow and the sequence of the line failures between Fig. 7.2B and Fig. 7.3, we observe that the line health dynamics in Eq. (7.7) well captures the sequence and timing of failures as well as the flow dynamics over the lines. Also from the line health dynamics plotted in Fig. 7.3B, one can see that

the lines quickly (but smoothly) transition from the healthy state to the failed state every time the flow threshold condition is violated for that line.

7.4 Modeling Attack Strategies

7.4.1 Constant Perturbations in the Power Consumed at Non-▮ generator Buses

We first consider the effect of a constant perturbation in the power consumption at a non-generator node. While in principle generator nodes could also be attacked, typically generator nodes are more securely protected, which makes them harder to attack. We focus on the 5 node network shown in Fig. 7.1. We numerically compute the sequence of line failures when one of the non generator nodes $i \in \{1, 3, 4\}$ is attacked. We assume that the power consumption at node i is purportedly changed from its nominal value equal to -1 and set to a constant value $P_i^L < -1$. We present the results of this analysis in table 7.1. The first column represents the node i which is being attacked and each columns represents the value of the constant perturbation P_i^L. In each panel, we report the sequence of line failures due to different amount of power consumption $P_i^L < -1$. The underbracing under two or more lines indicates a group of lines failing at approximately the same time, i.e., within a time window of 10^{-3} second. We see that the sequence of line failures may be different for different amounts of power consumption. For instance, the sequences for $P_1^L = -3$ and $P_1^L = -5$ are not the same.

Table 7.1: Temporal pattern of line failures due to a constant power consumption P_i.

Node i	$P_i = -1$	$P_i = -1.6$	$P_i = -3$	$P_i = -100$
1	no line fails	$3, 7$	$1, 2, 3, 7, 5$	$\underbrace{1, 2, 3}, 7, 5, 4$
3	no line fails	$\underbrace{3, 7}$	$4, \underbrace{2, 6}, \underbrace{3, 7}$	$\underbrace{2, 4, 6}$
4	no line fails	$7, 3$	$5, 6, 7, 3, 1$	$5, 6, \underbrace{7, 3}, 1, 4$

7.4.2 Most Devastating Attacks

We now consider the effects of a deliberate man-made cyber-attack perpetrated against the power grid. An attacker may take control of a generator, consume power from buses, or affect the transmission lines. Here we consider the case that the attack is limited to non-generator buses in which power is consumed in order to deliberately induce line failures in the power grid. We assume the attacker is able to affect P_i^L at one node or at a set of nodes and is interested in determining the particular function of time $P_i^L(t)$ that can be most harmful to the grid, under given constraints. The most devastating attack (MDA) is the one that maximizes the number of line failures over the network in a given time interval. In order to compute an MDA, we formulate a nonlinear optimal control problem (OCP),

$$\min \quad \sum_{ij} l_{ij}(t_f) \tag{7.10}$$

subject to the following constraints,

$$\dot{\mathbf{x}} = f(\mathbf{x}(t), \mathbf{P}(t)), \tag{7.11a}$$

$$0 \le \int_0^{t_f} -P_i^L(t)dt \le E_i^{max}. \tag{7.11b}$$

The constraints in Eq. (7.11b) indicate that there is an upper bound on the total energy available to the attacker.

Here the dynamics in Eq. (7.11a) represents the dynamics in Eqs. (7.8)–(7.9). By computing the solution to the optimal control problem, we will get insight into the particular sequence of line failures that follow an attack. We will also be able to produce a ranking of the buses in terms of the number of transmission lines failed, when the bus is attacked.

7.5   Method

In general, there exists no analytic framework that is able to provide the solution of the optimal control problems in Eqs. (7.10)-(7.11) . The Eqs. (7.10)-(7.11) can be written as Eq. (4.1). Hence, we will recur to a popular numerical technique called *Pseudospectral Optimal Control* (PSOC) [55, 111, 112]. The main concept behind PSOC is to convert the OCP into a nonlinear problem (NLP) by descritizing and approximating the OCP by an orthogonal set of polynomials (e.g. Legendre, Chebyshev). We have used $\mathcal{PSOPT}$ [112], an open-source PSOC toolbox written in C++, to perform the PSOC discretization and approximation procedure. The NLP then can be solved with a number of different techniques, but here we use an interior point algorithm [56] as implemented in the open-source C++ software Ipopt [113].

7.6   Results

To solve the optimal control problem in Eqs. (7.10)-(7.11), we now set the values of $E_i^{\max}$ in Eq. (7.11b). For this numerical experiment, we consider the previous 5 nodes network. We also set $t_0 = 0$ and $t_f = 6$. From the constant power consumption analysis in the previous section, we have seen that there is no line failures if a constant amount of load $P_i^L = -1$ is consumed from non-generator node 3. In our numerical experiment, we consider the node 3 is being attacked. We set $E_3^{\max} = P_3^L \times t_f =$

$-6s^{-1}$. In Fig. 7.4, we observe that due to the optimal amount of load $P_3^{L*}(t)$ consumed from node 3 causes the cascading line failures while the total amount of load is -6, i.e., $\int_0^{t_f} P_3^{L*}(t)dt = E_3^{\max}$. But there are no line failures when constant amount of of load $P_3^L = -1$ is consumed from non-generator node 3.

In another numerical experiment, we set $t_f = 6$ and $E_i^{\max} = -60s^{-1}$ in Eq. (7.11b). In Table 7.2, the first column is the bus i which is under attack. The second column presents the maximum number of line failures in the case of the most devastating attack. On third column, we present the sequence of line failures, and on the fourth column we place the rank of bus i in terms of its ability to fail the maximum number of lines. Namely, we see that for our example power grid network, bus 3 is the most vulnerable to MDA's.

7.7   Conclusions

In chapters 5 and 6, we have used the optimal control techniques to design the formal therapies for complex diseases. We have designed constrained optimal control problem where our goal was to minimize the total amount of drugs to achieve the desired goal. The solution of the optimal control problem yielded the drug schedules that require a minimum amount of drugs, maintaining drugs concentrations below the toxic level at all times, and that bring the final state of the target node near the desired level. In addition, we were able to find the sequencing protocol of using the drugs in multi-drug therapies. The same idea of the optimal control techniques can be used to design the most devastation attack on the power grid network by considering the point of view of attackers. In this chapter, we have presented an small example of how a temporal aspect of load taken from a node can create a cascade failures for a given fixed amount of load available to attacker (see Fig. 7.4). In an another example, we have seen that it is also possible to rank the most vulnerable node in the

power grid network (see Table 7.2). In this chapter we do not experiment further, but we can still use the optimal control techniques to design the most devastating coordinated attack, as particular sequences of attacks are more prone to generate the cascading failures (similar idea of finding the best combination of drug schedules).

Table 7.2: Ranking of the nodee(buses) in terms of ability to destroy the maximum number of transmission lines.

Bus	No. of lines failures	Sequence of lines failures	Rank
1	6	$3, 1, 7, 2, 4, 5$	2
3	7	$4, \underbrace{3, 7}, \underbrace{2, 6}, \underbrace{1, 5}$	1
4	6	$7, 5, 3, 6, 4, 1$	2
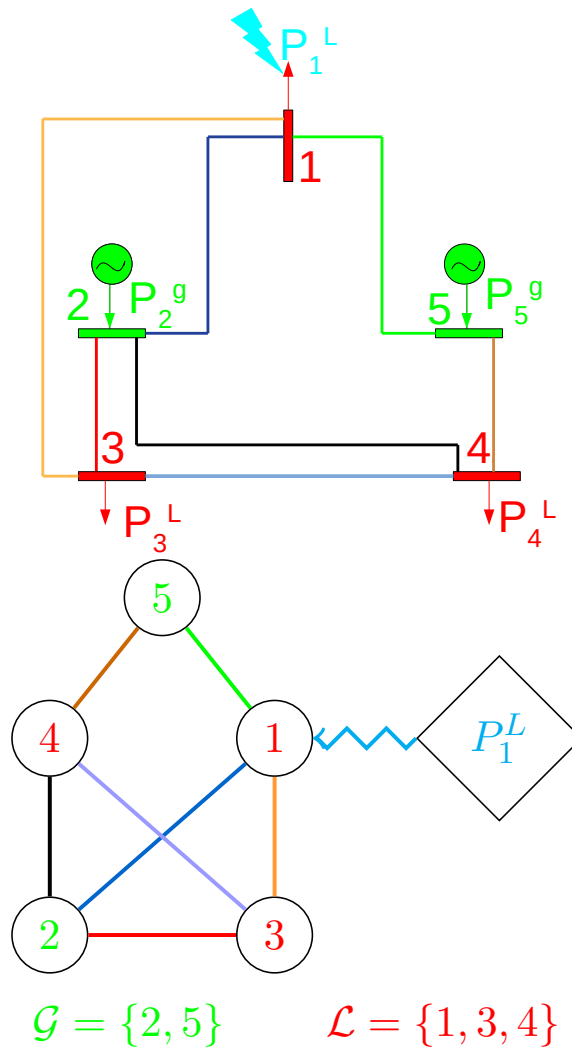
Figure 7.1: A schematic view of a five node network with generators and load buses. $\mathcal{G} = \{2, 5\}$ is the set of generator nodes and $\mathcal{L} = \{1, 3, 4\}$ is the set of non-generator nodes. The power demand P_1^L at node 1 is determined by an external event.
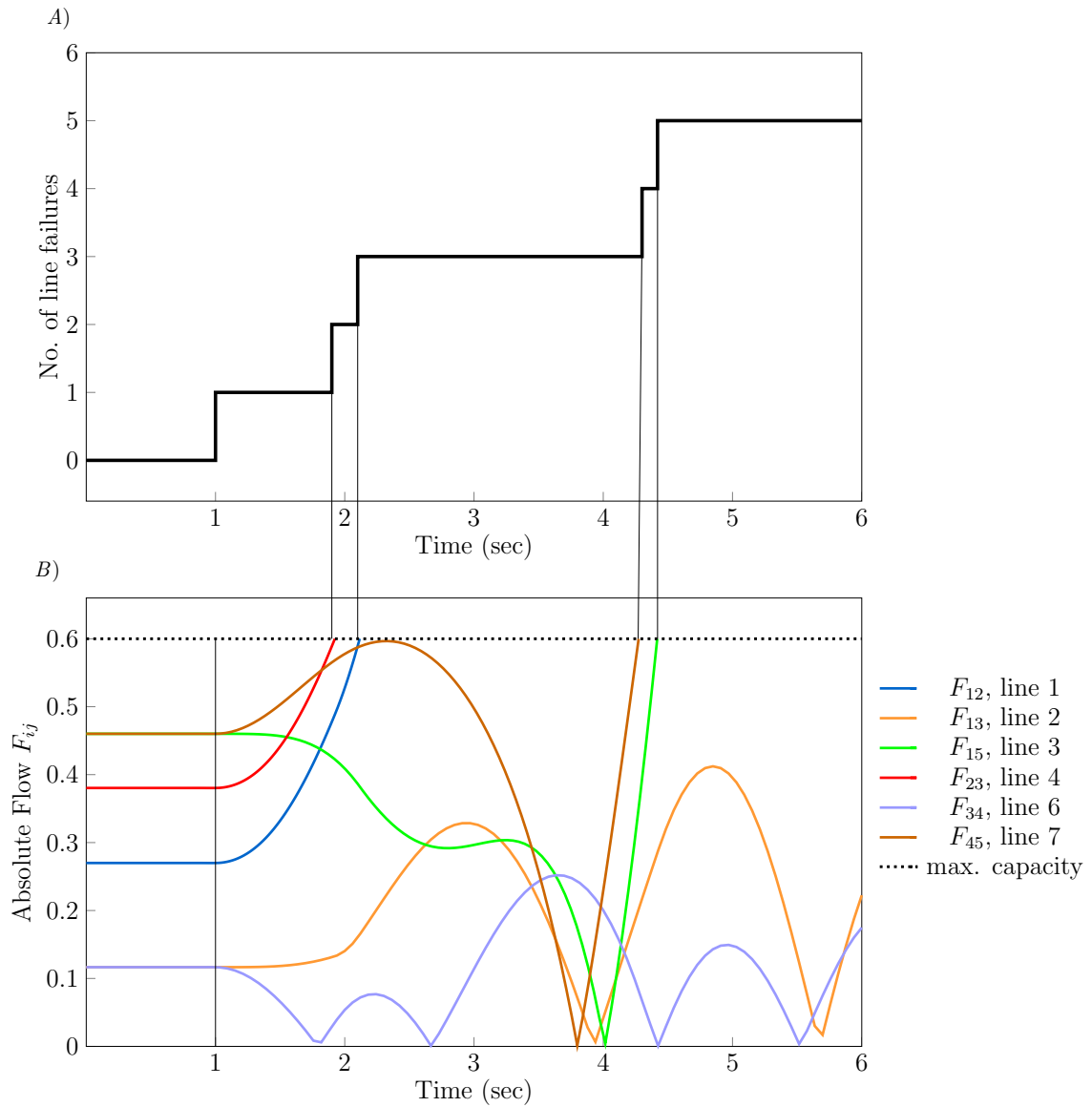
Figure 7.2: A) Time evolution of the number of line failures. B) Time evolution of normalized absolute flow of the transmission lines. Each one of the seven transmission lines has a different associated color.
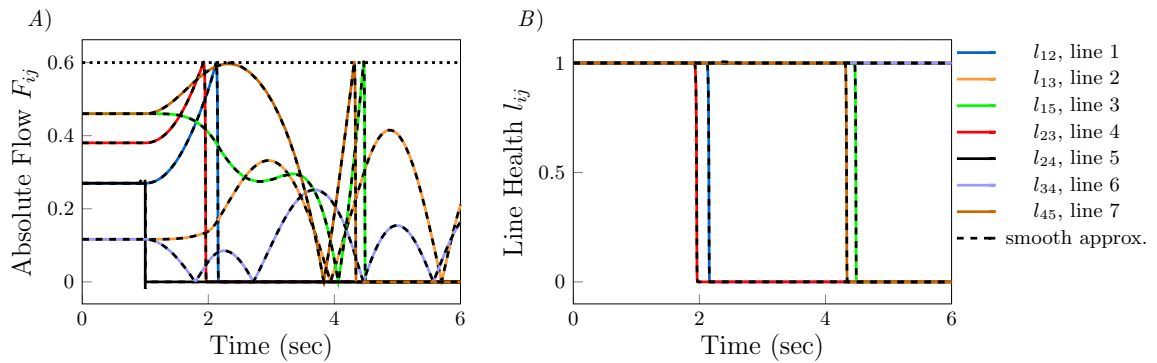
Figure 7.3: A) Time evolution of the normalized absolute flows over the transmission lines. Each curve is the flow calculated using Eq. (7.8) together with Eq. (7.7). Colors match the colors used to uniquely label the transmission lines in Fig. 1. The black dotted curves are the flows calculated using Eq. (7.8) together with Eq. (7.9). B) Time evolution of the health of the transmission lines. Each curve is the health calculated using Eq. (7.8) together with Eq. (7.7). Colors match the colors used to uniquely label the transmission lines in Fig. 1. The black dotted curves are the health calculated using Eq. (7.8) together with Eq. (7.9).
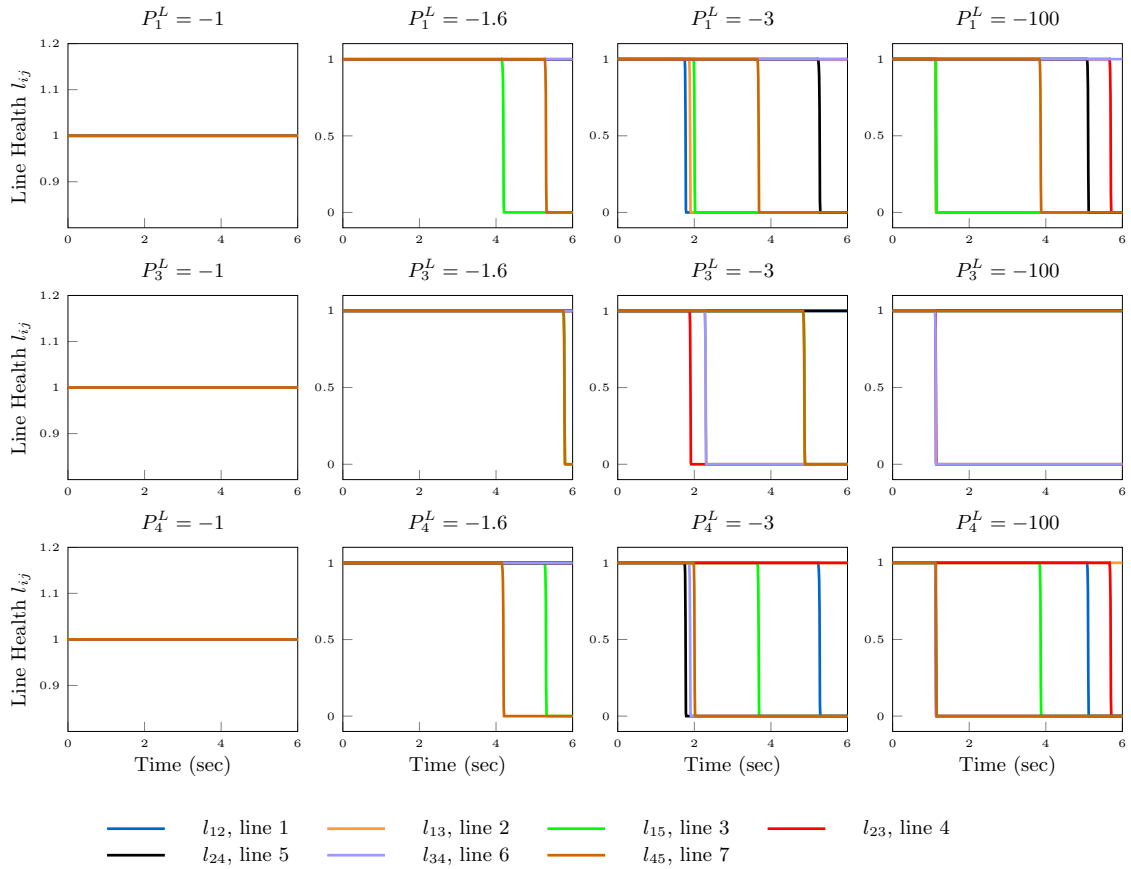
Figure 7.4: Line health time evolutions. Each row is for a different nongenerator node being affected ($i=1$ top row, $i = 3$ middle row, and $i = 4$ bottom row). Each column is for a different value of P_i^L modeled as a time-constant.
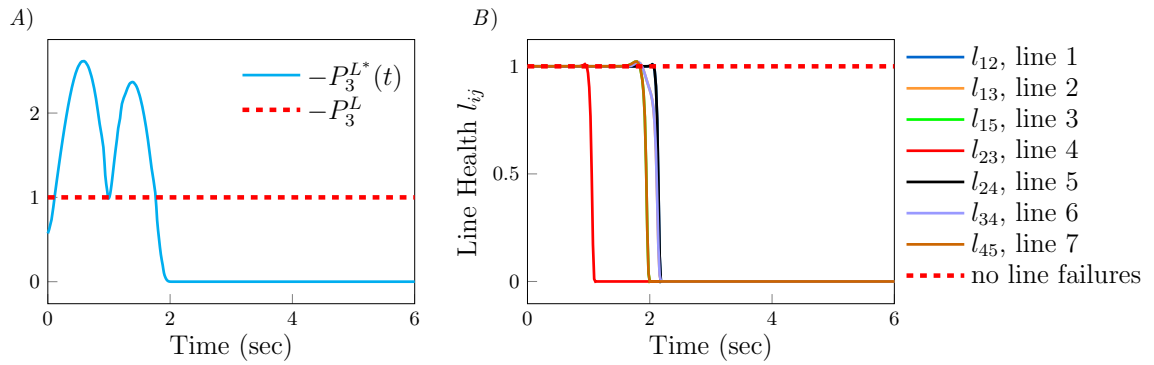
Figure 7.5: (A) The time evolution of the load P_3^{L*} (solid cyan curve) consumed by an attacker from node bus 3. The time evolution of the load P_3^{L*} (solid cyan curve) consumed by an attacker from node bus 3. The load P_3^L (red dashed line) constant in time. (B) Time evolution of the line health conditions due to the load consumption P_3^{L*} (solid) and P_3^L (dashed).

Chapter 8

Conclusion

The final overarching goal of this thesis was to use the theory of dynamical systems and controls to predict better therapies for complex diseases, such as diabetes or cancer. Such complex diseases are governed by either a physiological process in the human body or at the level of a cell, and key features of the physiological process can be captured mathematically by a complex mathematical model of differential equations. Moreover, the physiological model can respond appropriately to drugs when these drugs are exogenously supplied.

The formalism we have adopted is that of control of complex networks, where a biological system can be represented as a complex network, and the external drugs are modeled as control signals to the network. In general, while controlling the biological networks, we have set our objective to minimize the amount of drugs used to achieve a given physiological goal. This corresponds, in the jargon of optimal control, to reduce the control effort while controlling the process to a desired final state. In order to reduce the control effort, in chapter 2 we have introduced an optimal control technique, we call *target control*, which can reduce the control energy (a measure of control effort) by reducing the number of the system's state one is trying

to affect. Translated to networks, this corresponds to reducing the required control energy, as the number of target nodes is reduced. We provide an analytic solution to this problem, in the case of linear networks. We show that for a fixed number of control inputs, the energy required to control a portion of the network decreases exponentially with the cardinality of the target set, so even controlling a significant number of nodes requires much less energy than when every node is targeted.

Moreover, in chapter 3, we have seen how it is possible to reduce the control energy, by appropriately defining the control objectives and the constraints. We have seen that the control energy can be reduced further by allowing a small deviation from the desired final condition. We call this technique *balance control.*

This initial work has guided us to control complex biological systems and to design drug dosage schedules optimally for biomedical applications. While it is important to determine the optimal dosage amount for a given drug, it is also important to identify the best combination of drugs, as experimentally this may be very hard (expensive) to do, especially when the number of combinations becomes very large. We have found several potential benefits of using optimal control in this context. For example, in chapter 5, by posing the control objective as a minimum fuel problem while only insulin is administered, we have found the the total amount of insulin and the time of administering are similar to the *standard therapy* currently used by patients affected by diabetes, and optimized over decades of medical practice. This seems to suggest that the optimal control techniques can provide some useful insight in designing optimized therapies in a variety of contexts. By defining the control objectives in the same manner, we were then able to propose an *ad-hoc* rule for dual therapy when both insulin and glucagon are used in combination. The solution of this problem yielded drug schedules that require a minimum amount of drugs, maintaining drugs concentrations below a specific threshold (below the toxic level) at all times, and that bring the blood glucose level near the desired levels in the

most efficient manner. In addition, we were able to find a sequencing protocol for the administration of the drugs. These characteristics of the solution of the optimal control problem designed on the purpose of therapy design are not surprising. We have seen similar behavior in chapter 6, while we have used the optimal control techniques to modulate autophagy in a cell, either up or down. We have also seen in chapter 6 that the optimal control techniques when used in combinatorial therapy design, can predict the most effective drug schedules and drug combinations.

Chapter 5 considers the Glucose-Insulin-Glucagon mathematical model, which describes how the body responds to exogenously supplied insulin and glucagon in patients affected by Type I diabetes. While controlling this system, we have considered the blood glucose concentration ($G(t)$) as the only target node. We have set a final time condition on $G(t)$, while the final time condition on the other nodes of the system have been left unconstrained. We have used the target control technique together with PSOC to design an optimal dosing schedule of either insulin or insulin and glucagon together to regulate the blood glucose while limiting the total amount of insulin and glucagon administered. Besides, we have posed the control objectives in two ways: 1) blood glucose regulation with the minimum fuel problem (ReMF) and 2) blood glucose regulation with the minimum energy problem (ReME). In both cases, the control problem calls for usage of a minimum total amount of drug while regulating the blood glucose near the desired level. The numerical solution of the REMF problem leads to a pulsatile type (shot-like) drug administration with the optimal time of the shot and the numerical solution of the REME problem leads to a drug administration that is continuous in time. The pulsatile drug administration allows us to propose an *ad-hoc* dual therapy by using both insulin and glucagon.

In chapter 6, we have implemented our optimal control strategies to design drug schedules for manipulating autophagy in a cell. We have set the number of autophagy vesicles (AVs) as the only target of the target control technique. In the constraints of

the problem we set a relax bound on final time AVs, which is similar in a sense to the balance control techniques. We have posed the control objective as a minimum-fuel problem, in that our control problem calls for usage of a minimum total amount of drug. Numerical solution of this problem yielded monotherapy drug schedules that require a minimum amount of drug, maintain drug concentration below a specified threshold at all times, and bring about desired effects in the most efficient manner possible, in a well-defined sense. Furthermore, through the essentially same approach, but with consideration of adjustable time-dependent drug injection/input rates for two different drugs, we were able to predict synergistic drug pairs.

Our approach is generalizable to designing monotherapy and multi-therapy drug schedules that affect different biological networks of interest. Furthermore, this generalized approach can also be used to design optimal attacks perpetrated against critical infrastructures, such as power grid networks. In chapter 7, we have computed the most devastating attack to a power grid networks, given a fixed amount of resources available to attackers. Moreover, we have seen how this translates into an 'optimal' sequence of line failures for the case of an example power grid of interest.

References

1. Sorrentino, F., di Bernardo, M., Garofalo, F. & Chen, G. Controllability of complex networks via pinning. *Physical Review E* **75,** 046103 (Apr. 2007).

2. Mikhailov, A. S. & Showalter, K. Introduction to focus issue: Design and control of self-organization in distributed active systems. *Chaos: An Interdisciplinary Journal of Nonlinear Science* **18,** 026101 (2008).

3. Yu, W., Chen, G., Lu, J. & Kurths, J. Synchronization via pinning control on general complex networks. *SIAM Journal on Control and Optimization* **51,** 1395–1416 (2013).

4. Tang, Y., Gao, H., Kurths, J. & Fang, J.-a. Evolutionary pinning control and its application in UAV coordination. *Industrial Informatics, IEEE Transactions on* **8,** 828–838 (Nov. 2012).

5. Wang, X. F. & Chen, G. Pinning control of scale-free dynamical networks. *Physica A: Statistical Mechanics and its Applications* **310,** 521–531 (July 2002).

6. Liu, Y.-Y., Slotine, J.-J. & Barabási, A.-L. Controllability of complex networks. *Nature* **473,** 167–173 (May 2011).

7. Liu, Y.-Y., Slotine, J.-J. & Barabasi, A.-L. reply to: Few inputs can reprogram biological networks. *Nature* **478,** E4–E5 (2011).

REFERENCES

8. Ruths, J. & Ruths, D. Control profiles of complex networks. *Science* **343,** 1373–1376 (2014).

9. Summers, T. & Lygeros, J. *Optimal sensor and actuator placement in complex networks* in *Proceedings of the 19th IFAC World Congress* (2014).

10. Wang, B., Gao, L. & Gao, Y. Control range: a controllability-based index for node significance in directed networks. *Journal of Statistical Mechanics: Theory and Experiment* **2012,** P04011 (Apr. 2012).

11. Nepusz, T. & Vicsek, T. Controlling edge dynamics in complex networks. *Nature Physics* **8,** 568–573 (2012).

12. Yuan, Z., Zhao, C., Di, Z., Wang, W.-X. & Lai, Y.-C. Exact controllability of complex networks. *Nature communications* **4** (2013).

13. Müller, F.-J. & Schuppert, A. Few inputs can reprogram biological networks. *Nature* **478,** E4–E4 (2011).

14. Iudice, F. L., Garofalo, F. & Sorrentino, F. Structural permeability of complex networks to control signals. *Nature communications* **6** (Sept. 2015).

15. Gao, X.-D., Wang, W.-X. & Lai, Y.-C. Control efficacy of complex networks. *Scientific Reports* **6** (2016).

16. Yan, G. *et al.* Spectrum of controlling and observing complex networks. *Nature Physics* **11,** 779–786 (Aug. 2015).

17. Yan, G., Ren, J., Lai, Y.-C., Lai, C.-H. & Li, B. Controlling complex networks: how much energy is needed? *Physical review letters* **108,** 218703 (2012).

18. Chen, Y.-Z., Wang, L.-Z., Wang, W.-X. & Lai, Y.-C. Energy scaling and reduction in controlling complex networks. *Royal Society open science* **3,** 160064 (2016).

REFERENCES

19. Arianos, S., Bompard, E., Carbone, A. & Xue, F. Power grid vulnerability: A complex network approach. *Chaos: An Interdisciplinary Journal of Nonlinear Science* **19,** 013119 (2009).

20. Pagani, G. A. & Aiello, M. The power grid as a complex network: a survey. *Physica A: Statistical Mechanics and its Applications* **392,** 2688–2700 (2013).

21. Onnela, J.-P. *et al.* Analysis of a large-scale weighted network of one-to-one human communication. *New Journal of Physics* **9,** 179 (2007).

22. Kwak, H., Lee, C., Park, H. & Moon, S. *What is Twitter, a social network or a news media?* in *Proceedings of the 19th international conference on World wide web* (2010).

23. Palsson, B. *Systems biology* (Cambridge University Press, 2015).

24. Sporns, O. Structure and function of complex brain networks. *Dialogues Clin Neurosci* **15,** 247–262 (2013).

25. Papo, D., Buldú, J. M., Boccaletti, S. & Bullmore, E. T. Complex network theory and the brain. *Phil. Trans. R. Soc. B* **369,** 20130520 (2014).

26. Allhoff, K. T. & Drossel, B. When do evolutionary food web models generate complex networks? *Journal of theoretical biology* **334,** 122–129 (2013).

27. Lerman, K. & Ghosh, R. Information Contagion: An Empirical Study of the Spread of News on Digg and Twitter Social Networks. *ICWSM* **10,** 90–97 (2010).

28. Liu, Y.-Y. & Barabási, A.-L. Control principles of complex systems. *Reviews of Modern Physics* **88,** 035006 (July 2016).

29. Gao, J., Barzel, B. & Barabási, A.-L. Universal resilience patterns in complex networks. *Nature* **530,** 307–312 (Feb. 2016).

REFERENCES

30. Proskurnikov, A., Matveev, A. & Cao, M. Opinion dynamics in social networks with hostile camps: Consensus vs. polarization. *IEEE Trans. Autom. Control* **61,** 1524–1536 (June 2016).

31. Wang, W., Huang, J., Wen, C. & Fan, H. Distributed adaptive control for consensus tracking with application to formation control of nonholonomic mobile robots. *Automatica* **50,** 1254–1263 (Mar. 2014).

32. Zhou, Z., Menche, J., Barabási, A.-L. & Sharma, A. Human symptoms-disease network. *Nature communications* **5** (June 2014).

33. Klickstein, I., Shirin, A. & Sorrentino, F. Locally Optimal Control of Complex Networks. *Physical Review Letters* **119,** 268301 (2017).

34. Kirschner, D., Lenhart, S. & Serbin, S. Optimal control of the chemotherapy of HIV. *Journal of mathematical biology* **35,** 775–792 (1997).

35. Joshi, H. R. Optimal control of an HIV immunology model. *Optimal Control Applications and Methods* **23,** 199–213 (2002).

36. Martin, R. Optimal control drug scheduling of cancer chemotherapy. *Automatica* **28,** 1113–1123 (1992).

37. Świerniak, A., Ledzewicz, U. & Schättler, H. Optimal control for a class of compartmental models in cancer chemotherapy. *International Journal of Applied Mathematics and Computer Science* **13,** 357–368 (2003).

38. Ledzewicz, U. & Schättler, H. M. Drug resistance in cancer chemotherapy as an optimal control problem. *Discrete and Continuous Dynamical Systems Series B* **6,** 129 (2006).

39. Ledzewicz, U. & Schättler, H. Optimal controls for a model with pharmacokinetics maximizing bone marrow in cancer chemotherapy. *Mathematical Biosciences* **206,** 320–342 (2007).

REFERENCES

40. Zaman, G., Kang, Y. H. & Jung, I. H. Stability analysis and optimal vaccination of an SIR epidemic model. *BioSystems* **93,** 240–249 (2008).

41. Laarabi, H., Abta, A. & Hattaf, K. Optimal control of a delayed SIRS epidemic model with vaccination and treatment. *Acta biotheoretica* **63,** 87–97 (2015).

42. Macki, J. & Strauss, A. *Introduction to optimal control theory* (Springer Science & Business Media, 2012).

43. Morton, R. & Wickwire, K. H. On the optimal control of a deterministic epidemic. *Advances in Applied Probability* **6,** 622–635 (1974).

44. Cunniffe, N. J. *et al.* Thirteen challenges in modelling plant diseases. *Epidemics* **10,** 6–10 (2015).

45. Bienstock, D. *Optimal control of cascading power grid failures* in *Decision and control and European control conference (CDC-ECC), 2011 50th IEEE conference on* (2011), 2166–2173.

46. Amini, S., Pasqualetti, F. & Mohsenian-Rad, H. Dynamic load altering attacks against power system stability: Attack models and protection schemes. *IEEE Transactions on Smart Grid* **9,** 2862–2872 (2018).

47. Parker, R. S., Doyle, F. J. & Peppas, N. A. A model-based algorithm for blood glucose control in type I diabetic patients. *IEEE Transactions on biomedical engineering* **46,** 148–157 (1999).

48. Parker, R. S., Doyle, F. J. & Peppas, N. A. The intravenous route to blood glucose control. *IEEE Engineering in Medicine and Biology Magazine* **20,** 65–73 (2001).

49. Gillis, R. *et al. Glucose estimation and prediction through meal responses using ambulatory subject data for advisory mode model predictive control* 2007.

REFERENCES

50. Lynch, S. M. & Bequette, B. W. *Estimation-based model predictive control of blood glucose in type I diabetics: a simulation study* in *Bioengineering Conference, 2001. Proceedings of the IEEE 27th Annual Northeast* (2001), 79–80.

51. Thabit, H. *et al.* Home use of an artificial beta cell in type 1 diabetes. *New England Journal of Medicine* **373,** 2129–2140 (2015).

52. Zavitsanou, S., Mantalaris, A., Georgiadis, M. C. & Pistikopoulos, E. N. In Silico Closed-Loop Control Validation Studies for Optimal Insulin Delivery in Type 1 Diabetes. *IEEE Trans. Biomed. Engineering* **62,** 2369–2378 (2015).

53. Hovorka, R. *et al.* Nonlinear model predictive control of glucose concentration in subjects with type 1 diabetes. *Physiological measurement* **25,** 905 (2004).

54. Copp, D. A., Gondhalekar, R. & Hespanha, J. P. Simultaneous model predictive control and moving horizon estimation for blood glucose regulation in type 1 diabetes. *Optimal Control Applications and Methods* **39,** 904–918 (2018).

55. Ross, I. M. & Karpenko, M. A review of pseudospectral optimal control: From theory to flight. *Annual Reviews in Control* **36,** 182–197 (2012).

56. Nocedal, J. & Wright, S. *Numerical Optimization* (Springer, 2006).

57. Dalla Man, C., Rizza, R. A. & Cobelli, C. Meal simulation model of the glucose-insulin system. *IEEE Transactions on biomedical engineering* **54,** 1740–1749 (2007).

58. Man, C. D. *et al.* The UVA/PADOVA type 1 diabetes simulator: new features. *Journal of diabetes science and technology* **8,** 26–34 (2014).

59. Visentin, R. *et al.* The UVA/Padova Type 1 Diabetes Simulator Goes From Single Meal to Single Day. *Journal of diabetes science and technology* **12,** 273–281 (2018).

REFERENCES

60. Steil, G. M., Rebrin, K., Darwin, C., Hariri, F. & Saad, M. F. Feasibility of automating insulin delivery for the treatment of type 1 diabetes. *Diabetes* **55,** 3344–3350 (2006).

61. Magni, L. *et al.* Evaluating the efficacy of closed-loop glucose regulation via control-variability grid analysis. *Journal of Diabetes Science and Technology* **2,** 630–635 (2008).

62. Palerm, C. C., Zisser, H., Jovanovič, L. & Doyle III, F. J. A run-to-run control strategy to adjust basal insulin infusion rates in type 1 diabetes. *Journal of process control* **18,** 258–265 (2008).

63. Bergenstal, R. M. *et al.* Threshold-based insulin-pump interruption for reduction of hypoglycemia. *New England Journal of Medicine* **369,** 224–232 (2013).

64. Van Bon, A. C. *et al.* Feasibility of a portable bihormonal closed-loop system to control glucose excursions at home under free-living conditions for 48 hours. *Diabetes technology & therapeutics* **16,** 131–136 (2014).

65. Marchetti, G., Barolo, M., Jovanovic, L., Zisser, H. & Seborg, D. E. An improved PID switching control strategy for type 1 diabetes. *ieee transactions on biomedical engineering* **55,** 857–865 (2008).

66. Fisher, M. E. A semiclosed-loop algorithm for the control of blood glucose levels in diabetics. *IEEE transactions on biomedical engineering* **38,** 57–61 (1991).

67. Bequette, B. W. Challenges and recent progress in the development of a closed-loop artificial pancreas. *Annual reviews in control* **36,** 255–266 (2012).

68. Klionsky, D. J. & Emr, S. D. Autophagy as a regulated pathway of cellular degradation. *Science* **290,** 1717–1721 (2000).

69. Deretic, V., Saitoh, T. & Akira, S. Autophagy in infection, inflammation and immunity. *Nature Reviews Immunology* **13,** 722–737 (2013).

REFERENCES

70. Levine, B., Mizushima, N. & Virgin, H. W. Autophagy in immunity and inflammation. *Nature* **469,** 323–335 (2011).

71. Mizushima, N., Levine, B., Cuervo, A. M. & Klionsky, D. J. Autophagy fights disease through cellular self-digestion. *Nature* **451,** 1069–1075 (2008).

72. Nakatogawa, H., Suzuki, K., Kamada, Y. & Ohsumi, Y. Dynamics and diversity in autophagy mechanisms: lessons from yeast. *Nature Reviews Molecular Cell Biology* **10,** 458–467 (2009).

73. Shintani, T. & Klionsky, D. J. Autophagy in health and disease: a double-edged sword. *Science* **306,** 990–995 (2004).

74. Mulcahy Levy, J. M., Towers, C. G. & Thorburn, A. Targeting autophagy in cancer. *Nature Reviews Cancer* **17,** 528–542 (2017).

75. Jameson, J. L. & Longo, D. L. Precision medicine—personalized, problematic, and promising. *Obstetrical & Gynecological Survey* **372,** 2229–2234 (2015).

76. Gatzka, M. V. Targeted tumor therapy remixed—an update on the use of small-molecule drugs in combination therapies. *Cancers* **10,** 155 (2018).

77. Anderson, A. R. A. & Quaranta, V. Integrative mathematical oncology. *Nature Reviews Cancer* **8,** 227–234 (2008).

78. Michor, F. & Beal, K. Improving cancer treatment via mathematical modeling: surmounting the challenges is worth the effort. *Cell* **163,** 1059–1063 (2015).

79. Gao, J., Liu, Y.-Y., D'Souza, R. M. & Barabási, A.-L. Target control of complex networks. *Nature communications* **5** (2014).

80. Albert, R. & Barabási, A.-L. Statistical mechanics of complex networks. *Reviews of modern physics* **74,** 47 (2002).

81. Slotine, J.-J., Li, W. *et al. Applied nonlinear control* (Prentice-Hall Englewood Cliffs, NJ, 1991).

82. Kailath, T. *Linear systems* (Prentice-Hall Englewood Cliffs, NJ, 1980).

REFERENCES

83. Nacher, J. C. & Akutsu, T. Analysis of critical and redundant nodes in controlling directed and undirected complex networks using dominating sets. *Journal of Complex Networks* **2,** 394–412 (2014).

84. Li, G. *et al.* Minimum-cost control of complex networks. *New Journal of Physics* **18,** 013012 (2015).

85. Pasqualetti, F., Zampieri, S. & Bullo, F. Controllability metrics, limitations and algorithms for complex networks. *Control of Network Systems, IEEE Transactions on* **1,** 40–52 (2014).

86. Summers, T. H., Cortesi, F. L. & Lygeros, J. On Submodularity and Controllability in Complex Dynamical Networks. *IEEE Trans. Control of Network Systems* **3,** 91–101 (2016).

87. Tzoumas, V., Rahimian, M. A., Pappas, G. J. & Jadbabaie, A. Minimal actuator placement with bounds on control effort. *IEEE Transactions on Control of Network Systems* **3,** 67–78 (2016).

88. Cowan, N. J., Chastain, E. J., Vilhena, D. A., Freudenberg, J. S. & Bergstrom, C. T. Nodal dynamics, not degree distributions, determine the structural controllability of complex networks. *PLoS one* **7,** e38398 (2012).

89. Toolbox, M. C. *Advanpix, Tokyo*

90. Goh, K.-I., Kahng, B. & Kim, D. Universal behavior of load distribution in scale-free networks. *Physical review letters* **87,** 278701 (2001).

91. Milo, R. *et al.* Superfamilies of evolved and designed networks. *Science* (2004).

92. Jeong, H., Tombor, B., Albert, R., Oltvai, Z. N. & Barabási, A.-L. The large-scale organization of metabolic networks. *Nature* (2000).

93. Lafferty, K. D., Hechinger, R. F., Shaw, J. C., Whitney, K. & Kuris, A. M. Food webs and parasites in a salt marsh ecosystem. *Disease ecology: community structure and pathogen dynamics,* 119–134 (2006).

REFERENCES

94. Opsahl, T. Triadic closure in two-mode networks: Redefining the global and local clustering coefficients. *Social Networks* (2013).

95. Klickstein, I., Shirin, A. & Sorrentino, F. Energy scaling of targeted optimal control of complex networks. *Nature communications* **8** (2017).

96. *Pajek's dataset available at* http://vlado.fmf.unilj.si/pub/networks/data.

97. Martinez, N. D. Artifacts or attributes? Effects of resolution on the Little Rock Lake food web. *Ecological Monographs* (1991).

98. Hall, S. & Raffaelli, D. Food-web patterns: lessons from a species-rich web. *The Journal of Animal Ecology* (1991).

99. *Data available at* https://research.mssm.edu/maayan/datasets/qualitative_networks.shtml.

100. *R. D. Christie. IEEE 118-bus system available at* https://www.ee.washington.edu/research/pstca/pf118/pg_tca118bus.htm.

101. Menck, P. J., Heitzig, J., Kurths, J. & Schellnhuber, H. J. How dead ends undermine power grid stability. *Nature communications* (2015).

102. Colizza, V., Pastor-Satorras, R. & Vespignani, A. Reaction–diffusion processes and metapopulation models in heterogeneous networks. *Nature Physics* (2007).

103. Yu, H. *et al.* Next-generation sequencing to generate interactome datasets. *Nature methods* (2011).

104. *CCSB dataset abailable at* http://interactome.dfci.harvard.edu/S_cerevisiae/index.php?page=download.

105. Yu, H. *et al.* High-quality binary protein interaction map of the yeast interactome network. *Science* (2008).

REFERENCES

106. Guimera, R., Danon, L., Diaz-Guilera, A., Giralt, F. & Arenas, A. Self-similar community structure in a network of human interactions. *Physical review E* (2003).

107. Gleiser, P. M. & Danon, L. Community structure in jazz. *Advances in complex systems* (2003).

108. Freeman, L. C., Webster, C. M. & Kirke, D. M. Exploring social structure using dynamic three-dimensional color images. *Social Networks* (1998).

109. Opsahl, T. & Panzarasa, P. Clustering in weighted networks. *Social networks* (2009).

110. Kirk, D. E. *Optimal control theory: an introduction* (Courier Corporation, 2012).

111. Rao, A. V. A survey of numerical methods for optimal control. *Advances in the Astronautical Sciences* **135,** 497–528 (2009).

112. Becerra, V. M. *Solving complex optimal control problems at no cost with PSOPT* in *Computer-Aided Control System Design (CACSD), 2010 IEEE International Symposium on* (2010), 1391–1396.

113. Wächter, A. & Biegler, L. T. On the implementation of an interior-point filter line-search algorithm for large-scale nonlinear programming. *Mathematical Programming* **106,** 25–57 (2006).

114. Ross, I. M. *A primer on Pontryagin's principle in optimal control* (Collegiate Publishers, 2015).

115. Dalla Man, C., Raimondo, D. M., Rizza, R. A. & Cobelli, C. *GIM, simulation software of meal glucose—insulin model* 2007.

116. Magni, L. *et al.* Model predictive control of glucose concentration in type I diabetic patients: An in silico trial. *Biomedical Signal Processing and Control* **4,** 338–346 (2009).

REFERENCES

117. Nimri, R. *et al.* MD-Logic overnight control for 6 weeks of home use in patients with type 1 diabetes: randomized crossover trial. *Diabetes Care,* DC_140835 (2014).

118. Capel, I. *et al.* Artificial pancreas using a personalized rule-based controller achieves overnight normoglycemia in patients with type 1 diabetes. *Diabetes technology & therapeutics* **16,** 172–179 (2014).

119. Mauseth, R. *et al.* Stress testing of an artificial pancreas system with pizza and exercise leads to improvements in the system's fuzzy logic controller. *Journal of diabetes science and technology* **9,** 1253–1259 (2015).

120. Reddy, M. *et al.* Feasibility study of a bio-inspired artificial pancreas in adults with type 1 diabetes. *Diabetes technology & therapeutics* **16,** 550–557 (2014).

121. Bruttomesso, D. *et al. Closed-loop artificial pancreas using subcutaneous glucose sensing and insulin delivery and a model predictive control algorithm: preliminary studies in Padova and Montpellier* 2009.

122. Bergman, R. N., Ider, Y. Z., Bowden, C. R. & Cobelli, C. Quantitative estimation of insulin sensitivity. *American Journal of Physiology-Endocrinology And Metabolism* **236,** E667 (1979).

123. Bergman, R. N., Phillips, L. S. & Cobelli, C. Physiologic evaluation of factors controlling glucose tolerance in man: measurement of insulin sensitivity and beta-cell glucose sensitivity from the response to intravenous glucose. *The Journal of clinical investigation* **68,** 1456–1467 (1981).

124. Bergman, R. N., Finegood, D. T. & Ader, M. Assessment of insulin sensitivity in vivo. *Endocrine reviews* **6,** 45–86 (1985).

125. McCrimmon, R. J. & Sherwin, R. S. Hypoglycemia in type 1 diabetes. *Diabetes* **59,** 2333–2339 (2010).

REFERENCES

126. Castle, J. R. *et al.* Novel use of glucagon in a closed-loop system for prevention of hypoglycemia in type 1 diabetes. *Diabetes care* **33,** 1282–1287 (2010).

127. Bátora, V. *et al. The contribution of glucagon in an artificial pancreas for people with type 1 diabetes* in *American Control Conference (ACC), 2015* (2015), 5097–5102.

128. El-Khatib, F. H., Jiang, J. & Damiano, E. R. Adaptive closed-loop control provides blood-glucose regulation using dual subcutaneous insulin and glucagon infusion in diabetic swine. *Journal of Diabetes Science and Technology* **1,** 181–192 (2007).

129. El-Khatib, F. H., Russell, S. J., Nathan, D. M., Sutherlin, R. G. & Damiano, E. R. A bihormonal closed-loop artificial pancreas for type 1 diabetes. *Science translational medicine* **2,** 27ra27–27ra27 (2010).

130. Russell, S. J. *et al.* Blood glucose control in type 1 diabetes with a bihormonal bionic endocrine pancreas. *Diabetes care,* DC_120071 (2012).

131. El-Khatib, F. H. *et al.* Autonomous and continuous adaptation of a bihormonal bionic pancreas in adults and adolescents with type 1 diabetes. *The Journal of Clinical Endocrinology & Metabolism* **99,** 1701–1711 (2014).

132. Russell, S. J. *et al.* Outpatient glycemic control with a bionic pancreas in type 1 diabetes. *New England Journal of Medicine* **371,** 313–325 (2014).

133. Russell, S. J. *et al.* Day and night glycaemic control with a bionic pancreas versus conventional insulin pump therapy in preadolescent children with type 1 diabetes: a randomised crossover trial. *The lancet Diabetes & endocrinology* **4,** 233–243 (2016).

134. El-Khatib, F. H. *et al.* Home use of a bihormonal bionic pancreas versus insulin pump therapy in adults with type 1 diabetes: a multicentre randomised crossover trial. *The Lancet* **389,** 369–380 (2017).

REFERENCES

135. Herrero, P., Bondia, J., Oliver, N. & Georgiou, P. A coordinated control strategy for insulin and glucagon delivery in type 1 diabetes. *Computer methods in biomechanics and biomedical engineering* **20,** 1474–1482 (2017).

136. Boiroux, D. *et al.* Adaptive model predictive control for a dual-hormone artificial pancreas. *Journal of Process Control* **68,** 105–117 (2018).

137. Shirin, A. *et al.* prediction of optimal Drug schedules for Controlling Autophagy. *Scientific reports* **9,** 1428 (2019).

138. Shirin, A., Klickstein, I. & Sorrentino, F. Optimal control of complex networks: Balancing accuracy and energy of the control action. *Chaos: An Interdisciplinary Journal of Nonlinear Science* **27,** 041103 (2017).

139. Kovatchev, B. P., Cox, D. J., Gonder-Frederick, L. A. & Clarke, W. Symmetrization of the blood glucose measurement scale and its applications. *Diabetes Care* **20,** 1655–1658 (1997).

140. Kovatchev, B. P., Clarke, W. L., Breton, M., Brayman, K. & McCall, A. Quantifying temporal glucose variability in diabetes via continuous glucose monitoring: mathematical methods and clinical application. *Diabetes technology & therapeutics* **7,** 849–862 (2005).

141. Control, D. & Group, C. T. R. The effect of intensive treatment of diabetes on the development and progression of long-term complications in insulin-dependent diabetes mellitus. *New England journal of medicine* **329,** 977–986 (1993).

142. Chachuat, B. *Nonlinear and dynamic optimization: From theory to practice* tech. rep. (2007).

143. *JDRF website: http://www.jdrf.org* 2018.

REFERENCES

144. Russell-Jones, D., Gall, M.-A., Niemeyer, M., Diamant, M. & Del Prato, S. Insulin degludec results in lower rates of nocturnal hypoglycaemia and fasting plasma glucose vs. insulin glargine: a meta-analysis of seven clinical trials. *Nutrition, Metabolism and Cardiovascular Diseases* **25,** 898–905 (2015).

145. *MiniMed 670G System User Guide website: https://www.medtronicdiabetes.com/sites/user-guides/MiniMed* 2018.

146. Lorenzi, M., Bohannon, N., Tsalikian, E. & Karam, J. H. Duration of type I diabetes affects glucagon and glucose responses to insulin-induced hypoglycemia. *Western Journal of Medicine* **141,** 467 (1984).

147. Cox, D. J. *et al.* Frequency of severe hypoglycemia in insulin-dependent diabetes mellitus can be predicted from self-monitoring blood glucose data. *The Journal of Clinical Endocrinology & Metabolism* **79,** 1659–1662 (1994).

148. Townsend, C., Seron, M. M. & Goodwin, G. C. Characterisation of optimal responses to pulse inputs in the Bergman minimal model. *IFAC-PapersOnLine* **50,** 15163–15168 (2017).

149. Townsend, C., Seron, M. M., Goodwin, G. C. & King, B. R. Control Limitations in Models of T1DM and the Robustness of Optimal Insulin Delivery. *Journal of diabetes science and technology* **12,** 926–936 (2018).

150. Townsend, C. & Seron, M. M. Optimality of unconstrained pulse inputs to the Bergman minimal model. *IEEE Control Systems Letters* **2,** 79–84 (2018).

151. Goodwin, G. C., Medioli, A. M., Carrasco, D. S., King, B. R. & Fu, Y. A fundamental control limitation for linear positive systems with application to Type 1 diabetes treatment. *Automatica* **55,** 73–77 (2015).

152. Goodwin, G. C., Carrasco, D. S., Seron, M. M. & Medioli, A. M. A fundamental control performance limit for a class of positive nonlinear systems. *Automatica* **95,** 14–22 (2018).

REFERENCES

153. Hajizadeh, I. *et al.* Incorporating Unannounced Meals and Exercise in Adaptive Learning of Personalized Models for Multivariable Artificial Pancreas Systems. *Journal of diabetes science and technology* **12,** 953–966 (2018).

154. Beneyto, A., Bertachi, A., Bondia, J. & Vehi, J. A New Blood Glucose Control Scheme for Unannounced Exercise in Type 1 Diabetic Subjects. *IEEE Transactions on Control Systems Technology* (2018).

155. Shirin, A., Della Rossa, F., Klickstein, I., Russell, J. & Sorrentino, F. Optimal regulation of blood glucose level in Type I diabetes using insulin and glucagon. *PloS one* **14,** e0213665 (2019).

156. Vogelstein, B. *et al.* Cancer genome landscapes. *Science* **339,** 1546–1558 (2013).

157. Rukhlenko, O. S. *et al.* Dissecting RAF inhibitor resistance by structure-based modeling reveals ways to overcome oncogenic RAS signaling. *Cell Systems* **7,** 161–179 (2018).

158. Ramos, P. & Bentires-Alj, M. Mechanism-based cancer therapy: resistance to therapy, therapy for resistance. *Oncogene* **34,** 3617–3626 (2015).

159. Kahn, B. B., Alquier, T., Carling, D. & Hardie, D. G. AMP-activated protein kinase: ancient energy gauge provides clues to modern understanding of metabolism. *Cell Metabolism* **1,** 15–25 (2005).

160. Löffler, A. S. *et al.* Ulk1-mediated phosphorylation of AMPK constitutes a negative regulatory feedback loop. *Autophagy* **7,** 696–706 (2011).

161. Zoncu, R., Efeyan, A. & Sabatini, D. M. mTOR: from growth signal integration to cancer, diabetes and ageing. *Nature Reviews Molecular Cell Biology* **12,** 21 (2011).

162. Nazio, F. *et al.* mTOR inhibits autophagy by controlling ULK1 ubiquitylation, self-association and function through AMBRA1 and TRAF6. *Nature Cell Biology* **15,** 406 (2013).

REFERENCES

163. Shang, L. *et al.* Nutrient starvation elicits an acute autophagic response mediated by Ulk1 dephosphorylation and its subsequent dissociation from AMPK. *Proceedings of the National Academy of Sciences* **108,** 4788–4793 (2011).

164. Dunlop, E. A., Hunt, D. K., Acosta-Jaquez, H. A., Fingar, D. C. & Tee, A. R. ULK1 inhibits mTORC1 signaling, promotes multisite Raptor phosphorylation and hinders substrate binding. *Autophagy* **7,** 737–747 (2011).

165. Kim, J., Kundu, M., Viollet, B. & Guan, K.-L. AMPK and mTOR regulate autophagy through direct phosphorylation of Ulk1. *Nature Cell Biology* **13,** 132 (2011).

166. Fimia, G. M. *et al.* Ambra1 regulates autophagy and development of the nervous system. *Nature* **447,** 1121 (2007).

167. Di Bartolomeo, S. *et al.* The dynamic interaction of AMBRA1 with the dynein motor complex regulates mammalian autophagy. *The Journal of Cell Biology* **191,** 155–168 (2010).

168. Galluzzi, L., Bravo-San Pedro, J. M., Levine, B., Green, D. R. & Kroemer, G. Pharmacological modulation of autophagy: therapeutic potential and persisting obstacles. *Nature Reviews Drug Discovery* **16,** 487–511 (2017).

169. Moschetta, M., Reale, A., Marasco, C., Vacca, A. & Carratù, M. R. Therapeutic targeting of the mTOR-signalling pathway in cancer: benefits and limitations. *British Journal Pharmacology* **171,** 3801–3813 (2014).

170. Hardie, D. G. AMPK: a target for drugs and natural products with effects on both diabetes and cancer. *Diabetes* **62,** 2164–2172 (2013).

171. Edwards, S. R. & Wandless, T. J. The rapamycin-binding domain of the protein kinase mammalian target of rapamycin is a destabilizing domain. *Journal of Biological Chemistry* **282,** 13395–13401 (2007).

REFERENCES

172. Egan, D. F. *et al.* Small molecule inhibition of the autophagy kinase ULK1 and identification of ULK1 substrates. *Molecular Cell* **59,** 285–297 (2015).

173. Meley, D. *et al.* AMP-activated protein kinase and the regulation of autophagic proteolysis. *Journal of Biological Chemistry* **281,** 34870–34879 (2006).

174. Ronan, B. *et al.* A highly potent and selective Vps34 inhibitor alters vesicle trafficking and autophagy. *Nature Chemical Biology* **10,** 1013 (2014).

175. Cameron, K. O. *et al.* Discovery and preclinical characterization of 6-chloro-5-[4-(1-hydroxycyclobutyl) phenyl]-1 H-indole-3-carboxylic Acid (PF-06409577), a direct activator of adenosine monophosphate-activated protein kinase (AMPK), for the potential treatment of diabetic nephropathy. *Journal of Medicinal Chemistry* **59,** 8068–8081 (2016).

176. Burger, M. T. *et al.* Identification of NVP-BKM120 as a potent, selective, orally bioavailable class I PI3 kinase inhibitor for treating cancer. *ACS Medicinal Chemistry Letters* **2,** 774–779 (2011).

177. Szymańska, P., Martin, K. R., MacKeigan, J. P., Hlavacek, W. S. & Lipniacki, T. Computational analysis of an autophagy/translation switch based on mutual inhibition of MTORC1 and ULK1. *PLoS One* **10,** e0116550 (2015).

178. Martin, K. R. *et al.* Computational model for autophagic vesicle dynamics in single cells. *Autophagy* **9,** 74–92 (2013).

179. Cornelius, S. P., Kath, W. L. & Motter, A. E. Realistic control of network dynamics. *Nature communications* **4** (2013).

180. Wang, L.-Z. *et al.* A geometrical approach to control and controllability of nonlinear dynamical networks. *Nature Communications* **7,** 11323 (2016).

181. Zañudo, J. G. T., Yang, G. & Albert, R. Structure-based control of complex networks with nonlinear dynamics. *Proceedings of the National Academy of Sciences* **114,** 7234–7239 (2017).

REFERENCES

182. Sato, E. *et al.* Temporal decline in sirolimus elimination immediately after pancreatic islet transplantation. *Drug Metabolism and Pharmacokinetics* **21,** 492–500 (2006).

183. Baselga, J. *et al.* Buparlisib plus fulvestrant versus placebo plus fulvestrant in postmenopausal, hormone receptor-positive, HER2-negative, advanced breast cancer (BELLE-2): a randomised, double-blind, placebo-controlled, phase 3 trial. *The Lancet Oncology* **18,** 904–916 (2017).

184. Milkiewicz, K. L. *et al.* Improvement in oral bioavailability of 2,4-diaminopyrimidine c-Met inhibitors by incorporation of a 3-amidobenzazepin-2-one group. *Bioorganic & Medicinal Chemistry* **19,** 6274–6284 (2011).

185. Engers, D. W., Frist, A. Y., Lindsley, C. W., Hong, C. C. & Hopkins, C. R. Synthesis and structure–activity relationships of a novel and selective bone morphogenetic protein receptor (BMP) inhibitor derived from the pyrazolo [1.5-a] pyrimidine scaffold of Dorsomorphin: the discovery of ML347 as an ALK2 versus ALK3 selective MLPCN probe. *Bioorganic & Medicinal Chemistry Letters* **23,** 3248–3252 (2013).

186. Juric, D. *et al.* A First-in-human, phase I, dose-escalation study of TAK-117, a selective PI3Kα isoform inhibitor, in patients with advanced solid malignancies. *Clinical Cancer Research* (2017).

187. Lewis, F. L., Vrabie, D. & Syrmos, V. L. *Optimal Control* (John Wiley & Sons, 2012).

188. Fey, D. *et al.* Signaling pathway models as biomarkers: Patient-specific simulations of JNK activity predict the survival of neuroblastoma patients. *Science Signal* **8,** ra130–ra130 (2015).

189. Fröhlich, F. *et al.* Efficient parameter estimation enables the prediction of drug response using a mechanistic pan-cancer pathway model. *Cell Systems* **7,** 1–13 (2018).

REFERENCES

190. Palmer, A. C. & Sorger, P. K. Combination cancer therapy can confer benefit via patient-to-patient variability without drug additivity or synergy. *Cell* **171,** 1678–1691 (2017).

191. Holbeck, S. L. *et al.* The National Cancer Institute ALMANAC: a comprehensive screening resource for the detection of anticancer drug pairs with enhanced therapeutic activity. *Cancer Research* **77,** 3564–3576 (2017).

192. Du Toit, A., Hofmeyr, J.-H. S., Gniadek, T. J. & Loos, B. Measuring autophagosome flux. *Autophagy* **14,** 1060–1071 (2018).

193. Martin, K. R. *et al.* A potent and selective ULK1 inhibitor suppresses autophagy and sensitizes cancer cells to nutrient stress. *iScience* **8,** 74–84 (2018).

194. Bago, R. *et al.* Characterization of VPS34-IN1, a selective inhibitor of Vps34, reveals that the phosphatidylinositol 3-phosphate-binding SGK3 protein kinase is a downstream target of class III phosphoinositide 3-kinase. *Biochemical Journal* **463,** 413–427 (2014).

195. Malanowski, K. & Maurer, H. Sensitivity analysis for state constrained optimal control problems. *Discrete & Continuous Dynamical Systems-A* **4,** 241–272 (1998).

196. Castillo, E., Mínguez, R. & Castillo, C. Sensitivity analysis in optimization and reliability problems. *Reliability Engineering & System Safety* **93,** 1788–1800 (2008).

197. Hagen, D. R., White, J. K. & Tidor, B. Convergence in parameters and predictions using computational experimental design. *Interface Focus* **3,** 20130008 (2013).

198. Dehghannasiri, R., Yoon, B.-J. & Dougherty, E. R. *Efficient experimental design for uncertainty reduction in gene regulatory networks* in *BMC Bioinformatics* **16** (2015), S2.

REFERENCES

199. Chmielecki, J. *et al.* Optimization of dosing for EGFR-mutant non-small lung cancer with evolutionary cancer modeling. *Science Translational Medicine* **3,** 90ra59 (2011).

200. Chakrabarti, S. & Michor, F. Pharmacokinetics and drug interactions determine optimum combination strategies in computational models of cancer evolution. *Cancer Research* **77,** 3908–3921 (2017).

201. Stein, S., Zhao, R., Haeno, H., Vivanco, I. & Michor, F. Mathematical modeling identifies optimum lapatinib dosing schedules for the treatment of glioblastoma patients. *PLoS Computational Biology* **14,** e1005924 (2018).

202. Qiao, J. *et al.* Allocating security resources to a water supply network. *IIE Transactions* **39,** 95–109 (2007).

203. Jeong, H. S. *et al.* in *Computing in Civil Engineering (2005)* 1–12 (2005).

204. Berry, J. W., Fleischer, L., Hart, W. E., Phillips, C. A. & Watson, J.-P. Sensor placement in municipal water networks. *Journal of Water Resources Planning and Management* **131,** 237–243 (2005).

205. Shuang, Q., Zhang, M. & Yuan, Y. Node vulnerability of water distribution networks under cascading failures. *Reliability Engineering & System Safety* **124,** 132–141 (2014).

206. Seok Jeong, H. & Abraham, D. M. Operational response model for physically attacked water networks using NSGA-II. *Journal of computing in civil engineering* **20,** 328–338 (2006).

207. Hansman, S. & Hunt, R. A taxonomy of network and computer attacks. *Computers & Security* **24,** 31–43 (2005).

208. Schneider, C. M., Moreira, A. A., Andrade, J. S., Havlin, S. & Herrmann, H. J. Mitigation of malicious attacks on networks. *Proceedings of the National Academy of Sciences* **108,** 3838–3841 (2011).

REFERENCES

209. Brumley, D. & Boneh, D. Remote timing attacks are practical. *Computer Networks* **48,** 701–716 (2005).

210. Hariri, S., Qu, G., Dharmagadda, T., Ramkishore, M. & Raghavendra, C. S. Impact analysis of faults and attacks in large-scale networks. *IEEE Security & Privacy* **99,** 49–54 (2003).

211. Moitra, S. D. & Konda, S. L. An empirical investigation of network attacks on computer systems. *Computers & Security* **23,** 43–51 (2004).

212. Buldyrev, S. V., Parshani, R., Paul, G., Stanley, H. E. & Havlin, S. Catastrophic cascade of failures in interdependent networks. *Nature* **464,** 1025 (2010).

213. Wang, S., Hong, L., Ouyang, M., Zhang, J. & Chen, X. Vulnerability analysis of interdependent infrastructure systems under edge attack strategies. *Safety science* **51,** 328–337 (2013).

214. Zhang, P. *et al.* The robustness of interdependent transportation networks under targeted attack. *EPL (Europhysics Letters)* **103,** 68005 (2013).

215. Chen, Z., Du, W.-B., Cao, X.-B. & Zhou, X.-L. Cascading failure of interdependent networks with different coupling preference under targeted attack. *Chaos, Solitons & Fractals* **80,** 7–12 (2015).

216. Huang, X., Gao, J., Buldyrev, S. V., Havlin, S. & Stanley, H. E. Robustness of interdependent networks under targeted attack. *Physical Review E* **83,** 065101 (2011).

217. Allen, E. H., Stuart, R. B. & Wiedman, T. E. No light in August: power system restoration following the 2003 North American blackout. *IEEE Power and Energy Magazine* **12,** 24–33 (2014).

218. Berizzi, A. *The italian 2003 blackout* in *IEEE Power Engineering Society General Meeting, 2004.* (2004), 1673–1679.

REFERENCES

219. Van der Vleuten, E. & Lagendijk, V. Transnational infrastructure vulnerability: The historical shaping of the 2006 European "Blackout". *Energy Policy* **38,** 2042–2052 (2010).

220. Romero, J. J. Blackouts illuminate India's power problems. *IEEE spectrum* **49** (2012).

221. Kovanen, T., Nuojua, V. & Lehto, M. *Cyber Threat Landscape in Energy Sector* in *ICCWS 2018 13th International Conference on Cyber Warfare and Security* (2018).

222. Liang, G., Weller, S. R., Zhao, J., Luo, F. & Dong, Z. Y. The 2015 ukraine blackout: Implications for false data injection attacks. *IEEE Transactions on Power Systems* **32,** 3317–3318 (2017).

223. Liu, S. & Cheng, B. Cyberattacks: Why, what, who, and how. *IT professional* **11** (2009).

224. Obama, B. Taking the cyberattack threat seriously. *Wall Street Journal* **19** (2012).

225. Tootaghaj, D. Z. *et al.* Mitigation and Recovery from Cascading Failures in Interdependent Networks under Uncertainty. *IEEE Transactions on Control of Network Systems* (2018).

226. Xypolytou, E., Zseby, T., Fabini, J. & Gawlik, W. *Detection and mitigation of cascading failures in interconnected power systems* in *2017 IEEE PES Innovative Smart Grid Technologies Conference Europe (ISGT-Europe)* (2017), 1–6.

227. Rahnamay-Naeini, M., Wang, Z., Ghani, N., Mammoli, A. & Hayat, M. M. Stochastic analysis of cascading-failure dynamics in power grids. *IEEE Transactions on Power Systems* **29,** 1767–1779 (2014).

REFERENCES

228. Motter, A. E. & Lai, Y.-C. Cascade-based attacks on complex networks. *Physical Review E* **66,** 065102 (Dec. 2002).

229. Crucitti, P., Latora, V. & Marchiori, M. Model for cascading failures in complex networks. *Physical Review E* **69,** 045104 (2004).

230. Crucitti, P., Latora, V. & Marchiori, M. A topological analysis of the Italian electric power grid. *Physica A: Statistical mechanics and its applications* **338,** 92–97 (2004).

231. Van Cutsem, T. & Vournas, C. *Voltage stability of electric power systems* (Springer Science & Business Media, 2007).

232. Rohden, M., Jung, D., Tamrakar, S. & Kettemann, S. Cascading failures in ac electricity grids. *Physical Review E* **94,** 032209 (2016).

233. Schäfer, B., Witthaut, D., Timme, M. & Latora, V. Author Correction: Dynamically induced cascading failures in power grids. *Nat Commun* (2018).

234. Dabrowski, A., Ullrich, J. & Weippl, E. R. Grid shock: coordinated load-changing attacks on power grids. *system* **28,** 64 (2017).

235. Amini, S., Pasqualetti, F. & Mohsenian-Rad, H. *Detecting dynamic load altering attacks: A data-driven time-frequency analysis* in *2015 IEEE International Conference on Smart Grid Communications (SmartGridComm)* (2015), 503–508.

236. Kafle, I. *et al.* Optimal control of networks in the presence of attackers and defenders. *Chaos: An Interdisciplinary Journal of Nonlinear Science* **28,** 051103 (2018).

237. Parandehgheibi, M., Modiano, E. & Hay, D. *Mitigating cascading failures in interdependent power grids and communication networks* in *2014 IEEE International Conference on Smart Grid Communications (SmartGridComm)* (2014), 242–247.

REFERENCES

238. Liao, W., Salinas, S., Li, M., Li, P. & Loparo, K. A. Cascading failure attacks in the power system: a stochastic game perspective. *IEEE Internet of Things Journal* **4,** 2247–2259 (2017).

239. Amini, S., Pasqualetti, F. & Mohsenian-Rad, H. Dynamic load altering attacks against power system stability: Attack models and protection schemes. *IEEE Transactions on Smart Grid* (2016).

240. Soltan, S., Mazauric, D. & Zussman, G. Analysis of failures in power grids. *IEEE Transactions on Control of Network Systems* **4,** 288–300 (2017).

241. Korkali, M., Veneman, J. G., Tivnan, B. F., Bagrow, J. P. & Hines, P. D. Reducing cascading failure risk by increasing infrastructure network interdependence. *Scientific reports* **7,** 44499 (2017).

242. *The Epsilon Group* Available from https://tegvirginia.com/software/t1dms/. 2018.

243. *The implementation of the UVA/Pavoda model (1014) in this paper* Available from https://github.com/iklick/dallaman_2014. 2019.

244. Man, C. D. *Parameters* private communication by email. 2018.

245. Chylek, L. A. *et al.* Rule-based modeling: a computational approach for studying biomolecular site dynamics in cell signaling systems. *Wiley Interdisciplinary Reviews in Systems Biology and Medicine* **6,** 13–36 (2014).

246. Faeder, J. R., Blinov, M. L. & Hlavacek, W. S. Rule-based modeling of biochemical systems with BioNetGen. *Methods in Molecular Biology* **500,** 113–167 (2009).

Appendices

REFERENCES

Appendix A

Detailed Derivation of Target Control Strategy

A.1 Minimum Energy Output Control

The fixed-end point minimum energy control problem is well-known in the optimal control field, especially for a system described by linear dynamics,

$$
\dot{\mathbf{x}}(t) = A\mathbf{x}(t) + B\mathbf{u}(t)
$$

$$
\mathbf{y}(t) = C\mathbf{x}(t).
$$

(A.1)

What is less well known is the solution of the minimum energy control problem when the final condition is only prescribed to some subset of the states. We introduce the minimum energy target control problem for networks where the word *target* refers

Appendix A. Detailed Derivation of Target Control Strategy

to those nodes with a prescribed final condition. The problem is as follows:

$$\min_{\mathbf{u}(t)} \quad J = \frac{1}{2} \int_{t_0}^{t_f} \mathbf{u}^T(t)\mathbf{u}(t)dt$$

$$\dot{\mathbf{x}}(t) = A\mathbf{x}(t) + B\mathbf{u}(t)$$

$$\mathbf{y}(t) = C\mathbf{x}(t) \tag{A.2}$$

$$\mathbf{x}(t_0) = \mathbf{x}_0, \quad \mathbf{y}(t_f) = \mathbf{y}_f$$

The matrix $A \in \mathbb{R}^{n \times n}$ is the adjacency matrix that describes the topology, or inter-connectedness, of the n nodes, or states. The matrix $B \in \mathbb{R}^{n \times m}$ is the control input matrix that describes how the m control inputs are distributed to the nodes. The matrix $C \in \mathbb{R}^{p \times n}$ is the output matrix that relates how each output is a linear combination of the states. For the target control of complex networks formulation, we assume that B (C) has columns (rows) that are all versors, i.e., each control input, $u_i(t)$, $i = 1, \ldots, m$, is directed towards a single node and each output, $y_j(t)$, $j = 1, \ldots, p$, is the state of a single node (see Fig. 1A from the main manuscript for a graphical description). The dynamical equation of an arbitrary node i is,

$$\dot{x}_i = \sum_{j=1}^{n} a_{ij}x_j + \sum_{k=1}^{m} b_{ik}u_k \tag{A.3}$$

where if there exists at least one coefficient $b_{ik} \neq 0$ then node i is what we refer to as an *input node*. We will assume that the system, (A, B, C), is output controllable so that,

$$\text{rank}\left(CB|CAB|\ldots|CA^{n-1}B\right) = p \tag{A.4}$$

Each output is referred to as a targeted node. The solution of the minimization problem in Eq. (A.2) is found using Pontryagin's minimum principle [110] and is

Appendix A. Detailed Derivation of Target Control Strategy

provided here both as a review and to establish how the targeting aspect of our specific solution is applied. The Hamiltonian equation introduces n costates $\boldsymbol{\nu}(t)$.

$$\mathcal{H}(\mathbf{x}(t), \boldsymbol{\nu}(t), \mathbf{u}(t)) = \frac{1}{2}\mathbf{u}^T(t)\mathbf{u}(t) + \boldsymbol{\nu}^T(t)A\mathbf{x}(t) + \boldsymbol{\nu}^T(t)B\boldsymbol{u}(t) \tag{A.5}$$

From the Hamiltonian equation, the following dynamical relations can be determined,

$$\text{State Equation:} \qquad \dot{\mathbf{x}}(t) = \frac{\partial \mathcal{H}}{\partial \boldsymbol{\nu}} = A\mathbf{x}(t) + B\mathbf{u}(t)$$

$$\text{Costate Equation:} \qquad \dot{\boldsymbol{\nu}}(t) = -\frac{\partial \mathcal{H}}{\partial \mathbf{x}} = -A^T\mathbf{x}(t) \tag{A.6}$$

$$\text{Stationary Equation:} \quad \mathbf{0} = \frac{\partial \mathcal{H}}{\partial \mathbf{u}} = \mathbf{u}(t) + B^T\boldsymbol{\nu}.$$

The stationary equation is used to determine the optimal control input.

$$\mathbf{u}^*(t) = -B^T\boldsymbol{\nu} \tag{A.7}$$

The time evolution of the costates can be determined in a straightforward manner with a final condition of the form, $\boldsymbol{\nu}(t_f) = C^T\hat{\boldsymbol{\nu}}_f$, where $\hat{\boldsymbol{\nu}}_f \in \mathbb{R}^p$ as there are only p final conditions prescribed for the network.

$$\boldsymbol{\nu}(t) = e^{A^T(t_f-t)}C^T\hat{\boldsymbol{\nu}}_f \tag{A.8}$$

With the optimal control input known, the time evolution of the states can also be determined,

$$\mathbf{x}(t) = e^{A(t-t_0)}\mathbf{x}_0 - \int_{t_0}^{t_f} e^{A(t-\tau)}BB^T e^{A^T(t_f-\tau)}d\tau C^T\hat{\boldsymbol{\nu}}_f \tag{A.9}$$

Appendix A. Detailed Derivation of Target Control Strategy

The prescribed final condition for the targeted nodes is applied to determine the final, constant vector $\hat{\boldsymbol{\nu}}_f$.

$$\mathbf{y}_f = Ce^{A(t_f-t_0)}\mathbf{x}_0 - CWC^T\boldsymbol{\nu}_f \quad \Rightarrow \quad \hat{\boldsymbol{\xi}}_f = -\left(CWC^T\right)^{-1}\left(\mathbf{y}_f - Ce^{A(t_f-t_0)}\mathbf{x}_0\right) \quad \text{(A.10)}$$

The symmetric, positive semi-definite matrix $W = \int_{t_0}^{t_f} e^{A(t_f-\tau)}BB^T e^{A^T(t_f-\tau)}d\tau$ is the controllability Gramian. If the system (A, B, C) is output controllable, then W is positive definite. When C has p rows (versors), the matrix $W_p = CWC^T$, is the output controllability Gramian, and is a $p \times p$ principal submatrix of W.

A.2 Scaling of μ_1

54 of the main text provide numerical evidence that the energy required for a control action decreases exponentially as the number of target nodes decreases linearly. In the following derivation, we find that the exponential decay of the energy is a result of a more fundamental property of the output controllability Gramians W_p. Here we show that for a broad class of networks and a random selection of the target nodes the ratio of the smallest eigenvalues of two subsequent principal submatrices of the controllability Gramian W, by which we mean the submatrices W_p and W_{p-1} where W_{p-1} is W_p after removing one additional row-column pair, has a near constant value which we call $\eta_p = \min\{\text{eig}(W_{p-1})\}/\min\{\text{eig}(W_p)\} \approx constant$. This is true for a *typical* sequence of random removals of target nodes (here by typical we mean that each node is assigned the same probability of removal and the order of removal is random), while deviations from this behavior are possible for specific removal strategies (see Section S6).

In the main text we have considered the average energy scaling when the cardinality of the target set decreases from j to k, $j > k$. Here, we consider an iterative

Appendix A. Detailed Derivation of Target Control Strategy

process as we remove one node at a time from the target set. We say that two target node sets $\mathcal{P}_p$ and $\mathcal{P}_{p+1}$ are adjacent if $\mathcal{P}_{p+1} = \mathcal{P}_p \cup i$ and $i \notin \mathcal{P}_p$.

A symmetric, positive definite matrix $W \in \mathbb{R}^{n \times n}$ has principal submatrices $W_p \in \mathbb{R}^{p \times p}$, $p < n$ where $n - p$ corresponding rows and columns of W have been removed. A principal submatrix, W_p, has diagonal elements which are also diagonal elements of the original matrix W. The eigenvalues of W_p, $\mu_i^{(p)}$, $i = 1, \ldots, p$, are ordered such that,

$$0 < \mu_1^{(p)} \leq \mu_2^{(p)} \leq \ldots \leq \mu_p^{(p)} \tag{A.11}$$

Consider the case when W_p is W_{p+1} with one additional row-column pair removed, or in terms of the target sets, $\mathcal{P}_p \subset \mathcal{P}_{p+1}$ which are adjacent. From Cauchy's interlacing theorem, the eigenvalues of W_p thread between the eigenvalues of W_{p+1},

$$\mu_1^{(p+1)} \leq \mu_1^{(p)} \leq \mu_2^{(p+1)} \leq \ldots \leq \mu_p^{(p+1)} \leq \mu_p^{(p)} \leq \mu_{p+1}^{(p+1)} \tag{A.12}$$

The smallest eigenvalue of W_p cannot be smaller than the smallest eigenvalue of W_{p+1}. We perform an iterative process where at each step a row-column pair (without loss of generality here chosen to be the first row and first column) is removed.

$$W_{p+1} = \bar{W}_p + dW_p$$

$$= \begin{bmatrix} 0 & \mathbf{0}^T \\ \mathbf{w}_p & W_p \end{bmatrix} + \begin{bmatrix} w_{pp} & \mathbf{w}_p^T \\ \mathbf{0} & O_p \end{bmatrix} \tag{A.13}$$

The matrix $\bar{W}_p$ is a $p \times p$ principal submatrix of W_{p+1} with a first row of all zeros and a first column identical to that of W_{p+1}. The matrix dW_p consists of all zeros except for the first row which is identical to the first row of W_{p+1}. The scalar w_{pp} is the

Appendix A. Detailed Derivation of Target Control Strategy

leading term in W_{p+1} and $\mathbf{w}_p$ is the first column of W_{p+1}, after removing the entry w_{pp}. Note that the the set of eigenvalues of $\bar{W}_p$ is equal to the set of eigenvalues of W_p with one additional 0 eigenvalue.

The smallest eigenvalue of W_{p+1}, $\mu_1^{(p+1)}$, and the second smallest eigenvalue of $\bar{W}_p$, $\mu_1^{(p)}$ (which is also the smallest eigenvalue of W_p) are used to define the vectors $\mathbf{v}_{p+1}$ and $\bar{\mathbf{v}}_p$,

$$\mathbf{v}_{p+1}^T W_{p+1} = \mathbf{v}_{p+1}^T \mu_1^{(p+1)}, \quad \bar{W}_p \bar{\mathbf{v}}_p = \mu_1^{(p)} \bar{\mathbf{v}}_p \tag{A.14}$$

Pre- and post-multiplying Eq. (A.13) by $\mathbf{v}_{p+1}^T$ and $\bar{\mathbf{v}}_p$, respectively, will provide a relation between the smallest eigenvalues of W_{p+1} and W_p.

$$\mathbf{v}_{p+1}^T W_{p+1} \bar{\mathbf{v}}_p = \mathbf{v}_{p+1}^T \bar{W}_p \bar{\mathbf{v}}_p + \mathbf{v}_{p+1}^T dW_p \bar{\mathbf{v}}_p^T$$

$$\mu_1^{(p+1)} \mathbf{v}_{p+1}^T \bar{\mathbf{v}}_p = \mu_1^{(p)} \mathbf{v}_{p+1}^T \bar{\mathbf{v}}_p + \mathbf{v}_{p+1}^T W_{p+1} W_{p+1}^{-1} dW_p \bar{\mathbf{v}}_p \tag{A.15}$$

$$\mu_1^{(p+1)} = \mu_1^{(p)} + \mu_1^{(p+1)} \frac{\mathbf{v}_{p+1}^T W_{p+1}^{-1} dW_p \bar{\mathbf{v}}_p}{\mathbf{v}_{p+1}^T \bar{\mathbf{v}}_p}$$

The matrix product $W_{p+1} dW_p$ is a matrix of all zeros except for the leading term which is one. Thus, the product $\mathbf{v}_{p+1}^T W_{p+1}^{-1} dW_p \bar{\mathbf{v}}_p = [\mathbf{v}_{p+1}]_1 [\bar{\mathbf{v}}_p]_1$ where the notation $[\mathbf{v}]_1$ denotes the first value of a vector. The relation between successive smallest eigenvalues can be written explicitly,

$$\mu_1^{(p)} = \mu_1^{(p+1)} \left(1 - \frac{[\mathbf{v}_{p+1}]_1 [\bar{\mathbf{v}}]_1}{\mathbf{v}_{p+1}^T \bar{\mathbf{v}}_p} \right) = \mu_1^{(p+1)} \eta_p \tag{A.16}$$

We use the definition of the 'worst-case' energy, $E_{\max}^{(p)} = \mu_1^{(p)}$ to rewrite Eq. (A.16) in terms of energy,

Appendix A. Detailed Derivation of Target Control Strategy

$$E_{\max}^{(p+1)} = E_{\max}^{(p)} \eta_p \;\;\Rightarrow\;\; \frac{E_{\max}^{(p+1)}}{E_{\max}^{(p)}} = \eta_p \geq 1 \;\;\Rightarrow\;\; \log E_{\max}^{(p+1)} - \log E_{\max}^{(p)} = \log \eta_p \geq 0$$

$$(A.17)$$

The last of Eq. (A.17) can be written in terms of any two target sets of size k and j, $k < j$ and $\mathcal{P}_k \subset \mathcal{P}_j$,

$$\log E_{\max}^{(j)} - \log E_{\max}^{(k)} = \sum_{i=k}^{j-1} \log \eta_i \tag{A.18}$$

We define $\bar{\eta}_{(k \to j)}$, which depends only on the two sets of target nodes $\mathcal{P}_k$ and $\mathcal{P}_j$, as,

$$\log\left(\bar{\eta}_{(k \to j)}^{j-k}\right) = (j-k)\log \bar{\eta}_{(k \to j)} = \sum_{i=k}^{j-1} \log \eta_i \tag{A.19}$$

In general, there are $\frac{n!}{j!(n-j)!}\frac{j!}{k!(j-k)!} = \frac{n!}{k!(n-j)!(j-k)!}$ possible choices of the sets $\mathcal{P}_k \subset \mathcal{P}_j$ from the n nodes in the network. In the main text, we focus on the specific case when $k = n/10$ and $j = n$ which we use to approximate η,

$$\log E_{\max}^{(n)} - \log E_{\max}^{(n/10)} = \left(n - \frac{n}{10}\right) \log \bar{\eta}_{(\frac{n}{10} \to n)} \tag{A.20}$$

Note that for this specific choice of j and k, there are $\frac{n!}{\frac{n}{10}!(n-\frac{n}{10})!}$ choices of end point target sets, or in other words, values of $\log \bar{\eta}_{(\frac{n}{10} \to n)}$. We define η by computing the average of $\log \bar{\eta}_{(\frac{n}{10} \to n)}$,

$$\eta \equiv n \left\langle \log \bar{\eta}_{(\frac{n}{10} \to n)} \right\rangle, \tag{A.21}$$

173

Appendix A. Detailed Derivation of Target Control Strategy

where $\langle \cdot \rangle$ is the mean over all possible values. We show in the main text through both model and real network examples that η provides an approximation for $E_{\max}^{(p)}$ such that $\frac{n}{10} \leq p \leq n$, so that we can rewrite Eq. (A.20) as,

$$
\begin{aligned}
\left\langle \log E_{\max}^{(p)} \right\rangle &= \left\langle \log E_{\max}^{(n/10)} \right\rangle + \frac{p - n/10}{n} \eta \\
&= \frac{p}{n} \eta + \left(\left\langle \log E_{\max}^{(n/10)} \right\rangle - \frac{1}{10} \eta \right)
\end{aligned}
\tag{A.22}
$$

$$
\left\langle \log E_{\max}^{(p)} \right\rangle \sim \frac{p}{n} \eta
$$

In Figs. 2, 3 and 4 of the main text, the linear model in the last of Eq. (A.22) is shown to provide a good approximation of $\log E_{\max}^{(p)}$. In Fig. A.1, from Eqs. (A.18) and (A.19) we set $k = p_{\min} = n/10$, or 10% of the nodes in the network, and let $j = p_{\max}$ increase from 30% to 90%, to show how the standard deviation of $\log \bar{\eta}_{(p_{\min} \to p_{\max})}$ (that is of the $\log E_{\max}^{(p_{\max})}$, see Eq. (A.18)) decreases as we increase the cardinality of the target sets. As we consider more values of η_i corresponding to larger values of $p_{\max}$, the peak of the PDF grows, meaning the variation of values of $\log E_{\max}^{(p_{\max})}$ decreases. As we demonstrate the variation of $\log \bar{\eta}_{p_{\min} \to p_{\max}}$ becomes small when $p_{\max} - p_{\min}$ increases, we can rewrite Eq. (A.19) as approximately

$$
(p_{\max} - p_{\min}) \log \bar{\eta}_{p_{\min} \to p_{\max}} \approx (p_{\max} - p_{\min}) \langle \log \eta_i \rangle
\tag{A.23}
$$

where $i = p_{\min}, \ldots, p_{\max}$. It is seen through experiments that $\langle \log \eta_i \rangle$ is independent of the target set size (a generic example is shown in Fig. A.2) and can be computed for a given network. We stress that while we have not proven η_i is independent of the target node set cardinality i, we have provided ample numerical evidence through the exponential scaling as seen in Figs. 2, 3, and 4 in the main text that η_i is invariant. The network parameter η can be approximated simply as,

$$
\eta \approx n \langle \eta_i \rangle
\tag{A.24}
$$

Appendix A. Detailed Derivation of Target Control Strategy

as η_i can be approximated as being constant. In Fig. A.2 we show an example of when η_i is approximately constant and how η, the energy scaling value, can be closely approximated by assuming η_i is constant. The decrease of the standard deviation for each distribution is shown with respect to $p_{\max}$ in the inset.
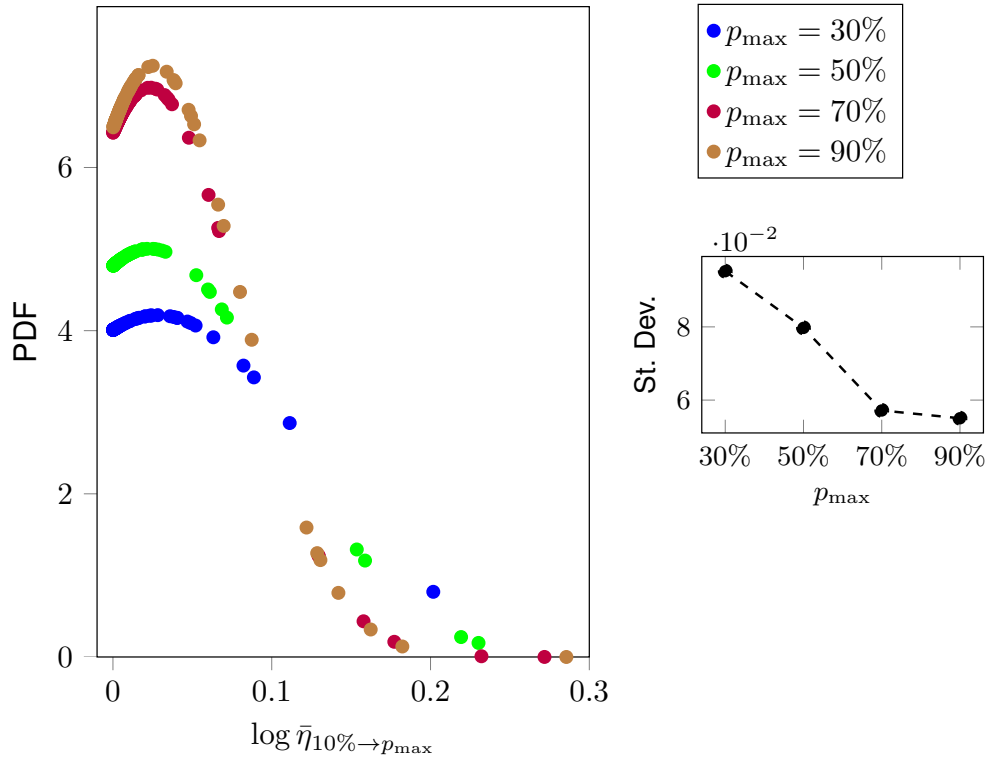
Figure A.1: **Computing η for different values of $p_{\min}$ and $p_{\max}$.** From the Methods section we see that η may be computed from one target set size to another (which we call $p_{\min}$ and $p_{\max}$). To ensure that we compute a value of η that describes the entire network, we keep $p_{\min} = 10\%$ and compute values of $\log \bar{\eta}_{p_{\min} \to p_{\max}}$ for larger values of $p_{\max}$. We see that the distributions as $p_{\max}$ increases becomes 'sharper', i.e., that the standard deviation decreases, which is shown in the inset plot. After $p_{\max}$ grows larger than 70%, we see that the improvement of the computed $\log \bar{\eta}_{p_{\min} \to p_{\max}}$ slows down so that we do not need to compute η_i for many additional points.
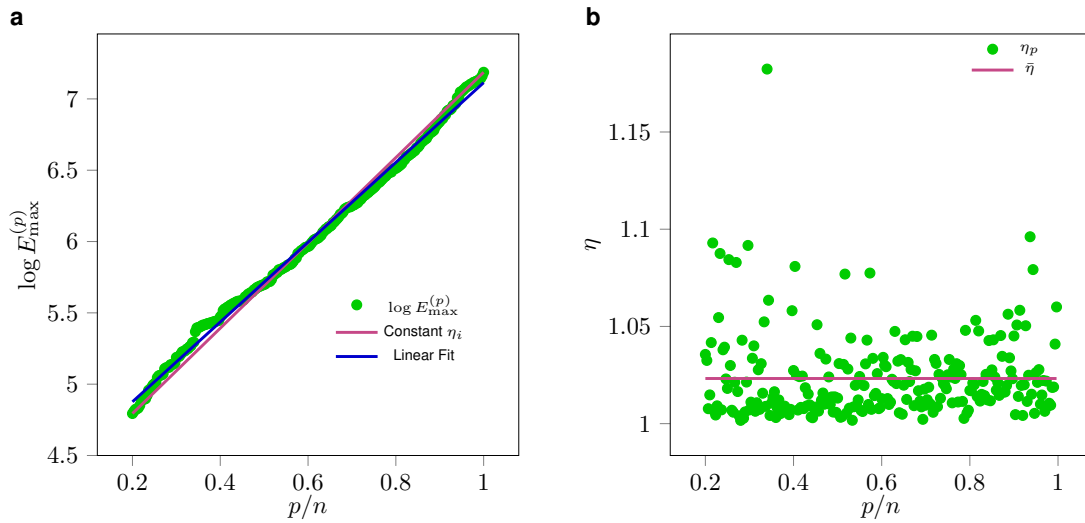
Figure A.2: **The ratio of maximum energies is approximately constant.** For a network, we compute each value of η iteratively as the cardinality of the target set is reduced from n to 1. In panel A, we plot the individual values of $\log E_{\max}^{(p)}$ as p is varied and compare the trend to a line with the slope of η if each value of η_i is assumed constant and a linear fit for the values of $\log E_{\max}^{(p)}$. We see good agreement between the two methods. In panel B, we plot the individual values of $\eta_i = E_{\max}^{(p+1)}/E_{\max}^{(p)}$. The deviation around the mean is fairly small.

Appendix B

Detailed Derivation of Balance Control Strategy

B.1   Minimum Balance Control

In our optimal balanced control problem, we attempt to minimize the following cost function,

$$
\begin{aligned}
\min_{\mathbf{u}(t)} J = {} & \frac{1-\alpha}{2} [\left(\mathbf{y}(t_f) - \mathbf{y}_f\right)^T \left(\mathbf{y}(t_f) - \mathbf{y}_f\right)] \\
& + \frac{\alpha}{2} \int_{t_0}^{t_f} \mathbf{u}(t)^T \mathbf{u}(t) dt
\end{aligned}
\tag{B.1}
$$

subject to the constraints,

$$
\begin{aligned}
\dot{\mathbf{x}}(t) &= A\mathbf{x}(t) + B\mathbf{u}(t) \\
\mathbf{y}(t) &= C\mathbf{x}(t), \quad \mathbf{x}(t_0) = \mathbf{x}_0
\end{aligned}
\tag{B.2}
$$

Here the final constraints are in the objective function and we call these constraints *soft constraints* as we do not require them to be satisfied exactly. Note that if we set $C = I_n$, where I_n is the $n \times n$ identity matrix, then $\mathbf{y}(t) = \mathbf{x}(t)$. The vector $\mathbf{y}_f$ is the

Appendix B. Detailed Derivation of Balance Control Strategy

prescribed final output state of the nodes described by the matrix C. Here $\alpha \in (0,1)$ is a scaling parameter by which we can penalize the two performance measures in the cost function in (B.1) to balance the control energy. Note that in the case in which $\alpha = 1$, the cost function in Eq. (B.1) becomes the cost function associated with the optimal output cost control problem in Eq. (2.3), where different from Eq. (B.1), the final desired state is imposed on as a *hard constraint*.

The solution of the optimization problem in Eq. (B.1) is obtained using Pontryagin's maximum principle [110] (See sections 5.1 and 5.2 in the book [110]). The Hamiltonian equation introduces n costates $\boldsymbol{\nu}(t)$,

$$\mathcal{H}(\mathbf{x}(t), \boldsymbol{\nu}(t), \mathbf{u}(t)) = \frac{\alpha}{2}\mathbf{u}^T(t)\mathbf{u}(t) + \boldsymbol{\nu}^T(t)A\mathbf{x}(t) + \boldsymbol{\nu}^T(t)B\boldsymbol{u}(t) \tag{B.3}$$

From the Hamiltonian equation, the following dynamical relations can be determined,

$$\text{State Equation:} \qquad \dot{\mathbf{x}}(t) = \frac{\partial \mathcal{H}}{\partial \boldsymbol{\nu}} = A\mathbf{x}(t) + B\mathbf{u}(t)$$

$$\text{Costate Equation:} \qquad \dot{\boldsymbol{\nu}}(t) = -\frac{\partial \mathcal{H}}{\partial \mathbf{x}} = -A^T\boldsymbol{\nu}(t) \tag{B.4}$$

$$\text{Stationary Equation:} \quad \mathbf{0} = \frac{\partial \mathcal{H}}{\partial \mathbf{u}} = \alpha\mathbf{u}(t) + B^T\boldsymbol{\nu}.$$

The stationary equation is used to determine the optimal control input.

$$\mathbf{u}^*(t) = -\frac{1}{\alpha}B^T\boldsymbol{\nu} \tag{B.5}$$

The time evolution of the costates can be determined with a final condition of the form, $\boldsymbol{\nu}(t_f) = (1-\alpha)C^T\bar{\boldsymbol{\nu}}$, where $\bar{\boldsymbol{\nu}} = \mathbf{y}(t_f) - \mathbf{y}_f$,

$$\boldsymbol{\nu}(t) = e^{A^T(t_f-t)}\boldsymbol{\nu}(t_f) = (1-\alpha)e^{A^T(t_f-t)}C^T\bar{\boldsymbol{\nu}} \tag{B.6}$$

where $\bar{\boldsymbol{\nu}}$ will be determined from the final output state. With the optimal control input known, the time evolution of the states can also be determined,

$$\begin{aligned}\mathbf{x}(t) = {} & e^{A(t-t_0)}\mathbf{x}_0 \\ & -\frac{1-\alpha}{\alpha}\int_{t_0}^t e^{A(t-\tau)}BB^Te^{A^T(t_f-\tau)}d\tau C^T\bar{\boldsymbol{\nu}}\end{aligned} \tag{B.7}$$

Appendix B. Detailed Derivation of Balance Control Strategy

The final state of the targeted nodes can be determined,

$$\mathbf{y}(t_f) = Ce^{A(t_f-t_0)}\mathbf{x}_0 - \frac{1-\alpha}{\alpha}CWC^T\bar{\boldsymbol{\nu}} \tag{B.8}$$

Here $W = \int_{t_0}^{t_f} e^{A(t_f-\tau)}BB^T e^{A^T(t_f-\tau)}d\tau$ is the controllability Gramian. When C is defined as above, i.e., its rows are linearly independent versors, the *reduced Gramian* W_p is a p-dimensional principal submatrix of W, i.e., we write $W_p = CWC^T$. The p dimensional vector $\bar{\boldsymbol{\nu}}$ can be determined in a straightforward manner,

$$\begin{aligned}
\bar{\boldsymbol{\nu}} &= \frac{\alpha}{1-\alpha}\left(\frac{\alpha}{1-\alpha}I_p + W_p\right)^{-1} \\
&\times \left(Ce^{A(t_f-t_0)}\mathbf{x}_0 - \mathbf{y}_f\right) = \frac{\alpha}{1-\alpha}U_p^{-1}\boldsymbol{\beta}
\end{aligned} \tag{B.9}$$

where $\boldsymbol{\beta} = \left(Ce^{A(t_f-t_0)}\mathbf{x}_0 - \mathbf{y}_f\right)$ and $U_p = \left(\frac{\alpha}{1-\alpha}I_p + W_p\right)$. For $0 < \alpha < 1$, the $p \times p$ matrix U_p is always symmetric, positive definite matrix and invertible. In fact, the matrix W_p is positive semidefinite and the eigenvalues of U_p are the same as the eigenvalues of W_p plus the positive quantity $\frac{\alpha}{1-\alpha}$. Moreover the eigenvectors of the matrices U_p and W_p are the same. From Eq. (B.5)-(B.9) , the optimal control input signal when the final condition is in the objective function is equal to,

$$\mathbf{u}^*(t) = -B^T e^{A^T(t_f-t)}C^T U_p^{-1}\boldsymbol{\beta} \tag{B.10}$$

The equation for the time evolution of the outputs is equal to,

$$\mathbf{y}(t) = Ce^{A(t-t_0)}\mathbf{x}_0 + C\int_{t_0}^{t} e^{A(t-\tau)}B\mathbf{u}^*(\tau)d\tau \tag{B.11}$$

B.1.1   Versor

A *versor* is a direction vector of unit length whose only nonzero element is 1. The nonzero element in a versor indicates the direction of an axis in Cartesian coordinate system. In linear algebra, the set of linearly independent versors are called the

standard basis. For instance, versors in the direction of the x, y, and z axes of a three three dimensional Cartesin coordinate system are,

$$\hat{\mathbf{i}} = \begin{bmatrix} 1 \\ 0 \\ 0 \end{bmatrix}, \hat{\mathbf{j}} = \begin{bmatrix} 0 \\ 1 \\ 0 \end{bmatrix}, \hat{\mathbf{k}} = \begin{bmatrix} 0 \\ 0 \\ 1 \end{bmatrix} \tag{B.12}$$

.

Appendix C

Glucose-Insulin-Glucagon Model and Parameters for Type I Diabetes

C.1 GIG Model and Parameters

C.1.1 Overview of GIG Model with Type I Diabetics

We consider the model in [58, 59] which is a system of nonlinear differential equations (ODEs). In all equations, t is the physical time (in min), all subscripts b denotes basal state, and all of the parameters are given in the table C.1. The system of nonlinear differential equations are given below:

Appendix C. Glucose-Insulin-Glucagon Model and Parameters for Type I Diabetes

Glucose Subsystem:

$$\dot{G}_p(t) = EGP(t) + Ra(t) - U_{ii} - E(t) - k_1 G_p(t) + k_2 G_t(t), \quad G_p(0) = G_{pb}$$

(C.1a)

$$\dot{G}_t(t) = -U_{id}(t) + k_1 G_p(t) - k_2 G_t(t), \qquad\qquad\qquad G_t(0) = G_{tb}$$

(C.1b)

$$G(t) = \frac{G_p}{V_G}, \qquad\qquad\qquad\qquad\qquad\qquad G(0) = G_b$$

(C.1c)

Here G_p (in mg/kg) is the mass of plasma glucose; G_t (in mg/kg) is the mass of tissue glucose; G (in mg/dL) is plasma glucose concentration and V_g (in dL/kg) is the distribution volume of glucose; EGP is the endogenous glucose production (in mg/kg/min); Ra (in mg/kg/min) is the rate of glucose appearance in plasma; U_{ii} (in mg/kg/min) and U_{id} (in mg/kg/min) are insulin-independent and insulin-dependent glucose utilizations, respectively. Also k_1 and k_2 are the parameters.

Insulin Subsystem:

$$\dot{I}_p(t) = -(m_2 + m_4)I_p(t) + m_1 I_l(t) + R_{ia}(t), \qquad I_p(0) = I_{pb} \qquad \text{(C.2a)}$$

$$\dot{I}_l(t) = -(m_1 + m_3)I_l(t) + m_2 I_p(t), \qquad\qquad I_l(0) = I_{lb} \qquad \text{(C.2b)}$$

$$I(t) = \frac{I_p(t)}{V_I}, \qquad\qquad\qquad\qquad\qquad I(0) = I_b \qquad \text{(C.2c)}$$

Here I_l (in pmol/kg) is the mass of liver insulin; I_p (in pmol/kg) is the mass of tissue insulin; I (in pmol/L) is the plasma insulin concentration; V_I (in L/kg) is the distribution volume of insulin; R_{ia} (in pmol/kg/min) is the rate of appearance of insulin in plasma; m_1, m_2, m_3 and m_4 are the parameters.

Appendix C. Glucose-Insulin-Glucagon Model and Parameters for Type I Diabetes

Glucose rate of appearance:

$$Q_{sto}(t) = Q_{sto1}(t) + Q_{sto2}(t), \qquad\qquad G_{sto}(0) = 0 \qquad \text{(C.3a)}$$

$$\dot{Q}_{sto1}(t) = -k_{gri}Q_{sto1}(t) + D\delta(t - \tau_D), \qquad\qquad Q_{sto1}(0) = 0 \qquad \text{(C.3b)}$$

$$\dot{Q}_{sto2}(t) = -k_{empt}(Q_{sto})(t)Q_{sto2}(t) + k_{gri}Q_{sto1}(t), \qquad Q_{sto2}(0) = 0 \qquad \text{(C.3c)}$$

$$\dot{Q}_{gut}(t) = -k_{abs}Q_{gut}(t) + k_{empt}Q_{sto}(t)Q_{sto2}(t), \qquad Q_{gut}(0) = 0 \qquad \text{(C.3d)}$$

$$Ra(t) = \frac{f.k_{abs}.Q_{gut}(t)}{BW}, \qquad\qquad Ra(0) = 0 \qquad \text{(C.3e)}$$

$$k_{empt}(Q_{sto}) = k_{min} + \frac{k_{max} - k_{min}}{2}. \qquad\qquad \text{(C.3f)}$$

$$\{\tanh[\alpha(Q_{sto} - b.D)] - \tanh[\beta(Q_{sto} - c.D)] + 2\} \qquad\qquad \text{(C.3g)}$$

Here Q_{sto} (in mg) is the amount of glucose in the stomach, Q_{sto1} (in mg) is the amount of liquid glucose in the stomach, Q_{sto2} (in mg) is the amount of solid glucose in the stomach, Q_{gut} (in mg) is the glucose mass in the intestine; D (in mg) is the amount of ingested glucose at time τ_D; BW (in kg) is body weight; k_{empt} is the rate constant of the gastric emptying; K_{gri}, k_{abs}, k_{max}, k_{min}, f, α, β are the parameters.

Endogenous glucose production:

$$EGP(t) = k_{p1} - k_{p2}G_p(t) - k_{p3}X^L(t) + \xi X^H(t), \quad EGP(0) = EGP_b \quad \text{(C.4a)}$$

$$\dot{I}'(t) = -k_i\left[I'(t) - I(t)\right], \qquad\qquad I'(0) = I_b \qquad \text{(C.4b)}$$

$$\dot{X}^L(t) = -k_i\left[X^L(t) - I'(t)\right], \qquad\qquad X^L(0) = I_b \qquad \text{(C.4c)}$$

$$\dot{X}^H(t) = -k_H X^H(t) + k_H \times \max\left[H(t) - H_b, 0\right], \quad X^H(0) = 0 \quad \text{(C.4d)}$$

Here X^L (in) is delayed insulin action on EGP; X^H is delayed glucagon action on EGP; I' is delayed insulin in compartment 1; k_{p1}, k_{p2}, k_{p3}, ξ, k_i, k_H are the parameters.

Appendix C. Glucose-Insulin-Glucagon Model and Parameters for Type I Diabetes

Glucose utilization:

$$U_{ii}(t) = F_{cns} \tag{C.5a}$$

$$U_{id}(t) = \frac{[V_{m0} + V_{mx}.X(t)]G_t(t)}{K_{m0} + G_t(t)} \tag{C.5b}$$

$$\dot{X}(t) = -p_{2U}X(t) + p_{2U}[I(t) - I_b], \qquad\qquad X(0) = 0 \tag{C.5c}$$

Here U_{ii} (in mg/kg/min) and U_{id} (in mg/kg/min) are insulin-independent and insulin-dependent glucose utilization; X (in pmol/L) is insulin in interstitial fluid; F_{cns}, V_{m0}, K_{m0}, p_{2U} are the parameters.

Renal excretion:

$$E(t) = \begin{cases} k_{e1}[G_p(t) - k_{e2}] & \text{if } G_p(t) > k_{e2} \\ 0 & \text{if } G_p(t) \leq k_{e2} \end{cases} \tag{C.6}$$

Here $E(t)$ (in mg/kg/min) is the glucose renal exertion; k_{e1} is the parameter.

Glucagon kinetics and secretion:

$$\dot{H}(t) = -nH(t) + SR_H(t) + Ra_H(t), \qquad\qquad H(0) = H_b \tag{C.7a}$$

$$SR_H(t) = SR_H^s(t) + SR_H^d(t), \tag{C.7b}$$

$$\dot{SR}_H^s(t) = -\rho\left[SR_H^s(t) - \max\left(\frac{\sigma[G_{th} - G(t)]}{\max(I(t) - I_{th}, 0) + 1} + SR_H^b, 0\right)\right], \quad SR_H^s(0) = nH_b \tag{C.7c}$$

$$SR_H^d(t) = \delta \max\left(-\frac{dG(t)}{dt}, 0\right) \tag{C.7d}$$

Here H (in ng/L) is the concentration of plasma glucagon; SR_H (in ng/L/min) is the glucagon secretion; Ra_H (in ng/L/min) is the rate of appearance of glucagon in plasma; SR_H^s (in ng/L/min) and SR_H^d (in ng/L/min) is the static and dynamic components of glucagon, respectively; n, ρ, I_{th}, δ are the parameters.

Appendix C. Glucose-Insulin-Glucagon Model and Parameters for Type I Diabetes

Subcutaneous insulin kinetics:

$$R_{ia}(t) = k_{a1}I_{sc1}(t) + k_{a2}I_{sc2}(t) \tag{C.8a}$$

$$\dot{I}_{sc1}(t) = -(k_d + k_{a1})I_{sc1}(t) + IIR(t), \qquad I_{sc1}(0) = I_{sc1ss} \tag{C.8b}$$

$$\dot{I}_{sc2}(t) = k_d.I_{sc1}(t) - k_{a2}I_{sc2}(t), \qquad I_{sc2}(0) = I_{sc2ss} \tag{C.8c}$$

$$IIR(t) = IIR_b + \frac{u_I(t)}{BW} \tag{C.8d}$$

Here R_{ia} (in pmol/kg/min) is the rate of appearance of insulin in plasma; I_{sc1} (in pmol/kg) is the amount of nonmonomeric insulin in the subcutaneous space; I_{sc2} is the amount of monomeric insulin in the subcutaneous space; $IIR(t)$ is the insulin infusion rate where IIR_b is the basal infusion rate (in pmol/kg/min) from body and u_I (in pmol/min) is the external insulin infusion rate; k_{a1}, k_{a2}, k_d are the parameters. As the exogenous insulin infusion rate appears in the above equation in pmol/kg/min, we divide u_I by the body weight BW in the equation. Note that here the u_I is in pmol/min. To convert the unit of insulin infusion rate u_I from U/min to pmol/min, we multiply u_I by 6944.4, that is the unit conversion is 1 U/min = 6944.4 pmol/min.

Subcutaneous glucagon kinetics:

$$\dot{H}_{sc1}(t) = -(k_{h1} + k_{h2})H_{sc1}(t) + GIR(t), \qquad H_{sc1}(0) = H_{sc1ss} \tag{C.9a}$$

$$\dot{H}_{sc2}(t) = k_{h1}H_{sc1}(t) - k_{h3}H_{sc2}(t), \qquad H_{sc2}(0) = H_{sc2ss} \tag{C.9b}$$

$$Ra_H(t) = k_{h3}H_{sc2}(t) \tag{C.9c}$$

$$GIR(t) = GIR_b + \frac{u_G(t)}{BV} \tag{C.9d}$$

Here H_{sc1} (in ng/L) and H_{sc2} (in ng/L) are the glucagon concentration in the subcutaneous space; IGR is the glucagon infusion rate where GIR_b is the basal glucagon infusion rate (in ng/L/min) from the body and u_I is the external glucagon infusion rate (in ng/min);k_{h1}, k_{h2}, k_{h3} are the parameters. As the exogenous glucagon infusion rate appears in the above equation in ng/L/min, we divide u_G by the body volume BV in the equation. Note that here the u_G is in ng/min. To convert the

unit of glucagon infusion rate from mg/min to ng/min, we multiply u_G by 10^6, that is the unit conversion is 1 mg/min $= 10^6$ ng/min.

We write the ODEs in Eqs. (C.1)-(C.9) in the form $\dot{\mathbf{x}}(t) = \mathbf{f}(\mathbf{x}(t), \mathbf{u}(t), \Theta_{Gb})$ where $\mathbf{x} \in \mathbb{R}^{17}$ and t is the physical time (in min). The variable x_1 represents G_p, the mass of glucose in plasma; the variable x_2 represents G_t, the mass of glucose in tissue; the variable x_3 represents the mass of liver insulin I_l; the variable x_4 represents the mass of plasma insulin I_p; the variable x_5 represents the amount of delayed insulin I' in compartment 1; the variable x_6 represents the amount of delayed insulin X^L action on EGP; the variable x_7 represents the amount of solid glucose Q_{sto1} in the stomach; the variable x_8 represents the amount of liquid glucose Q_{sto2} in the stomach; the variable x_9 represents the glucose mass Q_{gut} in the intestine; the variable x_{10} represents the amount of interstitial fluid X; the variable x_{11} represents the amount of static glucagon SR_H^s; the variable x_{12} represents the amount of plasma glucagon H; the variable x_{13} represents the amount of delayed glucagon X^H action on EGP; the variable x_{14} represents the amount of nonmonomeric insulin I_{sc1}; in the subcutaneous space; the variable x_{15} represents the amount of monomeric insulin I_{sc2} in the subcutaneous space; the variable x_{16} represents the amount of subcutaneous glucagon H_{sc1} in the subcutaneous space; the variable x_{17} represents the amount of subcutaneous glucagon H_{sc2} in the subcutaneous space. Also $\mathbf{u}(t) = [u_I(t) \quad u_G(t)]^T$, where u_I is the external insulin and u_G is the external glucagon. We define Θ_{G_b} as the set of parameters for which the basal glucose level is G_b.

C.1.2   Parameters

There are a total of 46 parameters in Eqs. (C.1)-(C.9). The parameters are not given in [58]. We set all the parameters for 'Glucose subsystem', 'Insulin subsystem', 'Glucose rate of appearance', 'Endogenous glucose production', 'Glucose utilization',

Appendix C. Glucose-Insulin-Glucagon Model and Parameters for Type I Diabetes

'Glucose utilization', 'Renal excretion', 'Subcutaneous insulin kinetics' from the references [57, 115], except k_{p1}, V_{m0} and HE_b. According to [115], the parameters are chosen to satisfy the steady-state constraints in type I diabetes. The parameters k_{p1} and V_{m0} are set so that the steady state solutions provide the basal Glucose level G_b and $EGP_b = 2.4$. In Type I diabetes, the endogenous glucose production is high [115], so we choose $EGP_b = 2.4$ mg/kg/min. We set $IIR_b = 0$ and $GIR_b = 0$ as the model we consider is for Type I diabetes. The commercial version of the UVA/Pavoda simulator [242] allows computing blood glucose responses to supplied dosages of insulin for some patients, but does not provide all of the parameters. We tune the parameter HE_b so that the blood glucose response to insulin of the *patient* we consider in this paper is qualitatively similar to the blood glucose response to insulin of a patient from the software [242] (adultaverage.mat). All of the parameters we use are listed in the Table C.1 for reproducibility of the results. Our implementation of the model [58] has been published in GitHub [243].

The equations for k_{p1} and V_{m0} are given below:

$$k_{p1} = EGP_b + k_{p2}G_{pb} + k_{p3}I_b \tag{C.10a}$$

$$V_{m0} = \frac{(EGP_b - F_{cns})(K_{m0} + G_{tb})}{G_{tb}} \tag{C.10b}$$

The basal steady states are given below:

$$G_{pb} = G_b.V_g \tag{C.11a}$$

$$G_{tb} = \frac{F_{cns} - EGP_b + k_1 G_{pb}}{k_2} \tag{C.11b}$$

$$I_{lb} = I_{pb}.\frac{m_2}{m_1 + m_3} \tag{C.11c}$$

$$I_{pb} = \frac{IIR_b}{m_2 + m_4 - \frac{m_1 m_2}{m_1 + m_3}} \tag{C.11d}$$

$$I_{sc1ss} = \frac{IIR_b}{k_d + k_{a1}} \tag{C.11e}$$

$$I_{sc2ss} = \frac{k_d}{k_{a2}} I_{sc1ss} \tag{C.11f}$$

$$SR_{Hb}^s = nH_b \tag{C.11g}$$

$$H_{sc1ss} = \frac{GIR_b}{k_{h1} + k_{h2}} \tag{C.11h}$$

$$H_{sc2ss} = \frac{k_{h1}}{k_{h3}} H_{sc1ss} \tag{C.11i}$$

Here, the basal values G_b (in mg/dL), IIR_b (in pmol/kg/min) and GIR_b (in ng/L/min) are settable by the user.

C.2 Continuous Approximation of Non-differential Function in ODEs

The optimization algorithms implemented in $\mathcal{PSOPT}$ require the derivatives of the function $\mathbf{f}(\mathbf{x}(t), \mathbf{u}(t), \Theta_{G_b})$ exists. We notice that there are discontinuities in Eqs. (C.1)-(C.9).

The smooth approximation of the Renal exertion function $E(t)$ in Eq. (C.6) by using

a Heaviside function is,

$$E(t) = k_{e1}(G_p(t) - k_{e2}) \times \mathcal{H}(G_p(t), k_{e2}, k), \tag{C.12}$$

where,

$$\mathcal{H}(G_p(t), k_{e2}, k) = \frac{1}{1 + e^{-k(G_p - k_{e2})}}, k \in \mathbb{Z}. \tag{C.13}$$

Here a larger k corresponds to a sharper transition around $G_p(t) = k_{e2}$.

We define a continuous approximation of the Dirac delta function $\delta(t - \tau_D)$ in Eq. (C.3c),

$$\delta(t - \tau_D) = \frac{d}{dt}\mathcal{H}(t, \tau_D, k), \tag{C.14}$$

where $\mathcal{H}(t, \tau_D, k) = \frac{1}{1 + e^{-k(t - \tau_D)}}, k \in \mathbb{Z}$. Here a larger k corresponds to a sharper transition at $t = \tau_D$.

We also define continuous approximation of the max(.) function, e.g. in Eq. (C.4d), as

$$\max(H(t) - H_b, 0) = (H(t) - H_b) \times \mathcal{H}(H(t), H_b, k), \tag{C.15}$$

where $\mathcal{H}(H(t), H_b, k) = \frac{1}{1 + e^{-k(H - H_b)}}, k \in \mathbb{Z}$. Here a larger k corresponds to a sharper transition at $H(t) = H_b$. In all our approximation we set $k = 4$.

Appendix C. Glucose-Insulin-Glucagon Model and Parameters for Type I Diabetes

Table C.1: Average parameters

Parameter	Type I Value	Unit
BW	78 [57]	Kg
BV	78 [57]	L
V_g	1.49 [57]	dL/kg
k_1	0.065 [57, 115]	min^{-1}
k_2	0.079 [57, 115]	min^{-1}
V_I	0.04 [57]	L/kg
m_1	0.379 [57]	min^{-1}
m_2	0.673 [57]	min^{-1}
m_4	0.269 [57]	min^{-1}
m_5	0.0526 [57]	min.kg/pmol
m_6	0.8118 [57]	dimensionless
HE_b	0.112[57]	dimensionless
k_{p1}	change Eq. (C.10)	mg/kg/min
k_{p2}	0.0021 [57, 115]	min^{-1}
k_{p3}	0.009 [57, 115]	mg/kg/min per pmol/L
k_{p4}	0.0786 [57]	mg/kg/min per pmol/L
k_i	0.0066 [57]	min^{-1}
$k_{\max}$	0.0465 [57]	min^{-1}
$k_{\min}$	0.0076 [57]	min^{-1}
k_{abs}	0.023 [57]	min^{-1}
k_{gri}	0.0465 [57]	min^{-1}
f	0.9 [57]	dimensionless
a	0.00016 [57]	mg^{-1}
b	0.68 [57]	dimensionless
c	0.00023 [57]	mg^{-1}
d	0.009 [57]	dimensionless
F_{cns}	1 [57]	mg/kg/min
V_{m0}	changes (Eq. (C.10)	mg/kg/min
V_{mx}	0.034 [57]	mg/kg/min per pmol/L
K_{m0}	4661.21	mg/kg
P_{2u}	0.084 [57]	min^{-1}
k_{e1}	0.0007 [57]	min^{-1}
k_{e2}	269 [57]	mg/kg
k_d	0.0164 [115]	min^{-1}
k_{a1}	0.0018 [115]	min^{-1}
k_{a2}	0.0182 [115]	min^{-1}
δ	0.682 [58]	(ng/L per mg/dL)
σ	1.093 [58]	min^{-1}
n	0.15 [58]	min^{-1}
ζ	0.009 [58]	(mg/kg/min per ng/L)
ρ	0.57 [58]	(ng/L/min per mg/dL)
k_H	0.16 [58]	min^{-1}

Appendix C.   Glucose-Insulin-Glucagon Model and Parameters for Type I Diabetes

Table C.2: Basal values

Basal	Type I Value	Unit
X_b^H	0 [244]	pmol/L
EGP_b	2.4 [115]	mg/kg/min
H_b	93 [244]	ng/L
IIR_b	0 [115]	pmol/kg/min

Appendix D

Supplementary information for Chapter 6

D.1   Formulation of the Model

Formulation of Eq. (6.1) was guided by the models of Szymańska et al.[177] (Ref. 33 in the main text) and Martin et al.[178] (Ref. 34 in the main text) mainly as follows. The model of Eq. (6.1) was formulated and parameterized so as to allow the model to predict oscillatory induction of autophagy in response to intermediate drug, energy, and nutrient stress inputs (as illustrated in Figs. 6.2 and 6.3), in accord with the predictions of the model of Szymańska et al.[177]. Moreover, as in both models considered by Martin et al.[178], Eq. (6.1) takes AVs to be turned over constitutively via a pseudo first-order degredative process. Another factor that drove model formulation and parameterization was the availability of measured AV dynamics induced by MTORC1 inhibition[178]. Eq. (6.1) was parameterized so as to reproduce the essential aspects of these dynamics (see below for more discussion).

Equation (6.1) differs from the earlier models of Szymańska et al.[177] and Martin

et al.[178] mainly as follows. In the model of Szymańska et al.[177], the regulatory influences depicted in Fig. 6.1 (e.g., mutual inhibition of MTORC1 and ULK1 and negative feedback from ULK1 to AMPK) are not explicitly represented, as is the case in the model of Eq. (6.1), where regulatory influences on enzymatic activities are represented explicitly using Hill functions. Rather, in the model of Szymańska et al.[177], regulatory influences emerge from formal representations of the biomolecular interactions considered in the model, which are termed rules[245]. In other words, Eq. (6.1) provides a model of regulatory influences and their effects, whereas the model of Szymańska et al.[177] provides a model of biomolecular interactions and their effects, which include emergent regulatory influences. The rules of the model of Szymańska et al.[177] can be processed automatically by the BioNetGen software package[246] to obtain a system of 173 coupled ordinary differential equations (ODEs). These equations account for various complexes (e.g., a complex of AMPK and ULK1 that is generated when AMPK docks to a particular site in ULK1) and protein phosphoforms. In contrast, the model of Eq. (6.1) does not track these details. Rather, it simply tracks the activities of AMPK, MTORC1, and ULK1 (and also the activity of VPS34, which was not considered by Szymańska et al.[177]). In the model of Szymańska et al.[177], AMPK, MTORC1, and ULK1 each has numerous states. In contrast, in the model of Eq. (6.1), these protein states are reduced to just two for each protein: active or inactive.

Although the model of Szymańska et al.[177] provides a mechanistically detailed representation of biomolecular interactions, it does not include a representation of autophagic vesicle (AV) population dynamics. To include a representation of AV population dynamics in Eq. (6.1), we started with the simple representation of AV production and clearance used in the AV population dynamics model of Martin et al.[178]:

$$\frac{dV}{dt} = P^* - cV,$$

where V is cellular AV count, P^* is a condition-dependent zero-order rate constant for AV production, and c is a pseudo first-order rate constant for clearance of AVs. In our model, we modified this equation by allowing the production rate to be time dependent. In Eq. (6.1) the rate of AV production is a linear function of VPS34 activity, $x_4(t)$. In other words, the rate of AV production is given by $k_3 x_4(t)$ (vs. a constant, P^*).

Parameter settings are summarized in Tables D.1 and D.1. These settings are not uniquely determined by data; they were guided by the considerations explained below.

Parameter settings for parameters in the h and H Hill functions were determined first, as follows. For each Hill function, we initially set $r_b = 0$, $r_m = 1$, $\theta = 0.5$, and $n = 2$. (We omit indices in referring to these parameters for convenience.) We then varied parameter values (by hand tuning) to obtain qualitative behavior consistent with that predicted by the model of Szymańska et al.[177]. The behaviors of the two models are compared directly in Fig. D.1. In panels A and B of Fig. D.1, AV count (x_5) and ULK1 activity (x_2) are shown, respectively, as a function of time. Initially, in these plots, we consider a nutrient/energy replete condition ($C_{\text{En}} = C_{\text{Nu}} = 1$) without rapamycin (or any other drug). A low dose of rapamycin is added at time $t = 100$ min and then a high dose of rapamycin is added at time $t = 200$ min. As can be seen, x_5 (Fig. D.1A) and x_2 (Fig. D.1B) initially have steady low values. After the initial introduction of rapamycin, these quantities begin to oscillate. After the second addition of rapamycin, the two quantities have steady high values. This behavior is qualitatively the same as the behavior predicted by the model of Szymańska et al.[177] (Fig. D.1C). It should be noted that the study of Szymańska et al.[177] did not establish that the AMPK-MTORC1-ULK1 network actually exhibits oscillatory behavior; this study only showed that oscillatory behavior is a possible consequence of known regulatory mechanisms. By requiring Eq. (6.1) to reproduce the qualitative

nonlinear dynamics of the model of Szymańska et al.[177], we made the optimal control problem considered here more of a challenging test of our methodology.

Next, parameter settings for the rate constants k_1, k_2, k_3 and k_4 were determined (again through hand tuning). In the study of Martin et al.[178], AV population dynamics were monitored after cells in a nutrient/energy replete condition were treated with a dose of rapamycin or AZD8055 (a catalytic MTOR inhibitor) sufficient to fully inhibit MTORC1 activity. We selected values for the rate constants that allow the model of Eq. (6.1) to roughly reproduce the observed dynamics induced by MTORC1 inhibition in the study of Martin et al.[178]. The behaviors predicted by Eq. (6.1) and the model of Martin et al.[178] are directly compared in panels D and E of Fig. D.1. The AV population dynamics model of Martin et al.[178] can be written as follows: $dV/dt = (1+k\delta)P - cV$, where $\delta = 0$ indicates a 0 dose of MTORC1 inhibitor, $\delta = 1$ indicates a saturating dose of MTORC1 inhibitor, P is the baseline rate of AV production, and $(1 + k)P$ is the induced rate of AV production stimulated by a saturating dose of MTORC1 inhibitor. By varying δ from 0 to 1, we obtain the plots shown in Fig. D.1E. Note that AV dynamics at intermediate values for δ are not oscillatory, as we would expect from the analysis of Szymańska et al.[177]. In contrast, Eq. (6.1) does predict oscillatory AV dynamics at intermediate doses of MTORC1 inhibitor (Fig. D.1D). Importantly, as desired, Eq. (6.1) makes predictions that are in qualitative agreement with the model of Martin et al.[178], in that both models predict that AV dynamics stimulated by MTORC1 inhibitor treatment unfold on a similar timescale and that the maximal range of regulation is similar. In Fig. D.2, we directly compare the AV dynamics predicted by Eq. (6.1) with AV dynamics measured by Martin et al.[178]. As can be seen, Eq. (6.1) is roughly consistent with the data.

Finally, parameter settings for the drug clearance rate constants in Eq. (6.1) $(\delta_1, \ldots, \delta_6)$ were set in accordance with measured drug lifetimes reported in the

literature, which have half-lives ranging from approximately 1 to 40 h. See Table D.2 and references cited therein. With this approach, the different drugs considered have different pharmacokinetics, arguably making the optimal control problem more realistic.

D.2   Pseudo-Spectral Optimal Control

We present here a brief overview of the theory of pseudo-spectral optimal control (PSOC) in the point of view of controlling of autophagy discussed in chapter 6.

General Problem

The OCP in Eqs. (6.5)–(6.6) in can be written as a general OPC,

$$
\begin{aligned}
\min_{\mathbf{u}(t)} \quad & J(\mathbf{x}(t), \mathbf{u}(t), t) = E\left(\mathbf{x}(t_0), \mathbf{x}(t_f), t_0, t_f\right) + \int_{t_0}^{t_f} F\left(\mathbf{x}(t), \mathbf{u}(t), t\right) dt \\
\text{s.t.} \quad & \dot{\mathbf{x}}(t) = \mathbf{f}(\mathbf{x}(t), \mathbf{u}(t), t) \\
& \mathbf{e}^L \leq \mathbf{e}(\mathbf{x}(t_0), \mathbf{x}(t_f), t_0, t_f) \leq \mathbf{e}^U \\
& \mathbf{h}^L \leq \mathbf{h}(\mathbf{x}(t), \mathbf{u}(t), t) \leq \mathbf{h}^U \\
& t \in [t_0, t_f]
\end{aligned}
\tag{D.1}
$$

The objective function (or cost function) $J(\mathbf{x}, \mathbf{u}, t)$ is composed of two parts, (i) $E : \mathbb{R}^n \times \mathbb{R}^n \times \mathbb{R} \times \mathbb{R} \mapsto \mathbb{R}$ which is a cost associated with the endpoint behavior of the system $\mathbf{x}(t_0)$ and $\mathbf{x}(t_f)$, and (ii) $F : \mathbb{R}^n \times \mathbb{R}^m \times \mathbb{R} \mapsto \mathbb{R}$ which is a running cost over the entire time interval $[t_0, t_f]$. The system dynamics is described by the function $\mathbf{f} : \mathbb{R}^n \times \mathbb{R}^m \times \mathbb{R} \mapsto \mathbb{R}^n$. Constraints on the endpoints ($\mathbf{x}(t_0)$ and/or $\mathbf{x}(t_f)$) are described by $\mathbf{e} : \mathbb{R}^n \times \mathbb{R}^n \times \mathbb{R} \times \mathbb{R} \mapsto \mathbb{R}^e$. While we only specify initial conditions, more complicated relations between the endpoints of the states can be specified as

well. Finally, path constraints, such as bounds on the states or control inputs, are described by $\mathbf{h} : \mathbb{R}^n \times \mathbb{R}^n \times \mathbb{R} \mapsto \mathbb{R}^h$.

Notation for Therapies

Let $\mathcal{D} = \{1, 2, 3, 4, 5, 6\}$ denote the possible drugs we may use (described in the main text) and $\mathcal{T}_k \subseteq \mathcal{D}$ denote the drugs chosen for our therapy such that $|\mathcal{T}_k| = k$. Let $\mathbf{w}(t) \in \mathbb{R}^k$ denote the drug concentrations and $\mathbf{u}(t) \in \mathbb{R}^k$ denote the drug injection rates for *only those drugs chosen to be in the therapy*. For example, if we consider the dual therapy $\mathcal{T}_2 = \{3, 6\}$, then

$$\mathbf{w}(t) = \begin{bmatrix} w_3(t) \\ w_6(t) \end{bmatrix}, \quad \mathbf{u}(t) = \begin{bmatrix} u_3(t) \\ u_6(t) \end{bmatrix} \tag{D.2}$$

Those drugs not chosen to be in $\mathcal{T}_k$ are denoted $\mathcal{D} \backslash \mathcal{T}_k$. In the example where $\mathcal{T}_k = \{3, 6\}$, those drugs not used are $\mathcal{D} \backslash \mathcal{T}_k = \{1, 2, 4, 5\}$. If a drug $i \in \mathcal{D} \backslash \mathcal{T}$ then we set $w_i(t) = 0$ for all time t.

The drug concentrations appear in the dynamical equations as inhibitory Hill functions $H(w_i(t))$.

$$H(w_i(t)) = r_{m,i} - (r_{m,i} - r_{b,i}) \frac{w_i^{n_i}(t)}{w_i^{n_i}(t) + \theta^{n_i}} \tag{D.3}$$

Note that if $i \notin \mathcal{T}_k$, then, as stated previously, $w_i(t) = 0$, and so, by Eq. (D.3), $H(w_i(t)) = 1$ for all time t.

The Minimum Drug OCP

In the main text, we present a *multi-phase optimal control problem*, i.e., two optimal control problems linked together by enforcing continuity at their interface. Despite this added complexity, we can develop a set of necessary conditions for each phase

individually and so for now we focus on the single phase problem. We will return to the multi-phase problem in the next section that covers the discretization procedure.

Either phase of the OCP presented in the main text can be mapped to the general formulation presented in Eq. (D.1) with the following definitions.

- The state variables $\mathbf{x}(t) = \begin{bmatrix} x_1(t) & x_2(t) & x_3(t) & x_4(t) & x_5(t) & \mathbf{w}^T(t) \end{bmatrix}^T \in \mathbb{R}^{5+k}$ and the control input $\mathbf{u}(t) \in \mathbb{R}^k$ so that $n = 5 + k$ and $m = k$.

- The cost function $J = \int_{t_0}^{t_f} u_i(t)dt$ (see Eq. (6.5) in the main text) so that, from Eq. (D.1), $E \equiv 0$ and $F = \sum_{i \in \mathcal{T}} u_i(t)$.

- The system dynamics, as presented in Eq. (6.1), are rewritten here,

$$
\dot{\mathbf{x}}(t) = \begin{bmatrix} \dot{x}_1(t) \\ \dot{x}_2(t) \\ \dot{x}_3(t) \\ \dot{x}_4(t) \\ \dot{x}_5(t) \\ \dot{\mathbf{w}}(t) \end{bmatrix} = \mathbf{f}(\mathbf{x}(t), \mathbf{u}(t)) = \bar{\mathbf{f}}(\mathbf{x}(t)) + B\mathbf{u}(t)
$$

$$
= \begin{bmatrix} (1 - x_1)C_{\mathrm{Nu}}H(w_1)H(w_2) - x_1 h_{12}(x_2)h_{13}(x_3) \\ (1 - x_2)h_{23}(x_3)H(w_3) - x_2 h_{21}(x_1) \\ (1 - x_3)k_1 H(w_4) - C_{\mathrm{En}}x_2 x_3 H(w_5) \\ (1 - x_4)h_{42}(x_2)H(w_2)H(w_6) - k_2 x_4 \\ k_3 x_4 - k_4 x_5 \\ -\Delta\mathbf{w}(t) \end{bmatrix} + \begin{bmatrix} \mathbf{0}_k^T \\ \mathbf{0}_k^T \\ \mathbf{0}_k^T \\ \mathbf{0}_k^T \\ \mathbf{0}_k^T \\ I_k \end{bmatrix} \mathbf{u}(t)
$$

$$\tag{D.4}$$

where $\mathbf{0}_k$ is a vector of all zeros of length k, I_k is the identity matrix of order k, and Δ is a diagonal matrix with the corresponding rates δ_i on the diagonal if $i \in \mathcal{T}$. For example, if $\mathcal{T} = \{3, 6\}$, then

$$
\Delta = \begin{bmatrix} \delta_3 & 0 \\ 0 & \delta_6 \end{bmatrix} \tag{D.5}
$$

Also, note that if $i \notin \mathcal{T}$, then $w_i(t) \equiv 0$ and $H(w_i(t)) = 1$.

- The only endpoint constraints are set at the initial time,

$$
\mathbf{e}(\mathbf{x}(t_0), \mathbf{x}(t_f), t_0, t_f) = \begin{bmatrix} x_1(0) \\ x_2(0) \\ x_3(0) \\ x_4(0) \\ x_5(0) \\ \mathbf{w}(0) \end{bmatrix}, \quad \mathbf{e}^L = \mathbf{e}^U = \begin{bmatrix} x_{1,0} \\ x_{2,0} \\ x_{3,0} \\ x_{4,0} \\ x_{5,0} \\ \mathbf{0}_k \end{bmatrix} \tag{D.6}
$$

where $x_{i,0}$ is chosen to either be the steady state value of the system in the absence of control inputs or the time-average of the time evolution of the system if the dynamics, in the absence of control inputs, is oscillatory. We assume there is no drug present initially so $w_i(0) = 0$, $i \in \mathcal{D}$.

- Finally, the path constraints consist of upper bounds on the drug concentrations and possibly a lower and/or upper bound on the AVs.

$$
\mathbf{h}(\mathbf{x}(t), \mathbf{u}(t), t) = \begin{bmatrix} x_5(t) \\ \mathbf{w}(t) \\ \mathbf{u}(t) \end{bmatrix}, \quad \mathbf{h}^L = \begin{bmatrix} x_5^L \\ \mathbf{0}_k \\ \mathbf{0}_k \end{bmatrix}, \quad \mathbf{h}^U = \begin{bmatrix} x_5^U \\ w^{\max}\mathbf{1}_k \\ \infty \end{bmatrix} \tag{D.7}
$$

where, for the first phase, $x_5^L = 0$ and $x_5^U = \infty$ but for the second phase we choose $x_5^L = x_5^f - \epsilon$ and $x_5^U + \epsilon$. Also, the upper bound on the drug concentration is chosen to be identical for all drugs in the therapy.

Solving Eq. (D.1) is not a trivial task, and typically there exists no closed form solution. Instead one typically must turn to numerical methods, such as PSOC, which we will discuss in the subsequent subsections in some detail. Nonetheless, one can derive a set of necessary conditions that any solution to Eq. (D.1) must satisfy using Pontryagin's minimum principle [110]. Developing these types of necessary

conditions allows us to construct a set of validation criteria with which we may test the quality of any solution returned by our numerical methods.

A full derivation of Pontryagin's minimum principle is beyond the scope of this work but it is readily available in many standard texts [110]. Here, we present the main results surrounding the Hamiltonian constructed from Eq. (D.1).

Minimizing the Hamiltonian

Define a vector of time-varying costates (or adjoint variables) as $\boldsymbol{\lambda}(t) = \begin{bmatrix} \boldsymbol{\lambda}_\mathbf{x}^T(t) & \boldsymbol{\lambda}_\mathbf{w}^T(t) \end{bmatrix}^T \in$ $\mathbb{R}^{5+k}$ so that $\boldsymbol{\lambda}_\mathbf{x}(t) \in \mathbb{R}^5$ and $\boldsymbol{\lambda}_\mathbf{w}(t) \in \mathbb{R}^k$. The Hamiltonian of the OCP in Eq. (D.1) is defined as,

$$
\begin{aligned}
H(\boldsymbol{\lambda}, \mathbf{x}, \mathbf{u}, t) &= F(\mathbf{x}, \mathbf{u}, t) + \boldsymbol{\lambda}^T \mathbf{f}(\mathbf{x}, \mathbf{u}, t) \\
&= \sum_{i \in \mathcal{T}} u_i + \boldsymbol{\lambda}^T \bar{\mathbf{f}}(\mathbf{x}) + \boldsymbol{\lambda} B \mathbf{u}
\end{aligned}
\tag{D.8}
$$

where $\boldsymbol{\lambda}(t) \in \mathbb{R}^n$ are the costates (or adjoint variables). A solution to Eq. (D.1) must also be a solution of the following minimization problem.

$$
\begin{aligned}
&\min_{\mathbf{u}(t)} \quad H(\boldsymbol{\lambda}, \mathbf{x}, \mathbf{u}, t) \\
&\text{s.t.} \quad \mathbf{h}^L \le \mathbf{h}(\mathbf{x}, \mathbf{u}, t) \le \mathbf{h}^U
\end{aligned}
\tag{D.9}
$$

To solve Eq. (D.9), we define the associated Lagrangian,

$$
\begin{aligned}
\bar{H}(\boldsymbol{\mu}, \boldsymbol{\lambda}, \mathbf{x}, \mathbf{u}, t) &= H(\boldsymbol{\lambda}, \mathbf{x}, \mathbf{u}, t) + \boldsymbol{\mu}^T \mathbf{h}(\mathbf{x}, \mathbf{u}, t) \\
&= \sum_{i \in \mathcal{T}} u_i + \boldsymbol{\lambda}^T \bar{\mathbf{f}}(\mathbf{x}) + \boldsymbol{\lambda}^T B \mathbf{u} + \mu_{x_5} x_5 + \boldsymbol{\mu}_\mathbf{w}^T \mathbf{w} + \boldsymbol{\mu}_\mathbf{u}^T \mathbf{u}
\end{aligned}
\tag{D.10}
$$

where $\boldsymbol{\mu} = \begin{bmatrix} \mu_{x_5} & \boldsymbol{\mu}_\mathbf{w}^T & \boldsymbol{\mu}_\mathbf{u}^T \end{bmatrix}^T \in \mathbb{R}^h$ is the copath vector with components associated with the components of the vector of path constraints in (D.7). A solution to Eq. (D.9), and thus to our original OCP, must satisfy,

$$
\frac{\partial \bar{H}}{\partial \mathbf{u}} = \mathbf{1}_k + B^T \boldsymbol{\lambda} + \boldsymbol{\mu}_\mathbf{u} = \mathbf{0}
\tag{D.11}
$$

where the costates evolve according to the dynamical equation,

$$\dot{\boldsymbol{\lambda}} = -\frac{\partial \bar{H}}{\partial \mathbf{x}} = -\left(\frac{\partial \bar{\mathbf{f}}}{\partial \mathbf{x}}\right)^{T} \boldsymbol{\lambda} + \begin{bmatrix} \mathbf{0}_4 \\ \mu_{x_5} \\ \boldsymbol{\mu}_{\mathbf{w}} \end{bmatrix} \tag{D.12}$$

The optimal control input $u_i(t)$, $i \in \mathcal{T}$, must satisfy the complementarity condition [56, 114]

$$\begin{cases} u_i(t) = 0 & \text{if} \quad \mu_i(t) < 0 \\ u_i(t) \geq 0 & \text{if} \quad \mu_i(t) = 0 \\ u_i(t) \to \infty & \text{if} \quad \mu_i(t) > 0 \end{cases} \tag{D.13}$$

Combining Eqs. (D.11) and (D.13), we can relate $\boldsymbol{\mu}_{\mathbf{u}}$ to the time-varying costates by noting from the structure of B, $B^T \boldsymbol{\lambda} = \boldsymbol{\lambda}_{\mathbf{w}}$ so that,

$$\boldsymbol{\mu}_{\mathbf{u}}(t) = -\mathbf{1}_k - \boldsymbol{\lambda}_{\mathbf{w}}(t) \tag{D.14}$$

Thus, if $\lambda_{w_i} > -1$ then $u_i = 0$, but if $\lambda_{w_i} = -1$, then all we can say is that $u_i \geq 0$. When $\lambda_{w_i} > -1$, the optimal control is said to have a *singular arc* (see chapter 5 in [110]). Despite the technical difficulties, we have arrived at our first set of validation conditions, that is,

$$u_i \cdot (-\lambda_{w_i} - 1) = 0, \quad \forall i \in \mathcal{T} \tag{D.15}$$

Let us now assume that we have solved Eq. (D.9), that is,

$$\mathcal{H}(t) = \min_{\mathbf{u} \in \mathbb{U}} H(\boldsymbol{\lambda}, \mathbf{x}, \mathbf{u}, t) \tag{D.16}$$

where $\mathbb{U}$ is the set of feasible control inputs, i.e., they satisfy all of the constraints imposed by Eq. (D.1). The evolution of the Hamiltonian at the optimal solution can be written,

$$\frac{d\mathcal{H}}{dt} = \frac{\partial H}{\partial t} \tag{D.17}$$

where, since in our OCP, H does not explicitly depend on time, we expect that $d\mathcal{H}/dt = 0$ and so $\mathcal{H}$ should be constant. This is the second validation condition.

While in the paper and the sections in appendix D, we display time traces of the states and the control inputs as they are the quantities of interest to the general reader, we are also able to access the costate and copath time traces, as well as the time trace of the Hamiltonian. In Fig. D.11 we show a typical set of output that we use for measuring the quality of our returned numerical solution. The sample shows a monotherapy where $\mathcal{T} = \{4\}$. Panel (a) shows the level of AVs, $x_5(t)$, and panel (b) shows the drug concentration $w_4(t)$. Panel (c) contains the copath associated with the level of AVs, $\mu_{x_5}(t)$. Note that during the first phase when there is no finite bound on $x_5(t)$ the copath $\mu_{x_5}(t) = 0$, while during second phase if $\mu_{x_5}(t) \neq 0$ then $x_5(t) = x_5^f \pm \epsilon$. In panel (d) we plot the other copath $\mu_{w_4}(t)$. The control input $u_4(t)$ itself is shown in panel (e) along with the costate $\lambda_{w_4}(t)$ in panel (f). Note that the times at which $u_4(t) > 0$ correspond to times when $\lambda_{w_4}(t) = -1$ as expected. Panel (g) plots the time evolution of the Hamiltonian evaluated at the optimal solution. Note that the y-axis is scaled by 10^{-2}. We see that $\mathcal{H} \approx const$ within each phase, with a jump occurring at the interface between the two phases. As we cannot say anything about the value of the Hamiltonian at the interface, a discontinuity at this point in time can be expected.

D.2.1 Discretization of the OCP

As presented in the previous subsection, we have seen that the set of necessary conditions which must be satisfied consist of a system of coupled nonlinear differential equations for $\mathbf{x}(t)$ and $\boldsymbol{\lambda}(t)$ along with a set of non-trivial constraints. Searching for an analytic solution is unlikely to be successful and so instead we turn to pseudo-spectral optimal control (PSOC).

In short, PSOC is a methodology by which one may discretize an OCP, approximating the integrals by quadratures and the time-varying states and control inputs with interpolating polynomials.

The key to PSOC is choosing the discretization points properly. Let $\{\tau_i\}$, $i = 0, \ldots, N$, denote the discretization points. Typically these are chosen as the roots of an orthogonal polynomial such as a Legendre polynomial or a Chebyshev polynomial of order N. For some popular choices of discretization schemes see [111]. For concreteness, we will assume that $\tau_0 = -1$ and $\tau_N = 1$, i.e., we are using a discretization scheme that includes the endpoints and is normalized by the mapping,

$$t = \frac{t_f - t_0}{2}\tau + \frac{t_f + t_0}{2} \tag{D.18}$$

For the discretization scheme chosen, we also compute the associated quadrature weights. For instance, if we choose the roots of a Legendre polynomial as the discretization scheme, the associated quadrature weights can be found in the typical way for Gauss quadrature. The time-varying states and control inputs are found by approximating them with a Lagrange interpolating polynomial.

$$\mathbf{x}(\tau) \approx \hat{\mathbf{x}}(\tau) = \sum_{i=0}^{N} \hat{\mathbf{x}}_i L_i(\tau)$$
$$\mathbf{u}(\tau) \approx \hat{\mathbf{u}}(\tau) = \sum_{i=0}^{N} \hat{\mathbf{u}}_i L_i(\tau) \tag{D.19}$$

The Lagrange interpolating polynomials are defined as,

$$L_i(\tau) = \prod_{j=0,j\neq i}^{N} \frac{\tau - \tau_j}{\tau_i - \tau_j} \tag{D.20}$$

Note that the Lagrange interpolating polynomials satisfy the isolation property, that is, $L_i(\tau_j) = \delta_{i,j}$. We can thus construct a set of algebraic equations corresponding to the discretization points $\{\tau_i\}$. Define $D_{k,i} = \frac{dL_i}{d\tau}(\tau_k)$ so that the derivative of the states at the discretization points can be approximated as,

$$\dot{\hat{\mathbf{x}}}(\tau_k) = \sum_{i=0}^{N} \hat{\mathbf{x}}_i D_{k,i} \tag{D.21}$$

With Eqs. (D.19) and (D.21), we can approximate the original system of n differential equations as $n(N + 1)$ algebraic equations.

$$\sum_{i=0}^{N} D_{k,i}\hat{\mathbf{x}}_i - \frac{t_f - t_0}{2}\mathbf{f}(\hat{\mathbf{x}}_k, \hat{\mathbf{u}}_k, \tau_k) = \mathbf{0}_n, \quad k = 1, \ldots, N$$

$$\hat{\mathbf{x}}_N - \hat{\mathbf{x}}_0 - \sum_{k=1}^{N}\sum_{i=0}^{N} w_k D_{k,i}\hat{\mathbf{x}}_i = \mathbf{0}_n$$

(D.22)

The last set of algebraic constraints arise from the consistency condition $\int_{t_0}^{t_f} \dot{\mathbf{x}}(t)dt = \mathbf{x}(t_f) - \mathbf{x}(t_0)$. Similarly to the consistency condition, the integral in the cost function is approximated as,

$$J = \int_{t_0}^{t_f} F(\mathbf{x}, \mathbf{u}, t) \approx \hat{J} = \frac{t_f - t_0}{2}\sum_{k=1}^{N} F(\hat{\mathbf{x}}_k, \hat{\mathbf{u}}_k, \tau_k)$$

(D.23)

The discretized approximation of the original OCP is compiled into the following nonlinear programming (NLP) problem.

$$\min_{\mathbf{u}_i} \quad \hat{J} = \frac{t_f - t_0}{2}\sum_{k=1}^{N} F(\hat{\mathbf{x}}_k, \hat{\mathbf{u}}_k, \tau_k)$$

$$\text{s.t.} \quad \sum_{i=0}^{N} D_{k,i}\hat{\mathbf{x}}_i - \frac{t_f - t_0}{2}\mathbf{f}(\hat{\mathbf{x}}_k, \hat{\mathbf{u}}_k, \tau_k) = \mathbf{0}, \quad k = 1, \ldots, N$$

$$\hat{\mathbf{x}}_N - \hat{\mathbf{x}}_0 - \sum_{k=1}^{N}\sum_{i=0}^{N} w_k D_{k,i}\hat{\mathbf{x}}_i = \mathbf{0}$$

$$\mathbf{e}^L \leq \mathbf{e}(\hat{\mathbf{x}}_0, \hat{\mathbf{x}}_N, \tau_0, \tau_N) \leq \mathbf{e}^U$$

$$\mathbf{h}^L \leq \mathbf{h}(\hat{\mathbf{x}}_k, \hat{\mathbf{u}}_k, \tau_k) \leq \mathbf{h}^U$$

(D.24)

With the above results, we now present the application to the full multi-phase optimal control problem. In general, let us assume there are p phases where $p = 2$ in our problem. Each phase is active within the interval $t \in [t_0^{(p)}, t_f^{(p)}]$. In each phase there is a cost function $J^{(p)}$, a dynamical system $\mathbf{f}^{(p)}$, a set of endpoint constraints $\mathbf{e}^{(p)}$, and a set of path constraints $\mathbf{h}^{(p)}$. If two phases, p and q, are linked, then there

also exists a set of linkage constraints $\Phi^{(p,q)}$.

$$\min_{\mathbf{u}^{(p)}} \sum_{p=1}^{P} J^{(p)} = \sum_{p=1}^{P} \int_{t_0^{(p)}}^{t_f^{(p)}} F^{(p)}(\mathbf{x}^{(p)}, \mathbf{u}^{(p)}, t)dt$$

$$\text{s.t.} \quad \dot{\mathbf{x}}^{(p)}(t) = \mathbf{f}^{(p)}(\mathbf{x}^{(p)}, \mathbf{u}^{(p)}, t)$$

$$\mathbf{h}^{L,(p)} \le \mathbf{h}^{(p)}(\mathbf{x}^{(p)}, \mathbf{u}^{(p)}, t) \le \mathbf{h}^{U,(p)} \tag{D.25}$$

$$\mathbf{e}^{L,(p)} \le \mathbf{e}^{(p)}(\mathbf{x}^{(p)}(t_0^{(p)}), \mathbf{x}^{(p)}(t_f^{(p)}), t_0^{(p)}, t_f^{(p)}) \le \mathbf{e}^{U,(p)}$$

$$\Phi^{L,(p,q)} \le \Phi^{(p,q)}(\mathbf{x}^{(p)}, \mathbf{x}^{(q)}, \mathbf{u}^{(p)}, \mathbf{u}^{(q)}) \le \Phi^{U,(p,q)}$$

Each phase is discretized with its own set of points, $\{\tau_i^{(p)}\}$ so that,

$$\mathbf{x}^{(p)}(\tau) \approx \hat{\mathbf{x}}^{(p)}(\tau) = \sum_{i=1}^{N} \hat{\mathbf{x}}_i^{(p)} L_i(\tau) \tag{D.26}$$

so that the full multi-phase NLP is,

$$\min_{\mathbf{u}_i^{(p)}} \sum_{p=1}^{P} \frac{t_f^{(p)} - t_0^{(p)}}{2} \sum_{k=1}^{N} F^{(p)}(\hat{\mathbf{x}}_k^{(p)}, \hat{\mathbf{u}}_k^{(p)}, \tau_k)$$

$$\text{s.t.} \quad \sum_{i=0}^{N} D_{k,i}\hat{\mathbf{x}}_i^{(p)} - \frac{t_f^{(p)} - t_0^{(p)}}{2}\mathbf{f}^{(p)}(\hat{\mathbf{x}}_k^{(p)}, \hat{\mathbf{u}}_k^{(p)}, \tau_k) = \mathbf{0}_n, \quad p = 1, \ldots, P, \quad k = 1, \ldots, N$$

$$\hat{\mathbf{x}}_N^{(p)} - \hat{\mathbf{x}}_0^{(p)} - \frac{t_f^{(p)} - t_0^{(p)}}{2} \sum_{k=1}^{N} \sum_{i=0}^{N} w_k D_{k,i}\hat{\mathbf{x}}_i = \mathbf{0}_n, \quad p = 1, \ldots, P$$

$$\mathbf{e}^{L,(p)} \le \mathbf{e}^{(p)}(\hat{\mathbf{x}}_0^{(p)}, \hat{\mathbf{x}}_N^{(p)}, t_0^{(p)}, t_f^{(p)}) \le \mathbf{e}^{U,(p)}, \quad p = 1, \ldots, P$$

$$\mathbf{h}^{L,(p)} \le \mathbf{h}^{(p)}(\hat{\mathbf{x}}_k^{(p)}, \hat{\mathbf{u}}_k^{(p)}, \tau_k) \le \mathbf{h}^{U,(p)}, \quad k = 1, \ldots, N, \quad p = 1, \ldots P$$

$$\Phi^{L,(p,q)} \le \Phi^{(p,q)}(\hat{\mathbf{x}}_0^{(p)}, \hat{\mathbf{u}}_0^{(p)}, \hat{\mathbf{x}}_N^{(q)}, \hat{\mathbf{u}}_N^{(q)}) \le \Phi^{U,(p,q)}, \quad p, q = 1, \ldots, P$$

$$\tag{D.27}$$

To perform the discretization described in this subsection, we use the open-source C++ PSOC package $\mathcal{PSOPT}$ [112].

Next we show that Eq. (D.27) can be expressed in the typical NLP form [56]. Let

$\mathbf{z}^{(p)}$ contain all of the variables for phase p.

$$\mathbf{z}^{(p)} = \begin{bmatrix} \hat{\mathbf{x}}_0^{(p)} \\ \vdots \\ \hat{\mathbf{x}}_N^{(p)} \\ \hat{\mathbf{u}}_0^{(p)} \\ \vdots \\ \hat{\mathbf{u}}_N^{(p)} \end{bmatrix} \in \mathbb{R}^{(n+m)} \tag{D.28}$$

Next, let $\mathbf{z}$ contain the variables for every phase,

$$\mathbf{z} = \begin{bmatrix} \mathbf{z}^{(1)} \\ \vdots \\ \mathbf{z}^{(P)} \end{bmatrix} \in \mathbb{R}^{(N+1)(n+m)} \tag{D.29}$$

With some algebraic manipulation, the entire discretized multi-phase OCP can be rewritten as an NLP in the typical form.

$$\begin{aligned} \min_{\mathbf{z}} \quad & c(\mathbf{z}) \\ \text{s.t.} \quad & \mathbf{g}(\mathbf{z}) = \mathbf{0} \\ & \mathbf{d}(\mathbf{z}) \leq \mathbf{0} \end{aligned} \tag{D.30}$$

To solve the large-scale NLP in Eq. (D.30) we employ an interior-point algorithm [56]. Specific details of the algorithm are outside the scope of this paper. We used the open-source C++ package Ipopt [113] to solve each instance of Eq. (D.30). We direct interested readers who would like to learn more about the technical detailed involved when solving Eq. (D.30) to the documentation provided with Ipopt.

The optimal solution returned, $\mathbf{z}^*$, is separated into its component parts; first by splitting it into the phases $\mathbf{z}^{(p)*}$, and second by reconstructing the discrete states and contrlol inputs, $\hat{\mathbf{x}}_i^*$ and $\hat{\mathbf{u}}_i^*$. The continuous time control inputs and states are then reconstructed using the Lagrange interpolating polynomials in Eq. (D.19). With the continuous time states and control inputs, $\mathbf{x}^*(t)$ and $\mathbf{u}^*(t)$, we then verify that the necessary conditions are met to within an acceptable tolerance.

D.3   The Response of AVs to Constant Perturbation by Dual Therapies

Before solving the optimal control problem presented in the main text, we explore the capabilities of the dual therapies in terms of upregulate and downregulate with constant drug concentration as we did in Fig. 6.3 of the main manuscript. There, we plotted the long-time response of the system to an individual time-constant drug concentration (w) perturbation for the two sets of parameters $C_{\text{Nu}} = C_{\text{En}} = 0.1$ and $C_{\text{Nu}} = C_{\text{En}} = 0.6$. Similarly, in Fig. D.3 and D.4, we plot the long-time system AV response for the case of dual therapies with time-constant drug concentration perturbations.

In Fig. D.3, we set the parameters $C_{\text{Nu}} = C_{\text{En}} = 0.1$. For these parameter values, in the absence of any drugs (control inputs), the sole attractor of the dynamical system corresponds to a high AV count (≈ 37). Fig. D.3 shows the long-time AV response when the system is perturbed by different combinations of constant inputs. Note that those subsets that contain either drug 2 or 6 are capable of driving the AVs to zero if w^{max} is made large enough (pairs $\{2,3\}$, $\{2,4\}$, $\{2,6\}$, $\{3,6\}$, $\{4,6\}$, and $\{1,6\}$). For each pair $\{i,j\}$, we set $w_i = w_j$ and all other values $w_k = 0$, $k \neq i$ and $k \neq j$. The pair $\{3,4\}$ on the other hand is only capable of driving the AVs to ≈ 10 where any increase of w^{max} afterwards can produce no further results. Also, dual therapy $\{1,5\}$ is incapable of downregulate .

In Fig. D.4, we set the parameters $C_{\text{Nu}} = C_{\text{En}} = 0.6$, for which the free evolution of the system is periodic (see Fig. 6.2 in the main text), and show the same long-time AV response results under constant drug concentration perturbation. For all dual therapies shown, small drug concentrations are unable to remove the oscillations present (denoted by the shaded regions). Similar to Fig. D.3, we see that all drug combinations that contain either drug 2 or 6 are capable of driving the level of AVs

to zero for w^{max} set large enough. Also, dual therapy $\{3, 4\}$, as before, is only able to reduce the AVs level to ≈ 10 while the dual therapy $\{1, 5\}$ instead upregulates the AVs.

D.4 Exhaustive Analysis of Two-Drug Combinations

In this section, we present simulation results for all possible dual therapies. First, we set both the parameters $C_{\mathrm{Nu}} = C_{\mathrm{En}} = 0.1$ for which the number of AVs at steady state in the absence of control inputs is equal to ≈ 37. We attempt to downregulate the number of AVs using pairs of drugs from the set $\{2, 3, 4, 6\}$ so that there are a total of $\binom{4}{2} = 6$ combinations. A pair of drugs drawn from this set is called a dual therapy. If $\{i, j\}$ is a dual therapy, then we say $\{i\}$ and $\{j\}$ are its component monotherapies.

The goal is to investigate our ability to downregulate the number of AVs from the steady state value ≈ 37 to a lower value in a specified control time interval $[0, t_0]$ and, subsequently, to maintain the number of AVs near the target level for a second time interval $[t_0, t_f]$, by using each different dual therapy. We say a dual therapy is *viable* if it is capable of performing the goal stated. A dual therapy is deemed efficient if;

- the dual therapy is viable while at least one of its component monotherapies is not, and

- the total amount of drugs provided by the dual therapy is less than either of the component monotherapies.

To compare the efficiencies of the dual therapies we define $r^*_{i,k}(t) = \int_0^t u^*_i(\tau)d\tau$ as the total amount of drug i administered at time t as part of a $k = \mathrm{dual}$ or $k = \mathrm{mono}$

and introduce the quantities ρ_i and τ_i.

$$0 \leq \rho_i = \frac{r_{i,\text{dual}}^*(t_f)}{r_{i,\text{mono}}^*(t_f)} \leq 1, \tag{D.31}$$

Note that $r_{i,\text{dual}}^*(t_f) \leq r_{i,\text{mono}}^*(t_f)$, as otherwise the solution of the dual therapy optimal control problem would be suboptimal with respect to the case that only drug i is used. We also define the ratio

$$\tau_i = \frac{\bar{t}_{i,\text{dual}} - \bar{t}_{i,\text{mono}}}{\bar{t}_{i,\text{mono}}} \tag{D.32}$$

where $\bar{t}_{i,\text{dual}}$ is the time when drug i is activated (that is, the earliest time at which the drug injection rate is nonzero) as a part of a dual therapy and $\bar{t}_{i,\text{mono}}$ is the time when drug i is activated as a monotherapy . Note that $\tau_i > 0$ ($\tau_i < 0$) indicates a later (earlier) activation time of drug i as a part of dual therapy compared to as a monotherapy .

For our simulations, we set the upper bound of the drug concentrations to $w_i^{\max} = 2$ for each drug i, the time at which we apply the upper bound to the AVs to $t_0 = 120$ minutes, the time at which we end the simulation to $t_f = 240$ minutes, and we set the initial condition $\mathbf{x}(0)$ to be equal to the steady state solution of the system in the absence of control inputs with parameters $C_{\text{En}} = C_{\text{Nu}} = 0.1$. In Fig. D.5, we plot the total drug administered $r_i(t) = \int_0^t u_i(\tau)d\tau$ in the interval $[0, t_f]$. The plots on the diagonal panels, labeled (u_i, u_i), correspond to the monotherapies and the plots on the upper triangular panels, labeled (u_i, u_j), correspond to the dual therapies . Symmetric to each upper triangular panel (u_i, u_j), the corresponding lower triangular panel (u_j, u_i) contains the values of the ratios ρ_i and τ_i in Eqs. (D.31) and (D.32), respectively.

We notice from Fig. 6.3A in the main text that the only monotherapies which can downregulate the number of AVs from ≈ 37 to ≈ 10, with $w_i \leq 2$, is $\{4\}$. Thus, the red crosses in panels (u_2, u_2), (u_3, u_3) and (u_6, u_6) in Fig. D.5 indicate that those monotherapies cannot solve the downregulate problem. Clearly, dual therapies

$\{2,4\}$, $\{3,4\}$ and $\{4,6\}$ are viable as drug $\{4\}$ as a monotherapy is viable. On the other hand, the dual therapies $\{2,3\}$ and $\{3,6\}$ are not viable. The most interesting dual therapy is $\{2,6\}$ as neither component monotherapy is viable yet as a pair they are variable Thus by our stated goal and definitions, the dual therapy $\{2,6\}$ is efficient according to our criteria. Also, dual therapy $\{3,4\}$ is deemed efficient as the total consumption of drug 4 is much lower ($\rho_4 = 0.29$) than the total consumption of drug 4 as a monotherapy as shown in panel (u_3, u_4) in Fig. D.5. We also observe the faster response of drug 4 as a part of the $\{3,4\}$ dual therapy than its response as a monotherapy because $\tau_4 = 0.32 > 0$.

In Fig. D.6, we consider the dual therapies by combining one of the downregulate drugs, 2, 3, 4 or 6, with one of the upregulate drugs, 1 or 5. A red cross in a panel again represents a monotherapy or a dual therapy that is not viable. While the dual therapies $\{1,4\}$ and $\{4,5\}$ are viable, they are not efficient as neither drugs 1 nor 5 are used (non-zero).

In Fig. D.7, we present detailed results when we set the parameters $C_{\text{En}} = C_{\text{Nu}} = 0.6$, for which the dynamics in the absence of control inputs is oscillatory. In our numerical experiments, we attempt to downregulate the number of AVs from its initial periodic behavior to $x_5(t_0) \approx 10$ and to maintain the number of AVs near that value for the time interval $[t_0 = 120, t_f = 240]$. The red cross in panel (u_6, u_6) indicates the inability of drug 6 as a monotherapy to downregulate the AVs to the desired level. However, we found this drug to be particularly beneficial when used as a component in a dual therapy . We find that while all dual therapies are viable, the most efficient dual therapy is $\{2,6\}$, as the total amount of drug 2 required is reduced by more than five folds when compared to the monotherapy $\{2\}$. A comparison with drug 6 alone is not possible as drug 6 as a monotherapy is not viable. The dual therapy $\{3,6\}$ is also efficient by our definition, but only slightly as the amount of drug 3 used is hardly reduced, $\rho_3 = 0.96$. For all other dual therapies , one of the

component drugs is never activated so while they may by viable, we do not consider them efficient.

In Fig. D.9, we summarize the results when we attempt to upregulate the number of AVs to ≈ 37 in the same control time interval $[0, t_0]$ and, subsequently, maintain the number of AVs throughout the time interval $[t_0, t_f]$ by using dual therapy $\{1, 5\}$. We observe that, while the dual therapy $\{1, 5\}$ is viable, it is not efficient as drug 1 is never activated and so we must use the same amount of drug 5 as when it is used as a monotherapy .

In Fig. D.10, we consider the dual therapies by combining one of the downregulate drugs, 2, 3, 4 or 6, with one of the upregulate drugs, 1 or 5. We observe that the dual therapies $\{1, 6\}$ and $\{5, 6\}$ are only efficient when $C_{\mathrm{En}} = C_{\mathrm{Nu}} = 0.6$. The other dual therapies while viable are not efficient as the upregulate component (either 1 or 5) is never activated (that is, non-zero).

Table D.1: Parameters of the model (Eq. (6.1)). See "Formulation of the Model" in Supplementary Methods for discussion. The parameter values are dimensionless except as indicated.

Parameter	Value	Parameter	Value
$r_{b,12}$	0	k_1	1.00×10^{-1}
$r_{m,12}$	1.00×10^1	k_2	3.00×10^{-1}
θ_{12}	3.00×10^{-1}	k_3	4.00×10^0
n_{12}	4.00×10^0	k_4	1.00×10^{-1}
$r_{b,13}$	0	δ_1	3.10×10^{-4}
$r_{m,13}$	1.00×10^1	δ_2	1.93×10^{-3}
θ_{13}	6.00×10^{-1}	δ_3	5.78×10^{-3}
n_{13}	6.00×10^0	δ_4	1.15×10^{-2}
$r_{b,23}$	0	δ_5	2.31×10^{-3}
$r_{m,23}$	6.00×10^0	δ_6	1.16×10^{-3}
θ_{23}	1.00×10^0	r_b	0
n_{23}	4.00×10^0	r_m	1.00×10^0
$r_{b,21}$	1.00×10^{-1}	θ	5.00×10^{-1}
$r_{m,21}$	6.00×10^0	n	2.00×10^0
θ_{21}	6.00×10^{-1}	T	1.00×10^0 (min)
n_{21}	4.00×10^0		
$r_{b,42}$	1.00×10^{-1}		
$r_{m,42}$	6.00×10^0		
θ_{42}	5.00×10^{-1}		
n_{42}	4.00×10^0		

Table D.2: Summary of measured drug half-lives used to set values for the drug clearance rate constants $\delta_1, \ldots, \delta_6$ in Eq. (6.1). Each half-life, $t_{1/2,i}$, is the measured half-life of a representative of drug type i. See the references cited in the table for details about the drugs and measurements.

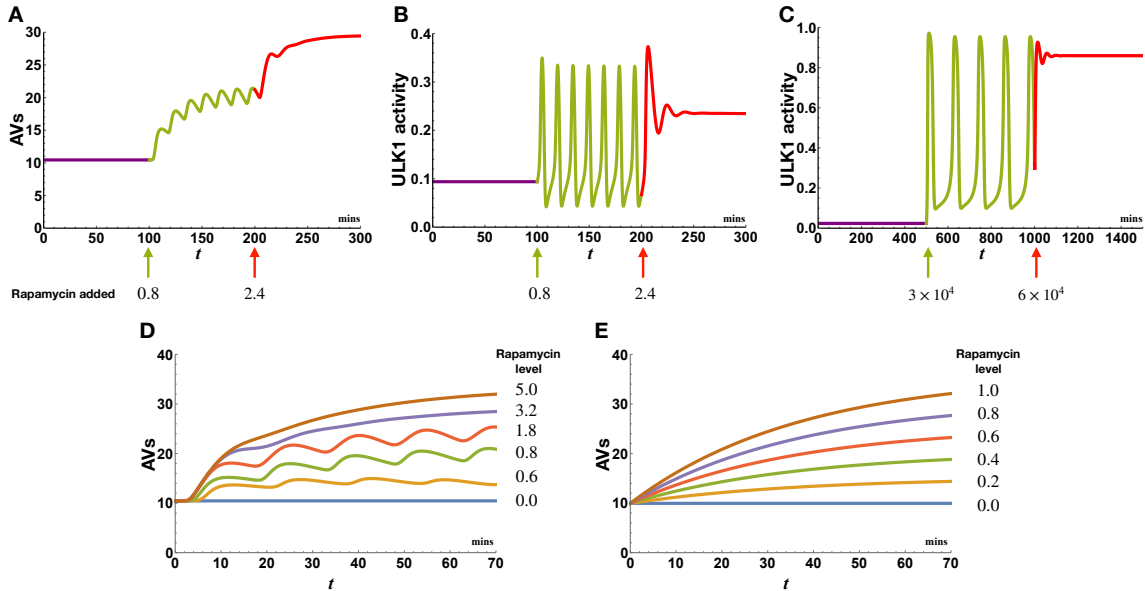| Drug i	Half-life $t_{1/2,i}$	Value (h^{-1})	Rate constant δ_i	Value (min^{-1})	Reference
1	$t_{1/2,1}$	~ 37	δ_1	3.10×10^{-4}	Sato et al.[182]
2	$t_{1/2,2}$	~ 6	δ_2	1.93×10^{-3}	Baselga et al.[183]
3	$t_{1/2,3}$	~ 2	δ_3	5.78×10^{-3}	Milkiewicz et al.[18
4	$t_{1/2,4}$	~ 1	δ_4	1.15×10^{-2}	Engers et al.[185]
5	$t_{1/2,5}$	~ 5	δ_5	2.31×10^{-3}	Cameron et al.[175
6	$t_{1/2,6}$	~ 10	δ_6	1.16×10^{-3}	Juric et al.[186]

Figure D.1: Comparison of simulations based on Eq. (6.1) and simulations based on models of Szymańska et al.[177] (Ref. 33 in the main text) and Martin et al.[178] (Ref. 34 in the main text). (A) AV dynamics, $x_5(t)$, predicted by Eq. (6.1). The value of x_5 is initially steady and low; the system is perturbed by two additions of rapamycin at time $t = 100$ and 200 min, as indicated. (B) Dynamics of ULK1 activity, $x_2(t)$, predicted by Eq. (6.1). The conditions considered are the same as those in panel A. (C) Dynamics of ULK1 activity predicted by the model of Szymańska et al.[177]. The conditions considered here correspond qualitatively to those considered in panels A and B. Initially, there is no rapamycin. Later, a low dose of rapamycin is added. Still later, a high dose of rapamycin is added. Note that the models of Eq. (6.1) and Szymańska et al.[177] have different timescales. This situation is partly a consequence of requiring Eq. (6.1) to reproduce the AV dynamics measured by Martin et al.[178]. Szymańska et al.[177] showed that the qualitative pattern of behavior illustrated here is a robust feature of known regulatory interactions among AMPK, MTORC1, and ULK1 (i.e., the pattern of behavior is insensitive to parameter variations). Furthermore, it should be noted that the model of Szymańska et al.[177] does not track AVs. Thus, there is no direct comparison to be made with the time course shown in panel A. (D) AV dynamics predicted by Eq. (6.1). AV production is stimulated by the addition of rapamycin at the (dimensionless) doses indicated in the legend. (E) AV dynamics predicted by the model of Martin et al.[178]. As in panel D, autophagy is induced by the addition of rapamycin at different doses, as indicated in the legend. For further discussion, see "Formulation of the Model" in Supplementary Methods.
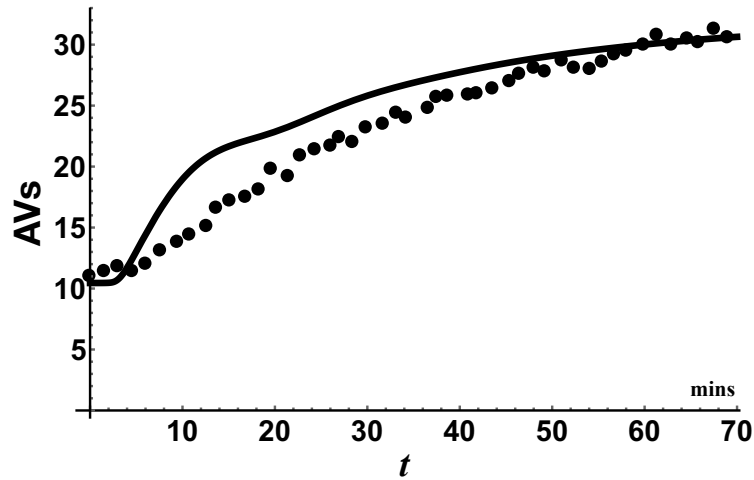
Figure D.2: Comparison of simulations based on Eq. (6.1) and data generated by Martin *et al.*[178] (Ref. 34 in the main text). We parameterized the model of Eq. (6.1) to roughly reproduce autophagic vesicle (AV) population dynamics reported by Martin et al.[178]. Our goal was not to reproduce the observed dynamics exactly but rather to select parameters that yield induction dynamics on a comparable timescale and a comparable maximal range of regulation. The measured dynamics were induced by inhibition of MTORC1 using AZD8055, a catalytic MTOR inhibitor. Dynamics were similar when autophagy was induced using rapamycin[178]. The curve corresponds to a simulation based on Eq. (6.1). Each dot corresponds to the average of AV counts measured in a series of fluorescence microscopy experiments[178]. The data shown here are taken from Figure 6B in Martin et al.[178]. For further discussion, see "Formulation of the Model" in Supplementary Methods.

Figure D.3: The dual therapy long-time response of the system in the case of time-constant drug concentration perturbations for the parameters $C_{\mathrm{Nu}} = C_{\mathrm{En}} = 0.1$. Note that when w is small, the system is oscillatory (represented by the shaded region in the panels). For each pair of drug, there is some value of w required to overcome the natural oscillatory behavior of the system.

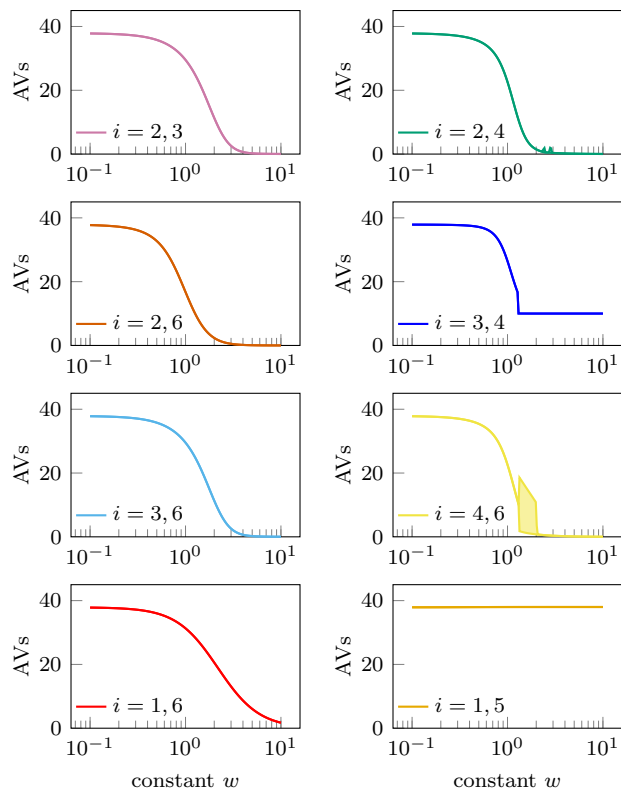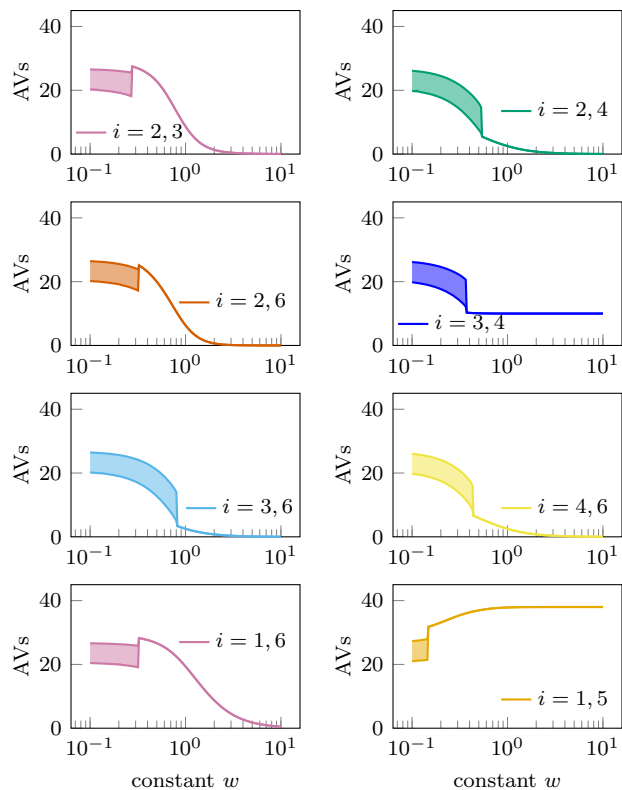Figure D.4: The dual therapy long-time response of the system in the case of time-constant drug concentration perturbations for the parameters $C_{\mathrm{Nu}} = C_{\mathrm{En}} = 0.6$.
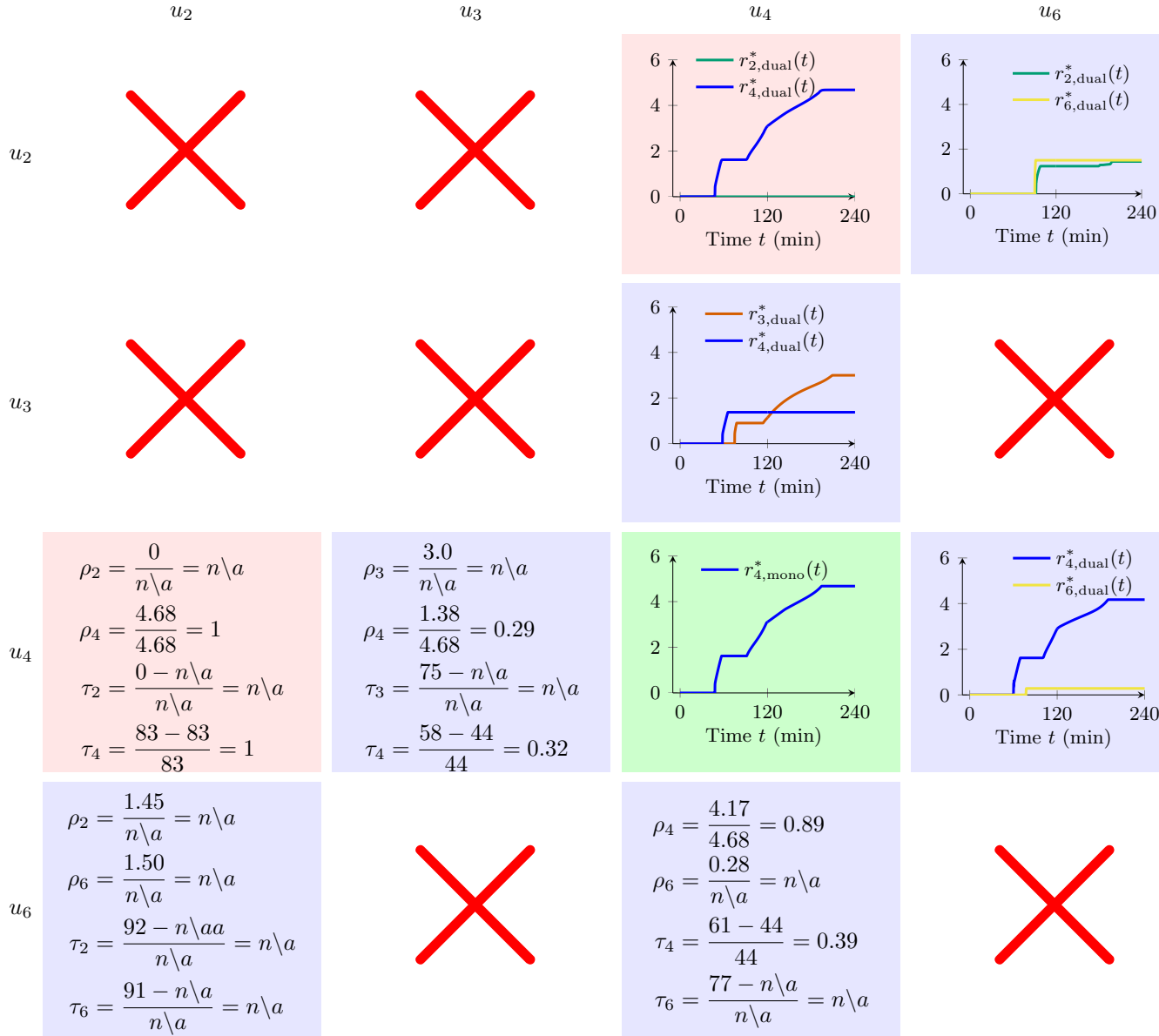
Figure D.5: The parameter set $C_{\mathrm{Nu}} = C_{\mathrm{En}} = 0.1$. The target level of AVs is set $x_5^f = 10$ and the maximum drug concentration is set $w_i^{\max} = 2$. The diagonal panels represent monotherapies while off-diagonal panels represent dual therapies . Super-diagonal panels plot the total drug administered and sub-diagonal panels show the efficiency ratios described in the text of the dual therapies . Those diagonal panels with a red cross correspond to those monotherapies which are not viable. The only viable monotherapy is $\{4\}$, which is shown with a green background. The off-diagonal panel with a red background for dual therapy $\{2, 4\}$ is viable, but it is not efficient as drug 2 is not activated. The other three viable dual therapies , $\{2, 6\}$, $\{3, 4\}$, and $\{4, 6\}$ are both viable and efficient, shown with a blue background.

Figure D.6: The parameter set $C_{\mathrm{Nu}} = C_{\mathrm{En}} = 0.1$. The target level of the AVs is set to $x_5^f = 10$ and the maximum drug concentration is set to $w_i^{\max} = 2$. Here we consider those dual therapies which combine one downregulate drug (2, 3, 4, or 6) with one of the upregulate drugs (1 or 5). Most of the dual therapies are not viable, which is represented with a red cross. The two viable dual therapies, $\{1, 4\}$ and $\{4, 5\}$, are not viable and so they are shown with a red background.
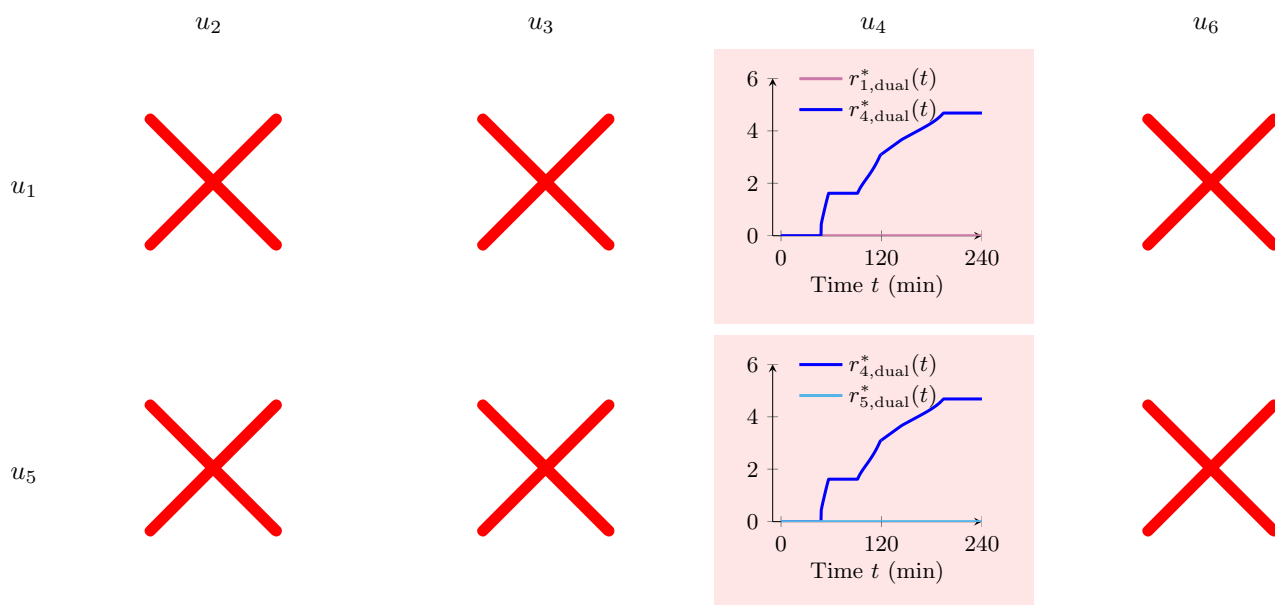
Figure D.7:   The parameter set $C_{\mathrm{Nu}} = C_{\mathrm{En}} = 0.6$. The target level of the AVs is set to $x_5^f = 10$ and the maximum drug concentration is set to $w_i^{\max} = 2$. The diagonal panels (u_i, u_i) (with a green background) show the total drug administered for monotherapies . The red cross on the diagonal panel corresponding to monotherapy $\{6\}$ represents the fact $\{6\}$ is not viable. The upper triangular panels (u_i, u_j), $i < j$, show the total drugs administered for dual therapies . In the lower triangular panels (u_j, u_i), $i < j$, we compare the dual therapies to their component monotherapies with the efficiency parameters τ and ρ. A red background in an off-diagonal panel represents those dual therapies which are viable but not efficient with respect to its component monotherapies . A blue background represents those dual therapies which are both viable and efficient.

$$u_1$$

$$u_6$$

$$u_1$$

$$u_6$$

$$\rho_1 = \frac{0.40}{n\backslash a} = n\backslash a$$

$$\rho_6 = \frac{1.70}{n\backslash a} = n\backslash a$$

$$\tau_1 = \frac{8 - n\backslash a}{n\backslash a} = n\backslash a$$

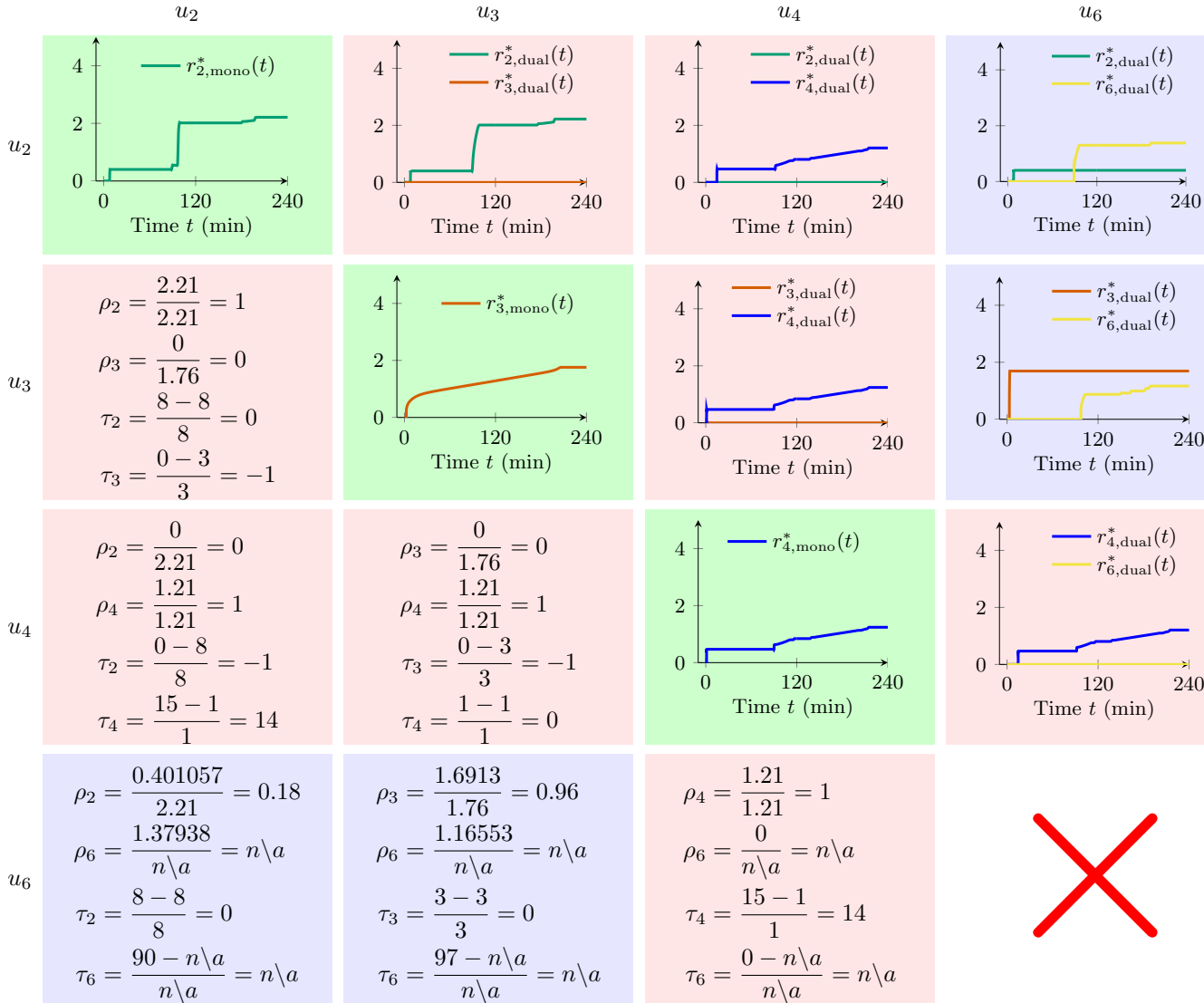$$\tau_6 = \frac{87 - n\backslash a}{n\backslash a} = n\backslash a$$

Figure D.8: The parameter set $C_{\mathrm{Nu}} = C_{\mathrm{En}} = 0.6$. The target level of the AVs is set to $x_5^f = 10$ and the maximum drug concentration is set to $w_i^{\max} = 2$. The red crosses on the diagonal panels represents the fact that the monotherapies $\{1\}$ and $\{6\}$ are not viable. On the other hand, the dual therapy $\{1, 6\}$ is both viable and efficient. The viable dual therapies composed of two monotherapies which are not viable alone are the type of dual therapies we find most interesting as they are not obvious when analyzing the monotherapies alone. In the lower triangular panel we compare the dual therapy to its component monotherapies with respect to the efficiency ratios ρ and τ.

$$\rho_1 = \frac{0}{n\backslash a} = n\backslash a$$

$$\rho_5 = \frac{0.55}{0.55} = 1$$

$$\tau_1 = \frac{0 - n\backslash a}{n\backslash a} = n\backslash a$$

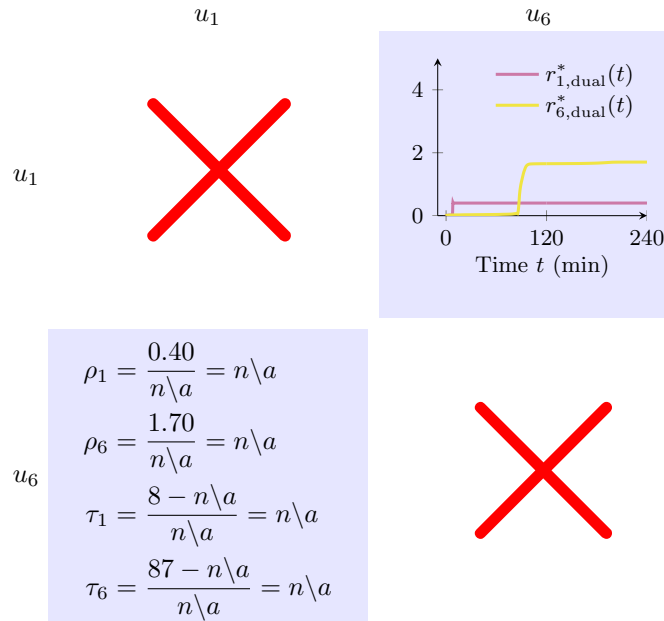$$\tau_5 = \frac{6 - 6}{6} = 0$$

Figure D.9: The parameter set $C_{\mathrm{Nu}} = C_{\mathrm{En}} = 0.6$. The target level of the AVs is set to $x_5^f = 10$ and the maximum drug concentration is set to $w_i^{\max} = 2$. The diagonal panels represent the monotherapies $\{1\}$ and $\{5\}$. A red cross on the diagonal panel for monotherapy $\{1\}$ represents the fact $\{1\}$ is not viable. On the other hand, monotherapy $\{5\}$ is viable (shown with a green background). The dual therapy $\{1, 5\}$ is viable (total drug administered is shown with the red background in the upper triangular panel) but is not efficient. The inefficiency is shown in the lower triangular panel with the efficiency ratios $\rho_5 = 1$.
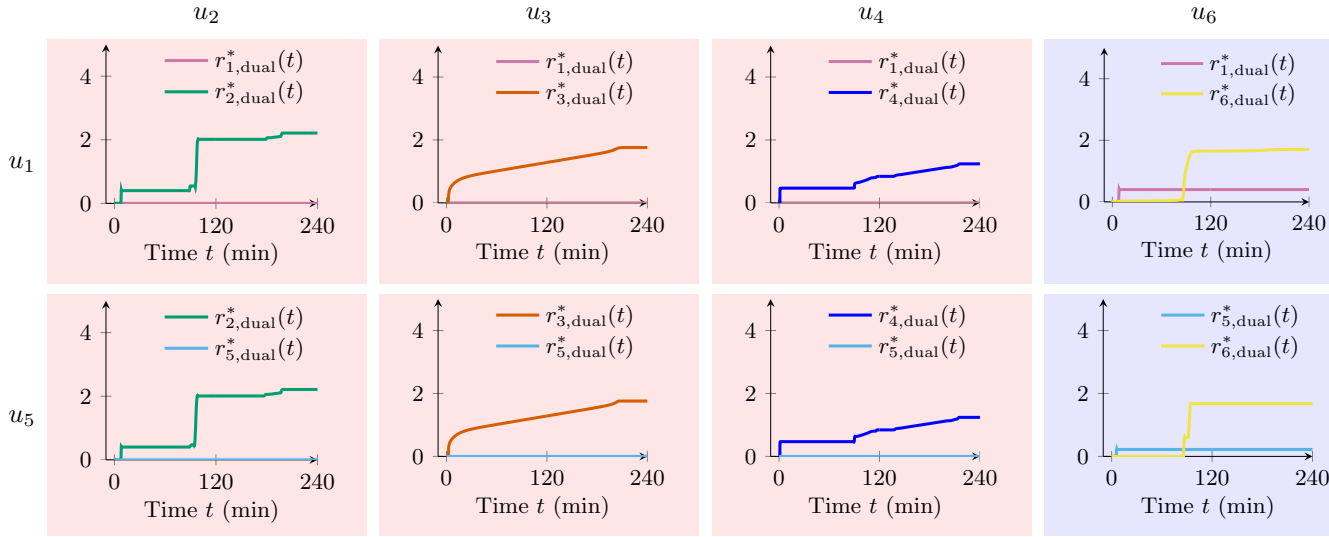
Figure D.10: The parameter set $C_{\mathrm{Nu}} = C_{\mathrm{En}} = 0.6$. The target level of AVs is set to $x_5^f = 10$ and the maximum drug concentration is set to $w_i^{\mathrm{max}} = 2$. Here we consider those dual therapies compose of one downregulate drug (2, 3, 4, or 6), and one upregulate drug (1 or 5). Those panels with a red background represent dual therapies which are viable but not efficient while the two dual therapies $\{1, 6\}$ and $\{5, 6\}$ are efficient. In fact, as seen before, neither the component monotherapy $\{6\}$ nor the upregulate drugs are viable for this parameter set, so these efficient dual therapies are particularly interesting as they could not be found when analyzing the monotherapies alone.
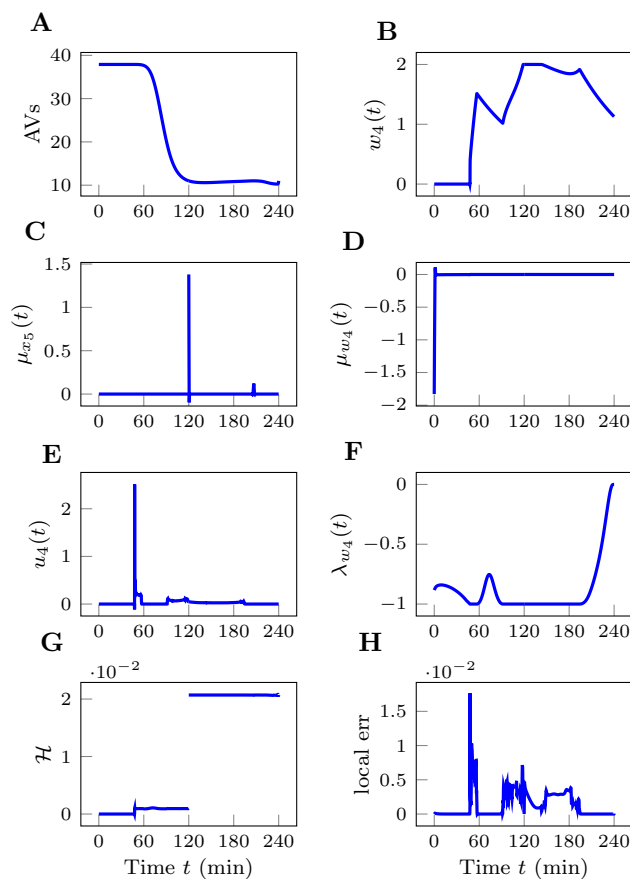
Figure D.11: A) The optimal time evolution of the amount of AVs. B) The optimal time evolution of the drug concentration $w_4(t)$. C) The time evolution of the path covector μ_{x_5} associated with the upper bound applied to $x_5(t)$. D) The time evolution of the path covector μ_{w_4} associated with the state $w_4(t)$. E) The optimal time evolution of the drug $u_4(t)$. F) The costate $\lambda_{w_4}(t)$ associated with the state $w_4(t)$. G) The time evolution of the lower Hamiltonian $\mathcal{H}$. H) The relative local discretization error at each time t.